LIGHTWEIGHT STRUCTURAL METALLIC MATERIALS

EDITED BY: Minghui Cai, Hua Ding, Peter Hodgson and Qi Chao
PUBLISHED IN: Frontiers in Materials

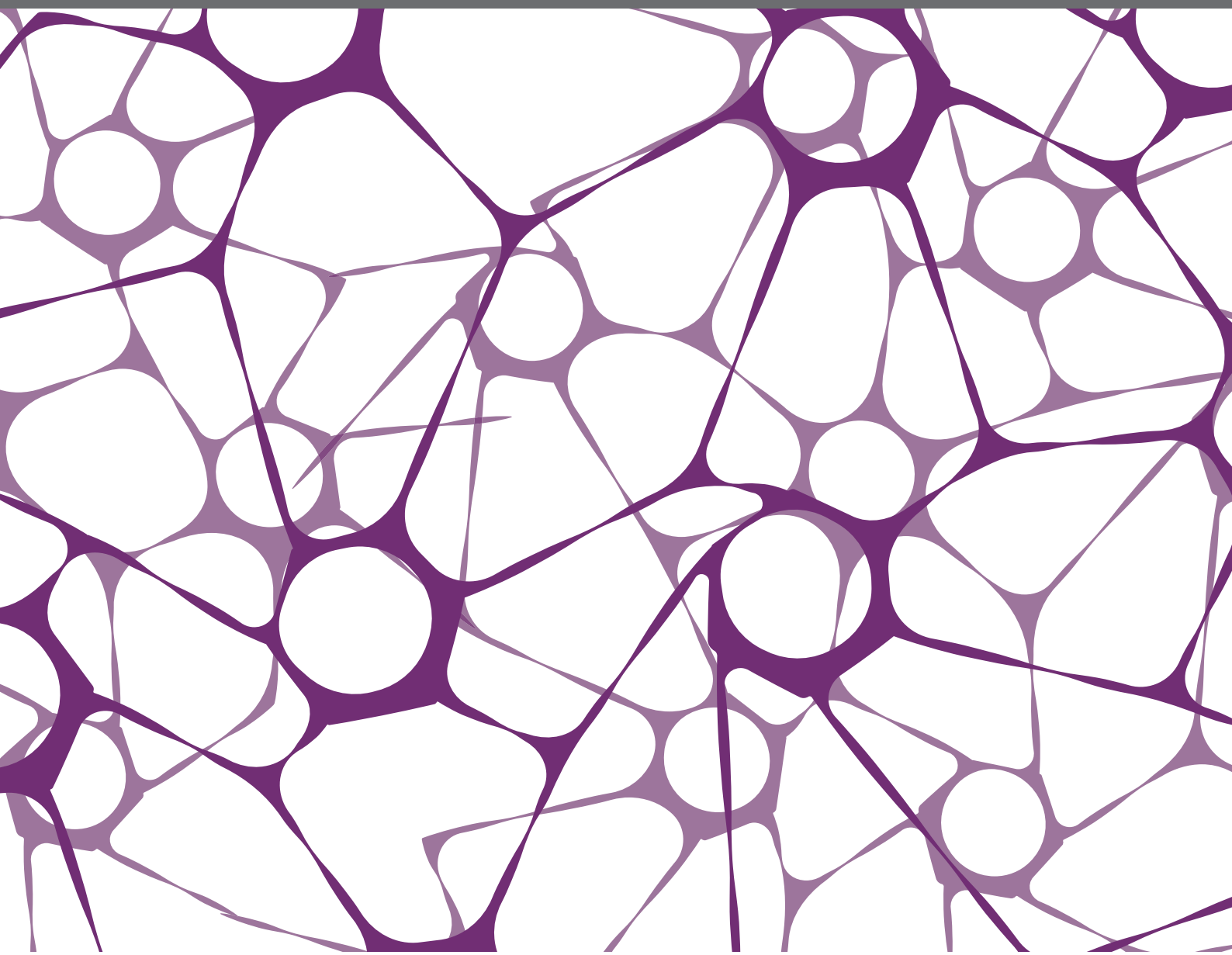

frontiers Research Topics

ISSN 1664-8714
ISBN 978-2-88974-798-6
DOI 10.3389/978-2-88974-798-6

About Frontiers

Frontiers is more than just an open-access publisher of scholarly articles: it is a pioneering approach to the world of academia, radically improving the way scholarly research is managed. The grand vision of Frontiers is a world where all people have an equal opportunity to seek, share and generate knowledge. Frontiers provides immediate and permanent online open access to all its publications, but this alone is not enough to realize our grand goals.

Frontiers Journal Series

The Frontiers Journal Series is a multi-tier and interdisciplinary set of open-access, online journals, promising a paradigm shift from the current review, selection and dissemination processes in academic publishing. All Frontiers journals are driven by researchers for researchers; therefore, they constitute a service to the scholarly community. At the same time, the Frontiers Journal Series operates on a revolutionary invention, the tiered publishing system, initially addressing specific communities of scholars, and gradually climbing up to broader public understanding, thus serving the interests of the lay society, too.

Dedication to Quality

Each Frontiers article is a landmark of the highest quality, thanks to genuinely collaborative interactions between authors and review editors, who include some of the world's best academicians. Research must be certified by peers before entering a stream of knowledge that may eventually reach the public - and shape society; therefore, Frontiers only applies the most rigorous and unbiased reviews.
Frontiers revolutionizes research publishing by freely delivering the most outstanding research, evaluated with no bias from both the academic and social point of view. By applying the most advanced information technologies, Frontiers is catapulting scholarly publishing into a new generation.

What are Frontiers Research Topics?

Frontiers Research Topics are very popular trademarks of the Frontiers Journals Series: they are collections of at least ten articles, all centered on a particular subject. With their unique mix of varied contributions from Original Research to Review Articles, Frontiers Research Topics unify the most influential researchers, the latest key findings and historical advances in a hot research area! Find out more on how to host your own Frontiers Research Topic or contribute to one as an author by contacting the Frontiers Editorial Office: frontiersin.org/about/contact

LIGHTWEIGHT STRUCTURAL METALLIC MATERIALS

Topic Editors:
Minghui Cai, Northeastern University, China
Hua Ding, Northeastern University, China
Peter Hodgson, Deakin University, Australia
Qi Chao, Deakin University, Australia

Citation: Cai, M., Ding, H., Hodgson, P., Chao, Q., eds. (2022). Lightweight Structural Metallic Materials. Lausanne: Frontiers Media SA. doi: 10.3389/978-2-88974-798-6

Table of Contents

frontiers in Materials

ORIGINAL RESEARCH
published: 16 November 2020
doi: 10.3389/fmats.2020.603464

Strain Accumulation and Microstructural Evolution During Friction Stir Welding of Pure Magnesium

Zhuoliang Li[1,2], Hua Ding[1,2], Yu Chen[3], Jizhong Li[4] and Lizhong Liu[1,2]*

[1]School of Material Science and Engineering, Northeastern University, Shenyang, China, [2]Key Laboratory of Lightweight Structural Materials, Northeastern University, Shenyang, China, [3]School of Mechanical Engineering and Automation, Northeastern University, Shenyang, China, [4]FSW Welding Technology (Shanghai) Co., LTD, Shanghai, China

In this study, the stain accumulation during friction stir welding of pure Mg was predicted and verified at different rotation speeds, together with the detailed microstructural evolution. The results indicate that the strain accumulation can be divided into three stages: 1) acceleration flow, 2) high velocity flow, and (III) decelerate and constant velocity flow. The rate of strain accumulation was relatively low at both stage I and stage III, while it became extremely high at stage III. The higher the speed of rotation, the severe plastic deformation more easily occurred within the material. The accumulated strain of pure Mg were determined to be approximately 12.8 and 14.5 at the rotation speed of 1,000 and 1,500 rpm, respectively. Relatively believable equations were established by calculation and derivation. In addition, the microstructural evolution shows that that the friction stir welding processed pure Mg first experienced significant grain refinement during plastic deformation but led to an obvious grain growth at the later stage due to the heat effect by high temperature field.

Keywords: friction stir welding, pure magnesium, strain, microstructural evolution, electron back-scattered diffraction, empirical equations

OPEN ACCESS

Edited by:
Liqiang Wang,
Shanghai Jiao Tong University, China

Reviewed by:
Wencai Liu,
Shanghai Jiao Tong University, China
Zhen Zhang,
Hefei University of Technology, China

****Correspondence:***
Hua Ding
dingh@smm.neu.edu.cn

Specialty section:
This article was submitted to Structural Materials, a section of the journal Frontiers in Materials

Received: *07 September 2020*
Accepted: *22 October 2020*
Published: *16 November 2020*

Citation:
Li Z, Ding H, Chen Y, Li J and Liu L (2020) Strain Accumulation and Microstructural Evolution During Friction Stir Welding of Pure Magnesium. Front. Mater. 7:603464. doi: 10.3389/fmats.2020.603464

INTRODUCTION

As one of structural metallic materials with the lowest density in engineering applications, magnesium (Mg) and its alloys have the following advantages such as high specific strength and high specific stiffness, high damping and electromagnetic shielding performance, and the excellent properties of casting and machining (Mordike and Ebert, 2001). Mg alloys have broad application prospects in automotive, electronics, aerospace and many other fields. However, low melting point, high thermal conductivity rate, and poor antioxidant capacity seriously influence the formability and welding performance of Mg and its alloys, thus restricting its further development and application (Avedesian and Baker, 1999).

As to the traditional welding processes, the welding performance of pure Mg material is poor. Mg materials are easily oxidized during welding processes, and MgO film with high melting point (~2,500°C) can be formed on the surface of the material. The MgO film covers the molten pool and groove, which seriously affects the welding formation process. MgO inclusions formed during the welding process also make effects on the plasticity of the weld metal. In addition, the high thermal conductivity rate always results in the widening of heat affected zone, overheating and the

microstructural coarsening. Thus, the mechanical properties of the welded joint become unsatisfactory. In recent years, much attention has been paid on friction stir welding (FSW) technology. As a new type of solid connection technology, cracks and inclusions caused by the melting welding can be effectively avoided by means of FSW technology (Chen et al., 2016a). Meanwhile, as one of the severe plastic deformation (SPD) technologies, FSW process can also result in the fine microstructure with excellent mechanical properties (Nikulin et al., 2012; Zhou et al., 2020).

According to the study of Yang et al. (2013), fine-grained Mg-10Gr-3Y-0.5Zr alloy was prepared by FSW. The alloy was subjected to superplastic deformation in the temperature range of 400–425°C, and a maximum tensile ductility of 1,110% was achieved. Yang et al. (2010) studied the effect of different shoulder dimensions on the FSWed Mg-3Al-Zn plates at a traverse speed of 100 mm/min and a rotation rate of 800 rpm. The results showed that as the shoulder diameter increased, the tensile strength of the welds tended to increase and the total elongation to fracture was significantly improved. Dissimilar FSW of ZK60 and AZ31 magnesium alloys was studied by Liu et al. (2013). The results showed that the dissimilar plates were joined successfully and no obvious defects were observed. Nevertheless, most studies merely focus on the forming ability of the FSWed Mg and its alloys and/or the corresponding microstructures and mechanical properties (Commin et al., 2012; Yang et al., 2011; Ahmadkhaniha et al., 2016). Studies on the variation of strain and/or strain rate of pure Mg during FSW processes are still limited. As one of the most important parameters of SPD process, the accumulated strain in the material can always directly affect the efficiency of the deformation process and the mechanical properties of the material, which can provide important reference to optimizing the processing parameters and the resultant mechanical properties of the materials (Pougis et al., 2012; Chen et al., 2018). Compared with equal channel angular pressing (Valiev and Langdon, 2006) and high pressure torsion (Zhilyaev and Langdon, 2008), the accumulated strain during FSW of pure Mg has not been yet determined until now (Liu et al., 2014; Liu et al., 2015a).

Some researchers attempted to acquire the strain and the metal flow state by numerical simulation. For instance, a new smooth particle hydrodynamics model for FSW technology was proposed by Pan et al. (2013). The flow behavior and the microstructure-mechanical properties relationship were analyzed during FSW of AZ31 Mg alloy. However, the value of strain and strain rate were not obtained according to their work. Dialami et al. (2018) established a kinematic framework for simulating the local flow during FSW, based on the Zener-Hollomon parameter and Hall-Petch relationship. The relationship among the average grain size, strain rate and temperature was studied. Nevertheless, it was still difficult to measure the temperature field of the actual FSW, considering multiple factors such as the geometry size of the probe and the cooling mechanisms, etc. Thus, the calculated strain was not consistent with the practical microstructural evolution. A computational fluid dynamics based- 3D thermo-mechanical model built by Albakri et al. (2013) was used to study the effect of FSW parameters on temperature field, material flow and strain rate of AZ31 Mg alloy. The results showed that the average stain rate was greatly affected by the rotational speed of the probe and traverse speed had seldom effect on the stain rate. Unfortunately, strong evidence was lacked in this research to verify the obtained strain rate values. Although simple numerical simulation method was proposed, it is still quite difficult to consider the effect of multiple factors, which may lead to the difference between the simulatedand measured results.

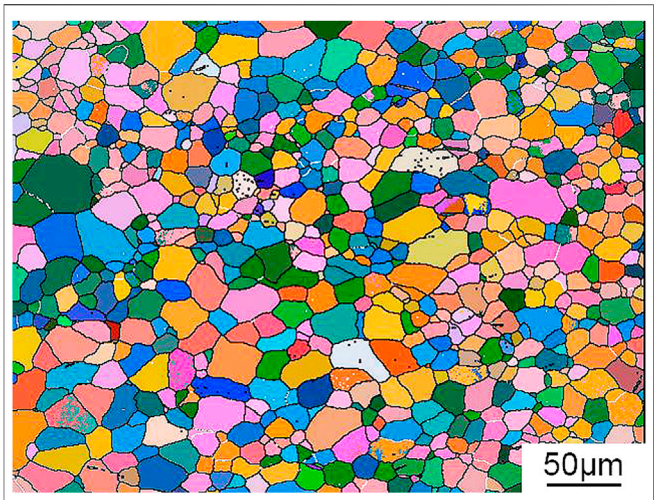

FIGURE 1 | The initial microstructure of the base metal.

Recently, studies have been done to develop experimental methods to evaluate the strain and strain rate during FSW. Kumar et al. (2018) used an experimental simulation method to approximate the strain rate during FSW. Micro-spherical glass tracers in a transparent viscoplastic material together with particle image velocimetry technique were used. Morisada et al. (2015) established a three-dimensional visualization experiment to determine the strain rate of pure Al during FSW. Nevertheless, the strain could not be obtained directly but reversely derived from the strain rate. Liu et al. (2019a; 2019b) developed an experimental method by inserting the marker to approximately determine the strain and strain rate during FSW process of pure copper. However, the detailed microstructural evolution was not involved in this study. In the present study, Liu's method was used for reference and pure Mg was selected to study the stain accumulation during FSW. Computational formula of stain accumulation was established according to the deformation process of the marker. Furthermore, the computational formula was derived so that its practicability was greatly improved. The stain accumulation of Mg material could be obtained directly by using the parameters of FSW process. In the present study, the microstructural evolution of the material was explored simultaneously. And the relationship between microstructural evolution and strain accumulation was obtained. This work can provide an important reference for the exploring the FSW parameters and tailoring the microstructures.

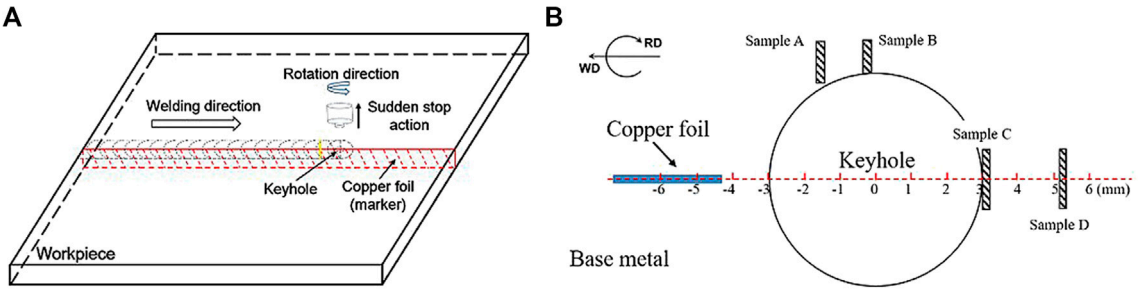

FIGURE 2 | Schematic illustration FWS process.

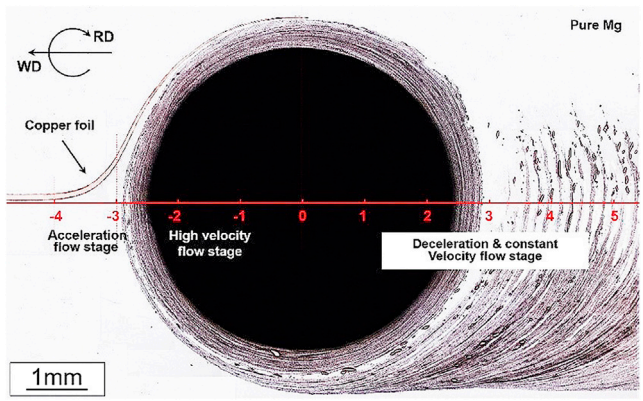

FIGURE 3 | Metallographic photo of the "stop action" of FSW (1,000 rpm, 200 mm/min).

MATERIALS AND METHODS

The 5 mm-thick pure Mg plates were selected, and the initialmicrostructure was shown in **Figure 1**. It can be seen that the microstructure of the base metal is consisted of coarse and equiaxed grains with an average grain size of about 40 μm. The fraction of low angle grain boundary (LAGB) is only 4.9%.

As shown in **Figure 2A**, a thin foil of pure Cu was pre-set into the abutting surface of the two workpieces as the marker. Compared with Mg materials, pure copper has better plasticity. Also, it is difficult to diffuse the two layers between pure Mg and pure Cu during FSW. Simultaneously, these two materials can be distinguished directly through their colors. The tool sudden "stop action" was applied using the emergency stop, i.e., the FSW machine lost power suddenly and the tool was pulled out quickly. As for the welding parameters, a tool containing a concave shoulder of 16 mm diameter and a smooth cylindrical probe of 5 mm diameter and 4.8 mm length was used. The tilt angle of the tool was about 3°. The welding speed in this study was 200 mm/min. And the rotational speeds were 1,000 and 1,500 rpm, respectively.

After the FSW process, the specimen containing the "stop action" zone and keyhole was collected using wire cutting. The specimen was ground 1 mm from the top using abrasive papers. Optical microscope was used to reveal the evolution of the marker in the "stop action" zone. As shown in **Figure 2B**, samples were collected from different positions of "stop action" zone for characterization. The samples were mechanically polished after grounding with abrasive papers of 800#, 1,500#, 3,000#, and 5,000#, respectively. Electron back-scattered diffraction was conducted on the samples which were final polished with Argon ion polishing to reveal the detailed microstructural features.

RESULTS AND DISCUSSION

Figure 3 shows the macro-graph of the keyhole ("stop action" zone). A plane-coordinate system is established: the center point of the probe hole is marked as the center position and the direction parallel to the welding direction is as the axis. The deformation status of pure Mg material at different positions can be obtained according to the shape and size of the marker. Compared with the study of Liu et al. (2019b), there exists obvious difference in the flow behavior of metals, resulting in different deformation states of the markers on the upper and lower surfaces. The appearance of this phenomenon is related to the nature of the material itself, which is affected by the shape of the stirring probe and the processing parameters (Han et al., 2019). In this study, the thickness of the Mg plates is relatively small (5 mm), and the shoulder diameter of the selected probe is large. The influence of the shoulder can reach the whole thickness, so that the metal flow at different layers is relatively consistent. The rotational speed of FSW selected in this study are 1,000–1,500 rpm. The higher the speed, the higher the temperature caused by FSW, and the better the fluidity of Mg. Meanwhile, a cylindrical probe is used in this study, and the length of the probe is close to the thickness of the pure Mg plate. The effect of probe on the metal flow on the upper and lower surfaces of the plate is basically the same. Thus, the metallographic observation of "stop action" zones of different thickness layers does not reveal obvious difference.

According to the status of the marker, the deformation process of FSW can be divided into three stages: 1) acceleration flow stage; 2) high velocity flow stage, and 3) deceleration and constant velocity flow stage. At stage I, the marker starts to deviate from the original position of the plate under the drive of the probe. The width of the marker becomes narrow,

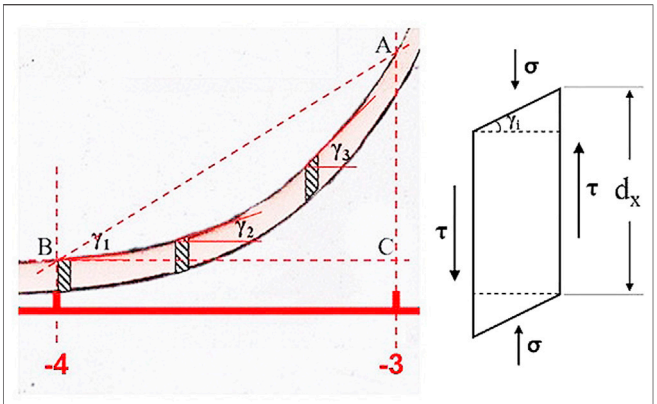

FIGURE 4 | Acceleration flow stage and approximate deformation model.

indicating that the flow velocity of the material gradually increases and the strain begins to accumulate. With the rotation of the probe, the material enters into the second stage. Together with the pure magnesium material flow, the marker is quickly stretched. The metal flow path becomes a circumferential movement around the probe. The width of the marker gradually decreases until it breaks, and the width of the copper foil in the end reaches ~30 μm. In addition, the change of the marker is relatively uniform, which indicates that the change of the metal flow velocity is relatively stable. With the proceeding of deformation, the material enters into the third stage. During this period, the metal flows as a circular motion around the probe at an approximately uniform speed after a short period of the deceleration process. Finally, the metal is separated from the influence of the probe due to the forward movement of the probe. And the flow speed decreases rapidly until stops. The final deceleration process is slightly affected by the probe, and the accumulated strain is negligible. Therefore, this study only discusses the constant velocity flow stage and its previous evolution process.

According to the deformation characteristics of the marker, a geometrical method can be used to evaluate the change of the material strain during FSW. During the acceleration flow stage, the width of the marker does not change significantly, and the marker gradually deviates from the original position with the rotation of the probe. The deformation state of the marker can be decomposed into the shear strain perpendicular to the welding direction ($\varepsilon_{x'}$) and the compressive strain in the width direction of the marker ($\gamma_{x'}$). As shown in **Figure 4**, the deformation of each small unit can be approximated as synthesis of pure shear deformation and compressive strain. Thus the strain of each unit can be calculated by the following equation:

$$\varepsilon_{x'}^{T} = \varepsilon_{x'} + \gamma_{x'} = tan\gamma_{x'} + \frac{d_B - d_A}{d_B}, \quad x' \le -3 \tag{1}$$

It can be seen from **Figure 4** that the value of γ increases from 0. When $x = -3$, γ_v reaches the maximum value. The accumulated strain of pure Mg during acceleration flow stage can be expressed by the following equation:

$$\varepsilon_{x'}^{T} = \varepsilon_{x'} + \int_0^{\gamma} tand\gamma \approx \frac{d_B - d_A}{d_B} + tan\gamma = \frac{d_B - d_A}{d_B} + \frac{AC}{BC}, \quad x' \le -3 \tag{2}$$

It can be calculated that the accumulated stain of the material during acceleration flow stage is very small, which is only ~0.65.

The deformed metal flows circumferentially with the rotation of the probe, entering the high velocity flow stage from the acceleration flow stage (**Figure 5**). It can be seen from the deformation state of the marker that the material flow path becomes longer and the flow speed increases in this stage. Strain accumulates rapidly, and SPD occurs in the material in this stage. During the high velocity flow stage, the rotational probe provides compressive stress on the marker from the side, and the upper and lower surfaces of the marker are subjected to the compressive stress provided by the shoulder and the bottom plate. The driving force for the material flow comes from both the shoulder and the probe simultaneously, thus the velocity of the inner side may actually a bit larger than that of the outer side of the marker. Because the marker strip is very thin, the velocity gradient must be very low. Therefore, the deformation of the material during high velocity flow stage can be approximately equivalent to a tensile strain. As shown in **Figure 5**, the entire high velocity flow stage is divided into several small units. The strain on the upper and lower surfaces of each small unit can be approximated as. ε_1 is the tensile strain along the flow direction, and ε_3 is the compressive strain laterally. According to the principle of constant volume before and after deformation, $\varepsilon_3 = -\varepsilon_1$. According to the Mises yield criterion, the equivalent strain of each small unit can be expressed as:

$$\varepsilon_x = \sqrt{\frac{2}{9}\left[(\varepsilon_1 - \varepsilon_2)^2 + (\varepsilon_2 - \varepsilon_3)^2 + (\varepsilon_3 - \varepsilon_1)^2\right]} = \frac{2}{\sqrt{3}}\varepsilon_1 = \frac{2}{\sqrt{3}}\left|\frac{l'' - l'}{l}\right| \tag{3}$$

Therefore, the equivalent strain accumulated in the high velocity flow stage can be approximately expressed as:

$$\varepsilon_x^{T} \approx \frac{2}{\sqrt{3}}\left|\frac{l_x - l_{-3}}{l_{-3}}\right| + \varepsilon_{x'}^{T}, \ (-3 \le x \le, x' \le -3) \tag{4}$$

where l_x is the width of the marker.

After SPD in the high velocity flow stage, the metal material reaches an approximately uniform flow state after a short deceleration process. As shown in **Figure 6**, during the forward movement of the probe, the flow of metal left noticeable band-like traces on the opposite side of the welding direction. The band-like traces are relatively uniform, indicating that the metal flow velocity is relatively stable. At this time, the metal flows in a circumferential direction around the probe. The deformation state of the material is close to the bending deformation, and the direction of the stress is directed to the center of the probe. According to Liu et al. (2015b) study, the

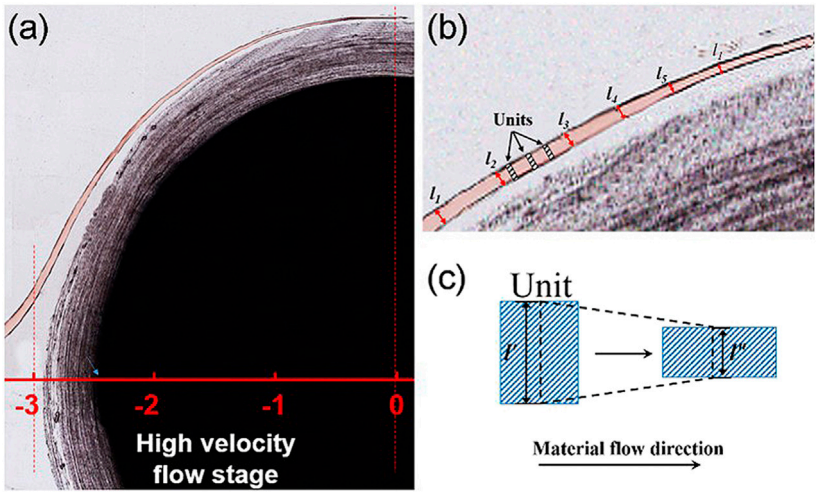

FIGURE 5 | High velocity flow stage and approximate deformation model.

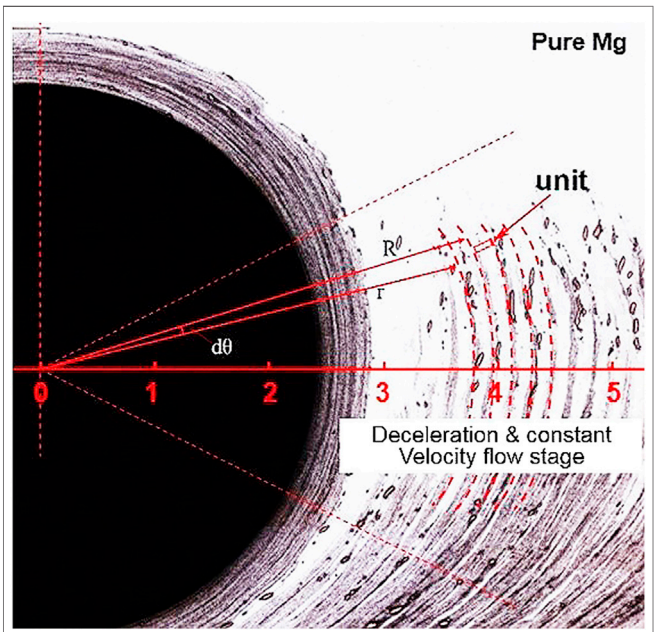

FIGURE 6 | Deceleration and constant velocity flow stage.

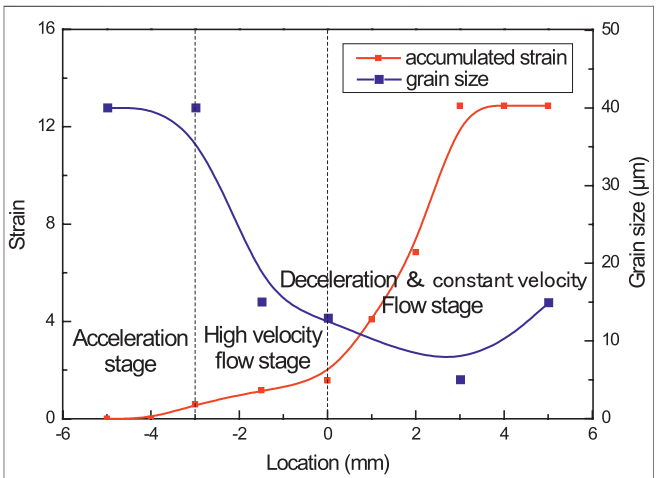

FIGURE 7 | Distributions of strain and grain sizes of the samples at different positions.

tangential strain of any small unit in the bending deformation zone can be expressed as:

$$\varepsilon_P = ln\frac{r_P}{r_0} \tag{5}$$

The equivalent strain ε^T is: $\varepsilon^T = \frac{2}{\sqrt{3}}|\varepsilon_P|$ (Liu et al., 2015b) (6) where r_P is the distance from the center of probe to the unit, r_0 is the distance from the center of probe to the neutral surface of bending deformation. Here $r_0 = \frac{R+r}{2}$.

Therefore, the accumulated strain when the metal flows through an angle of dθ is as follows:

$$\begin{aligned}\varepsilon_\theta &= \left(\int_{r_0}^{R} ln\frac{P}{r_0}dP - \int_{r}^{r_0} ln\frac{P}{r_0}dP\right)d\theta \\ &= \left[ln\left(\frac{P}{r_0}-1\right)\Big|_{r_0}^{R} - ln\left(\frac{P}{r_0}-1\right)\Big|_{r}^{r_0}\right]d\theta\end{aligned} \tag{7}$$

According to the equations above, the cumulative strains of the materials in different positions in **Figure 2B** can be obtained as: $\varepsilon_A = 1.23$, $\varepsilon_B = 1.63$, $\varepsilon_C = 12.92$. The metal at position D is separated from the influence of the rotational probe, so that no more strain is accumulated. Thus the strain of the sample at position D is approximately the same as that at position C. It can be seen from the calculation results that after the FSW process, the material has accumulated a large

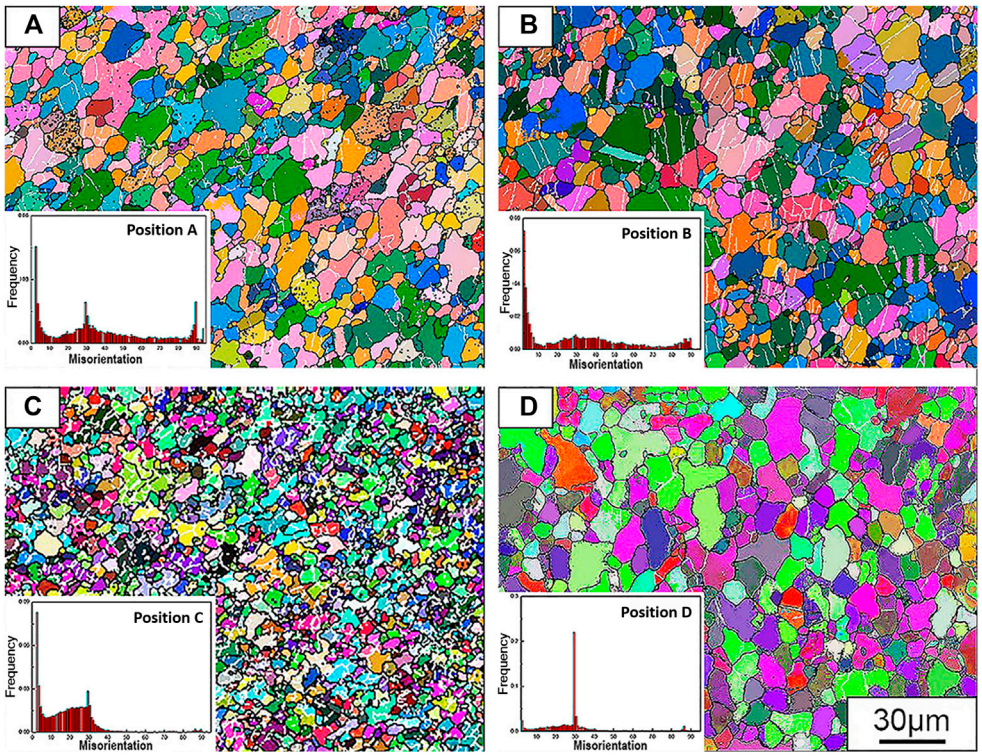

FIGURE 8 | Microstructures and grain size distributions of the samples at different positions of the "stop action" zone showed in **Figure 2B**. **(A)** position A; **(B)** position B; **(C)** position C; and **(D)** position D.

amount of strain. The change trend of the strain is shown with the red curve in **Figure 7**. The *x*-axis in the figure is consistent with that from **Figures 2–6**. The curve shows that the cumulative rate of strain increases slowly in the acceleration flow stage and the high velocity flow stage. The cumulative strain is close to 2 after high velocity flow stage. When the deformation process gradually enters the deceleration and constant velocity flow stage, the curve shows a rapid upward trend. A large amount of strain accumulates in this stage, and the material undergoes SPD. The deceleration and constant velocity flow stage is the dominant stage of strain accumulation during FSW.

In order to study the effect of deformation at different stages on the microstructures of the material, **Figure 8** shows the microstructures of the material at different positions during the FSW process at 1,000 rpm. After the FSW process, the microstructures of pure Mg were significantly refined and the grains were fine and uniform. The average grain sizes of Sample A (**Figure 8A**), Sample B (**Figure 8B**), and Sample C (**Figure 8C**) are 15.0, 12.9, and 8.1 μm, respectively. According to the results of electron back-scattered diffraction, the fraction of LAGBs in Sample A, Sample B, and Sample C are 24.2, 35.5, and 41.3%, respectively. In the FSW process, the temperature in the stir zone is high, and dynamic recrystallization is the main mechanism for the grain refinement and generally the fraction of LAGBs decreased as a result of recrystallization. However, due to the SPD induced by FSW process, a large number of LAGBs appeared in the material, and the fraction of LAGBs significantly increased with the proceeding of FSW. As the rate of increase in the fraction of LAGBs caused by deformation exceeded the rate of decrease in the fraction of LAGBs caused by recrystallization, the actual fraction of LAGBs continuously increased with the proceeding of FSW process. When the metal flows to position C, the SPD process caused by FSW is basically completed, and the obtained microstructure should be the final state of the material. However, it can be seen from **Figure 8D** that the final microstructure (sample D) is obviously coarse, and the average grain size reached 14.9 μm. Moreover, the fraction of LAGBs in sample D is quite low, only 15.9%. During the process from position C to D, the material does not undergo plastic deformation, but the recrystallization process still proceeds, so that the fraction of LAGBs decreases rapidly. After the recrystallization process is completed, under the influence of the high temperature, the microstructure of the material grows up obviously. The blue curve in **Figure 7** shows the variation tendency of the grain size of the material during the FSW process. During the acceleration flow stage, the strain introduced by FSW is very small, and the grain refinement is not obvious. In the high velocity flow stage, the metal flow is accelerated, resulting in SPD. Under the combined effect of recrystallization and SPD, the microstructure is significantly refined. In this stage, the grain size decreases the fastest, and the microstructure refinement is the most obvious. During the

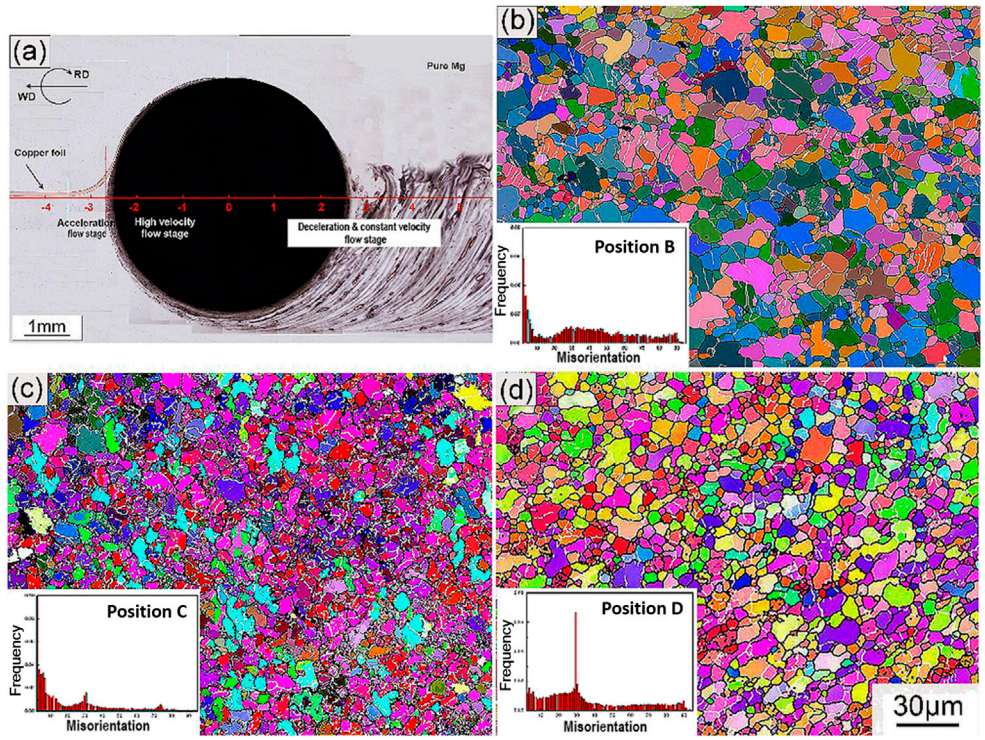

FIGURE 9 | Results of the experiments of the plates FSWed with 1,500 rpm. **(A)** Metallographic photo of the "stop action"; **(B)** Microstructure at position B; **(C)** Microstructure at position C; and **(D)** Microstructure at position D.

deceleration and constant velocity flow stage, the strain of the material increases rapidly, and the grains are further refined. Finally, a fine structure with an average grain size of <10 μm is obtained.

During the FSW process in this study, the cumulative strain from position C to position D did not change, but the microstructure grew up significantly and the fraction of LAGBs decreased significantly. The high temperature caused by friction is the main reason for this phenomenon. Studies by Lambrakos (2018) and Woo et al. (2017) show that the temperature of the stir zone of Mg alloy during FSW can exceed 450°C and even as high as 550°C. According to the study of Commin et al. (2009), the ultimate temperature of Mg alloy produced by FSW process can be expressed by the following empirical formula,

$$\frac{T}{T_m} = K\left(\frac{W^2}{V \cdot 10^4}\right)^{\alpha} \tag{8}$$

T_m is the melting temperature of the Mg material (610°C), W is the rotational speed of the probe, V is the welding speed, and the constants $\alpha = 0.0442$ and $K = 0.8052$ (Commin et al., 2009). It can be calculated that the resulting temperature under the FSW parameters (1,000 rpm of rotational speed and 200 mm/min of welding speed) can reach to ~475°C. At this temperature condition, recrystallization and grain growth will significantly take place in pure Mg material.

According to the results of accumulated strain calculated above (**Eqs. 2**, **4**, and **7**), the size evolution of the marker can be approximated with the rotational speed (W), welding speed (V) and the diameter (d) of the probe. Thus, the formula is derivated as follows:

$$\varepsilon_\theta^T = \begin{cases} \dfrac{d}{2}(sin\theta), \left(0 \le \theta < \dfrac{\pi}{12}\right) \\ \dfrac{24\left(\theta - \dfrac{\pi}{12}\right)}{5\sqrt{3}\pi} + \dfrac{d}{2}\left(sin\dfrac{\pi}{12}\right), \left(\dfrac{\pi}{12} \le \theta < \dfrac{\pi}{2}\right) \\ 2\ln\left(\dfrac{V}{V + dkW}\right) \cdot \left(\theta - \dfrac{\pi}{2}\right) + \dfrac{2}{\sqrt{3}} + \dfrac{d}{2}\left(sin\dfrac{\pi}{12}\right), \left(\theta \ge \dfrac{\pi}{2}\right) \end{cases} \tag{9}$$

where k is a coefficient with dimension of 1, whose value is affected by the nature of the material and the welding speed V. θ is the angle that the flowing metal turns with the probe. The strain can be approximately predict before FSW process by using **Eq. 9**.

In order to verify the rationality of the above results, the same pure Mg sheet was used for FSW process with different parameters (1,500 rpm, 200 mm/min), and the welded samples were characterized. As shown in **Figure 9**, the pure Mg material after FSW process at 1,500 rpm has a similar evolution process as that at 1,000 rpm. During the deceleration and constant velocity flow stage, obvious recrystallization and grain growth occurred. During the FSW process, the average grain sizes of the samples at positions B (**Figure 9B**), C (**Figure 9C**), and D (**Figure 9D**) were

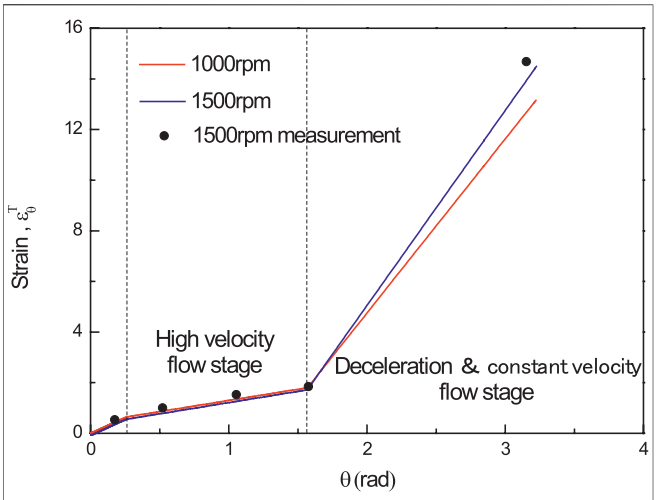

FIGURE 10 | Changes of the strain at different parameters of FSW.

11.9, 6.5, and 10.3 μm, respectively. Compared with the sample at the same position at 1,000 rpm, the microstructure of the material is obviously further refined. It can be obtained that the fianl temperature caused by friction at 1,500 rpm is about 485°C (**Eq. 8**). Although the rotational speed of the probe is increased, the temperature field does not change significantly. The experimental results of Chang et al. (2004) showed that, when the rotational speed exceeds 1,000 rpm, the temperature of Mg alloys caused by friction of FSW process does not change a lot with the further increase of the rotational speed. The results of Park and You (2015) show that the mechanical properties of Mg alloys change little when the deformation temperature is about 450–500°C.

In the present study, the temperature fields under different rotational speed conditions are not much different. It can be considered that the temperature influence on the microstructure evolution is relatively consistent at 1,000 and 1,500 rpm. Therefore, the ability of the FSW process to refine the microstructure of the material mainly depends on the rotational speed of probe. The faster the rotational speed of the probe, the more strain accumulated inside the material, the more obvious the grain refinement will happen. Studies (Albakri et al., 2013; Hung et al., 2007) show that the lower the speed of the probe during FSW process, the finer microstructure of Mg alloy can be obtained, which is contrary to the results obtained in the present study. The main reason for the opposite results is the difference in temperature fields. In the present study, the temperature fields obtained at different rotational speeds are not significantly different, and the effects of the temperature fields on the material are about the same. The temperature differences produced by the FSW process in Albakri et al. (2013) and Hung et al. (2007) are 60 and 70°C, respectively. The large temperature difference will obviously affect the grain growth process. Simultaneously, the higher temperature easily causes larger range of high temperature field, so that the grain growth process extends for a long period. Therefore, the lower temperature field during FSW process resulted in the finer microstructures.

Adopting to the method described in this study, the cumulative strain of pure Mg at different positions at 1,500 rpm was measured by inserting the marker into the butting surface of the workpieces. A plane-coordinate system is established: the cumulative strain and the position of the deformed material are as axes. The results are shown in **Figure 10**. The red and blue curves are the curves plotted by **Eq. 9** underboth 1,000 and 1,500 rpm, respectively. In the acceleration flow stage and high velocity flow stage, the cumulative speed of strain is slow, thus the curves are not significantly different. In the deceleration and constant velocity flow stage, the cumulative speed of strain is faster at 1,500 rpm than that at 1,000 rpm, and the value of accumulated strain is higher, thus the finer microstructure is obtained. In this study, the difference value between the cumulative strains at different rotational speeds is close to 2. Studies (Fan et al., 2012; Xu et al., 2017; Chen et al., 2016b) indicated that each increase of 1 in the accumulation of strain during SPD has a significant effect on the microstructure of the material. Especially when the grain size is large, the influence of the strain is more significant. The black dots are the strain values actually measured at 1,500 rpm (**Figure 9A**), and they agree well with the curve drawn by the formula (the blue curve), indicating that the obtained empirical formula (**Eq. 9**) is credible.

CONCLUSIONS

(1) The studied pure Mg plates were successfully welded at the welding speed of 200 mm/min, probe rotational speeds of 1,000 and 1,500 rpm. The final microstructure obtained after FSW is fine and homogeneous. The higher the rotational speed of the probe, the finer microstructure obtained.

(2) The accumulation of strains during the FSW process was calculated by inserting a marker (pure copper foil) into the butting surface of the two workpieces. The process of accumulating strain can be divided into three stages. The higher the rotational speed of the probe, the more severe the deformation occurs in the material. The values of the accumulated strain of the material are 12.86 and 14.5 at the rotational speed of 1,000 and 1,500 rpm, respectively.

(3) A credible empirical formula is established to characterize the cumulative process of the strain during FSW process. For this formula, only the welding parameters of the FSW process are needed to approximate the accumulated strain of the material at different deformation stages.

(4) The microstructural evolution during FSW of pure Mg shows that the final microstructure is is significantly refined due to the combined influence of SPD and recrystallization. However, significant grain growth occurred after strain accumulation, which is due to the high temperature field caused by friction.

DATA AVAILABILITY STATEMENT

The raw data supporting the conclusions of this article will be made available by the authors, without undue reservation, to any qualified researcher. The original contributions presented in the study are included in the article/supplementary materials, further inquiries can be directed to the corresponding author/s.

AUTHOR CONTRIBUTIONS

ZL conceived this experiment, analysed the data and the results of the experiments and wrote the manuscript. HD, YC, and LL discussed the results, commented on the manuscript and gave valuable advices for the manuscript. JL performed the friction stir welding process.

REFERENCES

Ahmadkhaniha, D., Jarvenpaa, A., Jaskari, M., Sohi, M. H., Zarei-Hanzaki, A., Fedel, M., et al. (2016). Microstructural modification of pure Mg for improving mechanical and biocorrosion properties. *J. Mech. Behav. Biomed. Mater.* 61, 360–370. doi:10.1016/j.jmbbm.2016.04.015

Albakri, A. N., Mansoor, B., Nassar, H., and Khraisheh, M. K. (2013). Thermo-mechanical and metallurgical aspects in friction stir processing of AZ31 Mg alloy-A numerical and experimental investigation. *J. Mater. Process. Technol.* 213, 279–290. doi:10.1016/j.jmatprotec.2012.09.015

Avedesian, M. M., and Baker, H. (1999). *Magnesium and magnesium alloys*, Materials Park, OH: ASM International.

Chang, C. I., Lee, C. J., and Huang, J. C. (2004). Relationship between grain size and Zener-Holloman parameter during friction stir processing in AZ31 Mg alloys. *Scripta Mater.* 51, 509–514. doi:10.1016/j.scriptamat.2004.05.043

Chen, C., Lv, B., Feng, X., Zhang, F., and Beladi, H. (2018). Strain hardening and nanocrystallization behaviors in Hadfield steel subjected to surface severe plastic deformation. *Mater. Sci. Eng. A* 729, 178–184. doi:10.1016/j.msea.2018.05.059

Chen, Y., Ding, H., Cai, Z., Zhao, J., and Li, J. (2016a). Effect of initial base metal temper on microstructure and mechanical properties of friction stir processed Al-7B04 alloy. *Mater. Sci. Eng. A* 650, 396–403. doi:10.1016/j.msea.2015.10.083

Chen, Y., Ding, H., Li, J., Cai, Z., Zhao, J., and Yang, W. (2016b). Influence of multi-pass friction stir processing on the microstructure and mechanical properties of Al-5083 alloy. *Mater. Sci. Eng. A* 650, 281–289. doi:10.1016/j.msea.2015.10.057

Commin, L., Dumont, M., Masse, J.-E., and Barrallier, L. (2009). Friction stir welding of AZ31 magnesium alloy rolled sheets: influence of processing parameters. *Acta Mater.* 57, 326–334. doi:10.1016/j.actamat.2008.09.011

Commin, L., Dumont, M., Rotinat, R., Pierron, F., Masse, J.-E., and Barrallier, L. (2012). Influence of the microstructural changes and induced residual stresses on tensile properties of wrought magnesium alloy friction stir welds. *Mater. Sci. Eng. A* 551, 288–292. doi:10.1016/j.msea.2012.05.021

Dialami, N., Cervera, M., and Chiumenti, M. (2018). Numerical modelling of microstructure evolution in friction stir welding (FSW). *Metals* 8, 183–198. doi:10.3390/met8030183

Fan, G. D., Zheng, M. Y., Hu, X. S., Xu, C., Wu, K., and Golovin, I. S. (2012). Improved mechanical property and internal friction of pure Mg processed by ECAP. *Mater. Sci. Eng. A* 556, 588–594. doi:10.1016/j.msea.2012.07.031

Han, Y., Jiang, X., Chen, S., Yuan, T., Zhang, H., Bai, Y., et al. (2019). Microstructure and mechanical properties of electrically assisted friction stir welded AZ31B alloy joints. *J. Manuf. Process.* 43, 26–34. doi:10.1016/j.jmapro.2019.05.011

Hung, F.-Y., Shih, C.-C., Chen, L.-H., and Lui, T.-S. (2007). Microstructures and high temperature mechanical properties of friction stirred AZ31-Mg alloy. *J. Alloys Compd.* 428, 106–114. doi:10.1016/j.jallcom.2006.03.066

Kumar, R., Pancholi, V., and Bharti, R. P. (2018). Material flow visualization and determination of strain rate during friction stir welding. *J. Mater. Process. Technol.* 255, 470–476. doi:10.1016/j.jmatprotec.2017.12.034

Lambrakos, S. G. (2018). Parametric modeling of AZ31-Mg alloy friction stir weld temperature histories. *J. Mater. Eng. Perform* 27, 5823–5830. doi:10.1007/s11665-018-3716-9

Liu, D., Xin, R., Xiao, Y., Zhou, Z., and Liu, Q. (2014). Strain localization in friction stir welded magnesium alloy during tension and compression deformation. *Mater. Sci. Eng. A* 609, 88–91. doi:10.1016/j.msea.2014.04.089

Liu, D., Xin, R., Zheng, X., Zhou, Z., and Liu, Q. (2013). Microstructure and mechanical properties of friction stir welded dissimilar Mg alloys of ZK60-AZ31. *Mater. Sci. Eng. A* 561, 419–426. doi:10.1016/j.msea.2012.10.052

Liu, F. C., Liao, J., Gao, Y., and Nakata, K. (2015a). Influence of texture on strain localization in stir zone of friction stir welded titanium. *J. Alloys Compd.* 626, 304–308. doi:10.1016/j.jallcom.2014.12.011

Liu, X. C., Wu, C. S., and Padhy, G. K. (2015b). Characterization of plastic deformation and material flow in ultrasonic vibration enhanced friction stir welding. *Scripta Mater.* 102, 95–98. doi:10.1016/j.scriptamat.2015.02.022

Liu, X. C., Sun, Y. F., Nagira, T., Ushioda, K., and Fujii, H. (2019a). Evaluation of dynamic development of grain structure during friction stir welding of pure copper using a quasi *in situ* method. *J. Mater. Sci. Technol.* 35, 1412–1421. doi:10.1016/j.jmst.2019.01.018

Liu, X. C., Sun, Y. F., Nagira, T., Ushioda, K., and Fujii, H. (2019b). Experimental evaluation of strain and strain rate during rapid cooling friction stir welding of pure copper. *Sci. Technol. Weld. Join.* 24, 352–359. doi:10.1080/13621718.2018.1556436

Mordike, B. L., and Ebert, T. (2001). Magnesium: properties — applications — potential. *Mater. Sci. Eng. A* 302, 37–45. doi:10.1016/s0921-5093(00)01351-4

Morisada, Y., Imaizumi, T., and Fujii, H. (2015). Determination of strain rate in Friction Stir Welding by three-dimensional visualization of material flow using X-ray radiography. *Scripta Mater.* 106, 57–60. doi:10.1016/j.scriptamat.2015.05.006

Nikulin, I., Malopheyev, S., Kipelova, A., and Kaibyshev, R. (2012). Effect of SPD and friction stir welding on microstructure and mechanical properties of Al-Cu-Mg-Ag sheets. *Mater. Lett.* 66, 311–313. doi:10.1016/j.matlet.2011.08.104

Pan, W., Li, D., Tartakovsky, A. M., Ahzi, S., Khraisheh, M., and Khaleel, M. (2013). A new smoothed particle hydrodynamics non-Newtonian model for friction stir welding: process modeling and simulation of microstructure evolution in a magnesium alloy. *Int. J. Plast.*, 48, 189–204. doi:10.1016/j.ijplas.2013.02.013

Park, S. H., and You, B. S. (2015). Effect of homogenization temperature on the microstructure and mechanical properties of extruded Mg-7Sn-1Al-1Zn alloy. *J. Alloys Compd.* 637, 332–338. doi:10.1016/j.jallcom.2015.03.030

Pougis, A., Tóth, L. S., Bouaziz, O., Fundenberger, J.-J., Barbier, D., and Arruffat, R. (2012). Stress and strain gradients in high-pressure tube twisting. *Scripta Mater.* 66, 773–776. doi:10.1016/j.scriptamat.2012.02.004

Valiev, R. Z., and Langdon, T. G. (2006). Principles of equal-channel angular pressing as a processing tool for grain refinement. *Prog. Mater. Sci.* 51, 881–981. doi:10.1016/j.pmatsci.2006.02.003

Woo, W., Feng, Z., Clausen, B., and David, S. A. (2017). *In situ* neutron diffraction analyses of temperature and stresses during friction stir processing of Mg-3Al-1Zn magnesium alloy. *Mater. Lett.* 196, 284–287. doi:10.1016/j.matlet.2017.03.117

Xu, R., Mahmudi, R., Pereira, P. H. R., Huang, Y., and Langdon, T. G. (2017). Microstructural evolution and superplasticity in an Mg-Gd-Y-Zr alloy after processing by different SPD techniques. *Mater. Sci. Eng. A* 682, 577–585. doi:10.1016/j.msea.2016.11.080

Yang, J., Xiao, B. L., Wang, D., and Ma, Z. Y. (2010). Effects of heat input on tensile properties and fracture behavior of friction stir welded Mg-3Al-1Zn alloy. *Mater. Sci. Eng. A* 527, 708–714. doi:10.1016/j.msea.2009.09.044

Yang, Q., Li, X., Chen, K., and Shi, Y. J. (2011). Effect of tool geometry and process condition on static strength of a magnesium friction stir lap linear weld. *Mater. Sci. Eng. A*, 528, 2463–2478. doi:10.1016/j.msea.2010.12.030

Yang, Q., Xiao, B. L., and Ma, Z. Y. (2013). Enhanced superplasticity in friction stir processed Mg-Gd-Y-Zr alloy. *J. Alloys Compd.* 551, 61–66. doi:10.1016/j.jallcom.2012.10.002

Zhilyaev, A., and Langdon, T. (2008). Using high-pressure torsion for metal processing: fundamentals and applications. *Prog. Mater. Sci.* 53, 893–979. doi:10.1016/j.pmatsci.2008.03.002

Zhou, L., Yu, M., Liu, B., Zhang, Z., Liu, S., Song, X., et al. (2020). Microstructure and mechanical properties of Al/steel dissimilar welds fabricated by friction surfacing assisted friction stir lap welding. *J. Mater. Res. Technol.* 9, 212–221. doi:10.1016/j.jmrt.2019.10.046

Conflict of Interest: Author JL was employed by company FSW Welding Technology (Shanghai) Co., LTD.

The remaining authors declare that the research was conducted in the absence of any commercial or financial relationships that could be construed as a potential conflict of interest.

frontiers in Materials

ORIGINAL RESEARCH
published: 07 December 2020
doi: 10.3389/fmats.2020.602441

Strain Hardening Behavior of Laminate Structure With Stable bcc/fcc Bimetal Interfaces

Xuqiang Huang[1], Zhaoyang Lu[1], Minghui Cai[2]* and Peter D. Hodgson[3]*

[1]School of Mechanical Engineering and Automation, Northeastern University, Shenyang, China, [2]State Key Laboratory of Rolling and Automation, Northeastern University, Shenyang, China, [3]Institute for Frontier Materials (IFM), Deakin University, Geelong, VIC, Australia

This work developed a well-bonded bcc/fcc bimetal interphase, which was produced by a two-step process involving diffusion bonding and conventional rolling. The high-quality interface maintained its integrity even at fracture. The earlier tensile instability in the core steel layer was constrained by the neighboring stable Cu layers on both sides, leading to extra strain hardening and consequently higher ductility. An increase in twin density or slip bands and shear deformation between the layers might be the primary causes for the observed hardening behaviors in the near-interface regions.

Keywords: bimetal interface, strain hardening, nanoindentation, fracture, laminate structure

OPEN ACCESS

Edited by:
Antonio Caggiano, Darmstadt University of Technology, Germany

Reviewed by:
Fuxing Yin, Hebei University of Technology, China
Yusheng Li, Nanjing University of Science and Technology, China

****Correspondence:***
Xuqiang Huang
caimh@smm.neu.edu.cn

Specialty section:
This article was submitted to Structural Materials, a section of the journal Frontiers in Materials

Received: *03 September 2020*
Accepted: *12 November 2020*
Published: *07 December 2020*

Citation:
Huang X, Lu Z, Cai M and Hodgson PD (2020) Strain Hardening Behavior of Laminate Structure With Stable bcc/fcc Bimetal Interfaces. Front. Mater. 7:602441. doi: 10.3389/fmats.2020.602441

INTRODUCTION

A major motivation for manufacturing bimetal materials is to satisfy unique combinations of enhanced properties while reducing the overall cost (Zheng et al., 2013; Beyerlein et al., 2014a; Beyerlein et al., 2014b; Kong et al., 2019; Li et al., 2020; Zhao et al., 2020). So far, there have been attempts to reduce material costs by cladding a high strength mild steel plate in an anticorrosive material such as aluminium, copper, titanium, stainless steels, etc. (Yang et al., 1996; Gurgutlu et al., 2005; Zhang et al., 2011). Although conventional cladding technology, i.e., diffusion bonding, possesses great advantages for joining these dissimilar materials (Zhao et al., 2020), the technique is inappropriate for practical application, especially for large-scale structural materials such as sheets, in part due to the limited dimensions and lower productivity (Guo, 2015).

Alternatively, accumulative roll-bonding (ARB) (Saito et al., 1999) has been applied to examine the possibility of bonding dissimilar materials, including Ti/Al (Yang et al., 2010), Cu/Ag and Cu/Zr (Ohsaki et al., 2007), Al/Cu (Toroghinejad et al., 2013), with the aim of studying the influence of processing parameters on the interface microstructure and overall mechanical properties. Additionally, the study of bimetal interfaces has recently been of interest. For example, Ma et al. (Wu et al., 2014) explored a laminate nanostructured (Cu-Zn)/coarse-grained (pure Cu) structure, and investigated the influence of grain size difference across the interface on the mechanical behavior. It was found that the interface caused by tensile instability plays a crucial role in the overall strengthening and co-deformability of GS materials. Beyerlein et al. (Beyerlein et al., 2014a; Beyerlein et al., 2014b) and Zheng et al. (Zheng et al., 2013) demonstrated the emergence of a plastically and thermally stable Cu_{fcc}/Nb_{bcc} interface during ARB. However, the deformation behavior of the bcc/fcc interface in these bimetallic materials during subsequent plastic deformation has yet to be fully investigated, even though it does play a crucial role in the overall strengthening and co-deformability (Beyerlein et al., 2012; Wu et al., 2014; Ma et al., 2015).

The aim of the present work is, therefore, to study the deformation behavior of a bcc/fcc bimetal interface in a tri-layered Cu/mild steel/Cu laminate sheet, which is produced by combining diffusion

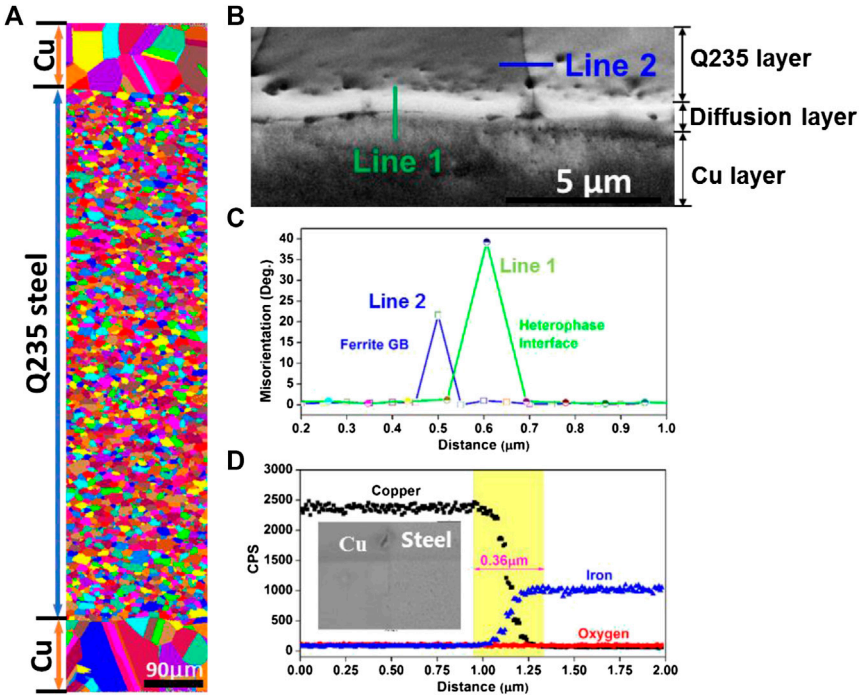

FIGURE 1 | A representative cross-sectional structure of the tri-layered Cu/steel/Cu composite and interface features: **(A)** Unique grain color EBSD map indicating a copper-clad steel microstructure; **(B)** High-magnification image quality (IQ) map displaying a well-bonded Fe/Cu interface and three distinct zones; **(C)** Difference in misorientation angles between the ferrite grain boundary (GB) and the heterophase interface, corresponding to Line 1 and 2 in b, respectively; **(D)** An energy-dispersive X-ray Spectroscopy (EDX) profile showing elemental distribution of copper, iron and oxygen across the bond interface.

bonding with commercial rolling. Particular emphasis is placed on the fundamental understanding of the co-deformability and hardening behaviors between the layers through interrupted tensile testing coupled with nano-indentation.

EXPERIMENTAL PROCEDURES

Commercial pure copper (~10 mm thick) and mild steel (0.12C-0.3Si-0.4Mn, ~50 mm thick) plates were used to produce the tri-layered Cu/steel/Cu laminate sheets. After a surface cleaning treatment, diffusion bonding was performed at 850°C and 20 MPa in a protective Ar atmosphere to form a strong interfacial bond, followed by hot rolling to an overall thickness of 3.5 mm at ~880 °C. After annealing at ~800°C for 1 h and furnace cooling to room temperature, the laminate sheets were further cold rolled to ~1 mm in one pass, perpendicular to the hot rolling direction.

A series of laminate samples with gauge dimension of 25 × 6 × 1 mm^3 were cut from the rolled sheets. Interrupted tensile tests were performed to four different levels of strain, i.e., 6, 13, 20, 24% (fracture) at a strain rate of 1.0×10^{-4} s^{-1}. Additionally, the pure Cu layers on both sides were removed by mechanical polishing to compare the core mild steel with the laminate sample under the same deformation conditions.

Microstructures and elemental mapping in the near-interface regions were characterized by a FEI Quanta 3D FEG-SEM with TSL OIM EBSD and Electron Dispersive X-ray Spectroscopy (EDS) systems. Scanning electron microscopy (FEG-SEM; Zeiss-Supra 55 VP) was used to examine the fracture surface and interfacial features.

Nano-indentation measurements were carried out on all interrupted and fractured laminate samples using a Berkovich indenter at room temperature, based on the continuous stiffness measurement mode. A peak force of 0.5 mN was applied with a constant loading rate of 5 μN/s. The average hardness value of each point was determined using experimental raw data from at least 10 separate indents.

RESULTS AND DISCUSSION

Figure 1A is a cross-sectional EBSD map showing the typical microstructures, consisting of pure copper layers (~130 μm) on each side and a mild steel layer inside (~870 μm). Further analysis of a high-resolution EBSD image (**Figure 1B**) reveals that the initial bimetal interface exhibits a continuity of the bond and no dramatic crack or delamination is visible from the bcc Fe to fcc Cu. The orientation profiles in **Figure 1C** demonstrate that the bimetal interface has much higher angle misorientations than the conventional ferrite grain boundary. The emergence of such a low-energy boundary structure probably leads to the excellent mechanical stability of the bimetal interface (Beyerlein et al., 2014a; Beyerlein et al., 2014b). The exact Cu/Fe interface can be

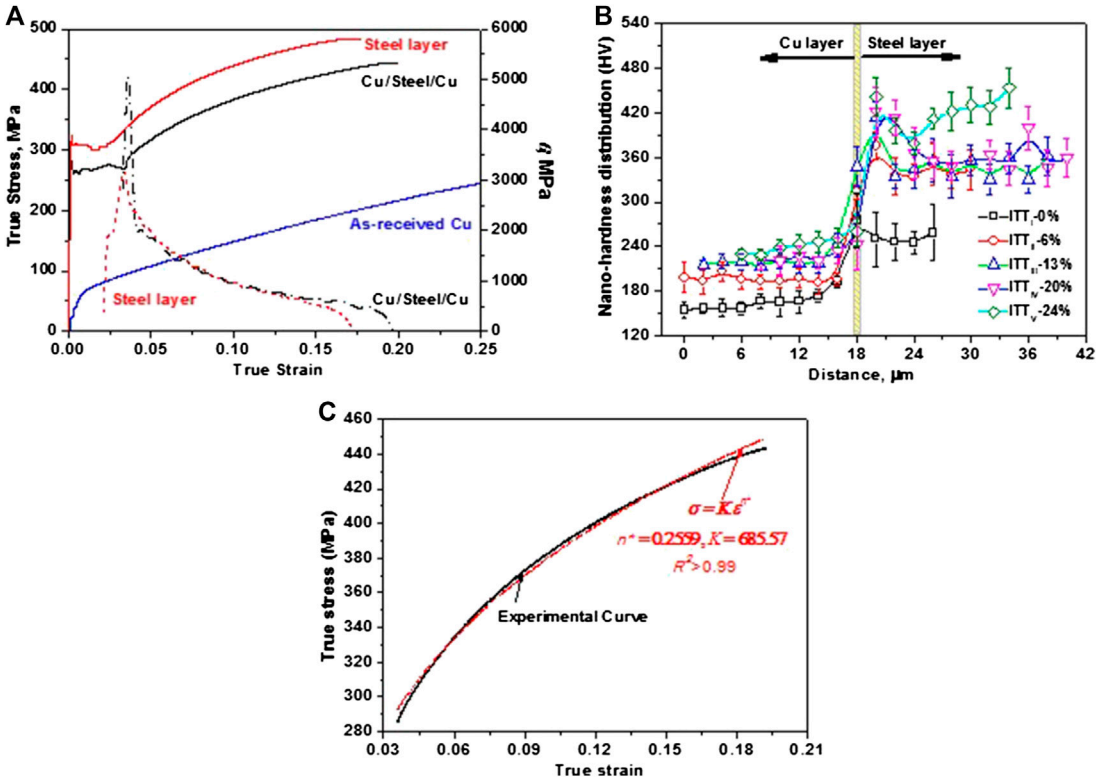

FIGURE 2 | (A) Representative true stress (σ) and strain hardening rate, θ vs. true strain curves obtained at the strain rate of 10^{-4} s^{-1}, in conjunction with interrupted tensile tests to 6%, 13% and 20%, respectively; **(B)** Nano-hardness distribution profiles near the bimetal interface with applied strain, and error bars are determined from a range of experimental data (>10) on different rows with the same distance away from the interface; **(C)** Comparison of the experimental and fitted flow curves by Hollomon's equation. Here, n^* is the average strain-hardening exponent, K is the strength coefficient and r^2 is the correlation coefficient.

identified by EDS, **Figure 1D**. The elemental distribution profiles of Fe and Cu have relatively steep slopes, implying no significant bulk diffusion from each side during processing. As demonstrated in the Fe-Cu binary phase diagram (Atabaki et al., 2011), there is very limited solubility of Fe in Cu, and the diffusion coefficient of Cu in Fe is very low (i.e., $1.3–2.4 \times 10^{-4}$ cm^2/s) even at a relatively high temperature (i.e., 1073–1173K) (Salje and Feller-Kniepmeier, 1977). Therefore, all of above characteristics confirm a well-bonded and sharp bcc/fcc bimetal interface.

Figure 2A shows the flow curves of the laminate samples interrupted at 6, 13, 20 and 24% (rupture), in conjunction with the steel layer after removing the pure Cu layers by mechanical polishing. One noteworthy feature of the stress-strain curves is that the overall yielding behavior is more like steel than Cu. The tensile uniform elongation increases by 2.5% with a slight decrease in flow stresses by ~40 MPa when compared to the steel layer. Another important fact is that such laminate structures offer the exceptionally high tensile stress over the pure copper i.e. the yield stress is ~4 times as high, while minimizing material cost by using a cheap steel core.

During uniform deformation, the relationship between true stress and true strain of each component, i.e., bcc steel or fcc Cu, can usually be described by the Hollomon equation $\sigma_i = k_i\varepsilon^{ni}$. It is found that there is relatively good agreement between the fitted and experimental curves (**Figure 2C**), probably due to relatively thinner and softer Cu layers when compared to the steel layer. However, the n^* value predicted by Hollomon law is 0.256, which is higher than the normal instantaneous n value (< 0.2) of a conventional mild steel at room temperature. The higher n value tends to restrict the onset of strain localization and the growth of sharp grain gradients.

Taking into account the negligible influence of thin Cu layers on the overall flow behavior of the laminate structure, the hardening behaviors are analyzed and compared with the steel layer using the curves of strain hardening rate ($\theta = d\sigma/d\varepsilon$) vs. true strain ($\varepsilon$), **Figure 2A**. In contrast, at the completion of a pronounced plateau in flow stress, the laminate sample exhibits an abrupt increase in stress with applied strain, corresponding to a stronger hardening capability with the maximum θ value of ~5,000 MPa. Interestingly, the laminate sample behaves in a more typical manner showing a slower decrease in θ than the steel layer over a large stain range (> 0.1). The dramatic difference in hardening behaviors suggests that extra strain hardening is produced near the bcc/fcc interfaces between the soft surface layers and hard middle layer.

A more detailed analysis of this hardening behavior has been performed utilizing a series of interrupted tensile tests coupled with nano-indentation. As is commonly observed the hardness (H) values increase with the applied strain, **Figure 2B**. However, further analysis of the data reveals that the increment in hardness

TABLE 1 | The increment in hardness of each individual layer as a function of the applied strain during tensile testing.

Strain		0%	6%	13%	20%	24% (Fracture)
Copper	H_0	162 ± 7	196 ± 5	218 ± 4	228 ± 9	243 ± 11
	$\triangle H/H_0$	0	21%	35%	41%	50%
Steel	H	250 ± 6	340 ± 8	345 ± 13	355 ± 9	418 ± 14
	$\triangle H/H_0$	0	35.9%	38.1%	40.2%	67.0%

($\triangle H$) is closely related to various plastic deformation stages, as summarized in **Table 1**.

Even though the overall flow behavior will be dominated by the much thicker steel layer, it is still interesting to examine the hardness of the Cu layer. Using an increase in hardness to indicate an increase in strength, after straining to 0.058 (stage I), the Cu layer is strengthened by ~21%, while the increase is ~36% for the steel layer. Even though both layers undergo relatively large strengthening at the initial stage, the hard steel layer is still the major contributor to the macroscopic strengthening compared to the soft Cu layer. Subsequently, the Cu layer exhibits stronger strengthening, with the relative increase in strength being equivalent to the steel layer at a true strain of 0.18. The unique strengthening is consistent with the above analysis of strain hardening behavior in **Figure 2A**. In this case, the earlier tensile instability in the middle steel layer is constrained by the neighboring stable Cu layers on both sides. Actually, the mutual constraint between the layers adds extra strain hardening, and consequently enables the steel layer to uniformly deform further (Wu et al., 2009). This is also the reason why the laminate sample has a slower decrease in strain hardening rate than the middle steel layer with the applied strain (> 0.1). Therefore, the unstable steel layer needs to form an integral bulk with the stable Cu layers to be effective in producing extra strain hardening to postpone the onset of necking (Evans and Hirth, 1992; Gutierrez Urrutia and Raabe, 2012).

Typical microstructural evolution with tensile strain in the near-interface region has also been illustrated in **Figure 3**, where two levels of engineering strain, 13 and 24% are selected. After straining of 13%, the Cu layer exhibits striations in the form of parallel packets that evolve preferentially in fcc grains with orientations close to <110> and <111>, **Figure 3A** (annealing twinning). In contrast, the steel layer has slip bands that form in the <111> and <001> textured bcc grains, **Figure 3B**. The activation of additional twinning or slip systems during straining can be explained by the fact that irregular crystal rotations happen, especially in the regions adjacent to the bcc/fcc interfaces, due to shear deformation (**Figure 4C**) by the mutual constraint between the soft and hard layers (Wu et al., 2009). With an increase in deformation strain to 24% (failure), there clearly exists the annealing twins (**Figures 3C, 4**), which act as an effective obstacle to dislocation movement and therefore decrease the ease of plastic deformation will strengthen the material. Therefore, it can be concluded that existence of annealing twins or an increase in slip bands during straining and shear phenomenon by the mutual constraint between the layers may be the primary causes for the observed strengthening in the near-interface regions.

The integrity of the bcc/fcc bimetal interface after tensile testing is examined by SEM, revealing a continuity of the

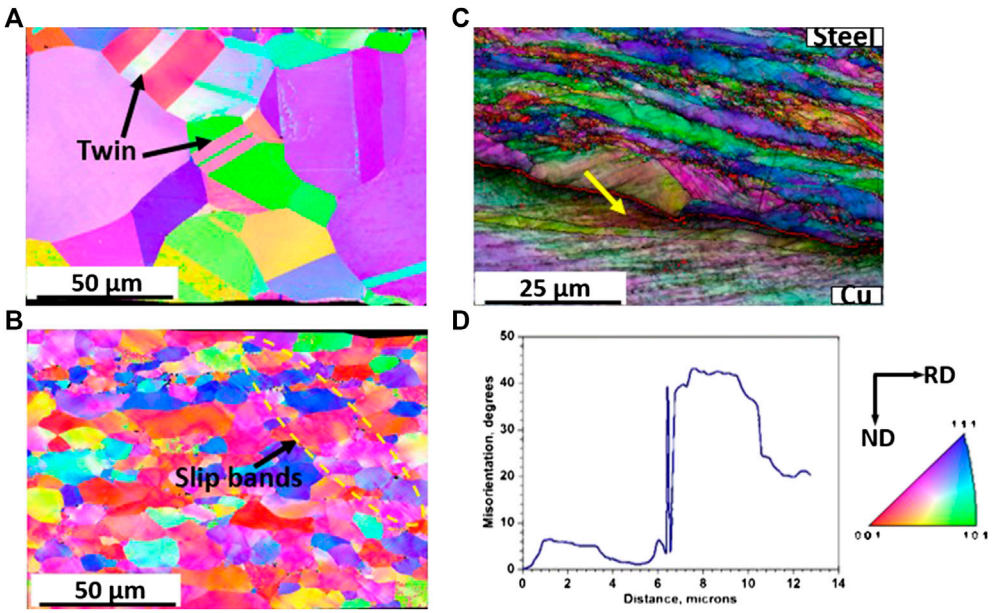

FIGURE 3 | Inverse pole figure maps showing the evolution of the cross-sectional microstructure with tensile deformation conditions: **(A)** fcc grains with twin boundaries in the Cu layer, and **(B)** bcc grains with slip bands after a tensile strain of 13%; **(C)** fcc-bcc bimetal interface in the sample fractured at a tensile strain of 24%. **(D)** shows a misorientation profile along the yellow line **(C)** cross the interface.

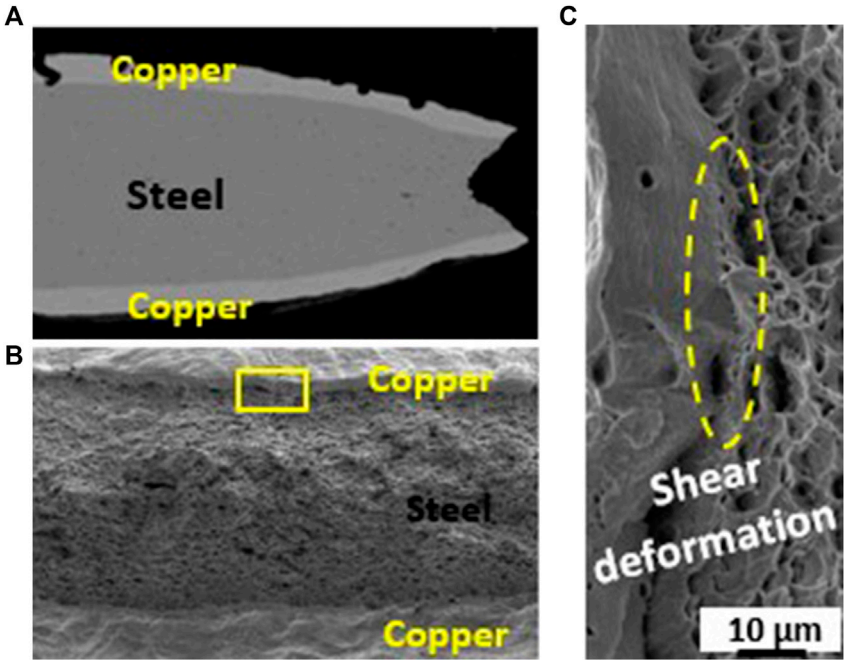

FIGURE 4 | Overview of SEM fractographs of the Cu/steel bimetal interface after tensile failure. **(A)** Representative morphology at the lateral fracture interface; **(B)** Overall fractograph after fracture and **(C)** Shear phenomenon between Cu and steel layers.

bond, i.e., no inner cracks or debonding over the entire deformation zone, **Figure 4A**. The fracture surface in **Figure 4B** demonstrates a typical dimple-like character in the near-interface regions, suggesting that the laminate samples fractures in a ductile manner. Another noteworthy feature of the fracture surface is shear deformation occurring between the interfaces, **Figure 4C**. The origin of the shear phenomenon is a result of the response to the mismatched tensile instabilities across the interfaces, and therefore, the mutual constraint between the soft and hard layers actually gives rise to extra strengthening. As a result, the earlier necking in the unstable steel layer may be quickly supressed by the neighboring stable Cu layers on both sides (Balke and De Hosson, 2001; Quadir et al., 2009; Wu et al., 2014; Ma et al., 2015; Liu et al., 2017; Liu et al., 2018).

CONCLUSION

In summary, a two-step process involving diffusion bonding and conventional rolling has been successfully applied to produce a well-bonded bcc/fcc bimetal interface. The laminate structure behaves in a more typical manner showing a slower decrease in θ than the steel layer over a large true strain range of 0.1–0.2, implying extra strain hardening, and thus higher ductility. The newly developed laminate structure offers a much higher tensile stress over the pure copper i.e., the yield stress is ~4 times as high, while minimizing material cost by using a cheap steel core. An increase in twin density or slip bands and shear deformation by the mutual constraint between the layers may be the primary causes for the strengthening behaviors in the near-interface regions. Furthermore, the high-quality bcc/fcc interface maintains its integrity even at fracture. This preliminary work indicates the well-bonded fcc/bcc bimetal interface plays a critical role in suppression of tensile instabilities of laminate composites.

DATA AVAILABILITY STATEMENT

The raw data supporting the conclusions of this article will be made available by the authors, without undue reservation.

AUTHOR CONTRIBUTIONS

XH: concept, writing, experiment; ZL: experiment; MC: writing, experiment; PH: supervision, modification.

ACKNOWLEDGMENTS

The present work was carried out with the support of the Deakin Advanced Characterization Facility. The authors gratefully acknowledge the financial support of the Natural Science Foundation of China (Grant Nos. 51975111/51671149) and the Fundamental Research Funding of the Central Universities, China (No. N2002002/N180702012).

REFERENCES

Atabaki, M. M., Wati, J. N., and Idris, J. B. (2011). *Proceedings of the 26th ASM heat treating society conference*. Editors B. L. Ferguson, R. Jones, D. S. Mavkenzie, and D. Weires (United States: ASM International), 20–43.

Balke, P., and De Hosson, J. T. M., (2001). Orientation imaging microscopic observations of *in situ* deformed ultra low carbon steel. *Scripta Mater.* 44, 461–466. doi:10.1016/s1359-6462(00)00632-1

Beyerlein, I. J., Mara, N. A., Wang, J., Carpenter, J. S., Zheng, S. J., Han, W. Z., et al.(2012). Structure-property-functionality of bimetal interfaces. *J. Occup. Med.* 64, 1192–1207. doi:10.1007/s11837-012-0431-0

Beyerlein, I. J., Mayeur, J. R., Mccabe, R. J., Zheng, S. J., Carpenter, J. S., and Mara, N. A., (2014a). Influence of slip and twinning on the crystallographic stability of bimetal interfaces in nanocomposites under deformation. *Acta Mater.* 72, 137–147. doi:10.1016/j.actamat.2014.03.041

Beyerlein, I. J., Mayeur, J. R., Zheng, S., Mara, N. A., Wang, J., and Misra, A. (2014b). Emergence of stable interfaces under extreme plastic deformation. *Proc. Natl. Acad. Sci. U. S. A.* 111, 4386–4390. doi:10.1073/pnas.1319436111

Evans, A. G., and Hirth, J. P. (1992). Deformation of nanoscale cermets. *Scripta Metall. Mater.* 26, 1675–1680. doi:10.1016/0956-716x(92)90532-j

Guo, J. F. (2015). "Solid state welding processes in manufacturing, handbook of manufacturing engineering and technology," in *Handbook of manufacturing engineering and technology*. Editor A. Y. C. Nee (London: Springer), 569–592.

Gurgutlu, A., Gülenc, B., and Findik, F. (2005). Examination of copper/stainless steel joints formed by explosive welding. *Mater. Des.* 26 497–507. doi:10.1016/j.matdes.2004.07.021

Gutierrez-Urrutia, I., and Raabe, D. (2012). Multistage strain hardening through dislocation substructure and twinning in a high strength and ductile weight-reduced Fe-Mn-Al-C steel. *Acta Mater.* 60, 5791–5802. doi:10.1016/j.actamat.2012.07.018

Kong, X. F., Beyerlein, I. J., Liu, Z. R., Yao, B. N., Legut, D., Germann, T. C., et al. (2019). Stronger and more failure-resistant with three-dimensional serrated bimetal interfaces. *Acta Mater.* 166, 231–245. doi:10.1016/j.actamat.2018.12.051

Li, Z., Zhao, J., Jia, F., Liang, X., Zhang, Q., Yuan, X., et al. (2020). Interfacial characteristics and mechanical properties of duplex stainless steel bimetal composite by heat treatment. *Mater. Sci. Eng.* 787, 139513. doi:10.1016/j.msea.2020.139513

Liu, B. X., Yin, F. X., Dai, X. L., He, J. N., Fang, W., Chen, C. X., et al. (2017). The tensile behaviors and fracture characteristics of stainless steel clad plates with different interfacial status. *Mater. Sci. Eng.* 679, 172–182. doi:10.1016/j.msea.2016.10.033

Liu, B. X., Wei, J. Y., Yang, M. X., Yin, F. X., and Xu, K. C. (2018). Effect of heat treatment on the mechanical properties of copper clad steel plates. *Vacuum* 154, 250–258. doi:10.1016/j.vacuum.2018.05.022

Ma, X. L., Huang, C. X., Xu, W. Z., Zhou, H., Wu, X. L., and Zhu, Y. T. (2015). Strain hardening and ductility in a coarse-grain/nanostructure laminate material. *Scripta Mater.* 103, 57–60. doi:10.1016/j.scriptamat.2015.03.006

Ohsaki, S., Kato, S., Tsuji, N., Ohkubo, T., and Hono, K. (2007). Bulk mechanical alloying of Cu-Ag and Cu/Zr two-phase microstructures by accumulative roll-bonding process. *Acta Mater.* 55, 2885–2895. doi:10.1016/j.actamat.2006.12.027

Quadir, M. Z., Ferry, M., Al-Buhamad, O., and Munroe, P. R. (2009). Shear banding and recrystallization texture development in a multilayered Al alloy sheet produced by accumulative roll bonding. *Acta Mater.* 57, 29–40. doi:10.1016/j.actamat.2008.08.056

Saito, Y., Utsunomiya, H., Tsuji, N., and Sakai, T. (1999). Novel ultra-high straining process for bulk materials-development of the accumulative roll-bonding (ARB) process. *Acta Mater.* 47, 579–583. doi:10.1016/s1359-6454(98)00365-6

Salje, G., and Feller-Kniepmeier, M. (1977). The diffusion and solubility of copper in iron. *J. Appl. Phys.* 48, 1833–1839. doi:10.1063/1.323934

Toroghinejad, M. R., Jamaati, R., Dutkiewicz, J., and Szpunar, J. A. (2013). Investigation of nanostructured aluminum/copper composite produced by accumulative roll bonding and folding process. *Mater. Des.* 51, 274–279. doi:10.1016/j.matdes.2013.04.002

Wu, X. L., Jiang, P., Chen, L., Yuan, F. P., and Zhu, Y. T. (2014). Extraordinary strain hardening by gradient structure. *Proc. Natl. Acad. Sci. U.S.A.* 111, 7197–7201. doi:10.1073/pnas.1324069111

Wu, X. L., Zhu, Y. T., Wei, Q., and Wei, Y. G. (2009). Strong Strain Hardening in Nanocrystalline Nickel. *Phys. Rev. Lett.* 103, 205504. doi:10.1103/physrevlett.103.205504

Yang, D., Cizek, P., Hodgson, P., and Wen, C. E. (2010). Ultrafine equiaxed-grain Ti/Al composite produced by accumulative roll bonding. *Scripta Mater.* 62, 321–324. doi:10.1016/j.scriptamat.2009.11.036

Yang, Y., Xinming, Z., Zhenghua, L., and Qingyun, L. (1996). Adiabatic shear band on the titanium side in the Ti/mild steel explosive cladding interface. *Acta Mater.* 44, 561–565. doi:10.1016/1359-6454(95)00200-6

Zhang, G., Su, W., Zhang, J., and Wei, Z., (2011). Friction stir brazing: a novel process for fabricating Al/steel layered composite and for dissimilar joining of Al to steel. *Metall. Mater. Trans.* 42, 2850–2861. doi:10.1007/s11661-011-0677-0

Zhao, K. N., Xu, D. X., Li, H. X., Wang, J., Ma, Y. Z., and Zhang, J. S. (2020). Fabrication, microstructure, and properties of interface-reinforced Mg/Mg bimetal composites by long-period stacking ordered structures. *J. Alloys Compd.* 816, 152526. doi:10.1016/j.jallcom.2019.152526

Zheng, S. J., Beyerlein, I. J., Carpenter, J. S., Kang, K., Wang, J., Han, W. Z., et al. (2013). High-strength and thermally stable bulk nanolayered composites due to twin-induced interfaces. *Nat. Commun.* 4, 1–8. doi:10.1038/ncomms2651

Conflict of Interest: The authors declare that the research was conducted in the absence of any commercial or financial relationships that could be construed as a potential conflict of interest.

frontiers in Materials

ORIGINAL RESEARCH
published: 08 December 2020
doi: 10.3389/fmats.2020.620000

Hydrogen Diffusion and Its Effect on Hydrogen Embrittlement in DP Steels With Different Martensite Content

Zhen Wang[1,2], *Jing Liu*[1,2]*, *Feng Huang*[1,2], *Yun-jie Bi*[1,2] *and Shi-qi Zhang*[1,2]

[1]*The State Key Laboratory of Refractories and Metallurgy, Wuhan University of Science and Technology, Wuhan, China,* [2]*Hubei Engineering Technology Research Center of Marine Materials and Service Safety, Wuhan University of Science and Technology, Wuhan, China*

The hydrogen diffusion behavior and hydrogen embrittlement susceptibility of dual phase (DP) steels with different martensite content were investigated using the slow strain-rate tensile test and hydrogen permeation measurement. Results showed that a logarithmic relationship was established between the hydrogen embrittlement index (I_{HE}) and the effective hydrogen diffusion coefficient (D_{eff}). When the martensite content is low, ferrite/martensite interface behaves as the main trap that captures the hydrogen atoms. Also, when the D_{eff} decreases, I_{HE} increases with increasing martensite content. However, when the martensite content reaches approximately 68.3%, the martensite grains start to form a continuous network, D_{eff} reaches a plateau and I_{HE} continues to increase. This is mainly related to the reduction of carbon content in martensite and the length of ferrite/martensite interface, which promotes the diffusion of hydrogen atoms in martensite and the aggregation of hydrogen atoms at the ferrite/martensite interface. Finally, a model describing the mechanism of microstructure-driven hydrogen diffusion with different martensite distribution was established.

Keywords: dual phase steels, hydrogen embrittlement, hydrogen diffusion, martensite content, slow strain rate tensile test

OPEN ACCESS

Edited by:
Minghui Cai,
Northeastern University, China

Reviewed by:
Hui Weijun,
Beijing Jiaotong University, China
Yunbo Xu,
Northeastern University, China
Libo Pan,
Jianghan University, China

***Correspondence:**
Jing Liu
liujing@wust.edu.cn

Specialty section:
This article was submitted to Structural Materials, a section of the journal Frontiers in Materials

Received: *21 October 2020*
Accepted: *20 November 2020*
Published: *08 December 2020*

Citation:
Wang Z, Liu J, Huang F, Bi Y and Zhang S (2020) Hydrogen Diffusion and Its Effect on Hydrogen Embrittlement in DP Steels With Different Martensite Content. Front. Mater. 7:620000. doi: 10.3389/fmats.2020.620000

INTRODUCTION

As the automobile industry has developed rapidly, lightweight automobile components have become important means for conserving energy and reducing emissions (Li et al., 2003). Dual phase (DP) steel composed of ferrite and martensite has become a favored material for the manufacturing of automobile structural parts, reinforcement parts and anti-collision parts due to the inherent high strength, sound formability and weldability (Sirinakorn et al., 2014). DP steels of different strength grades can be obtained by controlling the martensite content (Khan et al., 2008). However, the presence of hydrogen permeation in materials during processing, pickling, welding and service is prone to the risk of hydrogen embrittlement (Robertson et al., 2015). Furthermore, the magnitude of the hydrogen influence increased with increasing strength, severely limiting the development of high strength DP steels (Loidl et al., 2011).

Using the *in-situ* tensile test and SEM observation, Koyama (Koyama et al., 2014) found that hydrogen atoms gathering on the martensite promoted the cleavage fracture of martensite phase. Under static hydrogen charging, the interface of ferrite/martensite and martensite lath would become wider with increasing hydrogen charging current density, resulting in microcracks (Sun et al., 1989). Therefore, hydrogen embrittlement susceptibility of DP steel is related to the martensite.

TABLE 1 | Chemical composition of the experimental steel (wt %).

C	Si	Mn	Cr	Al	S	P	Mo	Fe
0.210	0.240	1.280	0.300	0.040	0.011	0.007	0.001	Balance

Previous studies have shown that hydrogen embrittlement is generally caused by local hydrogen enrichment trapped at dislocations, grain boundaries etc. and a high density of hydrogen traps would reduce the diffusion coefficient of hydrogen (Hadžipašić et al., 2011a; Loidl et al., 2011; Robertson et al., 2015). Steels containing martensite phases have higher capacities for capturing hydrogen atoms than those containing other types of phases, such as ferrite, pearlite, etc., and therefore steels with relatively low hydrogen diffusion coefficients will be more susceptible to hydrogen embrittlement (Hadžipašić et al., 2011a; Hadžipašić et al., 2011b; Hui et al., 2019). Meanwhile, with the increase of the martensite content, the concentration of hydrogen traps increased, and the effective hydrogen diffusion coefficient decreased (Liu et al., 2016a; Liu et al., 2018). As a result, compared with the DP980 steel, DP1200 steel is more sensitive to hydrogen embrittlement and the tensile elongation decreased from 9 to 5% after hydrogen charging (Loidl et al., 2011).

However, the increasing of martensite content is often coupled with a change in distribution morphology. Davies (Davies, 1981; Davies, 1983) found that hydrogen embrittlement susceptibility of DP steel did not increase linearly with increasing the martensite content from 0 to 45%. When the martensite content is lower than 30%, hydrogen embrittlement susceptibility increases with martensite content increasing. However, when the martensite content increases to 30%, the martensite phase starts to distribute continuously along the grain boundary and hydrogen embrittlement susceptibility reaches a stable value. But up till date, how martensite content and morphology distribution affects hydrogen diffusion is still not investigated.

Therefore, in this study, we investigated the hydrogen embrittlement behavior of DP steels using slow-strain rate tensile tests. The electrochemical permeation technique was used to investigate hydrogen diffusion behavior, particularly focusing on the influence of martensite distribution on hydrogen diffusion. A mathematical relationship was established between the effective hydrogen diffusion coefficient and the hydrogen embrittlement index to evaluate the hydrogen embrittlement susceptibility from the perspective of hydrogen diffusion.

EXPERIMENTAL SECTION

Material Characterization

Cold rolled steel sheets with an as-received thickness of 1.4 mm were used in this study. The chemical composition of the steel is presented in **Table 1**. Samples of 200 mm × 50 mm cut along the rolling direction were annealed in a tube vacuum furnace for 30 min and quenched in water. Based on thermo-calc software (A_{c1} = 780°C, A_{c3} = 870°C), the annealing temperatures of 780, 810, 840, and 870°C were selected to obtain the desired quantity of martensite. A microstructural study of the samples was conducted using a high-resolution SEM (FEI Nova 400 Nano). Combined with Image Pro Plus software, martensite content, average grain size and length of the ferrite/martensite interface were counted by ten SEM photographs in 5,000× magnification. The detailed microstructure of the martensite was analyzed by JEM - 2101FXIITEM.

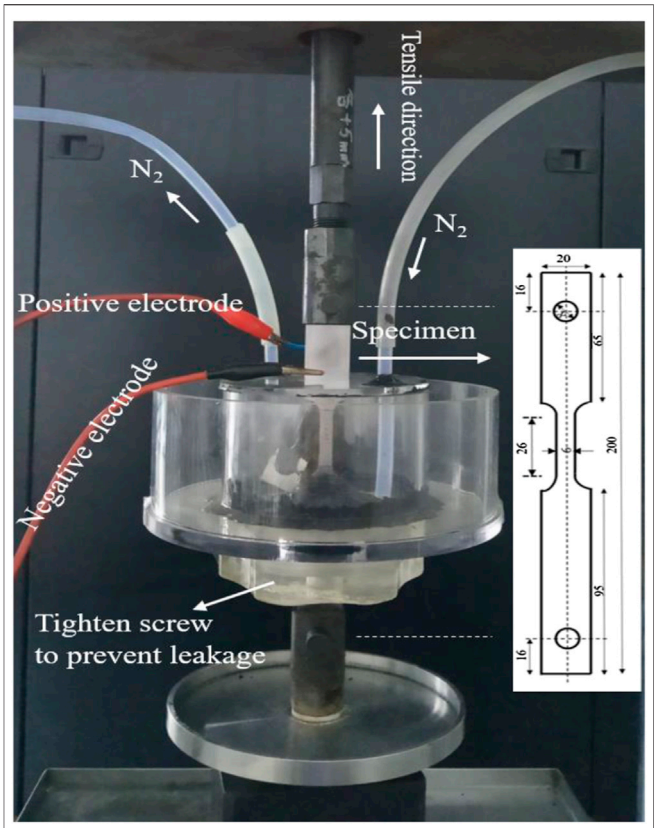

FIGURE 1 | Experimental set-up for tensile test under *in situ* electrochemical hydrogen charging, the dimensions of specimen are in mm.

Testing of Hydrogen Embrittlement Susceptibility

Hydrogen embrittlement susceptibility measurements were carried out on pre-polished tensile samples (26 mm × 6 mm × 1.4 mm) using a slow strain rate tensile test machine (WDML-3) under *in situ* electrochemical H-charging. The device and specimen shape were shown in **Figure 1**. The same method was also described in literature (Yuan et al., 2018). The strain rate was selected as 1×10^{-6} s^{-1} to facilitate keeping the diffusion of hydrogen atoms in step with the dislocation movement, thereby resulting in hydrogen embrittlement (Kumamoto et al., 2019). Both the hydrogen-charged and uncharged specimens were subjected to tensile test, with the former group referred as "H-charged" group, and the latter group referred as "air" group. For H-charged group, hydrogen charging tests were carried out in an aqueous solution of 0.5 mol/L H_2SO_4 and 1 g/L $Na_4P_2O_7$ with a current density of 10 mA/cm^2. The solution was purged with N_2 for 2 h prior to testing to remove any oxygen and continuously purged with N_2 throughout the experiment.

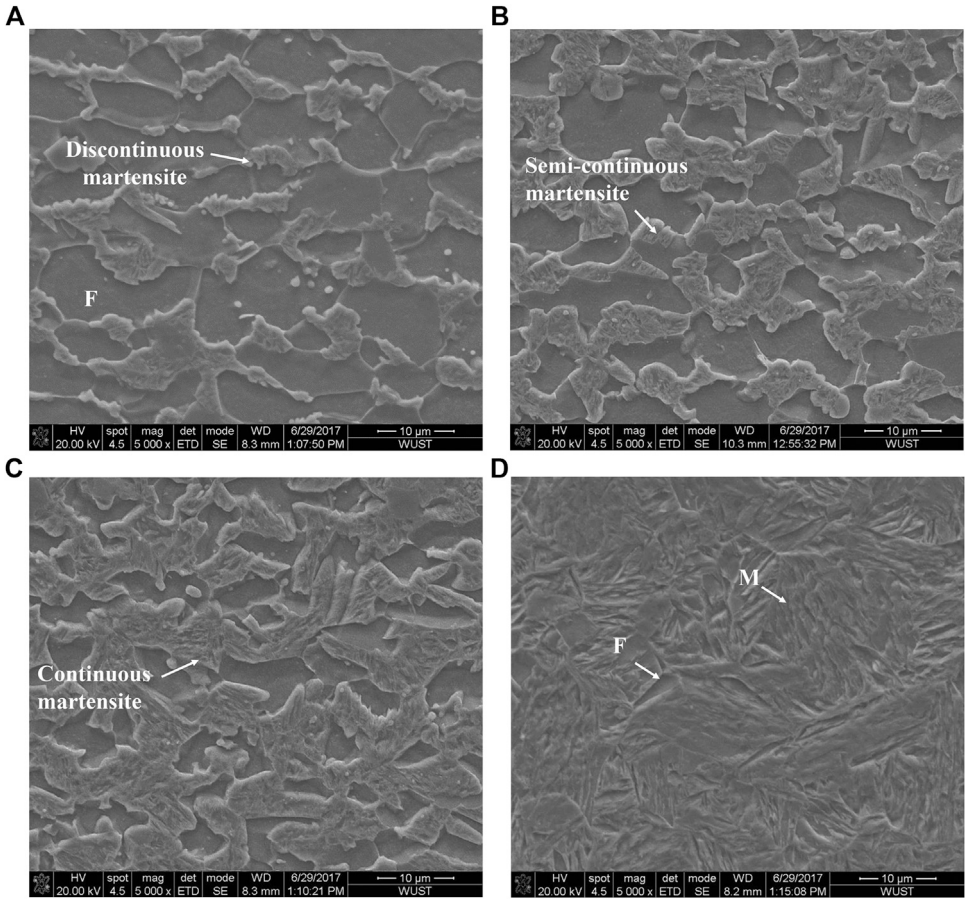

FIGURE 2 | SEM images of DP steels after annealing at **(A)** 780°C; **(B)** 810°C; **(C)** 840°C; and **(D)** 870°C.

Hydrogen Permeation Test

The hydrogen diffusion behavior of the DP steels was investigated using the hydrogen permeation test conducted in double electrolyte-cells (Chen et al., 2019). The dimensions of the samples used were 20 mm × 30 mm × 1.4 mm. Both sides of the specimens were polished to eliminate flux-limiting surface impedances and ensure the reliability of the measurement of the hydrogen oxidation current. A circular area of 1 cm^2 was exposed to the electrolytic cells. The receiving cell was filled with 300 ml of 0.1 mol/L NaOH before applying a constant positive voltage of 250mV to the steel membrane. When the anode current fell below 10^{-8} A, 300 ml of 0.5 mol/L H_2SO_4 and 1 g/L $Na_4P_2O_7$ were added to the hydrogen charging cell and a charging current of 10 mA/cm^2 was maintained. When the permeation rate achieved a steady-state level, the successive decay curve was measured after stopping the current and discharging the acid solution, until the anode current dropped below 10^{-8} A. The solution used was deoxidized in advance and the N_2 continued to pass through the solution during the experiment. All experiments were performed at room temperature. To ensure reliability of the experimental data, each test was repeated at least three times.

Hydrogen Microprint Test

Immediately after hydrogen charging, the charging sides of original samples without tensile were lightly polished and etched with 2% nital. Hydrogen microprinting was achieved by immersing the samples in a solution of a 10 g AgBr emulsion in 20 ml of 1.4 mol/L $NaNO_2$ at 45°C for 30 min in the darkroom. Hydrogen atoms were replaced by Ag on the specimen surface from the solution *via* a redox reaction (Ohmisawa et al., 2003). The specimens were rinsed in a 5% $NaNO_2$ aqueous solution. The microstructure was analyzed to determine the distribution of silver particles on SEM.

RESULTS

Microstructure Characterization

Figure 2 showed that the microstructure of annealed samples consisted of both ferrite (F) and martensite (M). The martensite was small and discontinuous when annealed at 780°C. However, with the increase of annealing temperature, the content and the size of martensite increased. Martensite grains were gradually in a continuous manner over the ferrite grain boundaries. Distribution of martensite changed from semi-continuous style

TABLE 2 | Content of martensite, average size of ferrite (F), average size of martensite (M) and length of ferrite/martensite (F/M) in DP steels.

Temperature (°C)	780	810	840	870
Content (%)	18.5	46.7	68.3	96.3
Size of M (μm)	2.63	7.14	10.52	12.63
Size of F (μm)	9.21	8.57	3.94	1.98
Length of F/M (10^{-2}μm/μm^2)	6.59	17.90	9.87	4.65

to a continuous network. The length of the ferrite/martensite (F/M) interface initially increased and subsequently decreased, as showing in **Table 2**. It is mainly because the length of the F/M interface depended largely on the size of dispersed martensite when the martensite distribution is discontinuous, while it depended on the ferrite size when martensite was distributed in a continuous network. **Figure 3** revealed a high density of dislocations in the ferrite region around the F/M interface. In

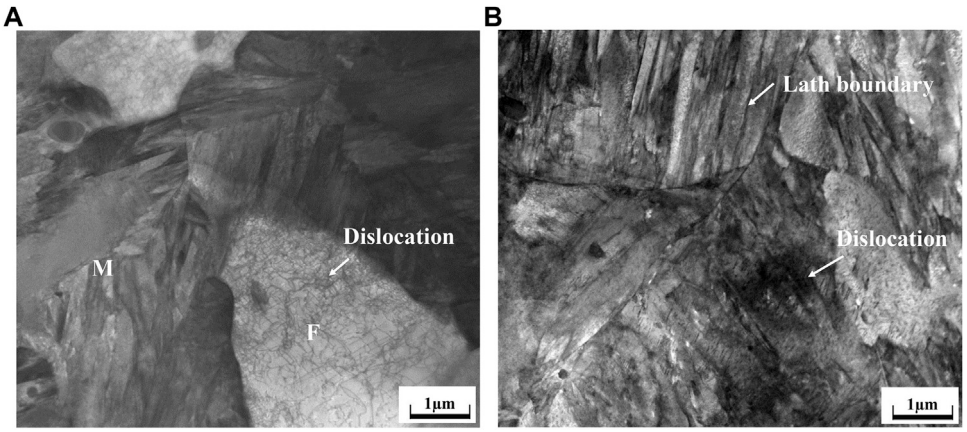

FIGURE 3 | TEM images of DP steel with 68.3% martensite content: **(A)** Dislocations in the ferrite region around the F/M boundary; and **(B)** dislocations and lath boundaries in the martensite.

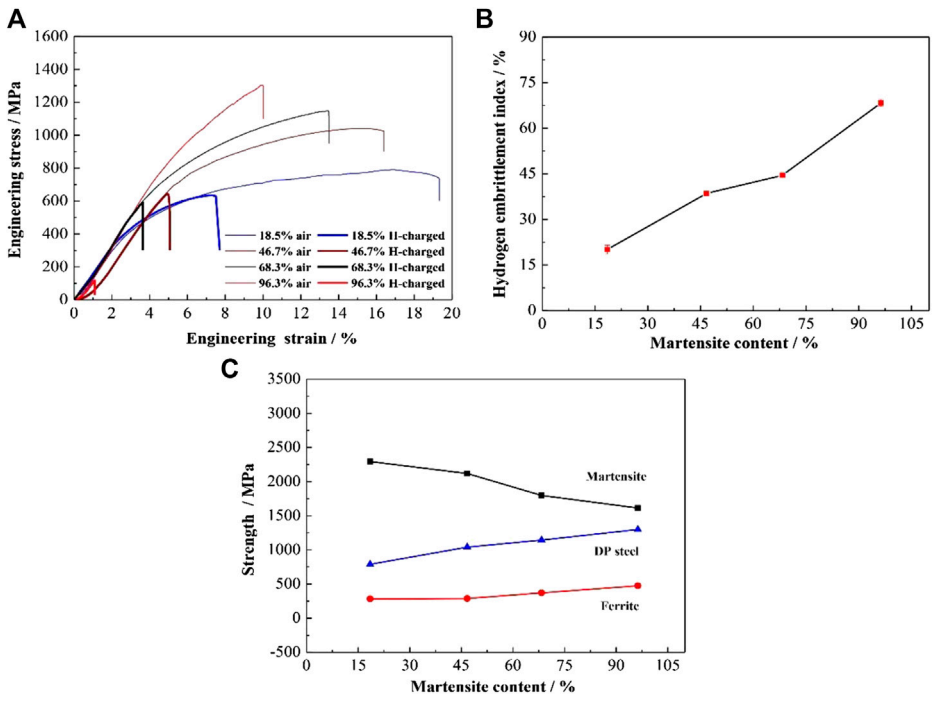

FIGURE 4 | (A) Stress-strain curves; **(B)** hydrogen embrittlement susceptibility; and **(C)** strength of ferrite and martensite of DP samples with different martensite content.

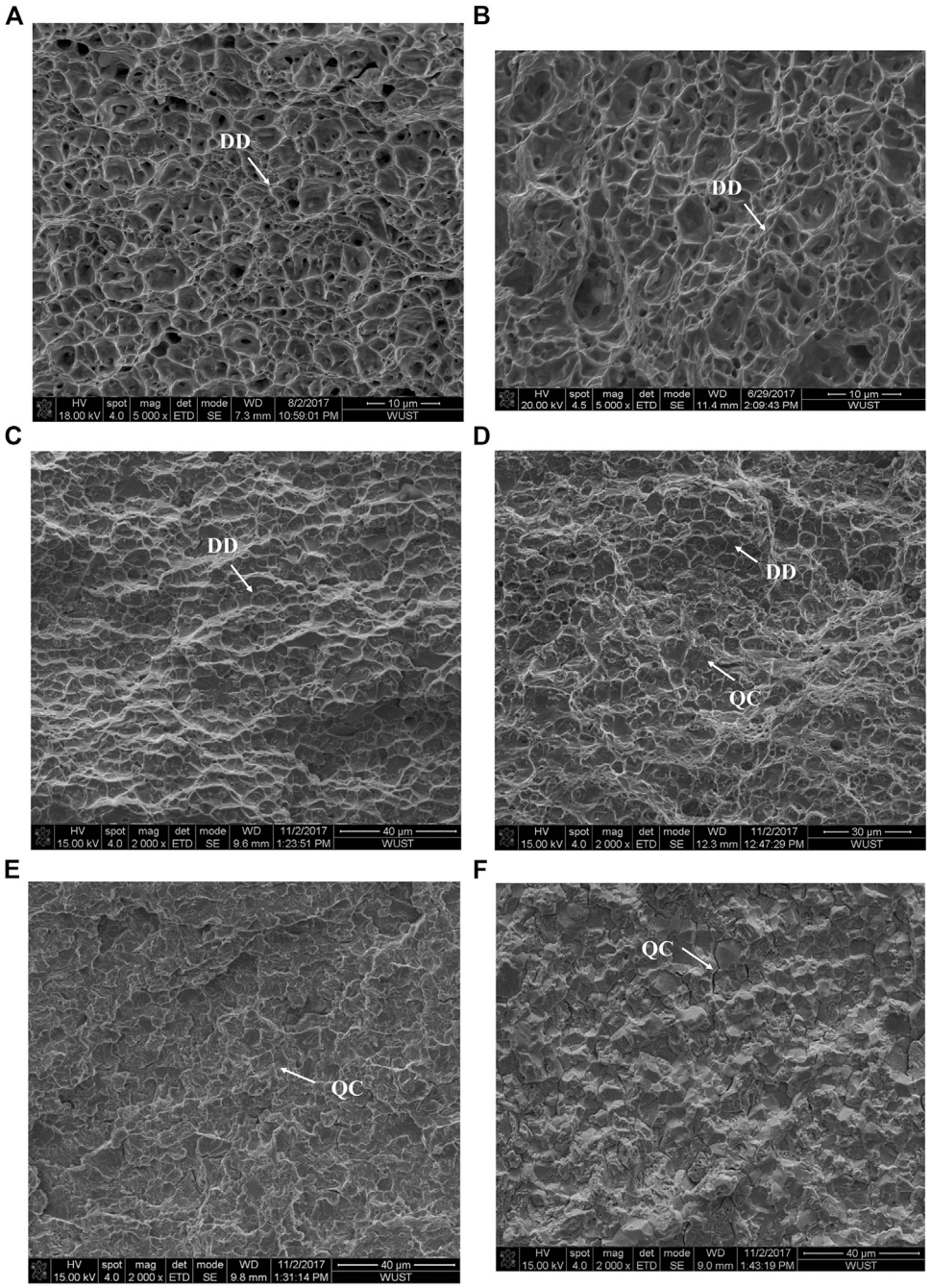

FIGURE 5 | Fracture surface morphologies of DP steels with different martensite content: **(A)** 18.5% with non-charged; **(B)** 96.3% with non-charged; **(C)** 18.5% with H-charged; **(D)** 46.7% with H-charged; **(E)** 68.3% with H-charged and **(F)** 96.3% with H-charged.

addition, a high density of lath boundaries and dislocations were observed within the martensite.

Hydrogen Embrittlement Susceptibility

When the specimen was stretched slowly in an acidic solution, the plastic index decreased, causing embrittlement of the material, known as hydrogen-induced plastic loss. The hydrogen embrittlement index (I_{HE}) is defined as (Loidl et al., 2011):

$$I_{HE} = (\delta_0 - \delta_H)/\delta_0 \times 100\% \quad (1)$$

where δ_0 is the elongation of specimens in air and δ_H is the elongation of specimens with hydrogen charging. I_{HE} can vary from 0% with no ductility loss, to 100% with total loss in ductility.

The tensile strength and total elongation of the samples decreased significantly due to hydrogen charging (**Figure 4A**). An increase in annealing temperature resulted in an increase in martensite content

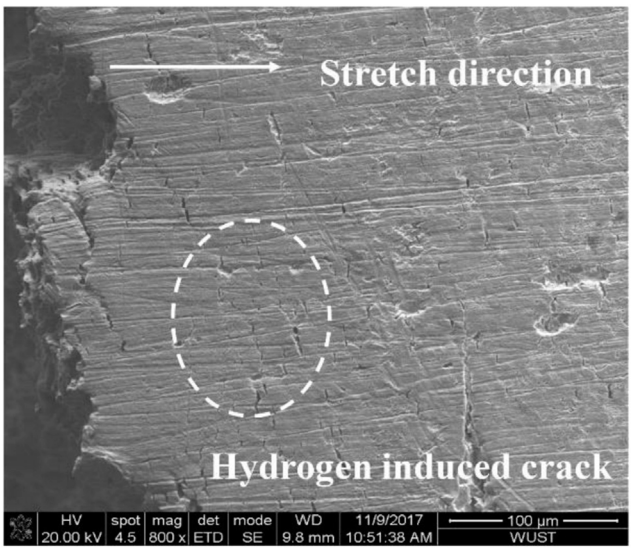

FIGURE 6 | Lateral fracture surface morphology of DP steel with martensite content in 18.5%.

and consequently the hydrogen embrittlement index (**Figure 4B**). **Figure 4C** shows the variation of strength in ferrite and martensite. With the increase of martensite content, the strength of ferrite increases while the martensite's decreases. The strength of ferrite can be calculated by the formula (Jahanara et al., 2019), $\sigma_b^F = \sigma_i + K_y d^{-1/2} + 69$, where σ_i is lattice friction (49 MPa), K_y is constant (500 MPa μm$^{1/2}$), and d is the grain size of ferrite (see **Table 2**). The martensite's strength can be achieved by the formula (Xia and Zhou, 2000), $\sigma_b^M = 541 + 2289\,(C_m)^{1/2}$, C_m is the carbon content in the martensite, which can be obtained by thermo-calc software. The values are 0.589, 0.475, 0.301, and 0.220% respectively corresponding to the martensite content with 18.5, 46.7, 68.3, and 96.3%.

Figure 5 shows the fracture surface morphologies of the tensile steels. The fracture surface morphologies of the non-charged samples present ductile fracture features (**Figures 5A,B**). After hydrogen charging, the proportion of brittle fracture characteristics increases gradually with increasing martensite content. Uniform ductile dimples (DD) appear on the sample with low martensite content 18.5% (**Figure 5C**), the dimples (DD) become shallower, and some quasi-cleavage (QC) fracture features appear with increasing martensite content (**Figure 5D**). When the martensite content reaches over 68.3%, the fracture completely exhibits brittle characteristics of a quasi-cleavage (QC) fracture (**Figure 5E**) and intergranular fracture (**Figure 5F**). Combined with microstructural observation in **Figure 2**, it was found that when the martensite content is low and the martensite are distributed, the steel is mainly characterized by ductile fracture. As the martensite content increased, the martensite became a continuous network and the fracture surface presents brittle features.

Lateral fracture surface morphology examination showed several secondary hydrogen-induced cracks, which formed on the surface of tensile samples with low martensite content, are perpendicular to the direction of tensile stress and adjacent to the main fracture (**Figure 6**). When the martensite content reached 68.3%, brittle fractures occurred directly in the hydrogen charging solution without any cracks on the side of the fracture. Detailed SEM observation revealed that the most secondary hydrogen-induced cracks was initiated at the F/M interface and propagated toward the martensite, whereas the ferrite acted as crack propagation barriers (**Figure 7A**). As the martensite content increased, the grain size of martensite increased, and the hydrogen-induced cracks started to propagate continuously throughout martensite grains (**Figure 7B**). Hydrogen microprinting confirmed that most of the silver particles clustered at the ferrite/martensite interfaces (**Figure 8**), indicating the aggregation of hydrogen atoms at the interface.

Hydrogen Permeation Test

Hydrogen diffusion in DP steel is strongly influenced by the presence of martensite. As the martensite content increased, both the permeation time and desorption time increased, while the steady state current decreased (**Figure 9**).

Permeation experiments allow the determination of hydrogen permeation parameters *via* the following methods (Liu et al., 2016b). The hydrogen flux through the sample was measured by the steady state hydrogen current density, I_∞, which is converted into hydrogen permeation flux, J_∞ by **Eq. 2**.

$$J_\infty = \frac{I_\infty}{FA} \tag{2}$$

where A is the sample area and F = 96,485 C/mol is the Faraday constant. In this study, A = 1 cm^2. The effective hydrogen diffusivity, D_{eff}, can be calculated by **Eq. 3**.

$$D_{\text{eff}} = \frac{L^2}{6t_{0.63}} \tag{3}$$

where L is the thickness of the sample and $t_{0.63}$ is the corresponding time for $0.63I_\infty$, as shown by the arrows in **Figure 9A**. In this work, L is 1.4 cm. The hydrogen concentration at the charging side, C_0, can be calculated by **Eq. 4**.

$$C_0 = \frac{J_\infty L}{D_{\text{eff}}} \tag{4}$$

The hydrogen trapping density can be estimated by **Eq. 5**.

$$N_T = \frac{C_0}{3}\left(\frac{D_L}{D_{\text{eff}}} - 1\right) \tag{5}$$

D_L is the lattice diffusion coefficient of hydrogen, which can be estimated by fitting the permeation **Eq. 6** to the experimental permeation during the 1–0.8 desorption step.

$$\frac{i_p - i_p^\infty}{i_p^0 - i_p^\infty} = 1 - \frac{2L}{\sqrt{\pi Dt}}\sum_{n=0}^{\infty}\exp\left(-\frac{(2n+1)^2L^2}{4Dt}\right) \tag{6}$$

where i_p^0 is the initial steady-state permeation rate at time t = 0, and i_p^∞ is the steady-state permeation. The accuracy of the fitting curve that can be met with n is 0, 1, 2, 3, 4.

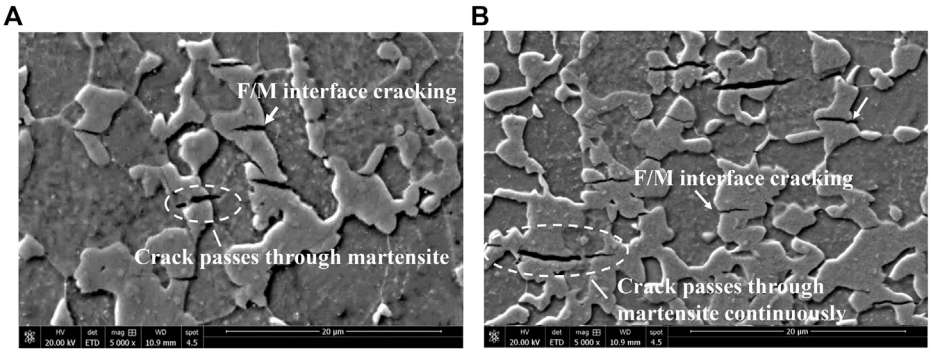

FIGURE 7 | Hydrogen-induced cracks of DP steels with different martensite content: **(A)** 18.5%; and **(B)** 46.7%.

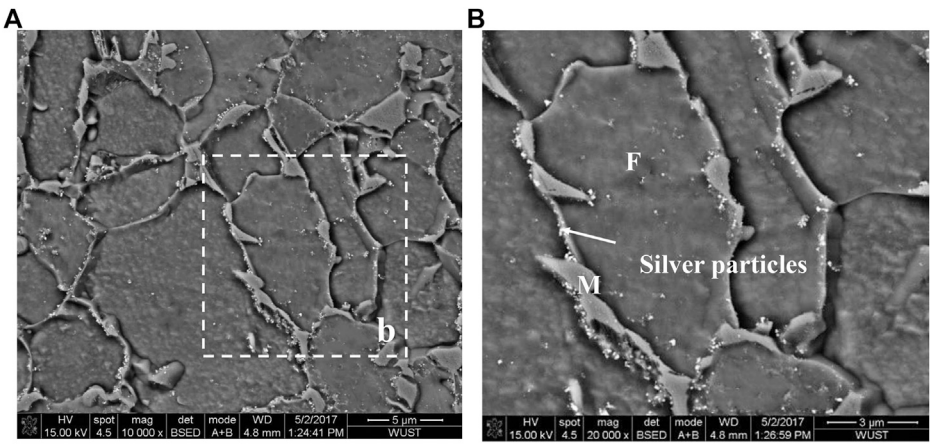

FIGURE 8 | (A) Hydrogen microprints showing hydrogen concentration at the F/M interface in a sample with 18.5% marteniste content; and **(B)** the corresponding enlarged image.

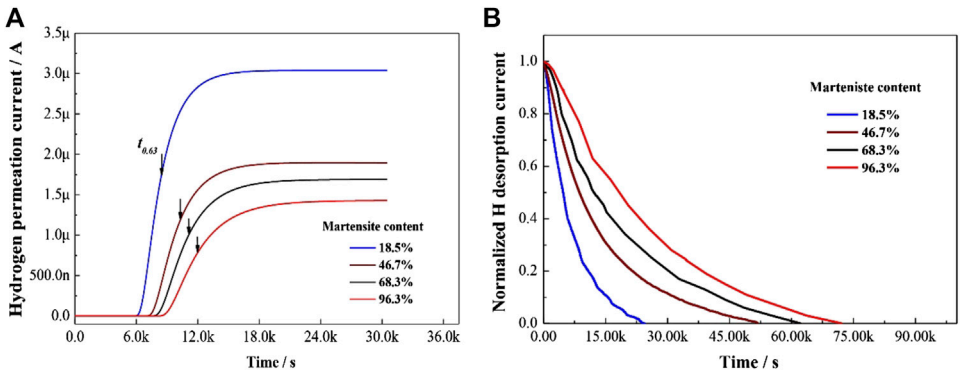

FIGURE 9 | Hydrogen permeation curves of DP samples: **(A)** Hydrogen permeation during charging step; and **(B)** hydrogen permeation during desorption step.

Table 3 shows the hydrogen permeability parameters in DP steels. As the martensite content increased, the hydrogen trapping density N_T increased, and the effective hydrogen diffusion coefficient D_{eff} and the hydrogen permeation flux J_{∞} decreased.

Figure 10 shows the relationship between martensite content and the calculated hydrogen diffusion coefficient. In order to ensure the accuracy of linear fitting, an DP steel with smaller martensite content (<18.5%) is needed. As it was hard to obtain a sample with martensite content below 18.5% using the current steel with 2.0 wt % carbon content, DP steel with 1.0 wt % carbon content and the similar content of other elements were subjected to heat treatment. After annealing in the two-phase zone, 6.49%

TABLE 3 | Hydrogen permeation parameters of DP steels.

Martensite content, %	J_∞, mol·cm^{-2}·s^{-1}	$t_{0.63}$, s	D_{eff}, cm^2·s^{-1}	N_T, mol/cm^3
18.5	3.16×10^{-11}	8,757	3.73×10^{-7}	2.13×10^{-6}
46.7	1.96×10^{-11}	11,264	2.90×10^{-7}	2.30×10^{-6}
68.3	1.74×10^{-11}	11,666	2.80×10^{-7}	2.61×10^{-6}
96.3	1.47×10^{-11}	11,793	2.77×10^{-7}	2.77×10^{-6}

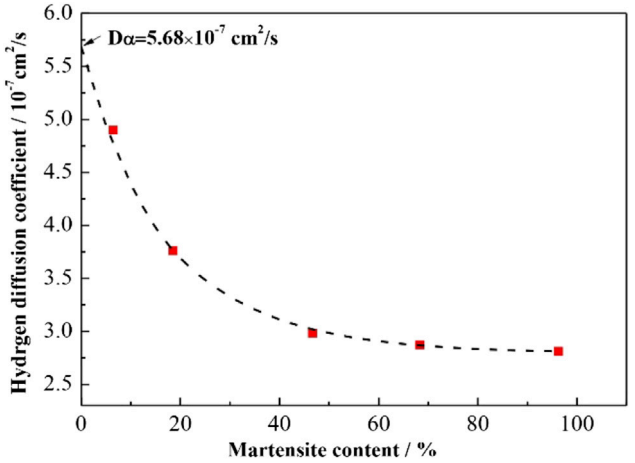

FIGURE 10 | The correlation of the hydrogen diffusion coefficient as a function of martensite content in DP steel.

martensite content was obtained. The hydrogen diffusion coefficient in this sample was 4.90×10^{-7} cm^2/s. Due to the very low martensite content, the hydrogen atoms primarily diffused along the ferrite (Owczarek and Zakroczymski, 2000). As most of the carbon atoms were presented in the martensite, the effect resulted by the decrease of carbon content from 2 to 1 wt % on the diffusion coefficient of steel could be ignored, which makes the linear fitting reliable. As the martensite content increased, the hydrogen diffusion coefficient decreased rapidly before leveling off at approximately 68.3% or higher martensite content. By extrapolating the curve to 0% martensite, the effective hydrogen diffusion coefficient (D_α) in the ferrite phase was about 5.68×10^{-7} cm^2/s.

According to the previous hydrogen diffusion model (Owczarek and Zakroczymski, 2000), the change in the desorption rate of hydrogen atoms in martensite i_m with time t can satisfythe **Eq. 7**:

$$i_m = 4\pi D_m C^*_{m,0}\left\{\exp\left[-\frac{D_m(2.404)^2 t}{R^2}\right] + \exp\left[-\frac{D_m(5.520)^2 t}{R^2}\right] + \exp\left[-\frac{D_m(8.654)^2 t}{R^2}\right] + \ldots\right\} \quad (7)$$

In the formula, $C^*_{m,0}$ is the initial concentration of hydrogen atoms in the martensite at the beginning of desorption; D_m is the effective hydrogen diffusion coefficient in the martensite; and R is the average equivalent diameter of the martensite. When the desorption time $t \to \infty$, only the first term in **Eq. 7** can make the equation hold, as shown in **Eq. 8**:

$$i_m = 4\pi D_m C^*_{m,0}\left\{\exp\left[-\frac{D_m(2.404)^2 t}{R^2}\right]\right\} \quad (8)$$

Using the logarithm of **Eq. 8**, a linear correlation with time, t is revealed:

$$\log i_m = \log\left(4\pi D_m C^*_{m,0}\right) - \frac{D_m(2.404)^2 t}{R^2} \quad (9)$$

Therefore, after a certain time, the logarithm of the desorption rate should be a linear function of time with a slope dependent only on D_m and R.

To establish the hydrogen desorption current curve in the martensite, i_m, we first calculated the hydrogen desorption current in the pure ferrite, i_α by substituting the ferrite's diffusion coefficient in **Eq. 6**. The hydrogen desorption curves in the martensite can be calculated by subtracting the desorption curve of the ferrite from the measured desorption curve of DP steel, i.e., $i_m = i - i_\alpha$, as shown in **Figure 11A**. Using the method, the hydrogen desorption curves in the martensite can be obtained, as showing in **Figure 11B**. Combining **Eq. 9**, the effective hydrogen diffusion coefficient D_m of hydrogen atoms can be obtained.

The results are largely consistent with the hydrogen diffusion coefficient in pure martensite steel (Frappart et al., 2012). The effective hydrogen diffusion coefficient in martensite (D_m) increased with the martensite content (**Figure 12A**), possibly due to a decrease in the carbon concentration of the martensite. Carbon content in martensite was obtained by thermo-calc software against intercritical annealing temperature. As the intercritical annealing temperature increased, the proportion of carbon in the martensite decreased (**Figure 12B**).

DISCUSSION

Effect of Martensite Content and Distribution on Hydrogen Diffusion of DP Steels

Previous studies have shown that the decrease in hydrogen diffusion coefficient of DP steel is correlated to martensite, which contains a high density of dislocations and other defects to capture hydrogen atoms (Sun et al., 1989; Hadžipašić et al., 2011a; Hadžipašić et al., 2011b; Koyama et al., 2014; Liu et al., 2016a; Liu et al., 2018; Hui et al., 2019). It is logical to deduce that the hydrogen diffusion coefficients decrease as martensite content increases. However, **Figure 10** showed that once the martensite content reached approximately 68.3%, the hydrogen diffusion coefficient started to level off. Therefore, the hydrogen diffusion is strongly influenced by not only the martensite content but also the distribution of the martensite phases. Depending on the characteristics of microstructure and hydrogen diffusion in DP steels, a model describing the mechanism of microstructure-driven hydrogen diffusion with different martensite distribution was established.

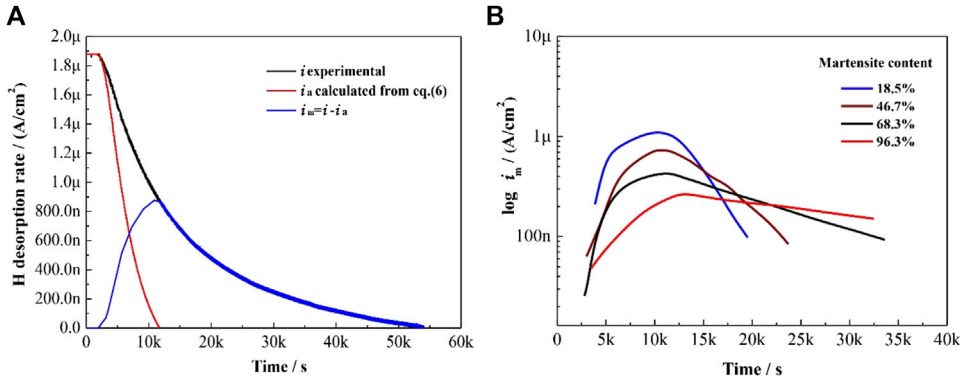

FIGURE 11 | (A) Desorption curves of ferritic and martensitic phases in DP steel with 46.7% martensite content; and **(B)** calculated hydrogen desorption rate in the martensitic phase vs time.

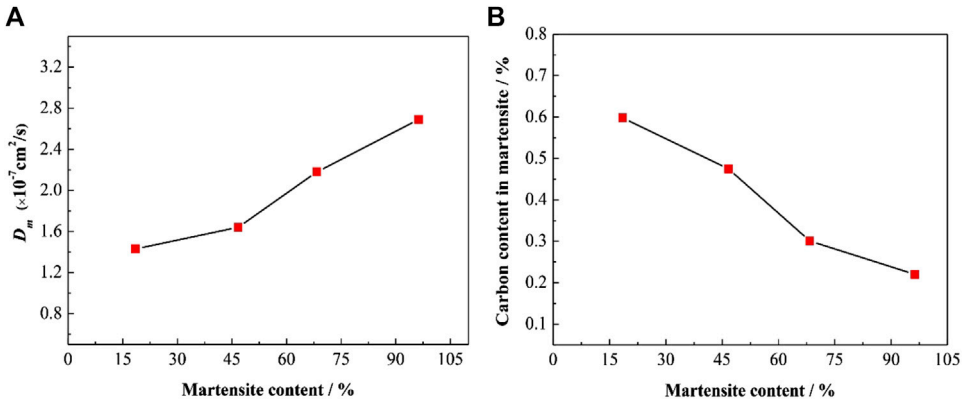

FIGURE 12 | (A) The hydrogen diffusion coefficient in martensite and **(B)** calculated carbon concentration vs the martensite content.

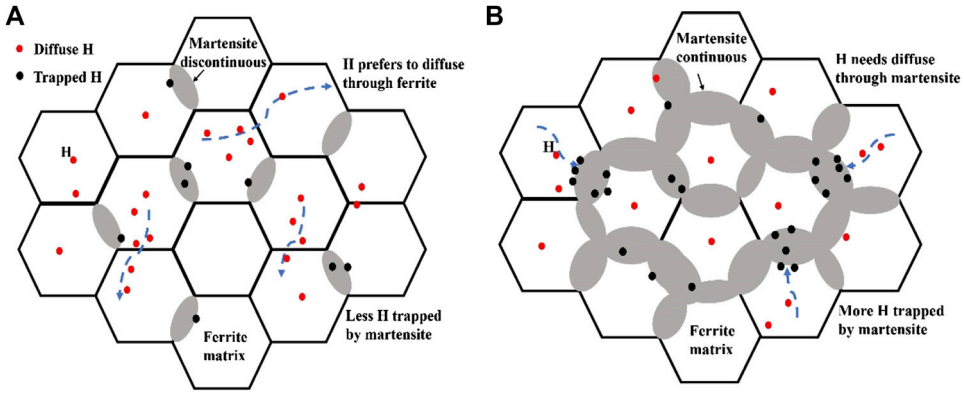

FIGURE 13 | Schematic representation of the microstructure-driven hydrogen diffusion in DP steel: **(A)** distribution of martensite is discontinuous; **(B)** ditribution of martensite is continuous.

When the martensite content was relatively low, the martensite phases were in the form of small isolated islands (**Figures 2A**,**B**). Hydrogen atoms preferentially passed through the ferrite for its higher hydrogen diffusion coefficient than martensite. And they were unlikely to be accumulated, which could be reflected by a higher hydrogen diffusion flux and

effective hydrogen diffusion coefficient in DP steel (**Table 3**). As the martensite content increased, the length of F/M interface increased (**Table 2**), which acted as hydrogen traps. Hydrogen trapping effect at the interface could be observed directly through the hydrogen microprint (**Figure 8**). More martensite content resulted in higher hydrogen trapping effect, which presented an obvious decrease in both hydrogen diffusion flux and the effective hydrogen diffusion coefficient (**Table 3**).

However, when the martensite content increased to approximately 68.3%, the distribution of martensite phases started to form a continuous network (**Figures 2C**,D). Hydrogen atoms have to diffuse across the martensite, and the fast diffusion channel of the hydrogen atoms along the ferrite disappears. (**Figure 13B**). Hydrogen atoms were captured by both the F/M interface and martensite during diffusion. On one side, with the increasing of martensite content, the effective hydrogen diffusion coefficient in the steel continued to decrease due to a high density of dislocation and lath boundary in the martensite phase that acted as hydrogen traps, which is similar to the previous studies (Hui et al., 2019; Liu et al., 2016a; Kumamoto et al., 2019). On the opposite side, the carbon content in martensite decreased as the martensite content increased, which leading to the decreasing hydrogen trapping effect of carbon. Then the effective hydrogen diffusion coefficient increased as shown in **Figure 12**. The trapping effect between carbon and hydrogen atoms could refer to the literature (Geng et al., 2018). Therefore, the counterbalancing effect of the two opposite aspects leaded the hydrogen diffusion coefficients started leveling off.

Effect of Martensite Content and Distribution on Hydrogen Embrittlement of DP Steels

When subjected to thermomechanical treatment, there is stress concentrating around the F/M interface due to the strain incompatibility between the soft ferrite and hard martensite, resulting in high density of dislocations around the interface (**Figure 3A**). During the process of hydrogen charging, hydrogen atoms could migrate with the movable dislocation and aggregated at the interface, then generated an attached stress and subsequently promoted the interface cracking (Zhang et al., 2003), thus the hydrogen-induced crack initiated at the F/M interface and passed though the martensite (**Figure 7**).

When the martensite content was relatively low and the martensite phases were in the form of small isolated islands, the low concentration of hydrogen traps resulted in a low aggregation of hydrogen atoms. Thus, the additional stress generated by the hydrogen atom is low. Additionally, the soft ferrite could absorb parts of the plastic deformation energy during tension and effectively prevented the expansion of the crack (**Figure 7A**). Therefore, the hydrogen embrittlement index was low, and the tensile fracture surface presented the clear characteristics of the ductile fracture when martensite content was 18.5% (**Figure 6A**). With the increase of martensite content, the concentration of hydrogen traps increased and trapped more hydrogen atoms, which led to an increased additional hydrogen-induced stress at the interface of F/M. Additionally, with the decrease of ferrite size, the ferrite's strength increased and the susceptibility of ferrite to hydrogen embrittlement was also increased, which weakens the inhibition effect of ferrite on crack propagation. Therefore, the hydrogen embrittlement index of test steel increased from 20.28 to 38.89% and the dimples of tensile fractures became shallower, showing higher hydrogen embrittlement susceptibility.

However, when the martensite content increased to approximately 68.3%, the distribution of martensite phases started to form a continuous network (**Figures 2C**,D). The concentration of hydrogen traps and the captured hydrogen atoms in steel were continued to increase. But the length F/M interface decreased with the decrease of ferrite size, and thus the additional hydrogen-induced stress at F/M interface would reach a critical fracture stress more easily. Additionally, the reduction of carbon content in martensite promoted the diffusion of hydrogen atoms in martensite. Therefore, the effective hydrogen coefficient reaches a plateau, but the hydrogen embrittlement sensitivity increased continuously with increasing martensite content and the tensile fracture showed obvious cleavage or brittle intergranular fracture morphology (**Figures 5C**,D). Therefore, the critical transition point of the influence of the martensite content on hydrogen embrittlement was the formation of a continuous network of martensitic phases. Previous studies (Davies, 1983) also showed that when the martensite content increased to 30% and formed a continuous network, the hydrogen embrittlement susceptibility of DP steel reached a stable value. This may be related to the distribution of the long trip martensite along the interface. And the length of F/M interface didn't significantly change when the martensite content exceeds 30%. However, in this study, the morphology of martensite is block and the length of F/M interface decreased significantly with the increasing martensite content when the distribution of martensite is continuous in DP steel, which results in a continuously increasing of hydrogen embrittlement susceptibility.

Additionally, with the increase of martensite content, the strength of ferrite increases while the martensite's decreases, which could improve the deformation compatibility between the two phases (**Figure 4C**). A better deformation compatibility results in a more uniformly distribution of strain during the tensile deformation and could reduce the occurrence of pores and microcracks at the interface of the ferrite/martensite. However, with the increase of martensite content, the total hydrogen concentration trapped by the steel increases (**Table 3**). More hydrogen atoms could aggregate in the defect sites (such as ferrite/martensite interfaces or inclusions) of steel, and thus promoting nucleation. Moreover, the martensite matrix is more susceptible to the hydrogen embrittlement and has lower crack resistance, hydrogen-induced cracks are easier to propagate in DP steel with higher martensite content (**Figure 7B**). In summary, the increasing martensite content played dual roles in the hydrogen embrittlement of DP steels, with the harmful role far outweighed the beneficial role, finally leading to the increased hydrogen embrittlement susceptibility.

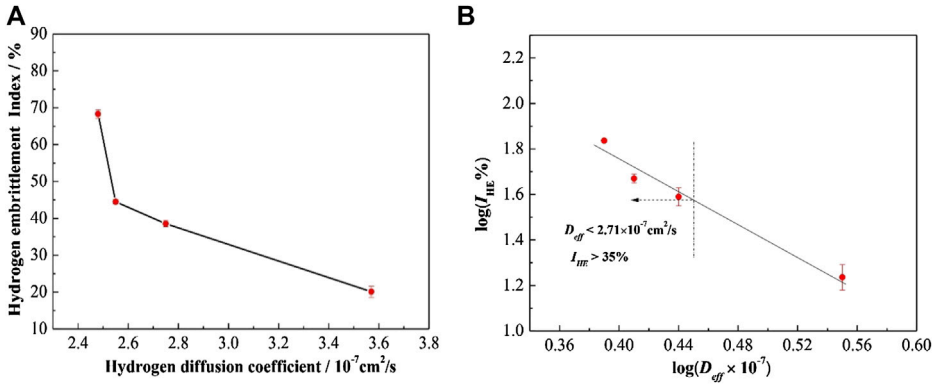

FIGURE 14 | Effect of the hydrogen diffusion coefficient on the embrittlement index of DP steels: **(A)** experimental dates; and **(B)** logarithmic values.

Correlation Between Hydrogen Diffusion and Hydrogen Embrittlement in DP Steels

The relationship between the D_{eff} and the I_{HE} is established in **Figure 14A** and the logarithmic value of the coordinate variables is taken in **Figure 14B**. The mathematical relationship between them could be expressed in **Eq. 10**. It showed that I_{HE} increased with a decrease in D_{eff}.

$$\log(I_{\text{HE}}) = 3.13 - 3.54 \times \log\left(D_{\text{eff}}\right) \tag{10}$$

Previous studies have shown that the influence of hydrogen diffusion on hydrogen embrittlement is mainly related to the aggregation of hydrogen atoms in hydrogen traps (Davies, 1981; Liu et al., 2016a). When $D_{\text{eff}} \rightarrow 0$, hydrogen atoms were captured by hydrogen traps such as martensite and F/M interface in DP steel, I_{HE} reached the maximum. With the increase of D_{eff}, the concentration of hydrogen atoms captured by the hydrogen traps decreased and less hydrogen enriched at the martensite phase and F/M interface, thus the hydrogen embrittlement susceptibility I_{HE} decreased. When D_{eff} reached infinity, the concentration of hydrogen captured in the hydrogen traps is almost zero, which results that the I_{HE} approached zero. Previous study has shown that when I_{HE} is over 35%, the material was sensitive to hydrogen embrittlement (Jahanara et al., 2019). We substituted 35% into **Eq. 10**, D_{eff} was calculated as 2.71×10^{-7} cm^2/s. The D_{eff} value could be used to evaluate hydrogen embrittlement susceptibility of DP steels and the material was sensitive to hydrogen embrittlement when the D_{eff} was less than 2.71×10^{-7} cm^2/s, which would need fewer test materials and shorter test time compared with the usual slow strain rate tensile test.

Through the above research, the hydrogen embrittlement problem in high strength steel is mainly caused by the trapping and aggregation of hydrogen atoms at the hydrogen traps such as ferrite/martensite interfaces or within the martensite phases. Therefore, during the development of new hydrogen resistant materials, reducing the number of hydrogen traps or the concentration of trapped hydrogen atoms can reduce the hydrogen embrittlement susceptibility of high strength steels containing martensite phase. The required strength of steel could be achieved by refining the grains if the quantity of martensite content were decreased to reduce the quantity of available hydrogen traps, such as martensite and ferrite/martensite phase boundaries. Besides, the distribution of the martensite phases can be refined through suitable heat treatments to avoid the formation of a continuous martensite network.

CONCLUSION

(1) In DP steels, the hydrogen trapping density increases with increasing martensite content, resulting in an increase in hydrogen aggregation concentration and hydrogen embrittlement susceptibility. When the martensite content reaches 68.3% and distributes to a continuous network, the decreasing length of the ferrite/martensite interface makes it easier for gathering hydrogen atoms to reach the critical concentration for the cracking of the ferrite/martensite boundary, resulting in the continuously increasing of hydrogen embrittlement.

(2) The hydrogen diffusion is strongly influenced by the distribution of the martensite phases in DP steel. When the martensite phases are isolated, the diffusion of hydrogen primarily occurs through ferrite grains and the ferrite/martensite interfaces are the main traps that decrease the effective hydrogen diffusion coefficient with increasing martensite content. When the martensite phase starts to form a continuous network, the hydrogen atoms have to diffuse through the martensite phases. The counterbalancing effect of the increasing hydrogen diffusion coefficient in the martensite phase with decreasing carbon content slows the decrease of D_{eff}.

(3) A logarithmic relationship between the hydrogen embrittlement index I_{HE} and the hydrogen diffusion coefficient D_{eff} is established as $\log(I_{\text{HE}}) = 3.13 - 3.54 \times \log(D_{\text{eff}})$. The susceptibility of the hydrogen embrittlement in high strength DP steel will decrease with an increasing hydrogen diffusion coefficient. Finely dispersed

martensite is conducive to reducing the hydrogen embrittlement susceptibility of DP steels with fewer hydrogen traps and a lower concentration of captured hydrogen atoms compared with martensite distribution in a continuous network.

DATA AVAILABILITY STATEMENT

The original contributions presented in the study are included in the article/Supplementary Material, further inquiries can be directed to the corresponding author.

AUTHOR CONTRIBUTIONS

ZW wrote the manuscript. All authors discussed the results and contributed the final manuscript.

ACKNOWLEDGMENTS

This work was supported by the National Natural Science Foundation of China (Grant no. 51871171 and 51871172). The authors would like to extend their gratitude to Bing Fu, Xuan Zhang, and Lin Cheng from the School of Materials Science and Engineering.

REFERENCES

Chen, Y., Liu, J., Huang, F., Chen, L., Su, Y. J., and Zhou, G. F. (2019). Influence of inclusions on hydrogen-induced delayed cracking in hot stamping steels. *J. Iron Steel Res. Int.* 26, 1199–1208. doi:10.1007/s42243-019-00312-z

Davies, R. (1981). Hydrogen embrittlement of dual-phase steels. *Metall. Trans. A* 12, 1667–1672. doi:10.1007/bf02643572

Davies, R. (1983). Influence of martensite content on the hydrogen embrittlement of dual-phase steels. *Scripta Metall.* 17, 889–892. doi:10.1016/0036-9748(83)90255-7

Frappart, S., Feaugas, X., Creus, J., Thebault, F., Delattre, L., and Marchebois, H. (2012). Hydrogen solubility, diffusivity and trapping in a tempered Fe–C–Cr martensitic steel under various mechanical stress states. *Mater. Sci. Eng. A* 534, 384–393. doi:10.1016/j.msea.2011.11.084

Geng, W. T., Wang, V., Li, J. X., Ishikawa, N., Kimizuka, H., Tsuzaki, K., et al. (2018). Hydrogen trapping in carbon supersaturated α–iron and its decohesion effect in martensitic steel. *Scripta Mater.* 149, 79–83. doi:10.1016/j.scriptamat.2018.02.025

Hadžipašić, A. B., Malina, J., and Malina, M. (2011a). The influence of microstructure on hydrogen diffusion and embrittlement of multiphase fine-grained steels with increased plasticity and strength. *Chem. Biochem. Eng. Q.* 25 (2), 159–169.

Hadžipašić, A. B., Malina, J., and Nižnik, Š. (2011b). The influence of microstructure on hydrogen diffusion in dual phase steel. *Acta Metall. Slovaca.* 17, 129–137.

Hui, W. J., Wang, Z. H., Xu, Z. B., Zhang, Y. J., and Zhao, X. L. (2019). Hydrogen embrittlement of a microalloyed bainitic forging steel. *J. Iron Steel Res. Int.* 26, 1011–1021. doi:10.1007/s42243-019-00272-4

Jahanara, A. H., Mazaheri, Y., and Sheikhi, M. (2019). Correlation of ferrite and martensite micromechanical behavior with mechanical properties of ultrafine grained dual phase steels. *Mater. Sci. Eng.* 764, 138206. doi:10.1016/j.msea.2019.138206

Khan, M. I., Kuntz, M. L., Biro, E., and Zhou, Y. X. (2008). Microstructure and mechanical properties of resistance spot welded advanced high strength steels. *Mater. Trans.* 49, 1629–1637. doi:10.2320/matertrans.mra2008031

Koyama, M., Tasan, C. C., Akiyama, E., Tsuzaki, K., and Raabe, D. (2014). Hydrogen-assisted decohesion and localized plasticity in dual-phase steel. *Acta Mater.* 70, 174–187. doi:10.1016/j.actamat.2014.01.048

Kumamoto, T., Koyama, M., Sato, K., and Tsuzaki, K. (2019). Strain-rate sensitivity of hydrogen-assisted damage evolution and failure in dual-phase steel: from vacancy to micrometer-scale void growth. *Eng. Fract. Mech.* 216, 106513. doi:10.1016/j.engfracmech.2019.106513

Li, Y. X., Lin, Z. Q., Jiang, A. Q., and Chen, G. L. (2003). Use of high strength steel sheet for lightweight and crashworthy car body. *Mater. Des.* 24, 177–182. doi:10.1016/s0261-3069(03)00021-9

Liu, Q., Venezuela, J., Zhang, M., Zhou, Q., and Atrens, A. (2016a). Hydrogen trapping in some advanced high strength steels. *Corrosion Sci.* 111, 770–785. doi:10.1016/j.corsci.2016.05.046

Liu, Q., Zhou, Q., Venezuela, J., Zhang, M., Wang, J., and Atrens, A. (2016b). A review of hydrogen embrittlement of martensitic advanced high-strength steels. *Corrosion Rev.* 34, 127–152. doi:10.1515/corrrev-2016-0006

Liu, Q., Zhou, Q., Venezuela, J., Zhang, M., and Atrens, A. (2018). The role of the microstructure on the influence of hydrogen on some advanced high-strength steels. *Mater. Sci. Eng. A* 715, 370–378. doi:10.1016/j.msea.2017.12.079

Loidl, M., Kolk, O., Veith, S., and Göbel, T. (2011). Characterization of hydrogen embrittlement in automotive advanced high strength steels. *Mater. Werkst.* 42, 1105–1110. doi:10.1002/mawe.201100917

Ohmisawa, T., Uchiyama, S., and Nagumo, M. (2003). Detection of hydrogen trap distribution in steel using a microprint technique. *J. Alloys Compd.* 356, 290–294. doi:10.1016/s0925-8388(03)00355-4

Owczarek, E., and Zakroczymski, T. (2000). Hydrogen transport in a duplex stainless steel. *Acta Mater.* 48, 3059–3070. doi:10.1016/s1359-6454(00)00122-1

Robertson, I. M., Sofronis, P., Nagao, A., Martin, M. L., Wang, S., Gross, D. W., et al. (2015). Hydrogen embrittlement understood. *Metall. Mater. Trans. A* 46, 2323–2341. doi:10.1007/s11663-015-0325-y

Sirinakorn, T., Wongwises, S., and Uthaisangsuk, V. (2014). A study of local deformation and damage of dual phase steel. *Mater. Des.* 64, 729–742. doi:10.1016/j.matdes.2014.08.009

Sun, S., Gu, J., and Chen, N. (1989). The influence of hydrogen on the sub-structure of the martensite and ferrite dual-phase steel. *Scripta Mater.* 23, 1735–1737. doi:10.1016/0036-9748(89)90352-9

Xia, Y. M., and Zhou, Y. X. (2000). The effect of strain rate and martensite volume fraction on tensile impact behavior of dual phase steels. *Key Eng. Mater.* 177, 231–236. doi:10.4028/www.scientific.net/kem.177-180.231

Yuan, W., Huang, F., Liu, J., Hu, Q., and Frank Cheng, Y. (2018). Effects of temperature and applied strain on corrosion of X80 pipeline steel in chloride solutions. *Corrosion Eng. Sci. Technol.* 53, 393–402. doi:10.1080/1478422X.2018.1491111

Zhang, T., Chu, W., Gao, K., and Qiao, L. (2003). Study of correlation between hydrogen-induced stress and hydrogen embrittlement. *Mater. Sci. Eng. A* 347, 291–299. doi:10.1016/s0921-5093(02)00600-7

Conflict of Interest: The authors declare that the research was conducted in the absence of any commercial or financial relationships that could be construed as a potential conflict of interest.

frontiers in Materials

ORIGINAL RESEARCH
published: 11 January 2021
doi: 10.3389/fmats.2020.617223

Hot Stamping of a B-Pillar Reinforced Panel With 7075 Aluminum Alloy and the Feasibility Study of Short-Time Aging

Yong Liu, Jiahao Li, Liang Wang, Kai Wang, Bin Zhu and Yisheng Zhang*

State Key Laboratory of Materials Processing & Die and Mould Technology, School of Materials Science and Engineering, Huazhong University of Science and Technology, Wuhan, China

The hot stamping of a B-pillar reinforced panel with 7075 aluminum alloy was carried out in an industrial production line. The effect of blank holding force (BHF) on the formability of the B-pillar reinforced panel and the effect of solution heat treatment (SHT) time on the mechanical properties were studied. Additionally, the forming precisions of a formed part before and after standard aging were detected further. Finally, both standard aging and short-time aging processes were carried out to investigate the feasibility of short-time aging for real parts. The stamping results demonstrated that lower BHF or no blank holding should be used during hot stamping to avoid cracking and wrinkling. The detection of forming precisions indicated that the great majority of measured points on the part were within ±1 mm of nominal. The mechanical property testing showed that the strength of the formed parts after a short-time aging was up to more than 90% of the as-received T6 state and more than 93% of the time can be reduced if the 90% of strength can be accepted.

Keywords: hot stamping, 7075 aluminum alloy, blank holding force, forming precision, short-time aging

OPEN ACCESS

Edited by:
Minghui Cai,
Northeastern University, China

Reviewed by:
Jianguo Lin,
Imperial College London, United Kingdom
Xianhong Han,
Shanghai Jiao Tong University, China
Yu Chen,
Northeastern University, China

****Correspondence:***
Kai Wang
wangkai@hust.edu.cn

Specialty section:
This article was submitted to Structural Materials, a section of the journal Frontiers in Materials

Received: *14 October 2020*
Accepted: *23 November 2020*
Published: *11 January 2021*

Citation:
Liu Y, Li J, Wang L, Wang K, Zhu B and Zhang Y (2021) Hot Stamping of a B-Pillar Reinforced Panel With 7075 Aluminum Alloy and the Feasibility Study of Short-Time Aging. Front. Mater. 7:617223. doi: 10.3389/fmats.2020.617223

INTRODUCTION

Increasing attention has been paid to the lightweight qualities of automobiles due to imperious demands for environmental protection and energy-saving. Benefitting from high specific strength, good impact energy absorption, high corrosion resistance and good recyclability, aluminum alloys have been proved to be excellent light material for automobiles (Mohamed et al., 2012; Jürgen, 2014; Ghiotti et al., 2019). When stamped at room temperature, aluminum alloy parts have large springback (Maeno et al., 2017) and sometimes there are cracks in the parts (Liu et al., 2018). Besides, these parts may have thermal deformation during high-temperature heat treatment, e.g. solution heat treatment. Thus, hot stamping for heat-treatable aluminum alloy sheet has been developed (Garrett et al., 2005). During hot stamping of aluminum alloy, the blank is heated up to the SHT temperature and held for a period of time. Then the hot blank is transferred to the cold tools and subsequently formed and quenched in the closed tools, followed by holding in the tools for about 10 s. At last, the aging process is carried out to improve the strength of the formed part.

In short, hot stamping of an aluminum alloy mainly includes three processes: SHT, forming and aging. SHT and aging are heat treatment processes, which means that time and temperature are the main factors affecting the two processes. There is an expected scenario that workpieces with good performance can be obtained on the production line by using appropriate temperature and less time, while maintaining the continuity of the production. For 7075 aluminum alloy, it usually takes more

than 10 min to complete SHT by conventional means (Liu et al., 2020; Zhang et al., 2020), and the aging treatment needed to obtain maximum aging strength is generally about 120 °C for 24 h (Zhang et al., 2020). Not only are the SHT and aging times long, but also the aging time is more than 100 times longer than the SHT time. It means that the production efficiency is low, and the synchronization of production cannot be guaranteed. As a result, it is necessary to develop the innovative methods and processes to reduce the SHT time and aging time. Xu X et al. (Xu et al., 2015) reduce the aging time by 50% by adding Ag into 7075 aluminum alloy. In automotive manufacturing lines, vehicle parts will finally go through a paint bake process (180 °C × 30 min), which can be considered as part of the artificial aging process (Li et al., 2015). Combining with the paint bake process, Li N (Li et al., 2015) and Zheng J (Zheng et al., 2019) carried out pre-aging process for 6082, and more than 90% of the strength at T6 state could be obtained. Omer K et al. (Omer et al., 2018) conducted the aging process for 7075 samples at 120 °C × 3 h + 177 °C × 0.5 h and the strength was close to the strength under T6 condition. Sun W et al. (Sun et al., 2019) presented a method of using a controlled, room-temperature cyclic deformation to sufficiently and continuously inject vacancies into the material and to mediate the dynamic precipitation of a very fine (1- to 2-nm) distribution of solute clusters. This method takes tens of minutes and is currently only suitable for small samples, not for real parts. The results mentioned above were carried out under laboratory conditions, thus, the authors would like to study the feasibility of short-time aging of 7075 aluminum alloy combining with paint bake process on production line, maximizing the post strength of the part and reducing the aging time.

Furthermore, forming is an important procedure in the hot stamping process of aluminum alloy. Parts with no defects and high forming precision are expected to be obtained. Blank holding is often used to avoid or reduce the forming defects like wrinkling. In comparison to cold stamping, the flow stress of the material is relatively low due to the high temperature during hot stamping, while the friction is more serious. Consequently, the parts are prone to crack in the forming process. Considering the friction and low flow stress at high temperature, blank holding may cause fracture during deep drawing. Therefore, it is of significance to study the effect of BHF on the formability of real aluminum alloy parts in hot stamping.

In this paper, hot stamping of a B-pillar reinforced panel with 7075 aluminum alloy was carried out in an industrial production line. The effect of BHF on the formability of the B-pillar reinforced panel and the effect of SHT time on the mechanical properties were studied. Further, the forming precisions of a formed part before and after standard aging were detected. Finally, the standard aging and short-time duplex aging processes were carried out to investigate the feasibility of short-time aging for real parts to reduce the aging time further. It is expected to provide guidance for the forming of aluminum alloy parts with complex geometric shape by hot stamping process in industry.

MATERIALS AND EXPERIMENTS

A typical commercially available 7075 aluminum alloy was used in this work. The as-received 7075 aluminum alloy was under the T6 condition. Its yield strength (YS) and ultimate tensile strength (UTS) are respectively 532 and 585 MPa. The material used does not necessarily represent the microstructure that a production material would have prior to SHT. The dimension of the blank is approximately 1,450 × 650 × 1.5 mm (thickness). Besides, graphite was used as lubricant in the experiment.

The host stamping experiments were carried out in a production line as shown in **Figure 1A**. A servo press with a tonnage of 1,200 tons and a multilayer chamber furnace were used in the stamping experiments. **Figure 1B** shows the aging furnace and there is a fan in it to produce more efficient heat convection and make the temperature distribution more uniform. As indicated in literature (Harrison and Luckey, 2014), the SHT for 7075 typically occurs between 460–500 °C. As a result, the SHT temperature was set as 490 °C in the stamping experiments. All of the formed parts were held in the tools for 10 s with a pressure of 400 tons after closing the tools. Designed experiment conditions are shown in **Table 1**. The BHF was controlled by the nitrogen gas spring and the position of the blank holder is shown in **Figure 2**. The full BHF was 6 tons. The standard aging (SA, 120 °C × 24 h) process and duplex aging process (DA, 110 °C × 1 h + 180 °C × 0.5 h) were carried out within 24 h after quenching. It took about 15 min for the furnace to reach the heating temperature in the SA process. As for the DA process, it took about 12 min for the furnace to reach 110 °C from room temperature and 13 min to reach 180 °C from 110 °C. To detect the forming precisions of the part before and after standard aging, the measurements of three-dimensional geometric data were carried out by a blue light scanner.

In order to test the mechanical properties of the formed parts, tension test samples were cut from the formed parts (No. 3–6). The locations and the dimensions of the tension test samples are shown in **Figures 3**, **4**, respectively. It should be noted that because the shape and dimensions of some tension test samples were not suitable for tensile testing, strengths at some locations were not tested. Besides, elongation values at some locations were missing because the fracture locations of these tension samples were out of the gauge range. The drawing speed in tensile tests was 2 mm/min.

RESULTS AND DISCUSSION

Effect of Blank Holder Force on the Part's Formability

The formed parts (No. 1–3) are shown in **Figure 5**. As can be seen, the formed part with full BHF cracked at both sidewalls of the big end (zones in the red circle in **Figure 5A**) while the formed part with half BHF only cracked at one sidewall of the big end (zone in the red circle in **Figure 5B**). Besides, the size of the crack in part with half BHF was smaller than that of the part with full BHF. No cracks were observed in the formed part without BHF. The results indicated that BHF in hot stamping of 7075 aluminum alloys may cause the crack and some researchers also noticed this phenomenon (Zhou et al., 2014).

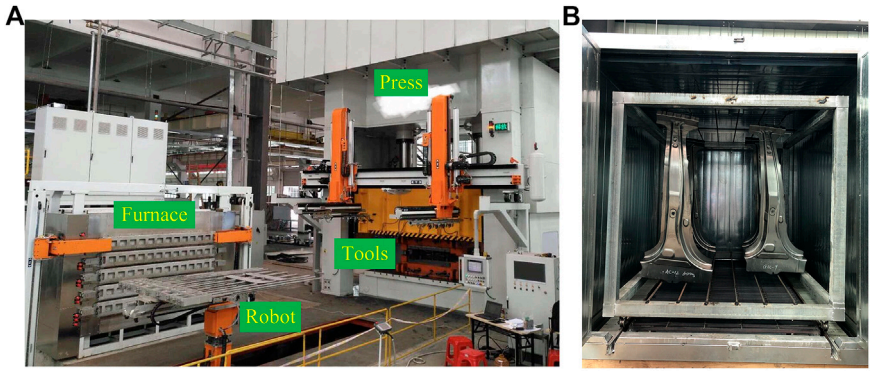

FIGURE 1 | (A) The hot stamping production line and **(B)** the aging furnace.

TABLE 1 | The designed experiment conditions.

Part Number	SHT time	BHF	Aging process
1	15	Full	SA
2	15	Half	SA
3	15	None	SA
4	20	None	SA
5	15	None	DA
6	10	None	DA

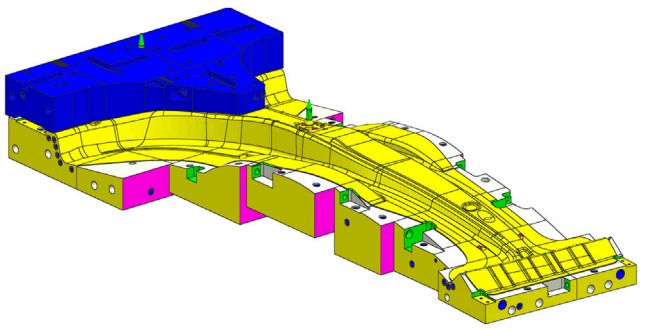

FIGURE 2 | The position of the blank holder.

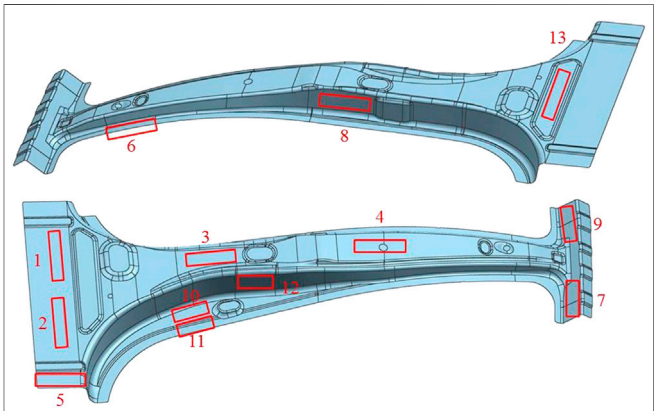

FIGURE 3 | The locations of the tension test samples in the formed parts.

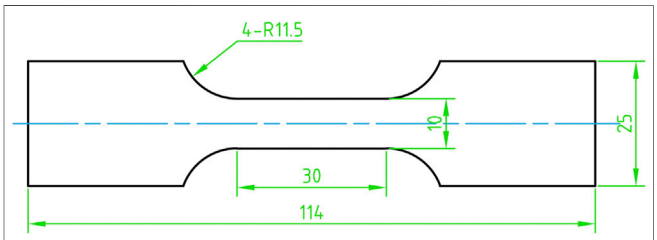

FIGURE 4 | Principle shape and dimensions of the tensile test specimen (unit: mm).

The cracking mechanism of the formed parts is similar to the cracking mechanism in previous experiments (Liu et al., 2018) and the large friction force caused by BHF in this work replaced the dry friction force in the previous study (Liu et al., 2018). It is well known that the flow stress of 7075 aluminum alloy decreases with the increasing temperature (Ghiotti et al., 2019). As a result, the deformation resistance and the ability to resist tensile stress of 7075 decreased with the increasing temperature. In hot stamping, the hot blank first contacted with the rounded corners of the tools, resulting in the temperature of these regions dropping early and deformation resistance increasing. However, the temperature of the sidewall was relatively higher because of the tool clearance, leading to lower flow stress and weaker ability to resist tensile stress. In the subsequent hot drawing stage, with full BHF, the material in the flange of the big end was held by large friction force caused by BHF and the material was difficult to draw to the sidewall. As a result, the soft material in the sidewall was eventually stretched to cracking. With lower BHF, the material in the flange was easy to flow to the sidewall with the assistance of lubricants, and thus the size of the crack reduced or even there were no cracks in the formed parts. Nevertheless, during hot stamping, a blank holder should have been designed to avoid wrinkling. Accordingly, a balance must be achieved to avoid

FIGURE 5 | Formed parts: **(A)** Part No. 1, with full BHF; **(B)** Part No. 2, with half BHF; **(C)** Part No. 3, no BHF.

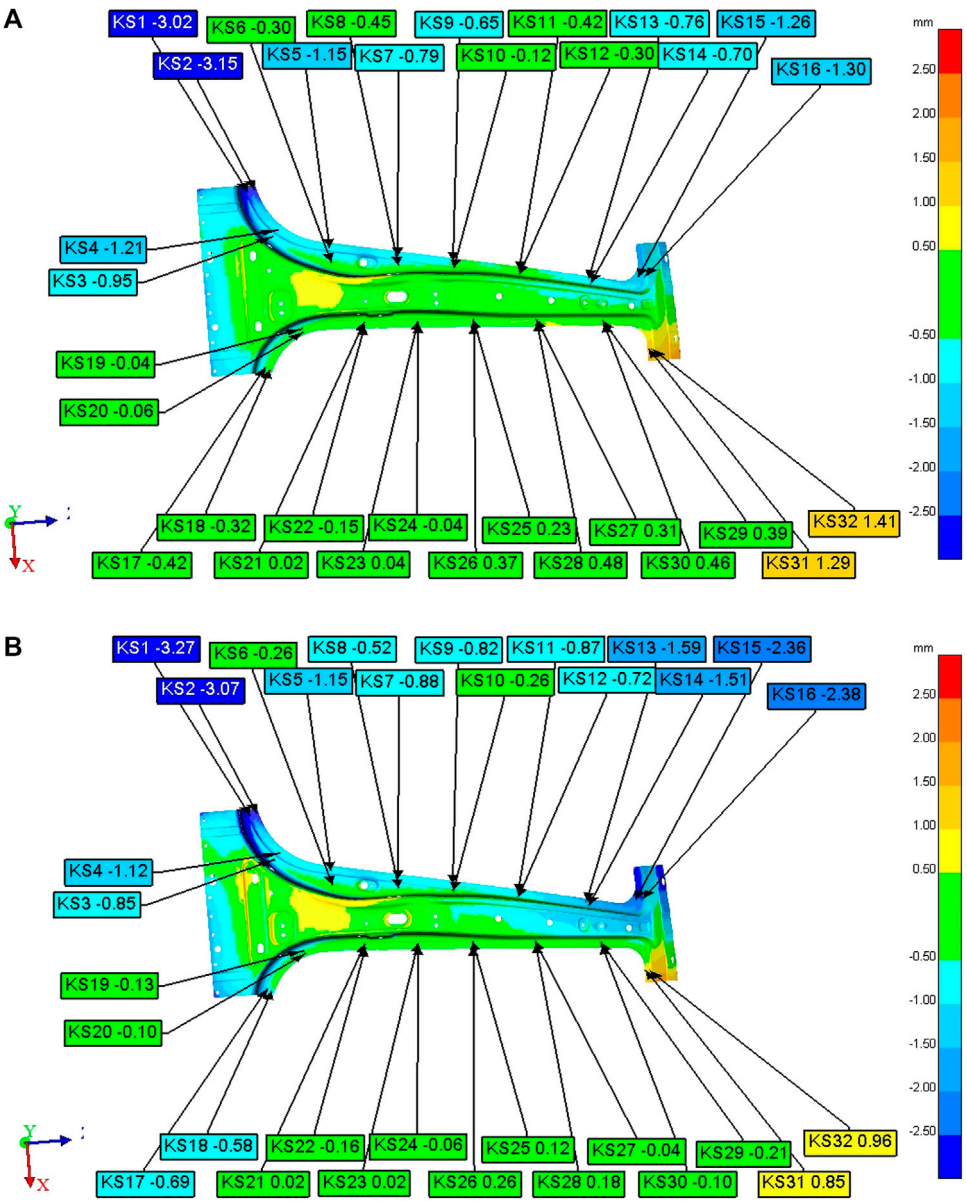

FIGURE 6 | The forming precisions of the part **(A)** before and **(B)** after standard aging.

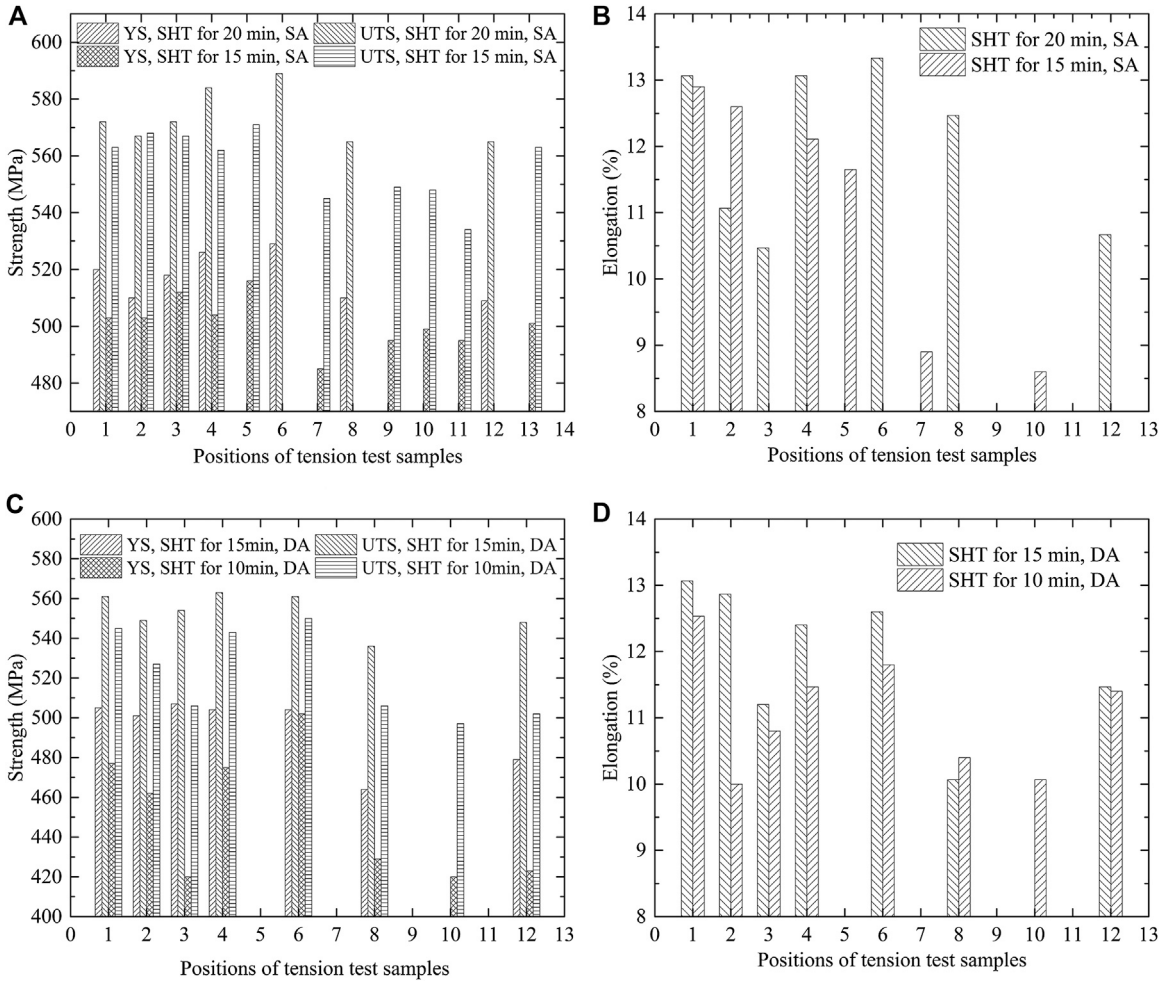

FIGURE 7 | Strength and elongation of samples under different process parameters.

wrinkling and cracking. In respect to the stamping experiments, lower BHF could be conducive to realize the balance between these two conflict factors.

In addition, it is promising to avoid wrinkling and cracking under the conditions of blank holding by reducing the forming temperature. In order to ensure the cooling rate of aluminum alloy sheet during quenching, some cooling methods could be used to make the blank temperature drop quickly to the forming temperature before the part is formed in the tools, which can be called hot stamping with pre-cooling (Zhu et al., 2019). Under this circumstance, the flow stress of the sheet is higher due to the lower temperature, and thus, larger BHF can be used to avoid wrinkling. Furthermore, it might also be useful to avoid wrinkling and cracking if the region of the part that is easily wrinkled can be formed before other regions. These two methods need to be studied in future work.

Forming Precisions of the Part Before and After Standard Aging

The measured three-dimensional geometric data of the B-pillar reinforced panel were compared with the original CAD model as shown in **Figure 3**. The forming precisions of the part before and after standard aging are shown in **Figure 6**. The great majority of measured points on the part are within ±1 mm of nominal. There is a maximum error of about 3 mm in the local regions of both ends of the part. It is clear that there are some yellow regions near the big end, indicating that the forming precisions in these regions are insufficient. In fact, this is due to the absence of BHF, which leads to wrinkling. Due to the effect of thermal deformation and residual stress releasing, the forming precisions decrease after aging. However, the reduction of forming precisions is not significant. Although these geometric data respectively represent a small sample size for the formed part, the magnitude of the deviations is acceptable.

Effect of SHT Time on the Mechanical Properties and Short-Time Aging

The strength and elongation of samples under different process parameters are shown in **Figure 7**, and the corresponding statistical results are shown in **Table 2**. The strength and

TABLE 2 | The statistical results of strength and elongation of samples under different process parameters.

Aging process	SHT time (min)	Category	Mean values	Standard deviation	Minimum values	Maximum values	Minimum/As-received
SA	20	YS (MPa)	517.4	8.1	509	529	95.7%
		UTS (MPa)	573.4	8.1	565	589	96.6%
		Elongation	12.0	1.2	10.5	13.3	—
	15	YS (MPa)	501.3	8.8	485	516	91.1%
		UTS (MPa)	557	12.2	534	571	91.3%
		Elongation	11.1%	1.9	8.6%	12.9%	—
DA	15	YS (MPa)	494.9	16.6	464	507	87.2%
		UTS (MPa)	553.1	9.7	536	563	91.6%
		Elongation	12.0	1.1	10.1	13.1	—
	10	YS (MPa)	451	32.0	420	502	78.9%
		UTS (MPa)	522	21.8	497	550	85.0%
		Elongation	11.1	0.9	10	12.5	—

elongation of samples with a standard aging process under different SHT times are illustrated in **Figures 7A,B**. As can be seen, formed parts with higher SHT times had larger values of YS and UTS. The elongations of samples subjected to SHT for 20 and 15 min were in a range of 10.5–13.3% and 8.6–12.9%, respectively. The values of YS, UTS and elongation were different at different locations in the formed parts because of the testing errors and different cooling rates during quenching due to the contact conditions differences between the blanks and tools. The minimum strength of the part subjected to SHT for 20 min was about 96% of that of the as-received T6 condition and the maximum strength was slightly greater than the as-received T6 condition. The variations of strength mainly resulted from the fact that the SHT temperature, cooling rate and aging process may be different from the process parameters used in this work.

Figures 7C,D show the strength and elongation of samples treated by the duplex aging process with different SHT times. Similarly, formed parts subjected to SHT for 15 min had larger values of YS and UTS than that of parts subjected to SHT for 10 min. The elongations of samples subjected to SHT for 15 and 10 min under the duplex aging process were in a range of 10.1–13.1% and 10–12.5%, respectively. The minimum YS of formed parts subjected to SHT for 15 min was only 87.2% of that of the as-received T6 condition and the minimum UTS was 91.6% of that of the as-received T6 condition. In comparison, both of the minimum YS and UTS of formed parts subjected to SHT for 10 min were lower than 90% of the YS and UTS of the as-received T6 condition.

It has been indicated that the solution is a process which was mainly controlled by diffusion and the diffusion of the alloying elements inside the solvent matrix consumes most of the whole time in SHT (Mohamed et al., 2008). As a result, more alloying elements or precipitates will dissolve into the matrix when the SHT time is longer under the same SHT temperature. Subsequently, more fine precipitates form after quenching and aging. Therefore, the strength is improved when the SHT time is longer.

Aging is a process that includes nucleation and growth of the precipitates, and the growth of the precipitates is solely controlled by diffusion in the matrix (Du et al., 2016). Besides, there exists one or more transition precipitating phases during the aging process of aluminum alloys. As a consequence, dissolution of precipitated phases also takes place during aging. Diffusion coefficient increases with the increasing temperature, resulting in the reduction of diffusion time at elevated temperatures. Therefore, a relatively higher aging temperature can reduce the aging time. However, on the other hand, the required precipitation phases or nucleation cores dissolve if the aging temperature is too high, even the coarse precipitates form and the strength decreases. As a result, the aging temperature should be chosen appropriately. In order to reduce the whole aging time, the multistage aging process may be a good choice. The specific principle is that a relatively high density of GP region forms at a lower temperature to provide a nucleation core for the formation of subsequent transition phases. The transition phase with a suitable shape and strengthening effect can be obtained by using a higher temperature and a shorter time in the subsequent aging process. This method not only makes use of the short-time aging at high temperature, but also avoids the massive dissolution of the nucleation cores.

The short-time aging experiment shows that the obtained strength of the full-scale part can be more than 90% of that of the as-received T6 condition under the duplex aging process of 110 °C × 1 h + 180 °C × 0.5 h. Compared to the standard aging process, the new short-time aging process can reduce more than 93% of the time if 90% of the T6 strength can be accepted. Besides, increasing the SHT temperature can also increase the part's strength after aging (Li et al., 2015). Therefore, the strength of formed part has a promising outlook to be improved further by increasing the SHT temperature.

CONCLUSION

(1) Large BHF in hot stamping of 7075 aluminum alloys caused the crack. The material in the flange was hard to flow to the sidewall due to large friction force caused by BHF, and the material in the sidewall was easily stretched under a relatively higher temperature because of non-uniform cooling, thus the parts cracked. Parts with no cracks can be obtained without BHF, but there are wrinkling on the parts. Methods to avoid wrinkling and cracking should be studied in future works.
(2) The great majority of measured points on the part were within ±1 mm of nominal, and there is a maximum error of about 3 mm in the local regions of both ends of the part. The forming precisions decrease after aging due to thermal deformation and release of the residual stress. However, the reduction of the forming precisions is small.

(3) The strength of the part can be improved by increasing the SHT time properly, since more alloying elements or precipitates will dissolve into the matrix when the SHT time is longer.
(4) Under the duplex aging process of 110 °C × 1 h + 180 °C × 0.5 h, the obtained strength of the full-scale part can be more than 90% of that of the as-received T6 condition. Compared to the standard aging process, the new short-time aging process can reduce more than 93% of the time if 90% of the T6 strength can be accepted.

DATA AVAILABILITY STATEMENT

The raw data supporting the conclusions of this article will be made available by the authors, without undue reservation.

AUTHOR CONTRIBUTIONS

The corresponding author is responsible for ensuring that the descriptions are accurate. YL: writing original draft, implementation of the experiments and data processing. JL: implementation of hot stamping and tensile testing. LW: supply of production line. KW: modifying and editing. BZ: suggestion and resource. YZ: supply of 7075 aluminum alloys and resource.

FUNDING

This research work was financially supported by the National Major Science and Technology Project of China (Grant No. 2018zx04023001).

REFERENCES

Du, Q., Holmedal, B., Friis, J., and Marioara, C. D. (2016). Precipitation of non-spherical particles in aluminum alloys Part II: numerical simulation and experimental characterization during aging treatment of an Al-Mg-Si alloy. *Metall. Mater. Trans. A*. 47A, 589–599. doi:10.1007/s11661-015-3196-6

Garrett, R. P., Lin, J., and Dean, T. A. (2005). Solution heat treatment and cold die quenching in forming AA6xxx sheet components: feasibility study. *Adv. Mater. Res*. 6, 673–680. doi:10.4028/www.scientific.net/AMR

Ghiotti, A., Simonetto, E., and Bruschi, S. (2019). Influence of process parameters on friction behaviour of AA7075 in hot stamping. *Wear*. 426-427, 348–356. doi:10.1016/j.wear.2018.11.031

Harrison, N. R., and Luckey, S. G. (2014). Hot stamping of a B-pillar outer from high strength aluminum sheet AA7075. *SAE Int. J. Mater. Manuf.* 7, 567–573. doi:10.4271/2014-01-0981

Jürgen, H. (2014). Recent development in aluminium for automotive applications. *Trans. Nonferrous Metals Soc. China*. 24, 1995–2002. doi:10.1016/S1003-6326(14)63305-7

Li, N., Zheng, J., Zhang, C., Zheng, K., Lin, J., and Dean, T. A. (2015). Investigation on fast and energy-efficient heat treatments of AA6082 in HFQ processes for automotive applications. *MATEC Web Conf*. 21, 05015. doi:10.1051/matecconf/20152105015

Liu, Y., Zhu, B., Wang, Y., Li, S., and Zhang, Y. (2020). Fast solution heat treatment of high strength aluminum alloy sheets in radiant heating furnace during hot stamping. *Int. J. Lightweight Mater. Manuf.* 3, 20–25. doi:10.1016/j.ijlmm.2019.11.004

Liu, Y., Zhu, Z., Wang, Z., Zhu, B., Wang, Y., and Zhang, Y. (2018). Flow and friction behaviors of 6061 aluminum alloy at elevated temperatures and hot stamping of a B-pillar. *Int. J. Adv. Manuf. Technol.* 96, 4063–4083. doi:10.1007/s00170-018-1790-7

Maeno, T., Mori, K., and Yachi, R. (2017). Hot stamping of high-strength aluminium alloy aircraft parts using quick heating. *CIRP Ann.—Manuf. Technol.* 66, 269–272. doi:10.1016/j.cirp.2017.04.117

Mohamed, M., Alistair, F., and Lin, J. (2008). "Solution heat treatment in HFQ process," in 12th International Conference on Metal Forming. (Dusseldorf, Germany: Verlag Stahleisen GmbH), 160–167.

Mohamed, S. M., Alistair, D. F., Lin, J., Daniel, S. B., and Trevor, A. D. (2012). Investigation of deformation and failure features in hot stamping of AA6082: experimentation and modelling. *Int. J. Adv. Manuf. Technol.* 53, 27–38. doi:10.1016/j.ijmachtools.2011.07.005

Omer, K., Abolhasani, A., Kim, S., Nikdejad, T., Butcher, C., Wells, M., et al. (2018). Process parameters for hot stamping of AA7075 and D-7xxx to achieve high performance aged products. *J. Mater. Process. Technol.* 257, 170–179. doi:10.1016/j.jmatprotec.2018.02.039

Sun, W., Zhu, Y., Marceau, R., Wang, L., Zhang, Q., Gao, X., et al. (2019). Precipitation strengthening of aluminum alloys by room-temperature cyclic plasticity. *Sci.* 363, 972–975. doi:10.1126/science.aav7086

Xu, X., Zhao, Y., Wang, X., Zhang, Y., and Ning, Y. (2015). The rapid age strengthening induced by Ag additions in 7075 aluminum alloy. *Mater. Sci. Eng. A*. 648, 367–370. doi:10.1016/j.msea.2015.09.044

Zhang, Z., Yu, J., and He, D. (2020). Effects of contact body temperature and holding time on the microstructure and mechanical properties of 7075 aluminum alloy in contact solid solution treatment. *J. Alloys Compd*. 823, 153919. doi:10.1016/j.jallcom.2020.153919

Zheng, J., Dong, Y., Zheng, K., Dong, H., Lin, J., Jiang, J., et al. (2019). Experimental investigation of novel fast-ageing treatments for AA6082 in supersaturated solid solution state. *J. Alloys Compd*. 810, 151934. doi:10.1016/j.jallcom.2019.151934

Zhou, J., Wang, B., Lin, J., Fu, L., and Ma, W. (2014). Forming defects in aluminum alloy hot stamping of side-door impact beam. *Trans. Nonferrous Metals Soc. China*. 24, 3611–3620. doi:10.1016/S1003-6326(14)63506-8

Zhu, L., Liu, Z., and Zhang, Z. (2019). Investigation on strengthening of 7075 aluminum alloy sheet in a new hot stamping process with pre-cooling. *Int. J. Adv. Manuf. Technol.* 103, 4739–4746. doi:10.1007/s00170-019-03890-0

Conflict of Interest: The authors declare that the research was conducted in the absence of any commercial or financial relationships that could be construed as a potential conflict of interest.

frontiers in Materials

ORIGINAL RESEARCH
published: 13 January 2021
doi: 10.3389/fmats.2020.623864

Preparation of 304 Stainless Steel Powder for 3D Printing by Vacuum-Induced Multistage Atomization

Xueyu Jiang, Xin Che, Chen Tian, Xiaofei Zhu, Ge Zhou, Lijia Chen and Jianlin Li*

School of Materials Science and Engineering, Shenyang University of Technology, Shenyang, China

A vacuum-induced multistage atomization process was adopted to fabricate the high-performance 304 stainless steel powder for 3D printing, based on the flexible control of the droplet spheroidization and solidification process. The 36.7 μm-median diameter (D_{50}) 304 stainless steel powder with high sphericity was successfully obtained, together with particle size proportion of 45–55 μm larger than 35% and the lower oxygen and nitrogen content increment below 0.04%.

Keywords: metals and alloys, powder technology, multi-stage atomization, particle size distribution, sphericity

OPEN ACCESS

Edited by:
Minghui Cai,
Northeastern University, China

Reviewed by:
Ye Tian,
Beijing Institute of Aeronautical Materials (BIAM), China
Zhiqiang Wu,
Hunan University of Science and Technology, China

****Correspondence:***
Xin Che
xiaoxin2004068@163.com

Specialty section:
This article was submitted to Structural Materials, a section of the journal Frontiers in Materials

Received: *30 October 2020*
Accepted: *30 November 2020*
Published: *13 January 2021*

Citation:
Jiang X, Che X, Tian C, Zhu X, Zhou G, Chen L and Li J (2021) Preparation of 304 Stainless Steel Powder for 3D Printing by Vacuum-Induced Multistage Atomization. Front. Mater. 7:623864. doi: 10.3389/fmats.2020.623864

INTRODUCTION

The 3D printing technique is an advanced forming process based on layer-by-layer "bottom-up" material stacking in the three-dimensional space. Compared with casting, forging, and other traditional processes, 3D printing suits for the near-net-shape forming of complex parts because it can significantly shorten the production period and save raw materials. Hence, 3D printing is regarded as a breakthrough technique in the new round of technological revolution and has been widely concerned worldwide (Jones, 2012; Preston et al., 2013).

Yang et al. prepared high-performance 316L stainless steel (σ_b = 755 MPa, δ = 18%) for vane wheels of high-precision planet gears using selective laser melting (SLM) (Yang et al., 2019). Khademzadeh, Tolosa, and Choi et al. found that metal powder particle size significantly affected the surface completeness and mechanical properties of 3D printing parts (Tolosa et al., 2010; Choi et al., 2012; Khademzadeh et al., 2015). Meier et al. reported that powder sphericity had an effect on the loose density, packed density, and fluidity of 3D printing parts (Meier et al., 2019). Park stated that the element purity (O, N) of 15-5ph stainless steel powder influenced the performance of 3D printing parts (Zhang et al., 2018). In terms processes (Lewandowski and Seifi, 2016; Bartolomeu et al., 2017; Ma et al., 2017; Suryawanshi et al., 2017; Fortunato et al., 2018; Kong et al., 2018), researchers believe that metal powder quality is one of the key factors influencing the forming process and the final performance of 3D printing [direct metal laser sintering (DMLS), SLM, laser-engineered net shaping (LENS), and electron beam melting (EBM)). Thus, preparation techniques of high-performance metal powder for 3D printing are of crucial importance.

In this study, contactless vacuum induction and multistage atomization flexible control were combined to improve the powder purity, particle size, and sphericity, which cannot be well tailored by the existing powder preparation processes, such as high-temperature plasma process and rotating electrode process. Finally, high-performance 304 stainless steel powder for 3D printing was successfully prepared.

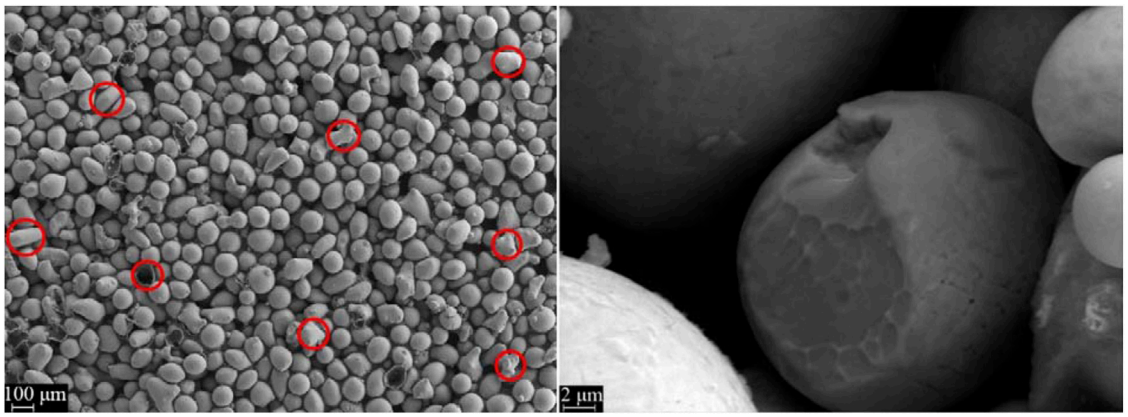

FIGURE 1 | Morphology of powder prepared from 304 stainless steel single-stage atomization process (atomization pressure: 8 MPa).

EXPERIMENTAL

The 304 stainless steel (AISI304) was selected as raw material, and a contactless induction heating and multistage atomization pressure flexible control process was used for powder preparation. During the preparation by EIGA, the quantity of 304 stainless steel powder from a single lot is 10 Kg. The process route involves as follows: 1) heating power W: 28 kW, 2) bar material feeding speed v: 0.04–0.06 mm/s, angular spin rate ω: 6 r/min; and 3) atomization stage pressure: 4.5–6–8 MPa, at an interval time of 7 s.

An 80-mesh screen was used for the 304 stainless steel powder. The morphology of powder was observed using a Gemini SEM 300 field-emission scanning electron microscope (SEM). Particle size and distribution were determined using a BETTERSIZE 2000 laser particle analyzer. The physical properties of powder were assessed through a BT1001 universal property analyzer. Elemental composition was analyzed by a chemical analytical method (ICP).

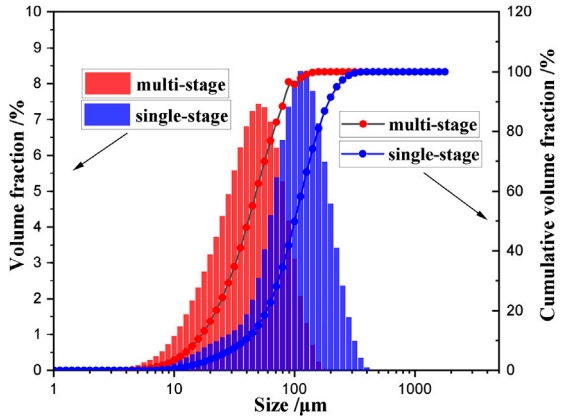

FIGURE 2 | Particle size curves of 304 stainless steel powder.

RESULTS AND DISCUSSION

The scientific essence for preparation of metal powder for 3D printing is a continuous process of droplet spheroidization and solidified coupling of metal materials. **Figure 1** shows the SEM images of 304 stainless steel powder prepared from a vacuum induction single-stage atomization process (8 MPa). It can be found that the large atomization pressure endowed the metal drops with large flying linear velocity, so the droplets were prone to ruleless collision and intensified breakage during atomization. Moreover, the surface of metal drops experienced very fast overcooling and solidification, leading to the ruleless and fast droplet solidification. Hence, the powder particles in this process were evenly distributed, and the median diameter D_{50} was determined as approximately 41.7 μm (**Figure 2**), but ellipsoidal or irregular powder was easily observed, so the entire powder sphericity was relatively low (**Figure 1A**).

To address the above problem, we fully considered the spheroidization control of metal droplets to ensure the appropriate overcooling of metal droplets during solidification, and designed a multistage atomization flexible process (atomization pressure: 4.5–6–8 MPa, time interval: 7 s), based on the nozzle structure and the physical properties of 304 stainless steel (density and droplet fluidity). **Figure 3** shows the SEM images of the powder, and the corresponding particle size was displayed in **Figure 2**.

At the initial stage of the multistage atomization process, as the pressure was approximately 4.5–6 MPa, the initial movement velocity of metal droplets and the gas flow of ring-like nozzle were flexibly controlled, and the motion path of metal droplets in the airflow field was distributed in order, which decreased the probability of ruleless collision of metal droplets. As the atomization pressure rose to 8 MPa, the droplets were rapidly solidified, and printed the nucleation and growth, causing the formation of smaller-size powder particles (**Figure 3**).

In addition, the distribution profile of peak particle diameter was left-shifted, indicating the present multistage atomization can increase the proportion of fine powder, and the final median diameter D_{50} was decreased to 36.7 μm (**Figure 2**). The overall sphericity of the powder was fine, and part of the powder slightly grew up (**Figure 3A**). Furthermore, these power particles were characterized by high surface quality, without fracture, convex, adhesion, or other defects (**Figure 3B**).

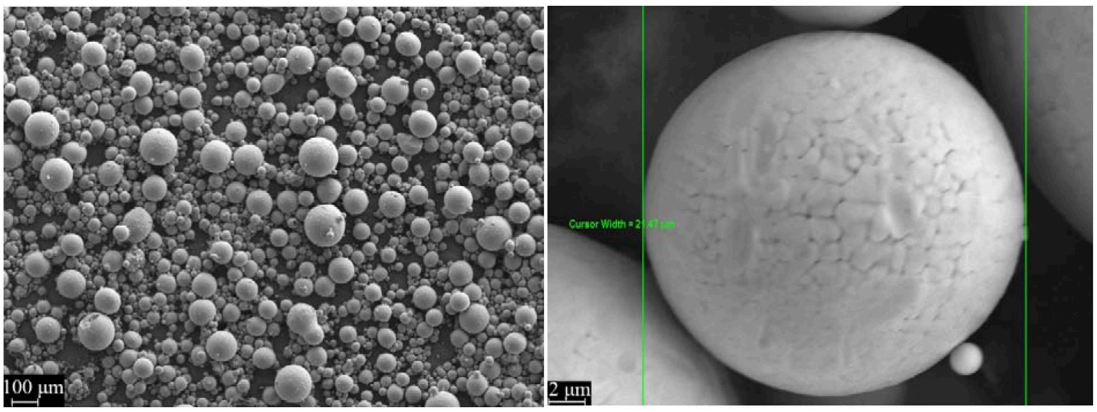

FIGURE 3 | Morphology of 304 stainless steel powder prepared from multistage atomization (atomization pressure: 4.5–6–8 MPa, interval 7 s).

TABLE 1 | Chemical composition and physical properties of 304 stainless steel powder prepared from different atomization processes.

Process procedure	Alloy element (wt%)								
	Ni	Cr	Si	Mn	C	O	N	S	Fe
AISI304	9.0–12	18.0–20.0	≤1.0	≤1.5	≤0.03	≤0.03	≤0.03	≤0.03	Balance
Single-stage atomization	10.72	18.80	0.72	0.85	0.021	0.023	0.0028	0.005	Balance
Multistage atomization	11.02	18.29	0.76	0.65	0.018	0.022	0.0031	0.006	Balance

Process procedure	Power property			
	Angle of repose/(°)	Angle of collapse/(°)	Loose density/(g·cm^{-3})	Tap density/(g·cm^{-3})
Single-stage atomization	31.85	28.77	5.04	5.68
Multistage atomization	32.02	27.15	4.46	5.49

Table 1 lists the compositional analysis and physical properties of the present 304 stainless steel powder. The contactless vacuum induction multistage atomization process can effectively decrease the increment of O and N concentrations and can significantly improve the elemental purity during powder preparation. Moreover, the overall physical properties of the powder changed slightly and can meet the requirement for exclusive use in 3D printing.

Thus, high-performance 304 stainless steel powder exclusive for 3D printing was successfully prepared, and the particle size proportion of 45–55 μm can reach approximately 40%. Through the multistage atomization process, the O and N elemental composition and overall physical properties—sphericity and particle size of 3D printing power—were flexibly controlled. Importantly, this process can also be used for preparation of other brands of stainless steels, such as 316L, or other metal material powder with similar density.

CONCLUSION

The high-performance 304 stainless steel metal powder exclusive for 3D printing was prepared by a vacuum induction multistage atomization process, which can improve the powder composition, overall physical properties, sphericity, and particle size by means of flexible control of multistage atomization pressure.

DATA AVAILABILITY STATEMENT

The original contributions presented in the study are included in the manuscript/Supplementary Material, and further inquiries can be directed to the corresponding author.

AUTHOR CONTRIBUTIONS

XJ, LC, and GZ conceived of and designed the experiments; CT and XJ carried out the experiments; LC, JL, and XZ analyzed the data; XJ and XC wrote the manuscript.

FUNDING

This study was funded by the Liaoning Provincial Department of Finance (No. LQGD2017024), the National Natural Science Foundation (No. 51805335), and Liaoning Provincial Natural Science Foundation projects (No. 20180550998).

ACKNOWLEDGMENTS

Thanks to the members of the research team.

REFERENCES

Bartolomeu, F., Buciumeanu, M., Pinto, E., Alves, N., Carvalho, O., Silva, F. S., et al. (2017). 316L stainless steel mechanical and tribological behavior-A comparison between selective laser melting, hot pressing and conventional casting. *Addit. Manuf.* 16, 81–89. doi:10.1016/j.addma.2017.05.007

Choi, S., Sohn, I., and Lee, H. (2012). Femtosecond laser-induced line structuring on mold stainless steel STAVAX with various scanning speeds and two polarization configurations. *Int. J. Precis. Eng. Manuf.* 13, 845–854. doi:10.1007/s12541-012-0110-7

Fortunato, A., Lulaj, A., Melkote, S., Liverani, E., Ascari, A., and Umbrello, D. (2018). Milling of maraging steel components produced by selective laser melting. *Int. J. Adv. Manuf. Technol.* 94, 1895–1902. doi:10.1007/s00170-017-0922-9

Jones, N. (2012). Science in three dimensions: the print revolution. *Nature*. 487, 22–23. doi:10.1038/487022a

Khademzadeh, S., Parvin, N., and Bariani, P. F. (2015). Production of NiTi alloy by direct metal deposition of mechanically alloyed powder mixtures. *Int. J. Precis. Eng. Manuf.* 16, 2333–2338. doi:10.1007/s12541-015-0300-1

Kong, D., Ni, X., Dong, C., Lei, X., Zhang, L., Man, C., et al. (2018). Bio-functional and anti-corrosive 3D printing 316L stainless steel fabricated by selective laser melting. *Mater. Des.* 152, 88–101. doi:10.1016/j.matdes.2018.04.058

Lewandowski, J. J., and Seifi, M. (2016). Metal additive manufacturing: a review of mechanical properties. *Annu. Rev. Mater. Res.* 46, 151–186. doi:10.1146/annurev-matsci-070115-032024

Ma, M., Wang, Z., and Zeng, X. (2017). A comparison on metallurgical behaviors of 316L stainless steel by selective laser melting and laser cladding deposition. *Mater. Sci. Eng.* 685, 265–273. doi:10.1016/j.msea.2016.12.112

Meier, C., Weissbach, R., Weinberg, J., Wall, W. A., and Hart, A. J. (2019). Modeling and characterization of cohesion in fine metal powders with a focus on additive manufacturing process simulations. *Powder Technol.* 343, 855–866. doi:10.1016/j.powtec.2018.11.072

Preston, Z., Nickels, L., and Capus, J. (2013). 3D printing of plastic and titanium parts for racing bicycles. *Met. Powder Rep.* 68, 30–32. doi:10.1016/S0026-0657(13)70172-3

Suryawanshi, J., Prashanth, K. G., and Ramamurty, U. (2017). Mechanical behavior of selective laser melted 316L stainless steel. *Mater. Sci. Eng.* 696, 113–121. doi:10.1016/j.msea.2017.04.058

Tolosa, I., Garciandia, F., Zubiri, F., Zapirain, F., and Esnaola, A. (2010). Study of mechanical properties of AISI 316 stainless steel processed by "selective laser melting", following different manufacturing strategies. *Int. J. Adv. Manuf. Technol.* 51, 639–647. doi:10.1007/s00170-010-2631-5

Yang, X., Liu, Y., Ye, J., Wang, R., Zhou, T-C., and Mao, B-Y. (2019). Enhanced mechanical properties and formability of 316L stainless steel materials 3D-printed using selective laser melting. *Intl. J. Min Met Mater.* 26, 1396–1404. doi:10.1007/s12613-019-1837-2

Zhang, J., Hu, B., Zhang, Y., Guoe, X., Wu, L., Park, H. Y., et al. (2018). Comparison of virgin and reused 15-5 PH stainless steel powders for laser powder bed fusion process. *Prog. Addit. Manuf.* 3, 11–14. doi:10.1007/s40964-018-0038-2

Conflict of Interest: The authors declare that the research was conducted in the absence of any commercial or financial relationships that could be construed as a potential conflict of interest.

frontiers in Materials

ORIGINAL RESEARCH
published: 14 January 2021
doi: 10.3389/fmats.2020.606092

Dislocation-Controlled Low-Temperature Superplastic Deformation of Ti-6Al-4V Alloy

Chao Liu[1], Xin Wang[1], Ge Zhou[1], Feng Li[1], Siqian Zhang[1], Haoyu Zhang[1], Lijia Chen[1] and Haijian Liu[2]*

[1]School of Materials Science and Engineering, Shenyang University of Technology, Shenyang, China, [2]Shanghai Spaceflight Precision Machinery Institute, Shanghai, China

The superplastic tension and deformation mechanism of Ti-6Al-4V alloy at 923 K and a tensile speed of 10^{-3}, 5×10^{-3}, or 5×10^{-2} s^{-1} was studied on an AG 250KNE electronic tension tester. Through theoretical modeling, the unit dislocation count of this alloy during superplastic deformation was introduced into the Ruano–Wadsworth–Sherby (R-W-S) deformation mechanism map, and a new deformation mechanism map involving dislocation count was plotted. Thereby, the mechanism underling the low-temperature superplastic deformation of this alloy was predicted. It was found the superplastic tension of Ti-6Al-4V at the tested temperature was controlled by dislocation movement, and with an increase in strain rate, the deformation transited from the dislocation-controlled mechanism with a stress index of 4 to the dislocation glide mechanism with a stress index of 5 or 7. At the strain rate of 10^{-3} s^{-1}, this alloy reached the largest tension rate of 790% and strain rate sensitivity index of 0.52 and had excellent low-temperature superplastic properties.

Keywords: Ti-6Al-4V alloy, low-temperature superplasticity, strain rate sensitivity index m, deformation mechanism map, dislocation

OPEN ACCESS

Edited by:
Minghui Cai,
Northeastern University, China

Reviewed by:
Yanbin Jiang,
Central South University, China
Qi Chao,
Deakin University, Australia

****Correspondence:***
Ge Zhou
zhouge@sut.edu.cn

Specialty section:
This article was submitted to Structural Materials, a section of the journal Frontiers in Materials

Received: *14 September 2020*
Accepted: *10 November 2020*
Published: *14 January 2021*

Citation:
Liu C, Wang X, Zhou G, Li F, Zhang S, Zhang H, Chen L and Liu H (2021) Dislocation-Controlled Low-Temperature Superplastic Deformation of Ti-6Al-4V Alloy. Front. Mater. 7:606092. doi: 10.3389/fmats.2020.606092

INTRODUCTION

Ti-6Al-4V alloy, as a typical α+β two-phase titanium alloy, possesses favorable comprehensive properties and thus is widely applied into forming manufacture of complex components in air navigation weapons, equipment, and ships (Vanderhasten et al., 2007; Li et al., 2014; Meng et al., 2016). In recent years, as the overall design performance indices of weapons and equipment are increasingly enhanced, the multilayer structured complex-shape parts are often manufactured via superplastic forming/bonding by diffusion and through one-time near-net-shape forming, based on the designing concept of reinforced rib sandwich structures. To improve the forming precision of complex structured parts, prolong the service life of dies, and lower energy consumption, researchers are interested in how to lower the superplastic forming temperature and control the structural stability of this alloy during superplastic forming while ensuring the feasibility of the superplastic forming process, which becomes hot spots in this field. Thus, the behaviors and mechanism of low-temperature superplastic deformation of Ti-6Al-4V have been studied worldwide.

As for the low-temperature superplasticity of Ti-6Al-4V (Shahmir et al., 2018; Zhang et al., 2018; Zhang et al., 2018; Zhou et al., 2018), Langdon et al. produced nanocrystal grains using high-pressure torsion and obtained a maximum tension rate of 815% at 1073 K. Ding et al. ultrafined cold-rolled Ti-6Al-4V sheets and acquired the maximum tension rate of 820% at 923 K. Cai et al. grain-refined

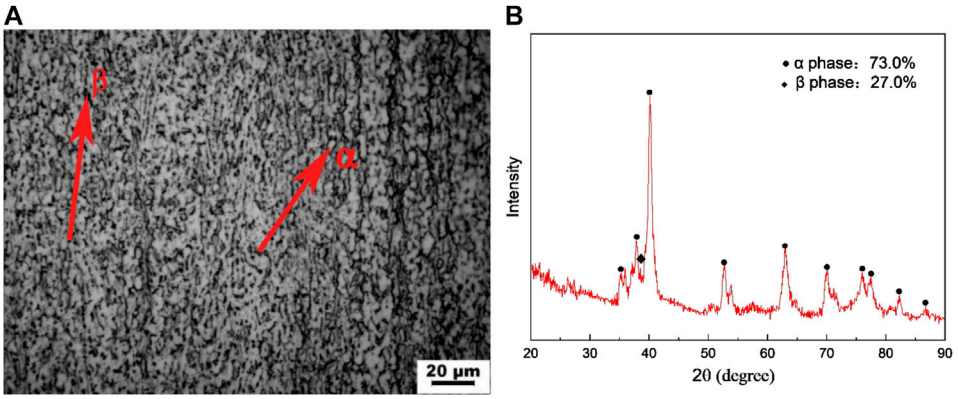

FIGURE 1 | Original structure of Ti-6Al-4V **(A)** OM (500) and **(B)** XRD.

this alloy through stirred friction and maximized the tension rate to 1,130% at 873 K. The above results indicate that the main method of improving low-temperature superplasticity of Ti-6Al-4 V alloy is grain refinement, in which the coordination of grain boundary slip during superplastic deformation is fully utilized. With deformation mechanism maps involving dislocation count, Zhou Ge et al. predicted the superplastic deformation mechanism of Ti-6Al-4 V at 973–1123 K and found the superplastic deformation mechanism transited from grain boundary sliding to dislocation glide (a stress index of 7) and grain boundary slip (a stress index of 4) with a decrease in temperature and observed that the superplastic deformation was modulated by dislocation. Thus, when the superplastic deformation temperature of Ti-6Al-4 V continually dropped while ensuring its elongation above 600%, both the grain boundary slip mechanism and the effects of dislocation on superplasticity should be considered. However, little has been studied about the superplastic deformation behaviors of Ti-6Al-4 V below 973 K, and no study has been conducted about the superplastic deformation of this alloy under the dislocation-controlled mechanism.

In this study, the superplastic tensile behaviors and deformation mechanism of Ti-6Al-4 V alloy at 923 K and different strain rates were studied. The Ruano–Wadsworth–Sherby (R-W-S) deformation mechanism maps involving dislocation count were used to predict the deformation mechanisms under different testing conditions. Together with microstructure characterization by transmission electron microscopy (TEM) and superplastic behaviors as feature parameters, the deformation mechanisms underlying the low-temperature superplastic deformation of this alloy under dislocation control were uncovered. The findings will theoretically support the low-temperature superplastic process optimization of Ti-6Al-4V.

MATERIAL AND METHODS

The studied material Ti-6Al-4V sheet alloy was chemically composed of (wt%) the following: Al, 6.01; V, 3.89; Fe, 0.21; C, 0.04; Ti, bal. Sheets were 2 mm thick and in grain size of 7.6 μm

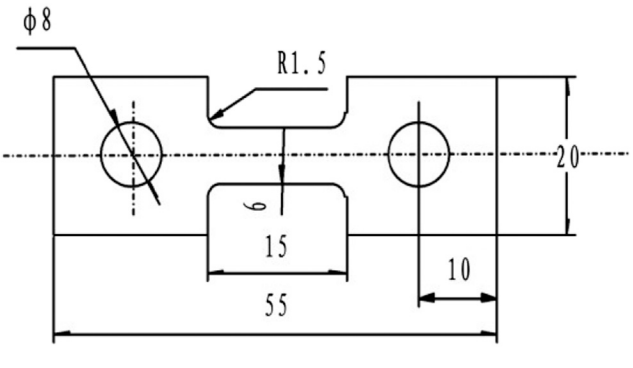

FIGURE 2 | Schematic diagram of tensile specimen dimension (unit: mm).

and consisted of 73% α phase and 27% β phase (**Figure 1**). The Ti-6Al-4V alloy sheets were prepared according to the alloy composition requirements above. Specifically, 4 mm-thick sheets were obtained after vacuum consumable melting and multipass hot rolling and cold rolling. The superplastic tensile specimens were prepared by linear cutting. Tensile specimen dimension is shown in **Figure 2**.

Using an AG 250KNE electronic tension tester, the specimens were heated to 923 K, kept there for 10 min, and then superplastically elongated at a constant crosshead speed and strain rate of 10^{-3}, 5×10^{-3}, or 5×10^{-2} s^{-1}. After water quenching to room temperature, the high-temperature deformed structures were reserved. The whole experiments were conducted under argon gas protection. The microstructures were observed under an OLYMPUS GX51 metallographic microscope, with 6 ml HNO_3+100 ml H_2O+3 ml HF as the etching agent. The α and β phases of specimens under different thermal treatment states were qualitatively analyzed by an XRD-7000 X-ray diffractometer (XRD; Shimadzu, Japan). The structural dislocation and grain

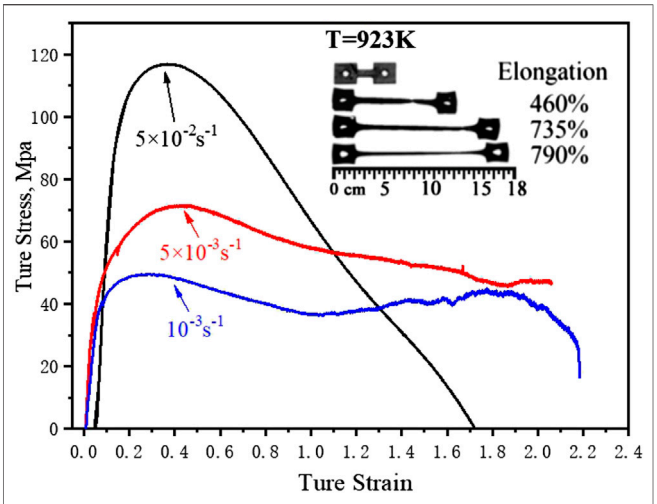

FIGURE 3 | Superplastic tensile stress-strain curves of Ti-6Al-4V (T = 923 K).

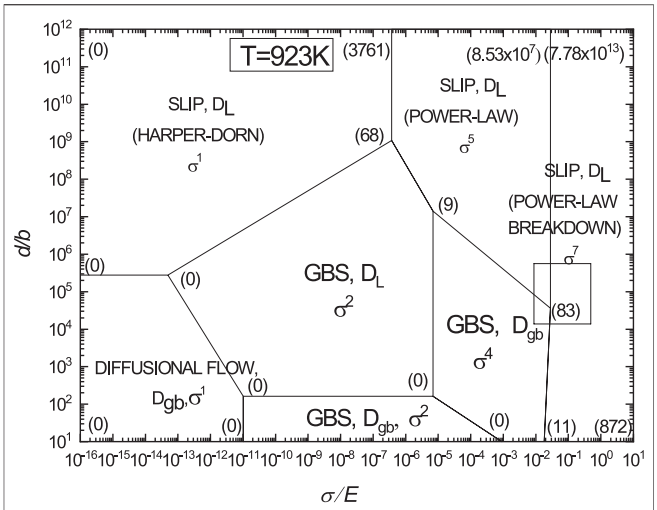

FIGURE 4 | Deformation mechanism maps of Ti-6Al-4V containing dislocation count (T = 923 K).

boundary morphology after deformation were observed and characterized by a TECNAI G^{20} TEM instrument.

RESULTS AND DISCUSSION

The stress-strain curves of Ti-6Al-4V at 923 K and strain rate of 10^{-3}, 5×10^{-3}, 5×10^{-2} s^{-1} are shown in **Figure 3**. Under the above conditions, the peak stress and steady-state stress of this alloy both decreased with the declining strain rate (**Fig. 3**). At the strain rate of 5×10^{-2} s^{-1}, the stress maximized and then rapidly decreased, and the interval of the steady-state rheological stress was narrow. At this moment, the total elongation was only 460%. When the strain speed decreased, the stress maximized and then slowly declined, and the curve was typical of steady-state rheological stress. The corresponding tension rates were 735 and 790%, respectively. These results indicate that the superplastic strain rate of this alloy is sensitive to some extent, and when the strain speed drops below 5×10^{-3} s^{-1}, the sensitivity is insignificant.

The high-temperature deformation of metals can be described by the following constitutive equation (Kim et al., 2001):

$$\dot{\varepsilon}_i = A_i \left(\frac{b}{d_i}\right)^p \cdot \frac{D}{k \cdot T \cdot b^2} \cdot \left(\frac{\sigma_i}{E}\right)^n, \quad (1)$$

where A_i, n, and p are material constants, σ_i is the stress, $\dot{\varepsilon}_i$ is the steady-state strain rate, E is Young's modulus, d_i is the grain size, b is the Burgers vector, and D is the diffusion coefficient (D_L is the lattice diffusion coefficient; D_{gb} is the crystal boundary diffusion coefficient).

The internal dislocation root count of unit crystal grains can be computed as follows (Cao et al., 2008):

$$n_i = 2[(1-\nu) \cdot \pi \cdot d_i \cdot \tau_i] / (Gb), \quad (2)$$

where n_i is the internal dislocation root count, ν is Poisson's ratio, and τ_i is the shear stress (MPa) in which $\tau_i = 0.5\sigma_i$. **Equation 1** is the constitutive equation about the high-temperature deformation of metal materials; **Eq. 2** is the dislocation control model of metal materials during superplastic deformation. **Equation 2** was mathematically transformed, and the dislocation count ni was introduced into **Eq. 1**, forming the deformation mechanism maps containing the dislocation count. Based on the experimental data in **Figure 3**, **Eqs. 1, 2** were solved; thereby, the RWS deformation mechanism maps of crystal grain sizes with dislocation count are plotted in **Figure 4**, with module compensation stress as X-axis and Burgers vector compensation as Y-axis. The physical parameters used in the calculation are listed in **Table 1**.

TABLE 1 | Physical parameters of Ti-6Al-4V alloys (Reca and Libanati, 1968; Stowell et al., 1984).

b = 2.95 × 10^{-10} m	**E = 2.87 × 10^{45} MPa**	**ν = 0.34**	**k = 1.38 × 10^{-23} J/K**
$D_{L\ 923K}$ = 3.01 × 10^{-17} m^2 s^{-1}		$D_{gb\ 923K}$ = 8.5 × 10^{-12} m^2 s^{-1}	

TABLE 2 | Calculated results of Ti-6Al-4V alloy after superplastic tensile tests.

T /K	(d/b)×10^{-7}	(σ/E)×10^4	$\dot{\varepsilon}$/(10^{-4}·s^{-1})
923	11.6–8.3	11.9–82.9	50–500

The normalized grain size with Burgers vector compensation ((d/b)×10^{-7}) and the normalized flow stress with modulus compensation ((σ/E)×10^4) of Ti-6Al-4V during superplastic tensile tests were calculated (**Table 2**).

According to **Figure 4** and **Table 2**, the superplastic deformation mechanism of Ti-6Al-4V at 923 K fell within the dislocation polygons of (8.53 × 10^7) (3,761) (68) (9) (83), (8.53×10^7) (7.78 × 10^{13}) (872) (11) (83), and (9) (0) (0) (11) (83) (the area surrounded by three sets of values). With an increase in strain rate, the superplastic deformation

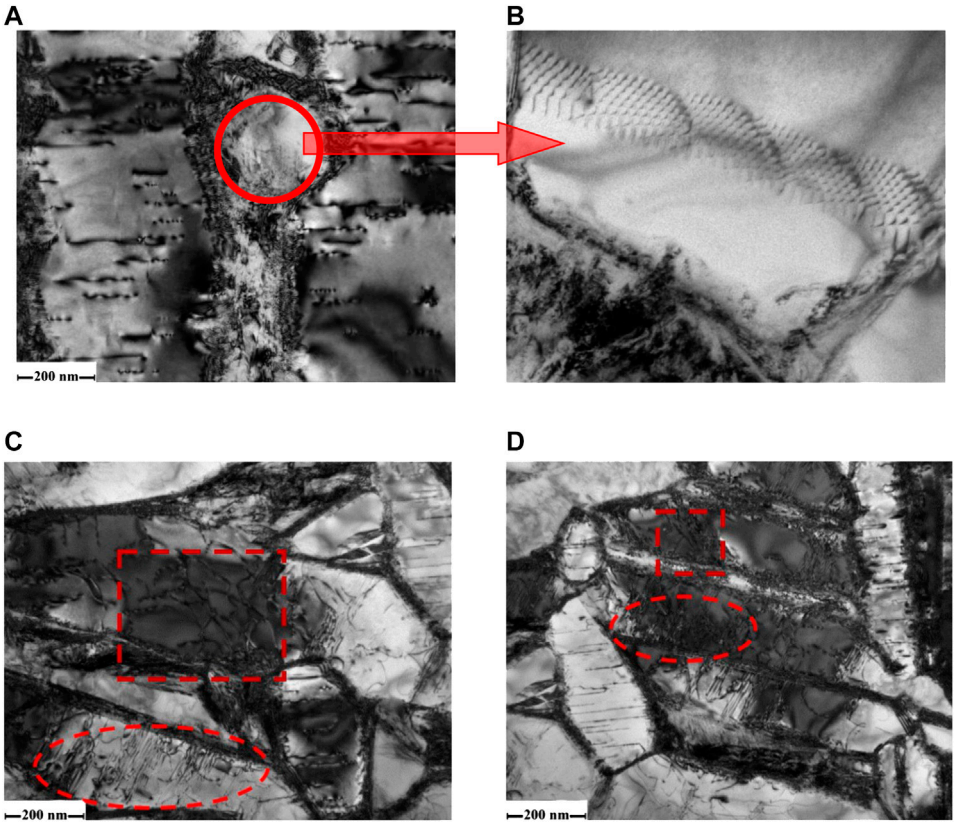

FIGURE 5 | TEM images of Ti-6Al-4V under the same superplastic tensile conditions. **(A,B)** $10^{-3}s^{-1}$; **(C)** 5×10^{-3} s^{-1}; **(D)** 5×10^{-2} s^{-1}.

mechanism transited from the dislocation-controlled grain boundary slip with a stress index of 4 to the dislocation glide with a stress index of 5 and 7, and the grain sizes during deformation affected the stress index *n*. Thus, it can be predicted from the deformation mechanism maps involving dislocation count that the superplastic deformation mechanisms of this alloy under the testing conditions were all affected by dislocation movement.

Figure 5 shows the TEM images of Ti-6Al-4V under different superplastic tensile conditions. At the strain rate of 10^{-3} s^{-1}, grain boundary deformation occurred during the superplastic tension of this alloy, and abundant irregular dislocations were formed around grain boundaries (**Figure 5A**), but the intracrystalline dislocations were arranged regularly (**Figure 5B**). With an increase in strain rate, the dislocation count gradually increased, the dislocation motion was intensified, and the dislocation slip was significant (**Figures 5C,D**), but no regular distribution, as shown in **Figure 5A**, was found. The above TEM images are consistent with the R-W-S deformation mechanism maps in **Figure 4**.

The superplastic deformation mechanism of Ti-6Al-4V at 923 K transited from dislocation-controlled grain boundary slip to dislocation glide along with an increase in strain rate. This is because the superplastic deformation of metal materials is essentially a synergy between dynamic softening mechanism and hardening mechanism, and the dynamic softening mechanism is the key factor that ensures the stable superplasticity of materials. As for Ti-6Al-4V, the softening mechanism of its superplastic tension is mainly dynamic recrystallization and recovery (Hiroaki et al., 2017). Owing to the low temperature, dislocation glide started firstly, and along with the superplastic tension, dislocation tangling occurred after the dislocation motion reached a certain extent. According to the first law of thermodynamics, the arrangement of the intertwined dislocations gradually became regular, and energy slowly dropped to the steady state, which induced recrystallization (Matsumoto et al., 2013). The proceeding of the above processes depends on appropriate dynamic conditions. Thus, the dynamic condition of this alloy at slow tension speed (10^{-3} s^{-1}) was sufficient, the irregular dislocation motion gradually turned into regular arrangement

TABLE 3 | Results of *m* and tension rate δ of Ti-6Al-4V at 923 K and different tension speeds.

Temperature *T*, K	Initial strain rate $\dot{\varepsilon}$, s^{-1}	Strain rate sensitivity exponent *m*	Tension to failure δ, %
923	10^{-3}	0.52	790
923	5×10^{-3}	0.51	735
923	5×10^{-2}	0.46	460

(**Figures 5A,B**), and the softening mechanism was the dislocation-controlled grain boundary slip (**Figure 4**). The strain rate sensitivity index m of this alloy calculated as m=(ln (1+δ))/(2 + ln (1+δ)) was 0.52 (**Table 3**). Together with the macroscopic mechanical property testing in **Figure 3**, it was known that the tension rate δ maximized to 790% and the steady-state flow stress was low. At a large strain rate (5×10^{-3} and $5 \times 10^{-2}\ s^{-1}$), the dislocation motion was still significant (**Figures 5C,D**), and due to the shortened superplastic deformation time, no regular tube-like arrangement was found, and the softening mechanism was controlled by dislocation glide and the stress index rose. At the strain rate of 5×10^{-2} $^{-1}$, the interval of steady-state rheological stress on the stress-strain curves was significantly shortened, the peak stress and steady-state stress both significantly increased, the strain rate sensitivity index m was 0.46 (**Table 3**), and the tension rate dropped by 490%. The above results also validate that the deformation mechanisms predicted by the R-W-S deformation mechanism maps are very accurate.

CONCLUSION

During the superplastic tensile deformation of Ti-6Al-4V at low temperature (923 K) and 10^{-3}, 5×10^{-3}, or $5 \times 10^{-2}\ s^{-1}$, the tension δ and strain rate sensitivity index m both rose with the decrease in tension speed and δ maximized to 790% at $10^{-3}\ s^{-1}$. Through mathematics modeling, the unit dislocation count was introduced into the R-W-S deformation mechanism map, and a new deformation mechanism map involving the dislocation count was plotted. Thereby, the mechanism of deformation of this alloy 923 K was predicted. Owing to the low temperature, the dislocation movement significantly impacted the softening effect of this alloy during superplastic deformation. Together with microstructure characterization, it was validated that as the strain rate increases from 10^{-3} to $5 \times 10^{-2}\ s^{-1}$, the deformation mechanism transited from dislocation-controlled grain boundary slip to dislocation glide, and the stress index increased.

DATA AVAILABILITY STATEMENT

The original contributions presented in the study are included in the article/Supplementary Material; further inquiries can be directed to the corresponding author.

AUTHOR CONTRIBUTIONS

CL, XW, and LC conceived of and designed the experiments; XW and CL carried out the experiments; FL, SZ, HL, and HZ analyzed the data; CL and GZ wrote the article.

FUNDING

This research was funded by the Liaoning provincial department of finance (No. LQGD2017024), National Natural Science Foundation (No. 51805335), and Liaoning Natural Science Guidance Plan (20180550998).

REFERENCES

Cao, F. R., Ding, H., Li, Y. L., Zhao, W. J., Guo, Y. L., and Gui, J. Z. (2008). Theoretical predicati on of dislocation-included high-temperature deformation mechanism maps for duplex magnesium lithium alloys. *J. Mater. Metall.* 7, 206–210. doi:10.14186/j.cnki.1671-6620.2008.03.008

Hiroaki, M., Takuro, N., Vincent, V., and Vanessa, V. (2017). Superplastic property of the Ti–6Al–4V alloy with ultrafine-grained heterogeneous microstructure. *Adv. Eng. Mater.* 20, 1. doi:10.1002/adem.201700317

Kim, W. J., Chung, S., Chung, C., and Kum, D. (2001). Superplasticity in thin magnesium alloy sheets and deformation mechanism maps for magnesium alloys at elevated temperatures. *Acta Mater.* 49, 3337–3345. doi:10.1016/S1359-6454(01)00008-8

Li, X., Guo, G., Xiao, J., Song, N., and Li, D. (2014). Constitutive modeling and the effects of strain-rate and temperature on the formability of Ti–6Al–4V alloy sheet. *Mater. Des.* 55, 325–334. doi:10.1016/j.matdes.2013.09.069

Matsumoto, H., Bin, L., and Lee, S. (2013). Frequent occurrence of discontinuous dynamic recrystallization in Ti-6Al-4V alloy with α′ martensite starting microstructure. *Metall. Mater. Trans.* 44, 3245–3260. doi:10.1007/s11661-013-1655-5

Meng, B., Fu, M. W., and Shi, S. Q. (2016). Deformation behavior and microstructure evolution in thermal-aided mesoforming of titanium dental abutment. *Mater. Des.* 89, 1283–1293. doi:10.1016/j.matdes.2015.10.105

Reca, N. E., and Libanati, C. M. (1968). Autodifusion de titanio beta y hafnio beta Self-diffusion in β-titanium and β-hafniumAutodiffusion du titane beta et de l'hafnium betaSelbstdiffusion in β-titan und β-hafnium. *Acta. Met.* 16, 1297–1305. doi:10.1016/0001-6160(68)90010-2

Shahmir, H., Naghdi, F., Pereira, P., Huang, Y., and Langdon, T. G. (2018). Factors influencing superplasticity in the Ti-6Al-4V alloy processed by high-pressure torsion. *Mater. Sci. Eng. A.* 718, 198–206. doi:10.1016/j.msea.2018.01.091

Stowell, M. J., Livesey, D. W., and Ridley, N. (1984). Cavity coalescence in superplastic deformation. *Acta Metall.* 32, 35–42. doi:10.1016/0001-6160(84)90199-8

Vanderhasten, M., Rabet, L., and Verlinden, B. (2007). Deformation mechanisms of Ti-6Al-4V during tensile behavior at low strain rate. *J. Mater. Eng. Perform.* 16, 208–212. doi:10.1007/s11665-007-9033-3

Zhang, W., Ding, H., Pereira, P., Huang, Y., and Langdon, T. G. (2018). Grain refinement and superplastic flow in a fully lamellar Ti-6Al-4V alloy processed by high-pressure torsion. *Mater. Sci. Eng. A.* 732, 398–405. doi:10.1016/j.msea.2018.07.010

Zhang, W., Ding, Hua., Cai, Minghui., Yang, Wenjing., and Li, Jizhong. (2018). Ultra-grain refinement and enhanced low-temperature superplasticity in a friction stir-processed Ti-6Al-4V alloy. *Mater. Sci. Eng. A.* 727, 90–96. doi:10.1016/j.msea.2018.03.009

Zhou, Ge., Chen, Lijia., Liu, Lirong., Liu, Haijian., Peng, Heli., and Zhong, Yiping. (2018). Low-temperature superplasticity and deformation mechanism of Ti-6Al-4V alloy. *Materials* 11, 1212. doi:10.3390/ma11071212

Conflict of Interest: The authors declare that the research was conducted in the absence of any commercial or financial relationships that could be construed as a potential conflict of interest.

frontiers in Materials

ORIGINAL RESEARCH
published: 12 February 2021
doi: 10.3389/fmats.2021.633789

Influence of Coarse Mg_3Bi_2 Particles on Deformation Behaviors of Mg-Bi Alloys

Tingting Guo[1†], Xuerong Lu[1†], Ramesh Kumar Varma[2], Cheng Zhao[3], Jun Wang[2], Jianwei You[1] and Jian Chen[1]*

[1]School of Materials Science and Chemical Engineering, Xi'an Technological University, Xi'an, China, [2]Institute for Frontier Materials, Deakin University, Geelong, VIC, Australia, [3]School of Materials Science and Engineering, Xi'an University of Technology, Xi'an, China

Mg-Bi binary alloys with concentrations of 1, 3, 6, and 9 wt% Bi and ternary Mg-9Bi-2.5Zn alloy were prepared by casting and hot extrusion. The results show that alloying with Bi refined as-cast grains of Mg alloys and the refinement efficiency of Bi is in between Al and Zr. It was also found that a critical value for the area fraction of constituent Mg_3Bi_2 particles seems to appear, which influences the dynamic recrystallization mechanism during extrusion. This influence results in either uniform or heterogenetic distribution of grain size and different extrusion texture intensities. Furthermore, the addition of Zn affected both the grain size and the area fraction/size of Mg_3Bi_2. Mechanical results and microstructure/fractography observation suggest that Mg_3Bi_2 particles do not impact the tensile nor compression yielding stress but act as fracture sources.

Keywords: magnesium, bismuth, zinc, coarse particles, deformation behavior

OPEN ACCESS

Edited by:
Minghui Cai,
Northeastern University, China

Reviewed by:
Hucheng Pan,
Northeastern University, China
Zhen Zhang,
Hefei University of Technology, China

****Correspondence:***
Tingting Guo
ttgu@outlook.com

†These authors have contributed equally to this work

Specialty section:
This article was submitted to Structural Materials, a section of the journal Frontiers in Materials

Received: *26 November 2020*
Accepted: *04 January 2021*
Published: *12 February 2021*

Citation:
Guo T, Lu X, Varma RK, Zhao C, Wang J, You J and Chen J (2021) Influence of Coarse Mg_3Bi_2 Particles on Deformation Behaviors of Mg-Bi Alloys. Front. Mater. 8:633789. doi: 10.3389/fmats.2021.633789

INTRODUCTION

Alloying is a common manner to modify the microstructure and the mechanical response of magnesium (Mg). Zinc (Zn), aluminum (Al), and rare earth (RE) are the main alloying elements for commercial applications of Mg alloys at present (Ahmad et al., 2019; Jayasathyakawin et al., 2020; Polmear et al., 2017c). With alloying and subsequent metallurgical/thermal treatments, intermetallic compounds, submicron-sized particles, or nanosized precipitations are usually formed in these magnesium alloys. These particles usually exert diverse influences on plastic deformation behaviors of the end products. A better understanding of the role played by them in the mechanical properties of Mg alloys is thereby essential for designing sophisticated new alloys.

Fine and densely dispersed particles are ideal for alloys to obtain a well-balanced strength and ductility. Efforts have been made to work on age-hardenable magnesium to achieve this goal for decades and an Mg-Bi system in recent years has attracted increasing attention due to its great mechanical properties (Go et al., 2020; Meng et al., 2020). Nanosized Mg_3Bi_2 precipitates are usually formed during the age heat treatment of Mg-Bi alloys and they show rod- or plate-like shapes lying parallel to $\langle 11\bar{2}0\rangle$ or $\langle 10\bar{1}0\rangle$ directions of Mg matrix (Sasaki et al., 2009; Sun and Sun, 2018). Zn coworks with bismuth (Bi) in Mg to further refine the Mg_3Bi_2 precipitates by around two- to fivefold while promoting the nucleation of Mg_3Bi_2 (Sasaki et al., 2009; He et al., 2020). Nanosized Mg_3Bi_2 particles could be obtained during the postthermal processing and the area fraction is in a positive linear relationship with Bi addition (Yu et al., 2020). The binary or multicomponent Mg-Bi-based alloys containing very fine precipitations were reported to show an improved hardening response (Sasaki et al., 2009; He et al., 2020). On the other hand, the constituent Mg_3Bi_2 phase formed during

TABLE 1 | Composition of the alloys studied in this work expressed in weight percentage.

Alloy	Bi	Zn	Mg
Mg-1Bi	1.05	—	Balance
Mg-3Bi	3.08	—	Balance
Mg-6Bi	5.69	—	Balance
Mg-9Bi	8.67	—	Balance
Mg-9Bi-2.5Zn	9.26	2.54	Balance

solidification cannot dissolve comprehensively in homogenization, due to its high incipient melting temperature (Go et al., 2020). This constituent Mg_3Bi_2 phase is expected to impose a different effect on mechanical performance compared to the same phase with much smaller sizes obtained by postthermal processing. However, this effect is not well understood.

Meng et al. (Meng et al., 2017) observed that stringers of coarse Mg_3Bi_2 intermetallic compounds, with an area fraction of ~5.9%, were aligned along the extrusion direction (ED) in an Mg-8Bi-1Al-1Zn alloy. This extruded alloy showed a yield stress of ~291 MPa with an elongation of ~14.6%. These good mechanical properties were ascribed to the refined grain size and the hardening effect by Mg_3Bi_2. In another investigation on Mg-6Bi and Mg-9Bi alloys (Go et al., 2020), the tensile yield stress was measured as ~129 MPa and 141 MPa, respectively, and both materials showed brittle fracture (~5% elongation). The stress increment was interpreted as a change of the coarse Mg_3Bi_2 particles' area fraction from 12.7% to 14.4%. In a very recent work by Yu et al. (Yu et al., 2020), the influence of 2, 5, and 8 wt% bismuth addition on the microstructure and plastic deformation of binary magnesium alloys was examined. Their results showed that the yielding systematically rises with Bi content, and the Mg-5Bi had the best ductility of ~19.8%. Both nanosized precipitates and coarse phase of Mg_3Bi_2 were observed and explained to contribute to the hardening. The crack types of either brittle or ductile fracture mentioned above were caused by the large Mg_3Bi_2 compounds judging from the fractography. However, the microstructure features, i.e., the size of these Mg_3Bi_2 particles, whether they are nanosized or coarse or a mixture of both, on the mechanical performance, were not well separated. It is expected that the size of these particles should play an important role. Therefore, the present study focuses on examining the effect of coarse Mg_3Bi_2 particles.

Specifically, in this work, binary Mg-Bi alloys with 1, 3, 6, and 9 wt% addition were employed for investigation. We aim at studying the role of coarse Mg_3Bi_2 particles obtained from the casting on plastic deformation, and the influence of Zn will also be discussed.

EXPERIMENTAL METHOD

Five alloys listed in **Table 1** were studied in this work, and pure Mg was used for the benchmark. The castings were heated to 730°C and then poured into a 300°C preheated brass mold to produce an as-cast cylinder of 85 mm in diameter and 200 mm in length. The compositions of all alloys were analyzed during the casting by Inductively Coupled Plasma (ICP) Spectroscopy to obtain the targeting compositions. The as-cast ingots were homogenized at 500°C for 24 h and then machined to a diameter of ϕ80 mm. The ingots were extruded at 380°C with an extrusion ratio of 25 : 1 at a ram speed of 2 m/min and finished with water quenching. Dog-bone shaped tensile samples with a gauge dimension of ϕ3 mm × 10 mm and cylindrical compression specimens with the size of ϕ10 mm × 15 mm were prepared. The ambient temperature tensile and compression tests were performed at a strain rate of 10^{-3}/s. The tensile strain is measured by a contact extensometer (Epsilon, produced by Epsilon Technology Corp, USA) until fracture.

The samples for Optical Microscopy (OM), Scanning Electron Microscopy (SEM), Energy-Dispersive X-ray (EDX) spectroscopy, and Electron Backscattered Diffraction (EBSD) observations were taken close to the cylindrical axis and polished on the cross-sectional surface of the casting or extrusion parts. The polishing procedure includes wet grinding using 2000 grit SiC paper and 6 and 3 μm diamond pastes. The 20 nm sized colloidal silica was used for the last step on a Struers DP-Pan cloth. Samples were ultrasonically cleaned for 2 min in ethanol between each step and dried with flowing air. The samples for OM observations were etched in acetic-nitric acid (15 ml acetic acid, 5 ml nitric acid, 60 ml ethanol, and 20 ml distilled water) for 5–10 s depending on the content of Bi. SEM and EDX analyses were performed using a VEGA3-SBH Tescan operated at 20 kV. ImageJ software (Schneider et al., 2012) was used for particle analysis. The textures obtained by EBSD mapping were carried out by a field emission Zeiss Sigma 500 and the scanning step size is 1–3 μm decided by the grain size of samples. An HKL channel five software (Oxford Instruments) was employed for EBSD analysis. Phase determination was performed on 2000 grid SiC polished surface using Bruker D2 Phaser X-Ray Diffractometer (XRD) by Cu Kα radiation. The lattice parameters were calculated by single peak refinement from the corrected peak positions [Suryanarayana and Norton, 1998]. A nonlinear least-square refinement over the observed *hkl* reflections and the corresponding *d* spacing gives lattice parameters.

RESULTS

Microstructure of As-Cast Alloys

Figure 1 shows the as-cast microstructures of alloys investigated in the present work. There is interdendritic segregation that occurs in the alloys with higher bismuth concentration (**Figures 1D,E**). Smaller dendritic arms were observed in ternary alloys due to the influence of Zn, shown in **Figure 1F**, and some large particles were also seen in the grain interior. Taking a close inspection of Mg-9Bi (**Figure 2A**) and Mg-9Bi-2.5Zn (**Figure 2B**), most of the intermetallic compounds lie along the grain boundaries, and there are rod-like submicron-sized particles located around. EDX results show that the intermetallic compounds and the submicron-sized particles are composed of

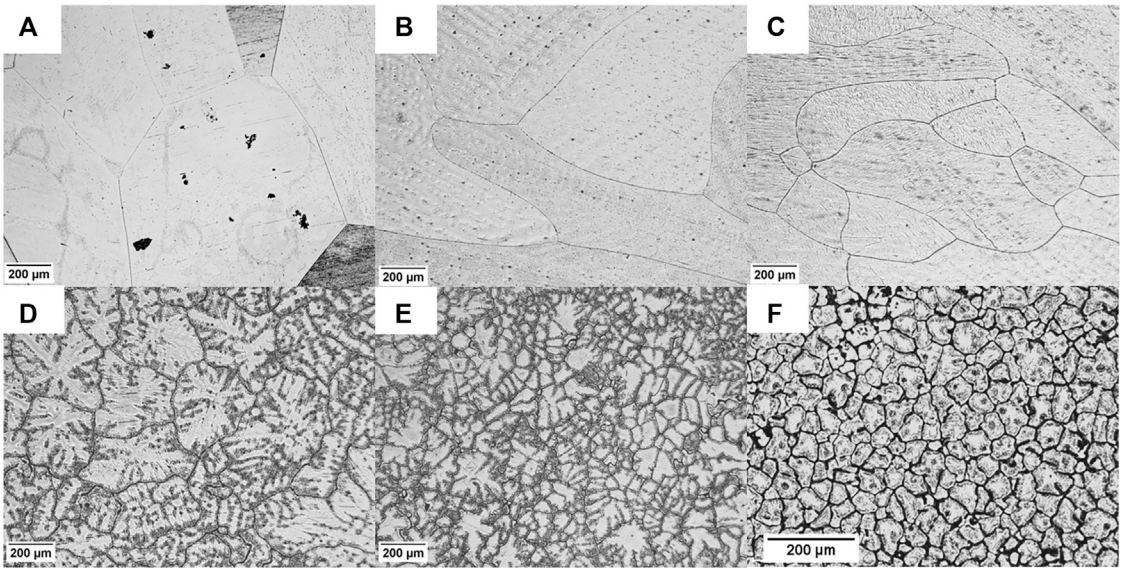

FIGURE 1 | As-cast microstructure of **(A)** pure Mg, **(B)** Mg-1Bi, **(C)** Mg-3Bi, **(D)** Mg-6Bi, **(E)** Mg-9Bi, and **(F)** Mg-9Bi-2.5Zn.

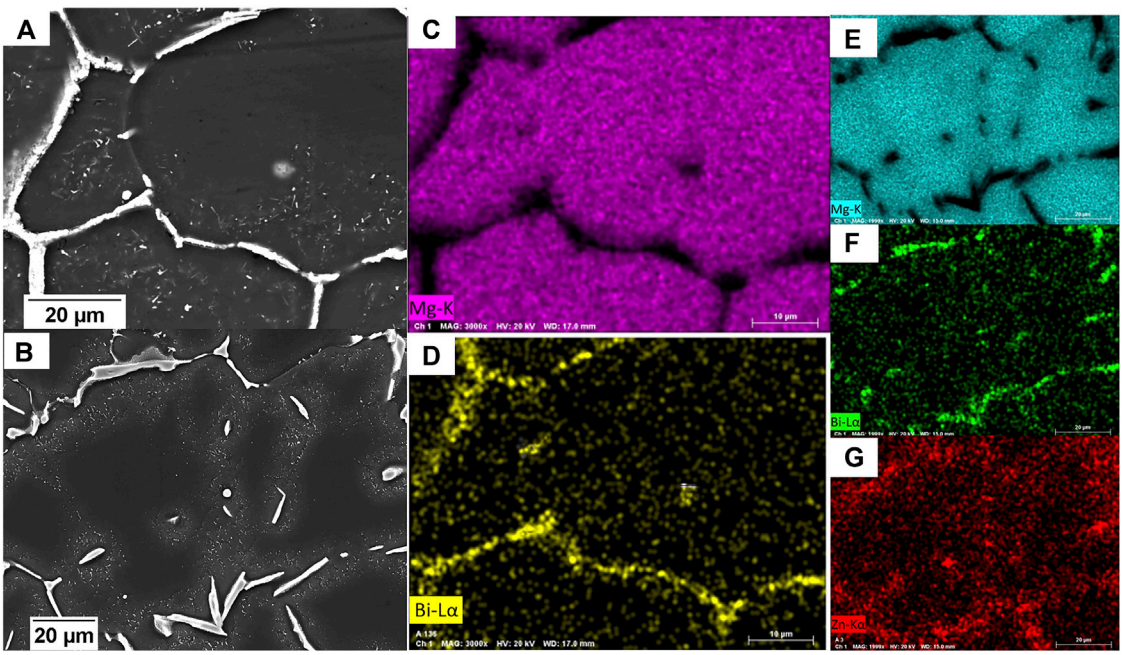

FIGURE 2 | EDX analysis of **(A) (C) (D)** Mg-9Bi alloy and **(B) (E) (F) (G)** Mg-9Bi-2.5Zn.

Mg_3Bi_2 phase, which has been further confirmed by XRD analysis (not shown here). The rod-shaped particles' size is estimated to be ~1.5 times smaller in ternary alloys than that in Mg-9Bi. It was shown in **Figure 2** that the Bi is rarely concentrated in the grain interior, indicative of the serious segregation feature of the Bi element. There is a segregation-free and precipitation-free zone adjacent to the coarse intermetallic compounds/grain boundaries, which is not uncommon in aged alloys (Watanabe et al., 2008; Zindal et al., 2018).

Figure 3A depicts the evolution of grain size with compositions. Bi acts as a grain refiner and reduces the average grain size from 880 μm of pure Mg to 115 μm when 9 wt% Bi is added. The grain size is further reduced to 47 μm by alloying with Zn. **Figure 3B** shows the statistics of area fraction of

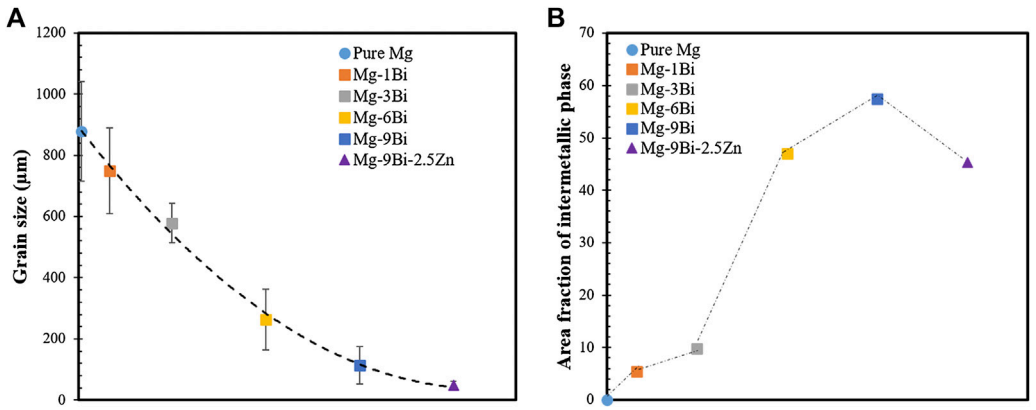

FIGURE 3 | (A) The evolution of grain size with Bi content and **(B)** the area fraction of Mg_3Bi_2 intermetallic compounds of alloys estimated by ImageJ. The error bars represent the standard deviation. The dashed line is used for guiding the eyes.

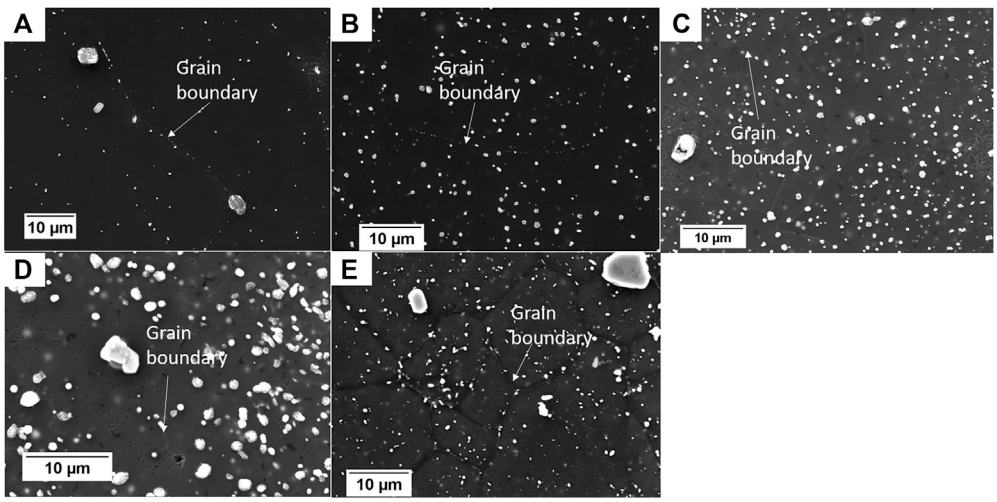

FIGURE 4 | SEM images showing microstructure of extruded **(A)** Mg-1Bi, **(B)** Mg-3Bi, **(C)** Mg-6Bi, **(D)** Mg-9Bi, and **(E)** Mg-9Bi-2.5Zn.

intermetallic phase along the grain boundaries. ImageJ was employed on OM images to analyze based on the contrast with Mg matrix. This method overestimates the amount of Mg_3Bi_2, because the area of Bi segregation is not easy to be excluded, and it are only used for rough comparison. It is observed that the amount of Mg_3Bi_2 phase (and Bi segregation) increases with Bi content and reaches a peak of 57% area fraction for the Mg-9Bi alloy. Further alloying with Zn, by contrast, decreases the Mg_3Bi_2 area fraction, which is even 1.7% less than that for the Mg-6Bi.

Microstructure and Texture of Extruded Alloys

Figure 4 shows the SEM images of the cross-sectional plane of the extruded alloys. The XRD profiles in **Figure 5** index the Mg_3Bi_2 particles in all alloys. Mg_3Bi_2 particles are observed on both grain boundaries and interiors. The average diameter of particles is shown to be the largest in Mg-9Bi of ~0.65 μm, although the data is widely scattered, as observed in **Figure 6A**. In contrast, the other alloys display a similar average size of ~0.4 μm. The area fraction of particles in **Figure 6B** follows the same trend as observed in **Figure 3B**. The values shown in **Figure 6B** drop sharply below 10%, which is possible due to the dissolution of the segregated Bi. Alloy of 9% Bi contains the largest area fraction of the second phase of ~7.3%, while only ~5.7% Mg_3Bi_2 particles are present in the ternary alloy.

Figure 5 shows XRD profiles of Mg-Bi and Mg-Bi-Zn alloys. The primary Mg phase and secondary Mg_3Bi_2 phase are readily indexed. It can be seen that the intensity of Mg_3Bi_2 phase increases with Bi concentration. However, due to the orientation effect in the irradiated area, the peak intensities do not follow the reference intensity ratio (RIR) values. Further, the

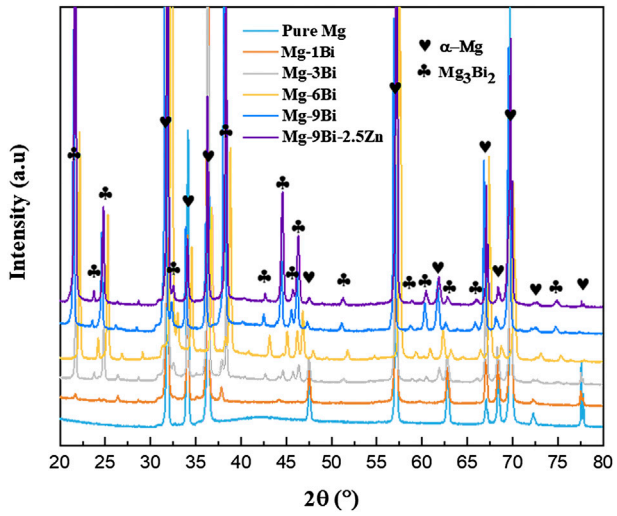

FIGURE 5 | XRD profiles of pure Mg, Mg-Bi, and Mg-Bi-Zn alloys.

effect of Bi on Mg matrix will be analyzed via lattice parameter variation in the discussion section.

The microstructures of the as-extruded materials and their corresponding inverse pole figure (IPF) are shown in **Figures 7** and **8**, respectively. The grains are dramatically refined (see caption of **Figure 7** for more details) compared to the as-cast counterpart. The heterogeneity of grain size in Mg-6Bi and Mg-9Bi indicates the partially dynamic recrystallized (DRXed) microstructure, which accounts for 38.8% and 89.4% in area fraction, respectively. The formation of DRXed grains in those two alloys might be due to a precipitation stimulated nucleation (PSN) mechanisms by the presence of isolated large Mg_3Bi_2 particles. It is generally accepted that PSN is observed to occur at particles with a diameter larger than 1 μm (Robson et al., 2009; Doherty et al., 1997; Humphreys et al., 2017), which accounts for ~4%, ~3.5%, ~7%, and ~19% of total particles in binary alloys with an increase of Bi content, and in Mg-9Bi-2.5Zn alloys, it is ~6%. The efficiency of PSN seems to be influenced by fraction of critical-sized (1 μm) particles, and a value of ~7% might be the threshold based on the dynamic recrystallization fraction changes. It is worth noting that the PSN-induced DRXed grains in the Mg-6Bi and Mg-9Bi alloys display the strongest [10$\bar{1}$0] fiber texture (~5.5 MUD, analyzed by partition DRXed grains according to kernel average misorientation). Inspection of the grain disorientation function in **Figure 9** reveals that all the materials have experienced recrystallization (>90% grain boundaries are high angle ones). The less intense texture (**Figures 8A–C,F**) and homogeneously distributed grain size in other alloys imply possible different DRXed mechanisms rather than PSN. For particle size smaller than the critical value, the recrystallization could be retarded resulting in an increase of grain size (Humphreys et al., 2017), which probably occurred in the current alloys Mg-1Bi, Mg-3Bi, and Mg-9Bi-2.5Zn. A careful examination of Mg_3Bi_2 particle-stimulated dynamic recrystallization will be presented in a separate paper.

Mechanical Properties

Engineering stress-strain curves obtained from tensile and compression tests for pure Mg and magnesium alloys are presented in **Figures 10A** and **10B**. The effect of alloying with Bi and Zn on the 0.2% offset yield strength is summarized in **Figure 10C**. Tensile yield stress increases with the Bi concentration up to 6%. A drop of yielding of ~26 and ~29 MPa can be observed when going from the addition of 6%–9% of Bi to 9% Bi-2.5% Zn, respectively. Mg-9Bi-2.5Zn shows the best ductility with total elongation of ~10%, which is 3 times better than that for Mg-9Bi alloy. All the other alloys are brittle with the elongation of less than 5%. In the case of compression testing, the drop of yielding stress occurs in Mg-9Bi-2.5Zn by 14 MPa compared to Mg-9Bi. It is clear that the Bi addition is favorable for dampening yield asymmetry and the final addition of 2.5% Zn to Mg-9Bi alloy makes the asymmetry ratio (compression yield stress/tensile yield stress) close to 1, as shown in **Figure 10D**.

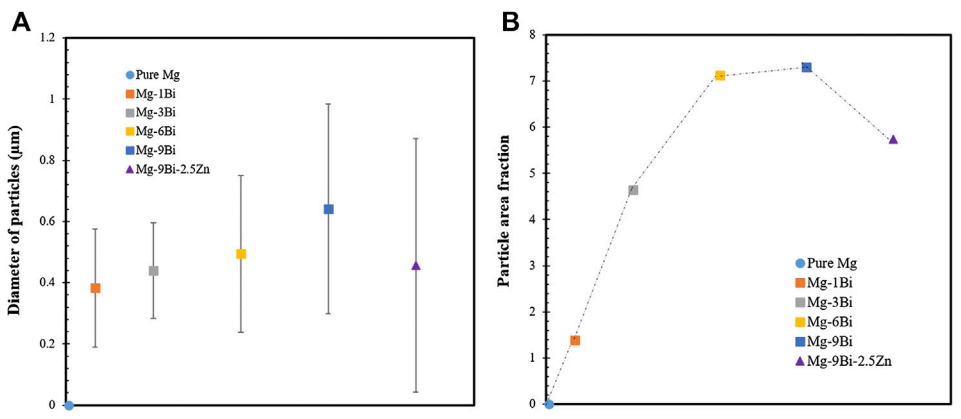

FIGURE 6 | (A) Diameter and **(B)** area fraction of Mg_3Bi_2 particles in pure Mg and alloys studied in the present work. ImageJ is used for analysis based on SEM images. The error bars represent the standard deviation. The dashed line is used for guiding the eyes.

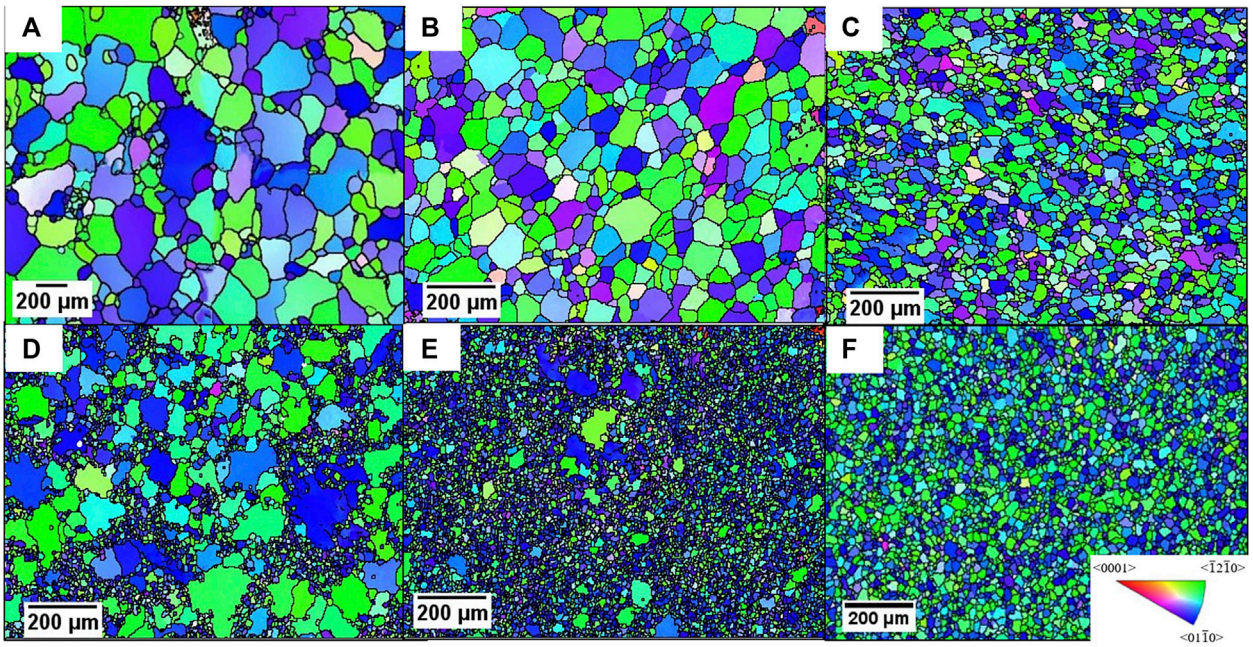

FIGURE 7 | Inverse pole figure colored EBSD maps of **(A)** pure Mg, **(B)** Mg-1Bi, **(C)** Mg-3Bi, **(D)** Mg-6Bi, **(E)** Mg-9Bi, and **(F)** Mg-9Bi-2.5Zn. The average grain size is 103, 38, 21, 15, 9, and 12 μm, respectively. The extrusion direction (ED) is normal to the page. The scanning area is in the center of the cross section of extrusion bars.

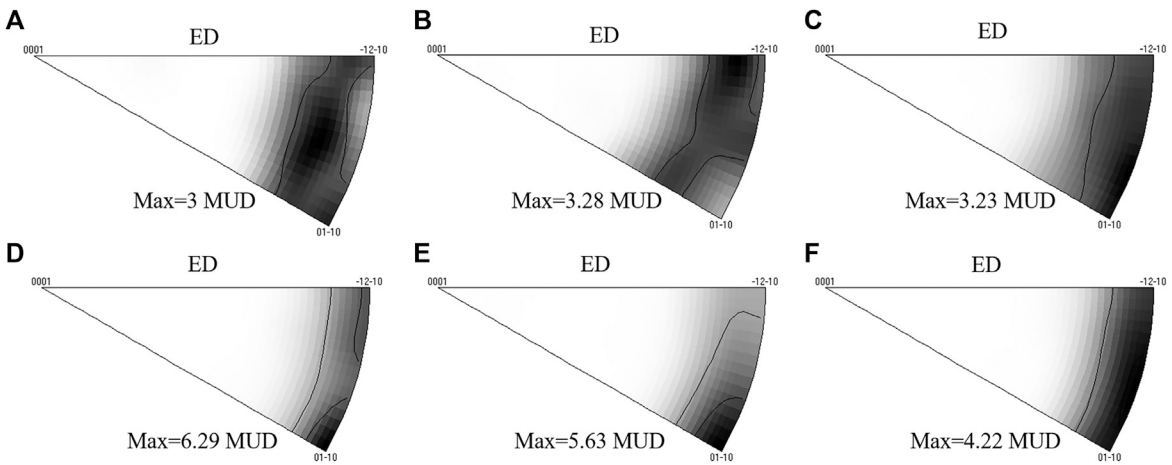

FIGURE 8 | Inverse pole figures of **(A)** pure Mg, **(B)** Mg-1Bi, **(C)** Mg-3Bi, **(D)** Mg-6Bi, **(E)** Mg-9Bi, and **(F)** Mg-9Bi-2.5Zn.

The fracture surface after tensile testing is shown in **Figure 11**. The typical brittle fracture featured with the cleavage plane is observed in pure Mg and Mg-1Bi. Both dimple-like failure and low ductility cleavage plane are observed in Mg-3Bi, Mg-6Bi, and Mg-9Bi. The Mg-9Bi-2.5Zn alloy demonstrates an almost uniform fracture consisting of dimples and river-like strips. Mg_3Bi_2 particles can be clearly seen inside the dimples in most alloys, except pure Mg and Mg-1Bi, indicating that these particles are probably the source of fracture. The average size of exposed particles is estimated to be ~0.27, 0.54, 0.62, and 0.34 μm for Mg-3Bi, Mg-6Bi, Mg-9Bi, and Mg-9Bi-2.5Zn, respectively, falling in the range of measurement shown in **Figure 6A**.

DISCUSSION

Grain Refinement of As-Cast Mg-Bi Alloys

Obtaining a fine-grained structure of as-cast alloys could reduce the need for postthermal processing or further refining the DRXed grains. As observed in **Figure 1**, alloying with Bi is a

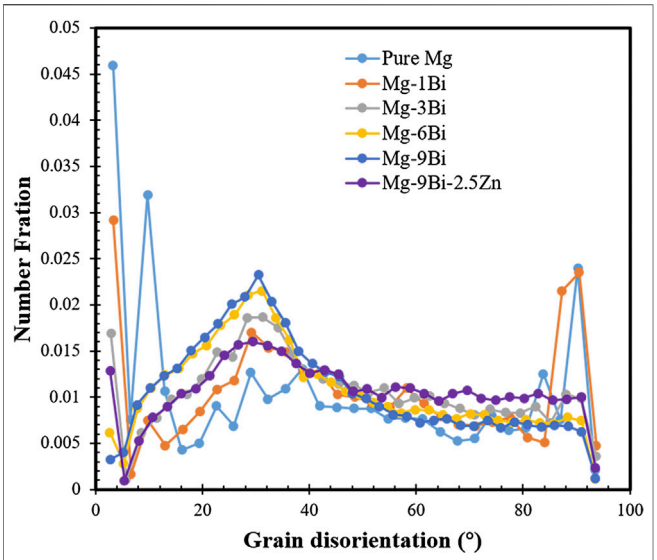

FIGURE 9 | Grain disorientation profile of as-extruded pure Mg and alloys studied in the present work.

potential option for grain refiner of magnesium alloys. The grain size is thought to be controlled by nucleant particles and growth restriction, Q. The solute with a strong segregation ability has a high Q value. The independence model incorporated two factors to predict the grain size, and the simplified version is (StJohn et al., 2013)

$$d = \frac{5.6Dz\Delta T_n}{v}\frac{1}{Q} + x_{sd}, \tag{1}$$

where D is the diffusion rate, z is the proportion of constitutional supercooling (CS) required to be regenerated after the nucleation, $1/\Delta T_n$ is the nucleant particle potency, v is the steady-state growth rate, and x_{sd} is the density of the particle. The growth restriction factor Q can be expressed as (Easton et al., 2016)

$$Q = C_0 m_1 (k - 1), \tag{2}$$

where C_0 is alloy composition, m_1 is the slope of the liquidus line, and k is the partition coefficient. The first term in **Eq. 1** is the distance of Nucleation Free Zone (NFZ), x_{nfz}, which is controlled by CS. Reducing the NFZ is the key to refine the grain size and the importance has been discussed in ref. (Easton et al., 2016; Prasad et al., 2013; StJohn et al., 2015). **Figure 12** plots the grain size against $1/Q$. The linear fitting equation though the data is d = 1194.5(1/Q) + 10. Joshi and Babu (Joshi and Hari Babu, 2017) studied the impact of 0.02 wt%–0.4 wt% Bi addition on the grain size of binary magnesium alloys and the relation of d_{gs} and $1/Q$ they obtained was d = 13.2(1/Q) + 403. Their result seems to show a greater grain refining effect by Bi. This is probably because the oxidation during casting which formed the Mg-Bi-O particles provides the nucleation sites in their work, while in our case, a

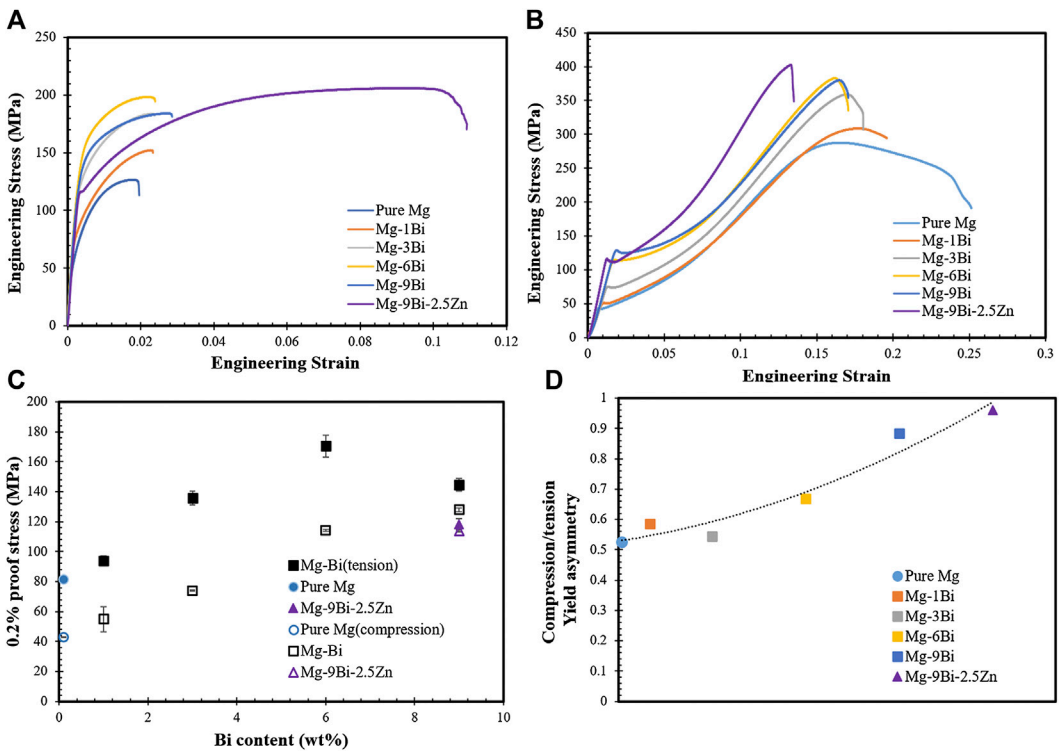

FIGURE 10 | Engineering stress-strain curve of **(A)** tensile, **(B)** compression tests, **(C)** summary of 0.2% offset proof stress, and **(D)** compression/tension yield asymmetry ratio in alloys studied in present work. The dashed line is used for guiding the eyes.

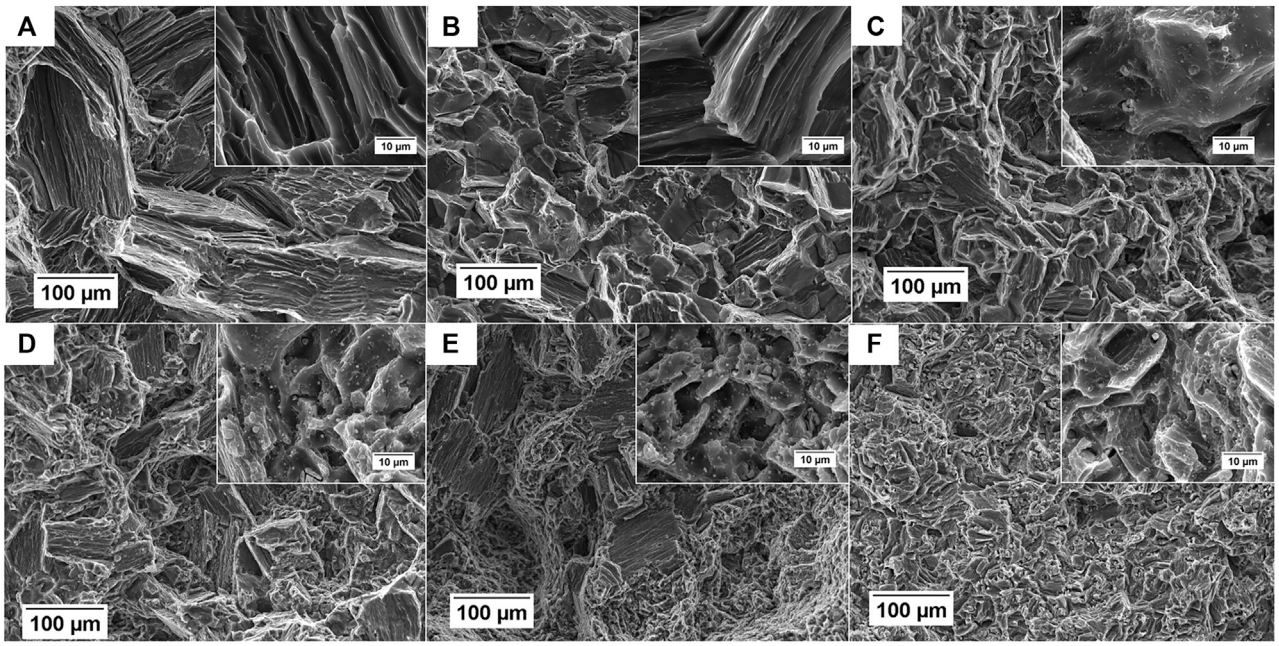

FIGURE 11 | Tensile fractograph of **(A)** pure Mg, **(B)** Mg-1Bi, **(C)** Mg-3Bi, **(D)** Mg-6Bi, **(E)** Mg-9Bi, and **(F)** Mg-9Bi-2.5Zn.

lower number of nucleating particles ($10/mm^3$) and large NFZ result in coarse grains. The data of Mg-Al and Mg-Zr cast in a mild steel mold reported by Lee et al. (Lee et al., 2000) are also plotted for comparison in **Figure 12**. If we neglect the effect of cooling rate (Bi is thought to be insensitive to the cooling rate by Joshi and Babu (Joshi and Babu, 2017)), the efficiency of Bi as a grain refiner for Mg is greater than Al but less than Zr. Zn is also thought to be a grain refiner to magnesium alloys (Polmear et al., 2017b) and leads to a further reduction of grain size when alloying with Zn.

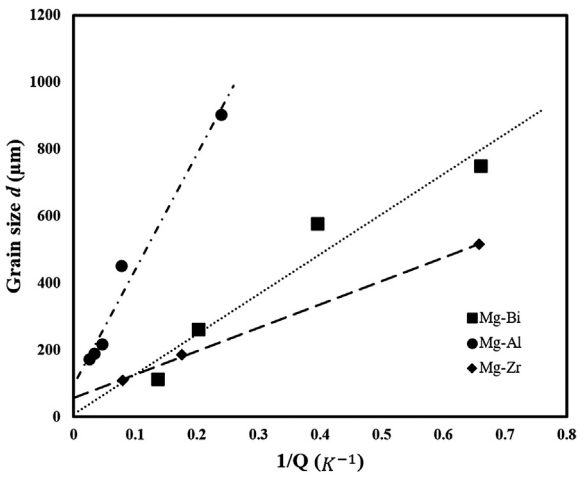

FIGURE 12 | Grain size vs. 1/*Q* for Mg-Bi (1-9 wt%) binary alloys. The casting was performed in a brass mold and the sample size is ϕ85 mm × L200 mm. The data of Mg-Al (1-9 wt%) and Mg-Zr (0.04-0.32 wt%) are reproduced from ref. Lee et al. (2000), and the sample dimension is ϕ25 mm × L70 mm.

The Variation of Yielding Stress

As observed in **Figure 10**, the tensile yielding stress increases with Bi addition in leaner alloys but drops at Mg-9Bi, and it has a further decrease in Mg-9Bi-2.5Zn alloy. The yield of compression rises as Bi concentration increases, and this is followed by a slight drop by 14 MPa alloyed with Zn. It seems that our work is controversial with previous reports (Yu et al., 2020; Go et al., 2020), in which the yielding monotonic increases with Bi content. The likely reasons will be analyzed in the following part.

As for textured extruded magnesium, tensile testing along the extrusion direction is controlled by prismatic slip, and for compression along the extrusion direction, the yielding is dominated by $\{10\bar{1}2\}$ extension twinning (Polmear et al., 2017c). The critical resolved shear stress (CRSS) for prismatic slip and extension twinning could thus be roughly estimated by multiplying the yielding stress (σ) and the average Schmid factor (M) as (Stanford and Barnett, 2013)

$$\mathrm{CRSS} = \sigma \Delta M. \tag{3}$$

Table 2 lists the CRSS of prismatic slip and twin for pure Mg and alloys, and the grain size is also presented for each extruded alloy. The CRSS values measured here are reasonable for both prismatic slip and extension twin for a range of grain sizes, which were reported by previous works (Ghaderi and Barnett, 2011; Stanford and Barnett, 2013). The grain size influences the activation of deformation modes; i.e., the smaller the grain size, the larger CRSS (Hall-Petch relation). This Hall-Petch type hardening is generally true for alloy up to 6 wt% Bi

TABLE 2 | Estimated critical resolved shear stresses for prismatic slip and extension twinning calculated from **Eq. 3**.

Material	*d* (μm)	$CRSS_{prism}$ (MPa)	$CRSS_{twin}$ (MPa)
Pure Mg	103	35.7	19
Mg-1Bi	38	40.5	23.6
Mg-3Bi	21	60.4	32.1
Mg-6Bi	15	77.7	48.1
Mg-9Bi	9	66.2	55.8
Mg-9Bi-2.5Zn	12	54.7	48.6

addition in our cases. It seems that alloying with 9% Bi softens the prismatic slip which is against this hardening law, and further alloying with 2.5% Zn softens both prismatic slip and extension twin.

Due to the consumption of Bi by a large amount of coarse Mg_3Bi_2 particles, we chose six different parts for each sample and carefully examined the Bi concentration that dissolved into the matrix as shown in **Figure 13A**. Zn is found to be ~2.5% in the matrix, which agrees with the ICP measurement. Note that the samples for ICP spectrometry are liquid so the Bi measured covers in both matrix and particles. Here, we focus on analyzing Mg-6Bi, Mg-9Bi, and Mg-9Bi-2.5Zn alloys because their grain sizes can be grouped into the same level. The concentration of Bi in Mg-6Bi matrix was measured the highest as ~4.8 wt% and was 3.5 wt% in Mg-9Bi and 1.84 wt% in Mg-9Bi-2.5Zn, respectively. The variations seem to follow the tendency of CRSS for the prismatic slip. It appears that the prismatic dislocations are more sensitive to Bi in solution than it is to the Mg_3Bi_2 particles. Besides, Stanford and Barnett (Stanford and Barnett, 2013) found the solute softening in binary Mg-Zn alloys because the stress for cross slip into the prismatic plane is lowered with higher solute content. It is believed that this is also a possible explanation for a further drop in the CRSS for prismatic slip in Mg-9Bi-2.5Zn. The coarse and brittle Mg_3Bi_2 particles could not effectively block the slip gliding but deteriorate the mechanical properties, e.g., ductility (**Figure 10A**). Similar findings were also seen in coarse particle-contained alloys (Gutierrez-Urrutia et al., 2005; Polmear et al., 2017a; Huang et al., 2018).

Figure 13B shows changes in the lattice parameter *a* "*a*" of the Mg phase, which can be calculated based on (Suryanarayana and Norton, 1998)

$$\frac{1}{d^2} = \frac{4}{3}\left(\frac{h^2 + hk + k^2}{a^2}\right) + \frac{l^2}{c^2}, \tag{4}$$

where *hkl* is the Miller indices, *a* and *c* are the lattice parameters, and *d* is the plane spacing. A systematic variation can be seen in the lattice parameter "*a*" with a dissolved solute concentration in the matrix in **Figure 13A**. The highest expansion was observed for the highest solution of Bi in the matrix. In contrast, a sharp contraction is observed upon the addition of Zn. These results are directly supportive of EDX measurement and can be understood via size effects. Bi is a slightly bigger atom than Mg. A gradual increase is observed in the lattice of Mg with an increase in Bi concentration. However, in the presence of Zn, a marked decrease in the lattice parameter is observed owing to the smaller atomic size of Zn. Similar behavior was reported in (Kennedy and Raynor, 1959). Therefore, we prefer to conclude that the hardening of the prismatic slip is dominated by solid solution strengthening mechanism and Hall-Petch type hardening. Mg_3Bi_2 particles have little impact on the observed yielding but cause a dramatic loss of ductility by acting as a brittle fracture source.

We turn now to the strengthening effect on twinning. Mg_3Bi_2 particles may provide sites for twin nucleation and possibly increase the twin number density, which is generally true in fine-precipitated magnesium alloys (Stanford and Barnett, 2009; Robson et al., 2010; Robson and Barnett, 2019; Jain et al., 2015). Based on the Orowan hardening law ($\Delta\tau \sim 1/\lambda \log(D_p/r_0)$, where λ is the interparticle spacing on twin plane, D_p is the diameter of particles, and r_0 is the dislocation core radius (Embury et al., 2016), the finer and close-spaced particles always show a good

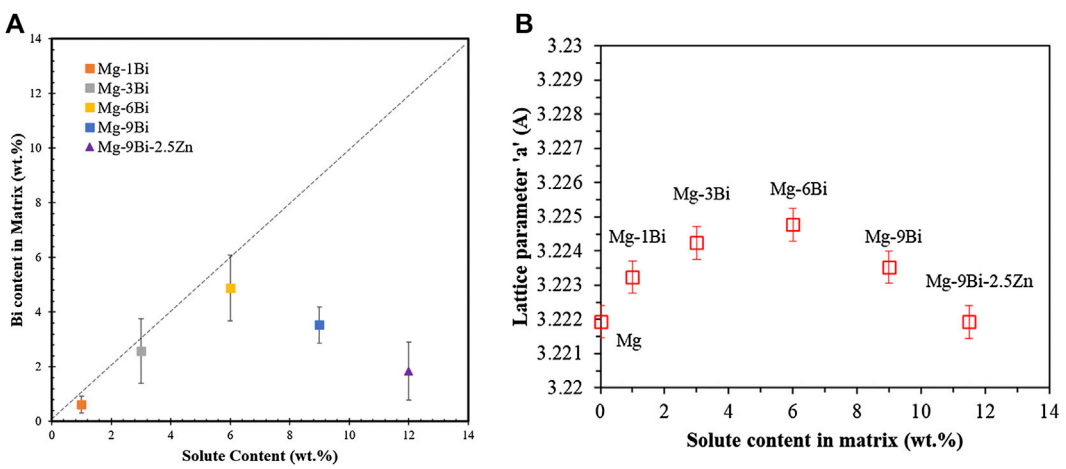

FIGURE 13 | (A) Bi concentration in matrix measured by EDX vs. Bi concentration obtained by ICP. The dashed line shows the idea case that Bi is dissolved thoroughly in the matrix. **(B)** Lattice parameter "*aa*" variation of Mg as a function of solute concentration in the matrix.

hardening against twinning. The overaged magnesium shows reduced hardening stress on twins compared with the peak-aged condition (Jain et al., 2015). As observed in **Figures 4** and **6A**, both the diameter and interparticle spacing are hundreds of times larger than the most effective fine precipitates generated during aging. It is less likely that the twin could be strengthened by the coarse Mg_3Bi_2 particles, at least on yielding. The hardening is more possibly caused by the reduced grain size in more heavily alloyed Mg, as shown in **Table 2**. It is not sure, to what extent, that the residual solute Bi left in the matrix plays a role in the hardening of twinning, which requires further examination.

CONCLUSION

In this study, a systematic investigation of the effect of Mg_3Bi_2 particles on deformation behavior in a series of Mg-Bi binary alloys and Mg-9Bi-2.5Zn was reported. The following are the conclusions drawn from this work:

1. The addition of Bi element to magnesium led to a reduction of grain size in casting. A linear expression of $d = 1194.5\,(1/Q) + 10$ was obtained. The grain refinement efficiency is greater than the addition of Al but less than Zr reported by Lee et al. (Lee et al., 2000).
2. The Mg_3Bi_2 particles could either stimulate or retard the dynamic recrystallization depending on the particle size and area fraction. The PSN DRXed grains show stronger $[10\bar{1}0]$ fiber texture intensity.
3. Coarse Mg_3Bi_2 particles cannot strengthen the prismatic slip nor the extension twin but cause ductility to lose. The tensile yielding dominated by prismatic slip is more sensitive to the Bi solute concentration. The compression yielding stress controlled by extension twin activation is influenced by Hall-Petch type strengthening. Mg_3Bi_2 particles serve as fracture source in the tensile testing.
4. The addition of Zn can refine the Mg-Bi casting microstructure and reduce the size and area fraction of Mg_3Bi_2 particles.

DATA AVAILABILITY STATEMENT

The original contributions presented in the study are included in the article/Supplementary Material; further inquiries can be directed to the corresponding author.

AUTHOR CONTRIBUTIONS

TG designed the experiments and wrote the manuscript. XL performed the experimental work of binary alloys and analyzed data. RK calculated the lattice parameter and revised the manuscript. CZ performed the experimental work of ternary alloy. JW designed the experiments and revised the manuscript. JY performed the XRD measurement. JC revised the manuscript.

FUNDING

The authors are grateful for the financial support from the National Natural Science Foundation of China (NSF) (Grant No. 51901169) and the Special Scientific Research Program of Shaanxi Provincial Department of Education (No. 2019-112-01). The authors would also like to thank the Yinguang Magnesium Industry Group for the provision of materials. Weihai Langu Institute for Material Analysis is also appreciated for providing advanced microscope.

REFERENCES

Ahmad, R., Yin, B., Wu, Z., and Curtin, W. A. (2019). Designing high ductility in magnesium alloys. *Acta Mater.* 172, 161–184. doi:10.1016/j.actamat.2019.04.019

Doherty, R. D., Hughes, D. A., Humphreys, F. J., Jonas, J. J., Jensen, D. J., Kassner, M. E., et al. (1997). Current issues in recrystallization: a review. *Mater. Sci. Eng. A.* 238 (2), 219–274. doi:10.1016/S0921-5093(97)00424-3

Easton, M. A., Qian, M., Prasad, A., and St John, D. H. (2016). Recent advances in grain refinement of light metals and alloys. *Curr. Opin. Solid State Mater. Sci.* 20 (1), 13–24. doi:10.1016/j.cossms.2015.10.001

Embury, J. D., Lloyd, D. J., and Ramachandran, T. R. (2016). "22 - strengthening mechanisms in aluminum alloys," in *Treatise on materials science and Technology*. Editors A. K. Vasudevan and R. D. Doherty Amsterdam, Netherlands: Elsevier, 579–601.

Ghaderi, A., and Barnett, M. R. (2011). Sensitivity of deformation twinning to grain size in titanium and magnesium. *Acta Mater.* 59 (20), 7824–7839. doi:10.1016/j.actamat.2011.09.018

Go, J., Jin, S.-C., Kim, H., Yu, H., and Park, S. H. (2020). Novel Mg–Bi–Al alloy with extraordinary extrudability and high strength. *J. Alloys Compd.* 843, 156026. doi:10.1016/j.jallcom.2020.156026

Go, J., Lee, J. U., Yu, H., and Park, S. H. (2020). Influence of Bi addition on dynamic recrystallization and precipitation behaviors during hot extrusion of pure Mg. *J. Mater. Sci. Technol.* 44, 62–75. doi:10.1016/j.jmst.2019.10.036

Gutierrez-Urrutia, I., Muñoz-Morris, M. A., and Morris, D. G. (2005). The effect of coarse second-phase particles and fine precipitates on microstructure refinement and mechanical properties of severely deformed Al alloy. *Mater. Sci. Eng. A.* 394 (1), 399–410. doi:10.1016/j.msea.2004.11.025

He, C., Liu, C. Q., Chen, H. W., and Nie, J. F. (2020). Enhanced age-hardening response in Mg–Zn–Co alloys with Bi additions. *J. Alloys Compd.* 815, 152419. doi:10.1016/j.jallcom.2019.152419

Huang, K., Marthinsen, K., Zhao, Q., and Logé, R. E. (2018). The double-edge effect of second-phase particles on the recrystallization behaviour and associated mechanical properties of metallic materials. *Prog. Mater. Sci.* 92, 284–359. doi:10.1016/j.pmatsci.2017.10.004

Humphreys, J., Rohrer, G. S., and Rollett, A. (2017). "Chapter 9 - recrystallization of two-phase Alloys," in *Recrystallization and related annealing phenomena*. 3rd Edn (Oxford, United Kingdom: Elsevier), 321–359.

Jain, J., Cizek, P., Poole, W. J., and Barnett, M. R. (2015). The role of back stress caused by precipitates on $\{101^{-}2\}$ twinning in a Mg–6Zn alloy. *Mater. Sci. Eng. A.* 647, 66–73. doi:10.1016/j.msea.2015.08.091

Jayasathyakawin, S., Ravichandran, M., Baskar, N., Anand Chairman, C., and Balasundaram, R. (2020). Mechanical properties and applications of Magnesium alloy – Review. *Mater. Today Proc.* 27, 909–913. doi:10.1016/j.matpr.2020.01.255

Joshi, U., and Hari Babu, N. (2017). The grain refinement potency of bismuth in magnesium. *J. Alloys Compd.* 695, 971–975. doi:10.1016/j.jallcom.2016.10.215

Kennedy, A. J., and Raynor, G. V. (1959). *The physical metallurgy of magnesium and its alloys*. London, United Kingdom: Pergamon Press, 531.

Lee, Y. C., Dahle, A. K., and Stjohn, D. H. (2000). The role of solute in grain refinement of magnesium. *Metall. Mater. Trans.* 31 (11), 2895–2906. doi:10.1007/BF02830349

Meng, S. J., Yu, H., Fan, S. D., Kim, Y. M., Park, S. H., Zhao, W. M., et al. (2020). A high-ductility extruded Mg-Bi-Ca alloy. *Mater. Lett.* 261, 127066. doi:10.1016/j.matlet.2019.127066

Meng, S., Yu, H., Zhang, H., Cui, H., Park, S. H., Zhao, W., et al. (2017). Microstructure and mechanical properties of an extruded Mg-8Bi-1Al-1Zn (wt%) alloy. *Mater. Sci. Eng. A*. 690, 80–87. doi:10.1016/j.msea.2017.02.095

Polmear, I., StJohn, D., Nie, J.-F., and Qian, M. (2017a). "2 - physical metallurgy of aluminium alloys," in *Light alloys*. 5th Edn (Boston, MA: Butterworth-Heinemann), 31–107.

Polmear, I., StJohn, D., Nie, J.-F., and Qian, M. (2017b). "3 - casting of light alloys," in *Light alloys*. 5th Edn (Boston: Butterworth-Heinemann), 109–156.

Polmear, I., StJohn, D., Nie, J.-F., and Qian, M. (2017c). "6 - magnesium alloys," in *Light alloys*. 5th Edn (Boston, MA: Butterworth-Heinemann), 287–367.

Prasad, A., Yuan, L., Lee, P. D., and StJohn, D. H. (2013). The Interdependence model of grain nucleation: a numerical analysis of the Nucleation-Free Zone. *Acta Mater.* 61 (16), 5914–5927. doi:10.1016/j.actamat.2013.06.015

Robson, J. D., and Barnett, M. R. (2019). The effect of precipitates on twinning in magnesium alloys. *Light Mater. Sci. Tech.* 21, 1800460. doi:10.1002/adem.201800460

Robson, J. D., Henry, D. T., and Davis, B. (2009). Particle effects on recrystallization in magnesium–manganese alloys: particle-stimulated nucleation. *Acta Mater.* 57 (9), 2739–2747. doi:10.1016/j.actamat.2009.02.032

Robson, J. D., Stanford, N., and Barnett, M. R. (2010). Effect of particles in promoting twin nucleation in a Mg–5wt.% Zn alloy. *Scripta Mater.* 63 (8), 823–826. doi:10.1016/j.scriptamat.2010.06.026

Sasaki, T. T., Ohkubo, T., and Hono, K. (2009). Precipitation hardenable Mg–Bi–Zn alloys with prismatic plate precipitates. *Scripta Mater.* 61 (1), 72–75. doi:10.1016/j.scriptamat.2009.03.015

Schneider, C. A., Rasband, W. S., and Eliceiri, K. W. (2012). NIH Image to ImageJ: 25 years of image analysis. *Nat. Meth.* 9 (7), 671–675. doi:10.1038/nmeth.2089

Stanford, N., and Barnett, M. R. (2009). Effect of particles on the formation of deformation twins in a magnesium-based alloy. *Mater. Sci. Eng A*. 516 (1), 226–234. doi:10.1016/j.msea.2009.04.001

Stanford, N., and Barnett, M. R. (2013). Solute strengthening of prismatic slip, basal slip and {101¯2} twinning in Mg and Mg–Zn binary alloys. *Int. J. Plast.* 47, 165–181. doi:10.1016/j.ijplas.2013.01.012

StJohn, D. H., Easton, M. A., Qian, M., and Taylor, J. A. (2013). Grain refinement of magnesium alloys: a review of recent research, theoretical developments, and their application. *Metall. Mater. Trans.* 44 (7), 2935–2949. doi:10.1007/s11661-012-1513-x

StJohn, D. H., Prasad, A., Easton, M. A., and Qian, M. (2015). The contribution of constitutional supercooling to nucleation and grain formation. *Metall. Mater. Trans.* 46 (11), 4868–4885. doi:10.1007/s11661-015-2960-y

Sun, Y. H., and Sun, B. Z. (2018). Investigation of structure, morphology and orientation of precipitates in Mg−Bi alloy. *Mater. Char.* 140, 129–133. doi:10.1016/j.matchar.2018.03.042

Suryanarayana, C., and Norton, M. G. (1998). "Crystal structure determination. II: hexagonal structures," in *X-ray diffraction: a practical approach*. (Boston, MA: Springer US), 125–152.

Watanabe, C., Monzen, R., and Tazaki, K. (2008). Effects of Al3Sc particle size and precipitate-free zones on fatigue behavior and dislocation structure of an aged Al–Mg–Sc alloy. *Int. J. Fatig.* 30 (4), 635–641 doi:10.1016/j.ijfatigue.2007.05.010

Yu, H., Fan, S., Meng, S., Choi, J. O., Li, Z., Go, Y., et al. (2020). Microstructural evolution and mechanical properties of binary Mg–xBi (x = 2, 5, and 8 wt%) alloys. *J. Magnesium Alloys* doi:10.1016/j.jma.2020.03.015

Zindal, A., Jain, J., Prasad, R., Singh, S. S., Sarvesha, R., Cizek, P., et al. (2018). Effect of heat treatment variables on the formation of precipitate free zones (PFZs) in Mg-8Al-0.5Zn alloy. *Mater. Char.* 136, 175–182. doi:10.1016/j.matchar.2017.12.018

Conflict of Interest: The authors declare that the research was conducted in the absence of any commercial or financial relationships that could be construed as a potential conflict of interest.

frontiers in Materials

ORIGINAL RESEARCH
published: 24 February 2021
doi: 10.3389/fmats.2020.620500

Research of Microstructure, Friction and Wear on Siliconized Aluminum-Bronze With Different Silicon Powder Ratio

Feng Tian, Chunyan Wu, Bin Zhu, Liang Wang, Yong Liu and Yisheng Zhang*

State Key Laboratory of Material Processing and Die & Mould Technology, School of Materials Science and Engineering, Huazhong University of Science and Technology, Wuhan, China

In order to enhance the wear resistance without changing the mechanical properties of the substrate, the aluminum-bronze alloy was siliconized by pack cementation in this paper. Its surface hardness was improved by a certain thickness of siliconized layer. The different processes and their influences on the siliconized layer and the substrate were investigated by changing the ratio of siliconizing powder. The microstructure and phase composition of the siliconized layer was detected and analyzed. Compared with the non-siliconized sample, the hardness of the siliconized layer of 30% Si content is increased by 93.54%, and the average friction coefficient is reduced to 40.38%. The maximum thickness of siliconized layer in the experiment is 200 μm when the silicon powder content is 30%. It can be concluded that surface siliconizing is effective to reduce the friction coefficient of aluminum-bronze and improve wear resistance.

Keywords: aluminum-bronze alloy, pack cementation, siliconized layer, lubrication friction coefficient, wear resistance

OPEN ACCESS

Edited by:
Hua Ding,
Northeastern University, China

Reviewed by:
Bingtao Tang,
Qilu University of Technology, China
Xiaohui Cui,
Central South University, China

****Correspondence:***
Liang Wang
wangliang@hust.edu.cn

Specialty section:
This article was submitted to Structural Materials, a section of the journal Frontiers in Materials

Received: *23 October 2020*
Accepted: *07 December 2020*
Published: *24 February 2021*

Citation:
Tian F, Wu C, Zhu B, Wang L, Liu Y and Zhang Y (2021) Research of Microstructure, Friction and Wear on Siliconized Aluminum-Bronze With Different Silicon Powder Ratio. Front. Mater. 7:620500. doi: 10.3389/fmats.2020.620500

INTRODUCTION

Compared with simple aluminum-bronze, complex aluminum-bronze has better wear resistance. It is mostly used to make frictional parts in the mechanical transmission system, such as screw and nut (Wharton et al., 2005; Equey et al., 2011; Wu et al., 2015). When used as a friction pair with harder parts, complex aluminum-bronze is easy to wear out by producing a lot of wear debris (Zhou et al., 2015) which affects the service life of the parts.

The wear resistance of copper alloys can be improved through adding alloying elements (Buchely et al., 2005), suitable heat treatment processes and the surface coating technology (Yang et al., 2005). There is evidence to suggest that the friction and wear properties of copper alloys are mainly determined by the plastic deformation and cracks of the surface layer (Mohseni et al., 2015; Rigney and Glaeser, 1978; Hirth and Rigney, 1976). Compared with heat treatment technology, the surface coating technology can improve the surface hardness and wear resistance without changing the performance of the aluminum bronze alloy. Among surface coating technologies, electroplating technology has a large environmental pollution, and laser cladding technology is costly. Chemical heat treatment uses chemical reaction and physical adsorption to deposit the infiltrated elements on the surface of the substrate, and gradually diffuse to the substrate with the extension of heating and holding time, and finally form a certain thickness of infiltration layer. The infiltration layer obtained by the chemical heat treatment has continuous structure, which belongs to metallurgical bonding, high bonding strength, and not easy to exfoliate (Qiao and Zhou, 2012;

TABLE 1 | The chemical composition of QAl10-5-5 aluminum bronze (wt.%).

Cu	Al	Ni	Fe	Mn	Zn	Si	Sn	Pb	Mg
Bal	8.0~11.0	4.0~6.0	4.0~6.0	0.5~2.5	0.5	0.25	0.2	0.05	0.1

Aragoudakisa et al., 2003; Koo and Yu, 2000). Therefore, the method of chemical heat treatment of pack cementation is used in this study to reduce the cost while effectively improving the surface properties. To achieve the chemical heat treatment for the metal surface, the atoms that need to be infiltrated are first deposited on the metal surface, and infiltrated into metal surface from penetrant through chemical reaction. When the surface atoms reach a certain concentration, they begin to infiltrate and diffuse into the metal substrate. The speed of chemical reaction and the diffusion rate of atoms in the metal substrate are mainly affected by the concentration of atoms and the heat treatment process. Parlikar et al. (Parlikar et al., 2013) obtained the Al_3Ti layer by pack cementation aluminizing with nearly α-Ti29A alloy and explored its effect on alloy tensile properties. In a major advance in 1983, Frank et al. (Frank and Falconer, 1983) revealed that Si and Cu form ordered compounds Cu_3Si and Solid solution alloy $Cu_{0.95}Si_{0.05}$ when Si atoms penetrate and diffuse into the copper alloy matrix. Wang et al. (Wang et al., 2009) achieved pack siliconizing on the surface of pure copper with nickel plating, and the siliconized layer improved the surface hardness and wear resistance of pure copper. The average micro hardness value of the surface reached HV760, and the friction coefficient was about 0.3.

In this paper, the Si content with different ratio were prepared for pack cementation. Si atoms are adsorbed on the surface of the aluminum bronze substrate and diffuse to form a silicon infiltration layer, which aims to improve the wear resistance of aluminum bronze's layer, reduce the amount of wear, and extend the life of the aluminum bronze friction pair. This article deals with the quality evaluation of some layers prepared in different Si content in terms of layer thickness, number of holes, hardness. Besides, the microstructure of siliconized aluminum bronze is analyzed. The wear resistance of the siliconized layer was investigated with hardness and friction coefficient.

EXPERIMENT

Pack Siliconizing

The aluminum bronze (QAl10-5-5) samples were taken from a nut in a mechanical servo press. Its chemical composition is shown in **Table 1**. The size of aluminum bronze sample is shown in **Figure 1A**. The samples were taken as the lower friction pair for the friction and wear test after pack siliconizing. Before siliconizing, the samples are mechanically polished and then removes surface stains in absolute ethanol using ultrasonic.

In this experiment, the penetrant is composed of three parts: the main penetrant, accelerator and filler. The main penetrant is Si powder with a purity of 99.99%. Its particle size is 40–200 mesh. NaF and NH_4Cl were used as accelerator to react with Si powder producing $SiCl_2$ and SiF_2 and the resulting compound replaces Cu with active Si atoms to penetrate into copper alloy substrate and form intermetallic compounds [16]. The role of SiC as a filler is to prevent powder sintering from affecting the reaction of active Si atoms.

The process of siliconizing test is shown in **Figure 1B**. Fill the prepared and mixed penetrant powder into a container with preloading samples and compact it. Ensure that the thickness of the powder on the top of the sample is more than 30 mm. Then seal the container with refractory mud, and keep the container without any gas leaking. Finally, put the container into a rapid heating box-type electric furnace for heat treatment. The heating rate was 3°C/s and the holding time was 12 h. Cool down the container within the furnace. The parameters of the test are shown in **Table 2**. The content of Si and SiC are mainly changed in the experiment. When the content of Si powder increases, the content of filler SiC decreases accordingly. The content of osmotic agent NH_4Cl and NaF each contains 3%.

Test for Wear Resistance and Hardness

In the friction test, the lower friction pair was siliconized aluminum bronze plates and non-siliconized aluminum bronze plates. The upper friction pair was used 38GrMoAl

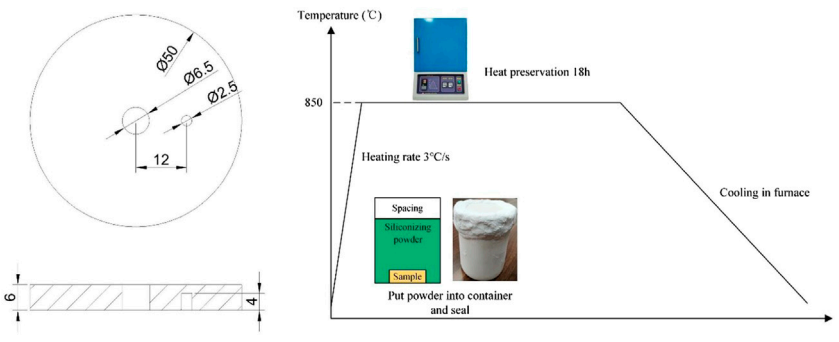

FIGURE 1 | (A) The size of aluminum bronze sample and **(B)** The process of pack siliconizing.

TABLE 2 | Process parameters of test.

No.	Si (wt.%)	NaF (wt.%)	NH_4Cl (wt.%)	SiC (wt.%)	Heating temperature (°C)	Holding time (h)
1	10%	3%	3%	84%	850	12
2	30%	3%	3%	64%	850	12
3	50%	3%	3%	44%	850	12
4	70%	3%	3%	24%	850	12

TABLE 3 | The parameters of friction and wear test.

Load (N)	Contact pressure (MPa)	Rotating speed (r/min)	Friction time (min)	Center distance (mm)
600	≥19.24	150	·90	16

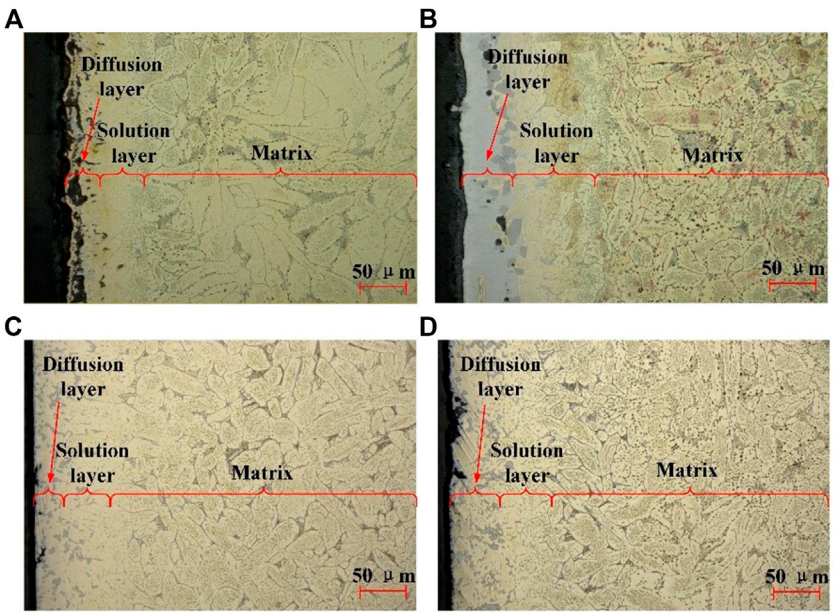

FIGURE 2 | Microstructure of the siliconized layer under the condition of different Si powder ratio. **(A)** 10%; **(B)** 30%; **(C)** 50%; **(D)** 70%.

high-grade nitride steel pin, which has high wear resistance, high fatigue strength and high strength, with a diameter of 6.3 mm and a length of 22 mm. The actual contact pressure between the actual force transmitting screw and nut in the mechanical servo press was 15 MPa~20 MPa, so the load applied to the pin should be in the range of 467.6N~623.4N. Friction and wear test parameters were shown in **Table 3**. Before the test, the lower friction pair was soaked in lubricating oil for 1 min to cover the surface of the sample with an oil film, and no lubricating oil was added during the test. Different lower friction pairs were tested three times and the average value was taken.

The Vickers hardness was measured using an applied load of 500 g for 15 s. At least three tests were carried out at different positions of the specimen, and the average value of hardness was obtained.

RESULTS AND DISCUSSION

Microstructure of Siliconized Aluminum Bronze under Various Si Content

Four penetrants with different ratios of Si content of 10%, 30%, 50% and 70% were applied to carry out the siliconizing. The microstructures of siliconized layer by different Si content were presented in **Figure 2**. The siliconized layer is discontinuous and contains many voids and holes when the Si content is 10% (**Figure 2A**). The maximum depth of the holes is 70 μm and the total thickness of the siliconized layer is about 100 μm. In **Figure 2B**, the diffusion layer and the solid solution layer can be distinguished. The layer is continuous and relatively smooth, but there are still holes in the siliconized layer. The maximum depth of the holes is 50 μm and the thickness of the diffusion layer and the solid

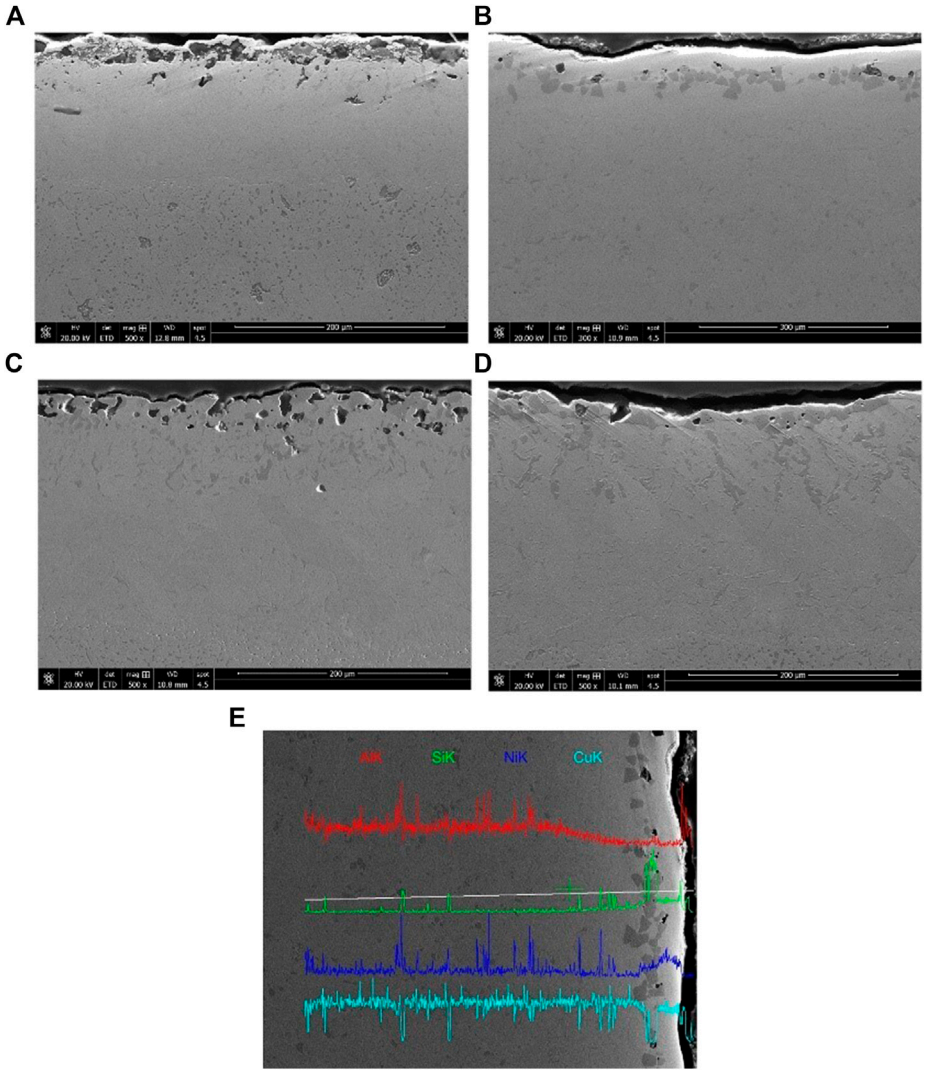

FIGURE 3 | Surfaces of the siliconized layer under the condition of different Si powder ratio. **(A)** 10%; **(B)** 30%; **(C)** 50%; **(D)** 70%; **(E)** EDS mapping of 30% Si content.

solution layer is about 200 μm. As shown in **Figures 2C,D**, the phase in the diffusion layer have uneven distribution. When the Si content is 50% and 70%, the siliconized layer is about 140 μm, 130 μm, respectively. Significantly reduction of holes is observed in **Figures 2C,D** compared with **Figure 2A**.

The SEM images of the siliconized layer under different penetrants are shown in **Figure 3**. The upper layer is the siliconized layer and the lower layer is the copper alloy substrate. When the Si content is 30%, 50%, 70%, the block structure appears in the siliconized layer. No clear block structure is found in the siliconized layer of 10% Si content of 10% (**Figure 3A**). There are two kinds of large blocks with different colors in **Figure 3B**. In the siliconized layers of 50% and 70% Si content (**Figures 3C,D**), the blocks are smaller than **Figure 3B** and distributed more scattered. It can be seen from **Figure 3E** that the Si content is the highest in the diffusion layer of the infiltration layer.

The Wear Resistance of the Siliconized Aluminum Bronze Layer

The Hardness of Siliconized Aluminum Bronze Layer

A Vickers hardness was used to measure the macroscopic hardness of the siliconized aluminum bronze and the non-siliconized aluminum bronze sample. The surface hardness is shown in **Figure 4A** by comparing the siliconized sample of 30% Si content and the non-siliconized aluminum bronze sample. The average Vickers hardness of the non-siliconized sample is 271HV1 and the siliconized sample is 525HV1. Compared with the non-siliconized sample, the hardness of the siliconized layer with the Si content of 30% is increased by 93.54%.

The Average Friction Coefficient of Siliconized Aluminum Bronze Layer

Lubricant failure may occur in the lubrication friction test. After the lubricating oil fails in the lubrication friction test, the friction gradually changes from the lubrication to the dry friction, and the

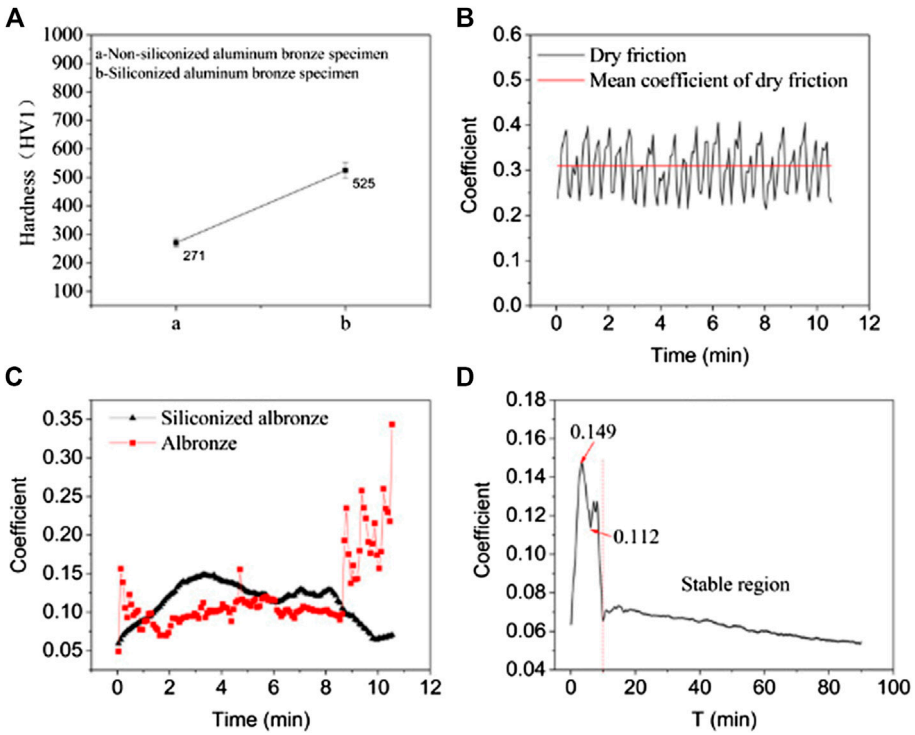

FIGURE 4 | (A) A Vickers hardness of the siliconized aluminum bronze and the non-siliconized aluminum bronze sample (30% Si content). **(B)** The dry friction test of the non-siliconized sample. **(C)** The Lubrication friction of the siliconized aluminum bronze and the non-siliconized aluminum. **(D)** The lubrication friction coefficient of the siliconized sample in 90 min.

friction coefficient changes drastically. The dry friction test is carried out on the non-siliconized sample firstly, and the dry friction coefficient is obtained, as shown in **Figure 4B**. The dry friction coefficient fluctuates in the range of 0.214~0.427, the fluctuation range is 0.213, and the average friction coefficient is 0.310.

The lubrication friction coefficient of the samples in the siliconized layer of 30% Si content and non-siliconized aluminum bronze is depicted in **Figure 4C**. It can be seen that the lubrication friction coefficient of the non-siliconized sample began to rise sharply after 8.79 min. At 12 min, the lubrication friction coefficient is 0.343, which exceeds the average value of the dry friction coefficient. The lubrication friction coefficient of siliconized aluminum bronze did not show lubrication failure within the first 11 min. Although the lubrication friction coefficient curve is not flat enough, the friction coefficient fluctuates more smoothly than the non-siliconized sample.

To understand the influence of the siliconized layer on the lubrication friction coefficient, the lubrication friction coefficient of the siliconized sample is observed for a longer time. The result, as shown in **Figures 4D**, is that the friction coefficient fluctuates greatly in the first 10 min, and the fluctuation range is between 0.112~0.149. After 10 min, the friction lubrication coefficient decreased to the stable region, and the average lubrication friction coefficient in the stable area is 0.063. The curve was shown a stable downward trend from 10 min to 90 min, and the fluctuation range is 0.020. The results have shown that the oil film on the surface of siliconized aluminized bronze remained undamaged within 90 min, and the two surfaces have not reached stage of the boundary lubrication. The samples after the 90 min friction test were shown in **Figures 5A,B**. It can be found that the wear marks on the surface of the non-siliconized sample were deep, and those on the surface of the siliconized sample were shallow. In **Figure 5C**, the wear rate of the non-siliconized sample is 0.085% under dry lubrication. Under lubricating conditions, the wear rate of the non-siliconized sample is 0.035% and the siliconized sample of 30% Si content is 0.012%. In **Figure 5D**, the wide of wear track is about 20 μm. There are a large number of small debris and a small part of large debris on the friction surface and the inside of the groove. The smallest particle diameter is less than 1 μm, and the large particle diameter is about 10 μm. And the wear debris is generally granular and cannot form a large adhesion layer like the wear debris of the non-siliconized sample.

CONCLUSION

1) When content of Si powder is small, the proportion of filler increases which cause the activity of Si atoms to penetrate into the aluminum bronze surface to decrease. Therefore, the infiltration layer is too thin in low Si powder content. On the other hand, Si powder is sintered due to too little filler which also reduce the generation of active Si atoms when the

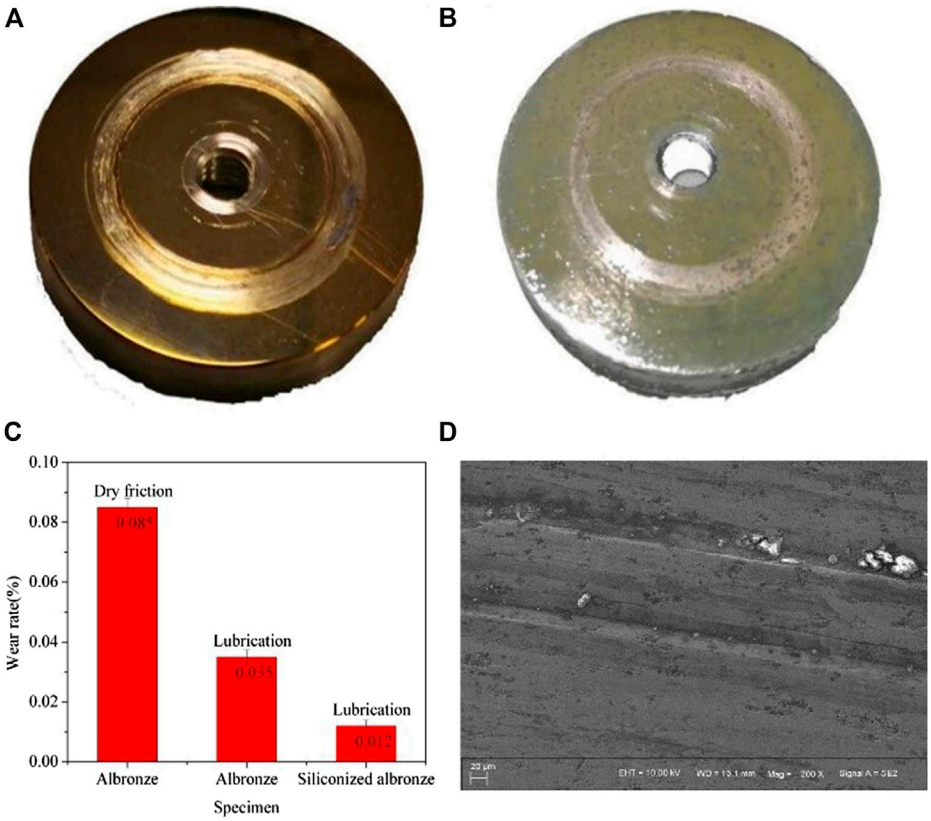

FIGURE 5 | The scratch on the surface of friction specimen: **(A)** non-siliconized sample; **(B)** siliconized sample aluminum bronze sample; **(C)** wear rate; **(D)** the SEM of the wear track.

content of Si powder is high. The appropriate ratio of Si powder and filler is beneficial to obtain a thicker infiltrated layer. Therefore, when the siliconizing powder is composed by 30% Si + 3% NaF +3% NH4Cl + 64% SiC, the heating temperature is 850°C, and the holding time is 18 h, a certain thickness of high-quality siliconized layer will be obtained and the substrate will not be affected.

2) The average Vickers hardness of the non-siliconized sample is 271HV1 and the siliconized sample is 524.5HV1. It can be concluded that the siliconized layer increases 93.54% of the hardness of the aluminum bronze alloy surface.
3) The average friction coefficient of the siliconized sample is reduced to 40.38% of that of the non-siliconized sample. In the 90 min friction test, the lubricating oil film did not break and fail and the coefficient of friction was extremely stable. The result proves that the siliconized layer can reduce the friction coefficient and improve wear resistance.
4) The surface of aluminum bronze forms a large adhesion layer after plastic deformation during friction and shows the characteristics of viscous wear. When the surface of aluminum bronze is siliconized, the plastic deformation area of the micro-protrusions becomes smaller, and the macroscopic performance is that the hardness of the siliconized surface increases. Therefore, wear debris is reduced during the friction process and wear resistance is improved.

DATA AVAILABILITY STATEMENT

The original contributions presented in the study are included in the article/Supplementary Material, further inquiries can be directed to the corresponding author.

AUTHOR CONTRIBUTIONS

The corresponding author is responsible for ensuring that the descriptions are accurate. FT: writing original draft and data processing. CW: implementation of the experiments. BZ: modifying and editing. LW: suggestion and resource. YL: experiment design. YZ: supply of aluminum bronze alloy and suggestions for the purpose of this article.

FUNDING

This research work was financially supported by the National Major Science and Technology Project of China (Grant No. 2018ZX04023001).

REFERENCES

Aragoudakisa, N. M., Stergioudisb, G., Haidara, O., and Tsipas, D. N. (2003). A comparative study of boride coatings obtained by pack cementation method and by fluidized bed technology. *Mater. Lett.* 57, 2399–2403. doi:10.1016/S0167-577X(02)01243-0

Buchely, M. F., Gutierrez, J. C., León, L. M., and Toro, A. (2005). The effect of microstructure on abrasive wear of hard facing alloys. *Wear* 259, 52–61. doi:10.1016/j.wear.2005.03.002

Equey, S., Houriet, A., and Mischler, S. (2011). Wear and frictional mechanisms of copper-based bearing alloys. *Wear* 273, 9–16. doi:10.1016/j.wear.2011.03.030

Frank, T. C., and Falconer, J. L. (1983). Surface compositions of copper-silicon alloys. *Appl. Surf. Sci.* 14, 359–374. doi:10.1016/0378-5963(83)90049-1

Hirth, J. P., and Rigney, D. A. (1976). Crystal plasticity and the delamination theory of wear. *Wear* 39, 133–141. doi:10.1016/0043-1648(76)90229-5

Koo, C. H., and Yu, T. H. (2000). Pack cementation coatings on Ti3Al-Nb alloys to modify the high-temperature oxidation properties. *Surf. Coat. Tech.* 126, 171–180. doi:10.1016/S0257-8972(00)00546-6

Mohseni, H., Mensah, B. A., Gupta, N., Srinivasan, S. G., and Scharf, T. W. (2015). Exceptional friction mitigation via subsurface plastic shear in defective nanocrystalline ceramics. *Mater. Res. Lett.* 3, 23–29. doi:10.1080/21663831.2014.935968

Parlikar, C., Alam, M. Z., Sarkar, R., and Das, D. K. (2013). Effect of oxidation resistant Al3Ti coating on tensile properties of a near α-Ti alloy. *Surf. Coat. Tech.* 236, 107–117. doi:10.1016/j.surfcoat.2013.09.036

Qiao, M., and Zhou, C. (2012). Codeposition of Co and Al on nickel base superalloys by pack cementation process. *Surf. Coat. Tech.* 206, 2899–2904. doi:10.1016/j.surfcoat.-2011.12.01910.1016/j.surfcoat.2011.12.019

Rigney, D. A., and Glaeser, W. A. (1978). The significance of near surface microstructure in the wear process. *Wear* 46, 241–250. doi:10.1016/0043-1648(78)90125-4

Wang, H., Chu, C., Sheng, X., Lin, P., and Dong, Y. (2009). Siliconizing formation mechanism and its property by slurry pack cementation on electro-deposited nickel layer into copper matrix. *J. Wuhan Univ. Technol.* 24, 883–887. doi:10.1007/s11595-009-6883-6

Wharton, J. A., Barik, R. C., Kear, G., Wood, R. J. K., Stokes, K. R., and Walsh, F. C. (2005). The corrosion of nickel-aluminium bronze in seawater. *Corros. Sci.* 47, 3336–3367. doi:10.1016/j.corsci.2005.05.053

Wu, Z., Cheng, Y. F., Liu, L., Lv, W., and Hu, W. (2015). Effect of heat treatment on microstructure evolution and erosion-corrosion behavior of a nickel-aluminum bronze alloy in chloride solution. *Corros. Sci.* 98, 260–270. doi:10.1016-/j.corsci.2015.05.03710.1016/j.corsci.2015.05.037

Yang, G.-r., Hao, Y., Song, W.-m., and Ma, Y. (2005). An investigation of the structure and properties of infiltrated layer on the surface of copper alloy. *Mater. Sci. Eng. A.* 399, 206–215. doi:10.1016/j.msea.2005.03.106

Zhou, K.-C., Xiao, J.-K., Zhang, L., Xie, X.-L., and Li, Z.-Y. (2015). Tribological behaviour of brass fiber brush against copper, brass, coin-silver and steel. *Wear* 326-327, 48–57. doi:10.1016/j.wear.2014.12.024

Conflict of Interest: The authors declare that the research was conducted in the absence of any commercial or financial relationships that could be construed as a potential conflict of interest.

frontiers in Materials

ORIGINAL RESEARCH
published: 25 February 2021
doi: 10.3389/fmats.2020.619315

Multilayer Maraging/CoCrNi Composites With Synergistic Strengthening-Toughening Behavior

C. X. Chen[1,2,3], *Y. F. Ge*[1,2,3], *W. Fang*[1,2,3]*, *X. Zhang*[1,2,3], *B. X. Liu*[1,2,3]*, *J. H. Feng*[1,2,3] and *F. X. Yin*[1,2,3]

[1]*Research Institute for Energy Equipment Materials, Hebei University of Technology, TianJin, China,* [2]*TianJin key laboratory of Materials laminating Fabrication and Interfacial Controlling Technology, Hebei University of Technology, TianJin, China,* [3]*School of Materials Science and Engineering, Hebei University of Technology, TianJin, China*

A novel multilayer maraging/CoCrNi composite with good mechanical properties was successfully fabricated by a vacuum hot-rolling and aging treatment. The yield strength, tensile strength, uniform elongation, and fracture elongation reached 1,151, 1,380 MPa, 15.7, and 24% respectively, realizing the aim of synergistic strengthening–toughening by effectively improving the yield strength of the CoCrNi alloy and strain-hardening capacity of the maraging steel. The vacuum state, high rolling reduction ratio, and alloy element diffusion are beneficial in strengthening the clad interface. The good work-hardening capacity of the CoCrNi alloy compensates for the poor strain-softening behavior of the maraging steel, effectively delaying the premature localized necking of the multilayer composites. The strengthening–toughening mechanism of the multilayer maraging/CoCrNi composites is mainly attributed to the strong interface, nanoscale precipitation, and strain-induced twinning.

Keywords: multilayer composites, CoCrNi alloy, work hardening capacity, vacuum hot rolling, synergistic deformation capacity

OPEN ACCESS

Edited by:
Minghui Cai,
Northeastern University, China

Reviewed by:
Gm Xie,
Northeastern University, China
Xiping Cui,
Harbin Institute of Technology, China

***Correspondence:**
W. Fang
fangwei@hebut.edu.cn
B. X. Liu
liubaoxi@hebut.edu.cn

Specialty section:
This article was submitted to Structural Materials, a section of the journal Frontiers in Materials

Received: *20 October 2020*
Accepted: *04 November 2020*
Published: *25 February 2021*

Citation:
Chen CX, Ge YF, Fang W, Zhang X, Liu BX, Feng J H and Yin FX (2021) Multilayer Maraging/CoCrNi Composites With Synergistic Strengthening-Toughening Behavior. Front. Mater. 7:619315. doi: 10.3389/fmats.2020.619315

INTRODUCTION

High-strength metals always display low ductility, toughness, and strain-hardening capacity, while ductile metals exhibit low yield strength and tensile strength, which seriously limits their practical applications (Lesuer et al., 1996; Yin et al., 2013; Jing et al., 2014; Zhang et al., 2014; Seok et al., 2016; Liu et al., 2019). Recently, multilayer metals containing different constituent metallic layers were reported to show outstanding comprehensive mechanical properties (Inoue et al., 2008; Ojima et al., 2012; Kang et al., 2016; Ding et al. 2018; Yu et al., 2018; Chang et al., 2019; Ding et al., 2021). For example, a novel multilayer twinning-induced plasticity (TWIP)/maraging steel with a tensile strength of 1,527 MPa and a fracture elongation of 21.5% was successfully fabricated by Yu et al. (2018). However, the TWIP layer could not compensate for the poor strain-softening behavior of the maraging steel layer, which leads readily to negative strain hardening of the multilayer steel. In the present study, a novel CoCrNi alloy with superior strain-hardening capacity was chosen to replace the TWIP steel layer, giving the CoCrNi alloy an excellent combination of tensile strength and ductility (Slone et al., 2018). Moreover, different from high manganese steel with a martensitic transformation, the CoCrNi alloy maintains the original face-centered cubic structure by forming twins (Grassel et al., 2000; Gutierrezurrutia and Raabe, 2011; Wu et al., 2014; Miao et al., 2017; Slone et al., 2018; Slone et al., 2019). We demonstrate a novel approach

TABLE 1 | The chemical composition of C300 maraging steel and CoCrNi medium-entropy alloy (wt%).

Element	Mn	Si	Al	C	Ni	Co	Mo	Ti	Fe	Cr
C300	≤0.1	≤0.1	0.1	≤0.03	18.0	9.0	5.0	0.7	67.2	—
CoCrNi	—	—	—	—	34.61	34.74	—	—	—	30.65

to overcoming the strengthening–toughening limit and delaying localized necking, which can provide a means of researching multilayer metal matrix composites.

MATERIALS AND METHODS

Two very different kinds of metals were used as the raw materials in this study. One is maraging steel (C300), which has superior yield strength and poor strain-softening behavior, while the other is a CoCrNi alloy, which has excellent fracture elongation and a low yield strength. The chemical compositions of the C300 maraging steel and the CoCrNi alloy are listed in **Table 1**. The C300 maraging steel and CoCrNi high-entropy alloy(HEA) were cut into thin plates with a thickness of 0.5 mm and a diameter of 48 mm by wire cutting. Then, the plates were alternately stacked to give a total of 60 layers, and the stacked plates were sealed into a carbon steel box under vacuum of 10^{-2} Pa. Subsequently, the box was heated at 1,200°C for 30 min, and then hot rolled to a final thickness of 4 mm (**Figure 1C**). After rolling, some specimens were cut from the hot-rolling multilayer maraging/CoCrNi composite and finally heated at 485°C for 4 h.

The microstructure and distribution of the alloying elements were examined by optical microscopy (OM), electron back-scattering diffraction (EBSD), scanning electron microscopy, electron probe microanalysis (EPMA), and transmission electron microscopy. The dog-bone tensile samples with a gauge length of 18 mm and a width of 3 mm were tested using an AGS 50 KN universal testing machine. The strain distribution and evolution were tested and recorded using a digital image correlation (DIC) method equipped with a contactless full-field strain-measuring system.

RESULTS AND DISCUSSION

The EBSD microstructures of the individual CoCrNi alloy and C300 maraging steel are shown in **Figures 1A,B**. Obviously, the CoCrNi alloy has rather coarse as-cast columnar grains with an average size of 500 μm, and the C300 maraging steel has a coarse lath-like martensite microstructure. The OM microstructures of the hot-rolled and aged samples are shown in **Figures 1D,E**. The straight clad interfaces and uniform layer with a thickness of approximately 65 μm can be clearly seen, which indicates that the two constituent alloys have superior deformation coordination capacity during the hot-rolling process.

Figure 2 shows the EBSD microstructure and EPMA mapping of the multilayer maraging/CoCrNi composites. After hot rolling, the grains of the individual layers were obviously refined compared with the original grains, and the average grain size of the CoCrNi layer and lath spacing of the C300 layers are about 5 and 3 μm, respectively. In addition, the grain orientations in the CoCrNi layers are relatively random, while the maraging layer shows an obvious <110>//RD texture. **Figures 2A–C** shows that many ultrafine grains appear along the clad interface, which is due to a high rolling reduction ratio and sufficient alloying element diffusion. This can also lead to the formation of a transition layer with a thickness of 3 μm. Additionally, **Figure 2D** shows that nanoscale rod-like precipitates with a length of 20 nm and width of 5 nm appear in the C300 layer after the aging treatment. Specifically, the precipitates are identified as the η-Ni_3Ti phase, as shown by the electron diffraction pattern in **Figure 2E**. This phase can effectively strengthen the C300 layers. Also, many microscale Al_2O_3 phases appear at the transition layer owing to the high Al content and surface oxidation in the C300 layer. Deformation twins are also generated in the CoCrNi layer, which is similar to the TWIP effect during the hot-rolling process (He et al., 2020). According to EPMA mapping scanning analysis, as shown in **Figure 2I–L**, many fine Al_2O_3 and TiN particles are located at the transition interface. Herein, the formation of Al_2O_3 and TiN is attributed to the selection of oxidation and nitridation at the surface of the C300 maraging steel layer. That is to say, a high vacuum of 10^{-2} Pa still cannot prevent the oxidation and nitridation of Al and Ti because of their strong chemical activity.

Figure 3 shows the tensile behavior and DIC whole-field strain distribution of the individual materials and multilayer C300/

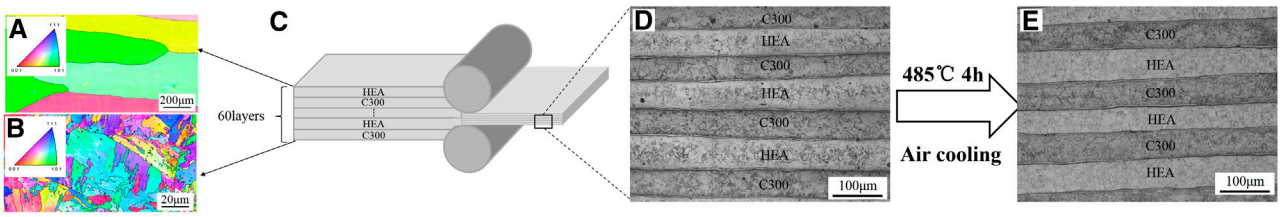

FIGURE 1 | (A,B) Inverse pole figure the IPF mapping of original the original CoCrNi alloy and C300. **(C)** a schematic diagram of the hot-rolling process, **(D,E)** the optical microstructures of the hot-rolled and aged multilayer maraging/CoCrNi composite.

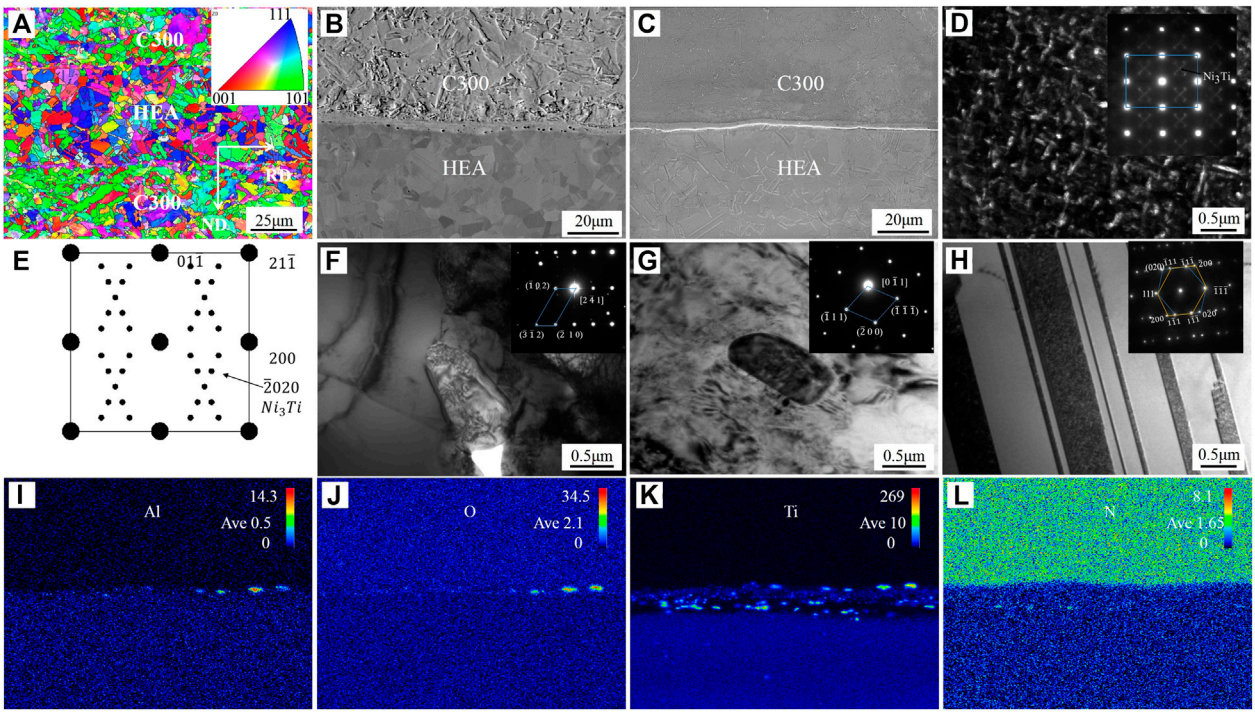

FIGURE 2 | (A) Electron back-scattering diffraction maps of the rolled multilayer maraging/CoCrNi composites. RD indicates the rolling direction and ND the normal direction. **(B)** Scanning electron microscopy (SEM) of hot-rolled sample. **(C)** SEM of an aged sample. **(D) (F) (G) (H)** Transmission electron microscopy of Ni_3Ti, Al_2O_3, TiN and twinning of aged multilayer maraging/CoCrNi composite; **(E)** Indexing of diffraction pattern illustration of **D**; **(I–L)** EPMA mapping distribution of an aged sample.

CoCrNi composites. Herein, the individual CoCrNi alloy has a high work-hardening capacity, a superior tensile fracture elongation of 50%, and a rather low yield strength of 269 MPa, as shown in **Figures 3A,B**. However, the individual C300 maraging steel reveals a superior yield strength of 1951 MPa, poor strain-softening behavior, and a poor work-hardening rate. Based on the above multilayer design idea, a relatively high tensile strength of 855 MPa and a uniform elongation of 21.7% can be obtained for the hot-rolled C300/CoCrNi multilayer composites. Moreover, after the aging treatment, the composites obtained a superior tensile strength of 1,380 MPa and a superior fracture elongation of 24% (uniform elongation of 15.7%). Here, the strengthening mechanisms of the multilayer metal matrix composites are mainly attributed to grain refining, strain-induced twinning, and nanometer precipitate strengthening. Noticeably, the excellent interface bonding is beneficial for deformation coordination and toughening of the C300/CoCrNi multilayer composites.

In order to analyze the contribution of each of the strengthening mechanisms in depth, the relevant theoretical calculations were introduced. The influence of the strengthening mechanism can be expressed as:

$$\sigma_{0.2} = \sigma_0 + \Delta\sigma_{refin} + \Delta\sigma_{twin} + \Delta\sigma_{pre}$$

where σ_0 is the value that the original material contributes to the yield strength, $\Delta\sigma_{refin}$ is the value of grain refining, $\Delta\sigma_{twin}$ is the value of strain-induced twinning, and $\Delta\sigma_{pre}$ is the value of the nanometer precipitate.

$$\sigma_0 = f_{CoCrNi}\sigma_{CoCrNi} + f_{C300}\sigma_{C300}$$

where f_{CoCrNi} and f_{C300} are the volume fractions of CoCrNi and C300 in the composites, respectively; $f_{CoCrNi} = f_{C300} = 0.5$; and σ_{CoCrNi} and σ_{C300} are the yield strengths of the original materials.

$$\Delta\sigma_{refin} = f_{CoCrNi}K_{CoCrNi}\Big/d_{CoCrNi}^{1/2} + f_{C300}K_{C300}\Big/d_{C300}^{1/2}$$

where K_{CoCrNi} (Liu et al., 2020) and K_{C300} (Rack, 1978) are the Hall–Petch constants of CoCrNi and C300, respectively, and d_{CoCrNi} and d_{C300} are the average grain diameters of the CoCrNi alloy layer and C300 layer, respectively, where $d_{CoCrNi} = 5$ μm and $d_{C300} = 3$ μm.

$$\Delta\sigma_{twin} = f_{CoCrNi}K_{twin}\Big/d_{CoCrNi}^{1/2}$$

where K_{twin} is a constant, $K_{twin} = 357$ MPa $\mu m^{1/2}$ (the Hall–Petch constant for twinning, which is similar to that for slip in TWIP steel (Gutierrez-Urrutia and Raabe, 2011)).

$$\Delta\sigma_{pre} = f_{C300} \times \frac{Gb}{2\pi(\lambda - d)} \times \frac{1 + 1/(1-\nu)}{2} \times ln\left[\frac{\lambda - d}{2b}\right]$$

where G is the shear modulus, $G = 71$ GPa; b is the Burger vector, $b = 0.25$ nm; λ is the particle spacing distance between precipitates, λ = 20 nm; d is the diameter of the precipitates,

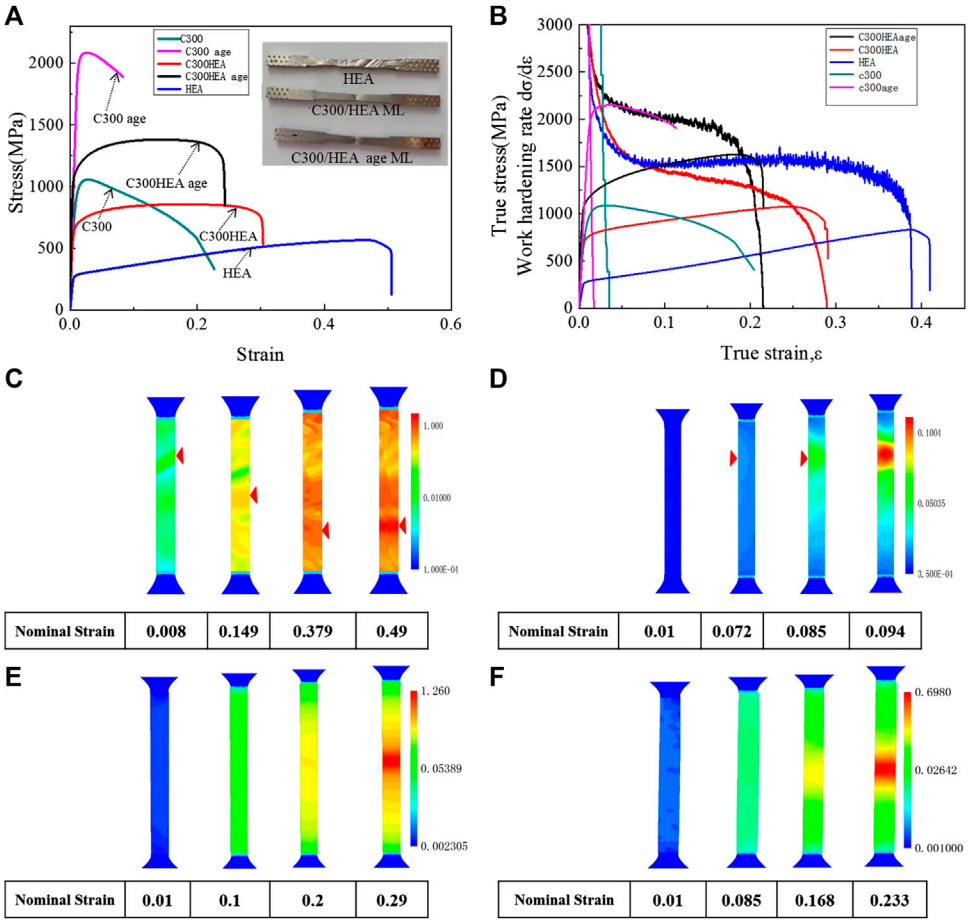

FIGURE 3 | (A) Stress–strain curve, **(B)** True stress–strain and work hardening rate curve, **(C–F)** Digital image correlation of the strain distribution, **(C)** CoCrNi alloy, **(D)** C300 aged, **(E)** rolled multilayer maraging/CoCrNi composite, and **(F)** aged multilayer maraging/CoCrNi composite.

d = 5 nm; and ν is Poisson's ratio, ν = 0.3 (Zhu et al., 2014; Yang et al., 2015). The corresponding values for each item are shown in **Table 2**. The calculated values are approximated to the experimental results.

Figure 3C shows the strain evolution process of the individual CoCrNi alloy. It can be seen that multiple localized strain concentrations occur during the tensile deformation process, forming obvious multiple shear bands and localized necking phenomena. However, poor diffuse necking is inhibited because of the mutual competition of multiple strain localization zones, revealing superior strain-hardening capacity and fracture elongation. **Figure 3D** shows that an obvious localized strain concentration zone is formed at a strain of 0.085 and proceeds until fracture failure. That is to say, in C300 maraging steel it is easy to generate strain localization, leading to the formation of premature localized necking. The full-field strain distributions of the hot-rolled and aged multilayer C300/CoCrNi composites are shown in **Figures 3E,F**. The hot-rolled and aged multilayer metal composites both undergo a prolonged uniform plastic deformation stage until the strain concentration points reach 0.2 and 0.168, respectively. Finally, an obvious strain localization zone is located in the middle of the multilayer metal composites, resulting in fracture failure with a slight localized necking. That is to say, the C300/CoCrNi multilayer composites can integrate the advantages of the individual layers, effectively delaying the localized necking of

TABLE 2 | The contributions of grain refining, strain-induced twinning, and nanometer precipitate strengthening, and the calculated and experimental values of the yield stress.

Material sample	σ_0 (MPa)	$\Delta\sigma_{refin}$ (MPa)	$\Delta\sigma_{twin}$ (MPa)	$\Delta\sigma_{pre}$ (MPa)	Calculated value (MPa)	Experimental value (MPa)
Hot-rolled sample	518.7	77.3	79.5	—	675.5	666.8
Aged sample	518.7	81.3	79.5	388.9	1,068.4	1,060.9

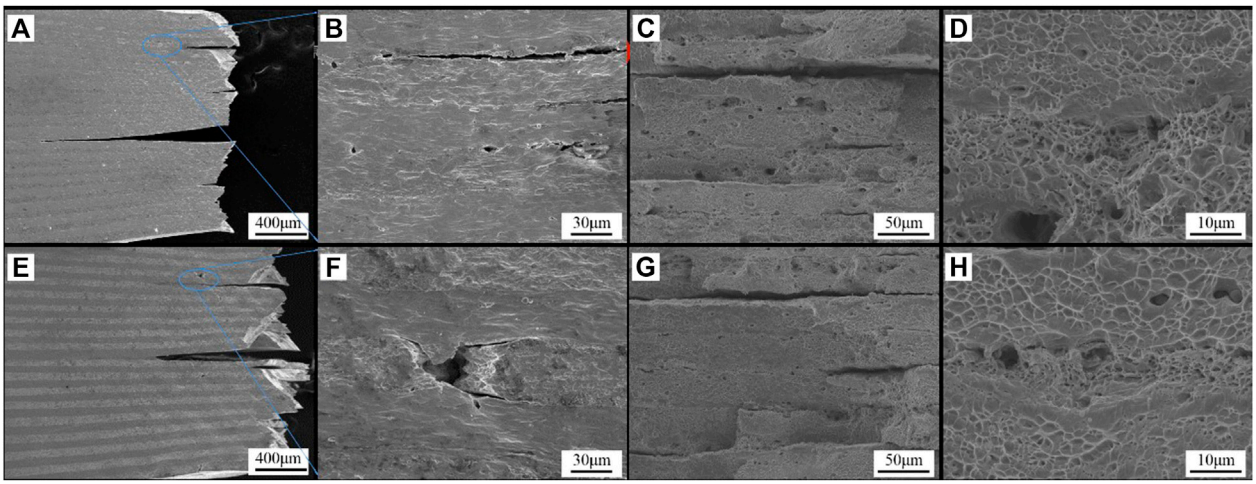

FIGURE 4 | (A–D) Fracture morphology of a hot-rolled multilayer maraging/CoCrNi composite, **(E–F)** fracture morphology of ageing treat multilayer maraging/CoCrNi composite.

C300 maraging steel and improving the yield strength of the CoCrNi alloy by reasonable interface bonding. Therefore, the C300/CoCrNi multilayer composite shows high yield strength and strain-hardening capacity.

Figure 4 shows the tensile fracture characteristics of the hot-rolled and aged multilayer metal matrix composites. The serious interface delamination cracks are located in the hot-rolled multilayer composites, as shown in **Figure 4A**, revealing a low interface bonding strength between the C300 and CoCrNi layers. The weak interface may be attributed to the high friction force and excessive interface inclusions during the hot-rolling process (Long et al., 2013; Li et al., 2008; Zhu et al., 2016). In addition, many discontinuous interface cracks and pores are located at the clad interface, as shown in **Figure 4B**; this can be attributed to the fractured interface inclusions. The above phenomenon reveals that the interface crack propagation of the multilayer composites experiences nucleation, growth, and convergence of microcracks (Liu et al., 2014). Also, the C300 and CoCrNi layers present coarse dimples with the same size of about 10 μm, which reveals a typical ductile fracture mode. Meanwhile, the interface transition zone possesses rather refined dimples with an average size of 2 μm, as shown in **Figure 4D**; these may be attributed to the ultrafine grains caused by severe plastic deformation. However, the aged C300/CoCrNi multilayer composites present slight and short interface delamination cracks, as shown in **Figure 4E**, which may be attributed to sufficient alloying element diffusion behavior at the clad interface during the long-time aging treatment (Seok et al., 2016). Moreover, the obvious tunnel cracks are located at the overall C300 maraging steel layer, as shown in **Figure 4F**. A relatively strong interface can effectively inhibit the strain concentration of the C300 layer, which is beneficial for enhancing the uniform plastic deformation capacity. Then the tunnel cracks cannot propagate into the overall sample owing to the existence of the CoCrNi alloy layer and strong interface, which can also delay the premature fracture failure of the C300 layer. Therefore, the slight interface delamination and formation of tunnel cracks are beneficial for toughening the multilayer composites. **Figures 4G,H** reveals the normal fracture characteristics of the C300/CoCrNi multilayer composites. Many bifurcated cleavage cracks are located at the C300 layer, indicating that the C300 layer can be toughened by forming multiple cracks. Compared with the hot-rolled sample, the aged C300 layer has many fine dimples, as shown in **Figure 4H**. That is to say, the nanoscale precipitates can play an important role in strengthening and toughening the multilayer composites.

CONCLUSION

In the present work, we design and fabricate a novel C300/CoCrNi multilayer composite by a vacuum hot-rolling and aging treatment. Herein, the ultimate tensile strength of the multilayer metal composites can reach 1,380 MPa with a high fracture elongation of 24%, as well as superior uniform elongation of 15.7%. This indicates an excellent strengthening–toughening behavior. The aging treatment eliminates the rolling friction stress and promotes diffusion of the alloying element at the clad interface, realizing strong interface bonding. The clad interface and tunnel crack play an important role in toughening the C300/CoCrNi multilayer composites. That is to say, a strong clad interface and CoCrNi layer with a high strain-hardening capacity can effectively delay premature localized necking and fracture failure of the C300 layer, achieving a superior strength–ductility balance.

DATA AVAILABILITY STATEMENT

The original contributions presented in the study are included in the article/Supplementary Material, further inquiries can be directed to the corresponding authors.

AUTHOR CONTRIBUTIONS

CX Writing: original draft preparation, conceptualization. YG Data curation. WFang Investigation. XZ Methodology, Validation. BXL Writing: reviewing and editing. JF Methodology. FY Funding acquisition. All authors contributed to the article and approved the submitted version.

FUNDING

The Joint Fund for Steel Research of National Natural Science Foundation of China and Baowu Steel Group Corporation Limited (No. U1860114), the foundation strengthening program (No. 2019-JCJQ-142) the National Natural Science Foundation of China (No. 51705129). The funder was not involved in the study design, collection, analysis, interpretation of data, the writing of this article, or the decision to submit it for publication.

ACKNOWLEDGMENTS

This work is supported financially by the National Natural Science Foundation of China (NSFC) under grant no. 51701061, the Joint Fund for Steel Research of the National Natural Science Foundation of China and Baowu Steel Group Corporation Limited (no. U1860114), the Foundation Strengthening Program (no.2019-JCJQ-142), and the National Natural Science Foundation of China (no. 51705129).

REFERENCES

Chang, R. B., Fang, W., Yu, H. Y., Bai, X., Zhang, X., Liu, B. X., et al. (2019). Heterogeneous banded precipitation of (CoCrNi)93Mo7 medium entropy alloys towards strength–ductility synergy utilizing compositional inhomogeneity. *Scripta Mater.* 172, 144–148. doi:10.1016/j.scriptamat.2019.07.026

Ding, H., Cui, X., Gao, N., Sun, Y., Zhang, Y., Huang, L., et al. (2021). Fabrication of (TiB/Ti)-TiAl composites with a controlled laminated architecture and enhanced mechanical properties. *J. Mater. Sci. Technol.* 62, 221–233. doi:10.1016/j.jmst.2020.06.011

Ding, H., Cui, X., Xu, C., Li, A., Geng, L., Fan, G., et al. (2018). Fabrication and mechanical characteristics of multi-laminated aluminum matrix composites reinforcedby continuous basalt fibers. 54, 1171–1178. doi:10.11900/0412.1961.2017.00530

Grassel, O., Kruger, L., Frommeyer, G., and Meyer, L. W. (2000). High strength Fe-Mn-(Al, Si) TRIP/TWIP steels development - properties- application. *Int. J. Plast.* 16, 1391–1409. doi:10.1016/S0749-6419(00)00015-2

Gutierrez-Urrutia, I., and Raabe, D. (2011). Dislocation and twin substructure evolution during strain hardening of an Fe–22wt.% Mn–0.6wt.% C TWIP steel observed by electron channeling contrast imaging. *Acta Mater.* 59, 6449–6462. doi:10.1016/j.actamat.2011.07.009

Gutierrezurrutia, I., and Raabe, D. (2011). Dislocation and twin substructure evolution during strain hardening of an Fe-22 wt.% Mn-0.6 wt.% C TWIP steel observed by electron channeling contrast imaging. *Acta Mater.* 59, 6449–6462. doi:10.1016/j.actamat.2011.07.009

He, G., Zhao, Y., Gan, B., Sheng, X., Liu, Y., and Tan, L. (2020). Mechanism of grain refinement in an equiatomic medium-entropy alloy CrCoNi during hot deformation. *J. Alloys Compd.* 815, 152382. doi:10.1016/j.jallcom.2019.152382

Inoue, J., Nambu, S., Ishimoto, Y., and Koseki, T. (2008). Fracture elongation of brittle/ductile multilayered steel composites with a strong interface. *Scripta Mater.* 59,1055–1058. doi:10.1016/j.scriptamat.2008.07.020

Jing, Y. A., Qin, Y., Zang, X., Shang, Q., and Hua, S. (2014). A novel reduction-bonding process to fabricate stainless steel clad plate. *J. Alloys Compd.* 617, 688–698. doi:10.1016/j.jallcom.2014.07.186

Kang, J. Y., Kim, J. G., Kim, S. K., Chin, K. G., Lee, S., and Kim, H. S. (2016). Outstanding mechanical properties of high-pressure torsion processed multiscale TWIP-cored three layer steel sheet. *Scripta Mater.* 123, 122–125. doi:10.1016/j.scriptamat.2016.06.009

Lesuer, D. R., Syn, C. K., Sherby, O. D., Wadsworth, J., Lewandowski, J. J., and Hunt, W. H. (1996). Mechanical behaviour of laminated metal composites. *Int. Mater. Rev.* 41, 169–197. doi:10.1179/imr.1996.41.5.169

Li, L., Nagai, K., and Yin, F. (2008). Progress in cold roll bonding of metals. *Sci. Technol. Adv. Mat.* 9, 023001. doi:10.1088/1468-6996/9/2/023001

Liu, B. X., An, Q., Yin, F. X., Wang, S., and Chen, C. X. (2019). Interface formation and bonding mechanisms of hot-rolled stainless steel clad plate. *J. Mater. Sci.* 54, 11357–11377. doi:10.1007/s10853-019-03581-x

Liu, B. X., Huang, L. J., Geng, L., Wang, B., and Cui, X. P. (2014). Fracture behaviors and microstructural failure mechanisms of laminated Ti–TiBw/Ti composites. *Mater. Sci. Eng.* 611, 290–297. doi:10.1016/j.msea.2014.05.089

Liu, X., Zhang, M., Ma, Y., Dong, W., Li, R., Lu, Y., et al. (2020). Achieving ultrahigh strength in CoCrNi-based medium-entropy alloys with synergistic strengthening effect. *Mater. Sci. Eng. A.* 776, 139028. doi:10.1016/j.msea.2020.139028

Long, L. I., Xin-Jin, Z., Hui-Yun, L. I. U., and Fu-Xing, Y. I. N. (2013). Formation mechanism of oxide inclusion on the interface of hot-rolled stainless steel clad plates. *J. Iron Steel Res.* 25, 43–47. doi:10.13228/j.boyuan

Miao, J., Slone, C. E., Smith, T. M., Niu, C., Bei, H., Ghazisaeidi, M., et al. (2017). The evolution of the deformation substructure in a Ni-Co-Cr equiatomic solid solution alloy. *M. Acta Mater.* 132, 35–48. doi:10.1016/j.actamat.2017.04.033

Ojima, M., Inoue, J., Nambu, S., Xu, P., Akita, K., Suzuki, H., and Koseki, T. (2012). Stress partitioning behavior of multilayered steels during tensile deformation measured by *in situ* neutron diffraction. *Scripta Mater.* 66, 139–142. doi:10.1016/j.scriptamat.2011.10.018

Rack, H. J. (1978). Age hardening-grain size relationships in 18Ni maraging steels. *Mater. Sci. Eng.* 34, 263–270. doi:10.1016/0025-5416(78)90058-7

Seok, M. Y., Lee, J. A., Lee, D. H., Ramamurty, U., Nambu, S., Koseki, T., et al. (2016). Decoupling the contributions of constituent layers to the strength and ductility of a multi-layered steel. *Acta Mater.* 121, 164–172. doi:10.1016/j.actamat.2016.09.007

Slone, C. E., Chakraborty, S., Miao, J., George, E. P., Mills, M. J., and Niezgoda, S. R. (2018). Influence of deformation induced nanoscale twinning and FCC-HCP transformation on hardening and texture development in medium-entropy CrCoNi alloy. *Acta Mater.* 158, 38–52. doi:10.1016/j.actamat.2018.07.028

Slone, C. E., Chakraborty, S., Miao, J., George, E. P., Mills, S. R., and Niezgoda, M. J. (2018). Influence of deformation induced nanoscale twinning and FCC-HCP transformation on hardening and texture development in medium-entropy CrCoNi alloy. *Acta Mater.* 158, 38–52. doi:10.1016/j.actamat.2018.12.015

Slone, C. E., Miao, J., George, E. P., and Mills, M. J. (2019). Achieving ultra-high strength and ductility in equiatomic CrCoNi with partially recrystallized microstructures. *Acta Mater.* 165, 496–507. doi:10.1016/j.actamat.2018.12.015

Wu, Z., Bei, H., Pharr, G. M., and George, E. P. (2014). Temperature dependence of the mechanical properties of equiatomic solid solution alloys with face-centered cubic crystal structures. *Acta Mater.* 81, 428–441. doi:10.1016/j.actamat.2014.08.026

Yang, S., Peng, Y., Zhang, X. M., and Tian, Z. L. (2015). Phase transformation and its effect on mechanical properties of C300 weld metal after aging treatment at different temperatures. *J. Iron Steel Res. Int.* 6, 527–533. doi:10.1016/S1006-706X(15)30036-4

Yin, F. X., Li, L., Tanaka, Y., Kishimoto, S., and Nagai, K. (2013). Hot rolling bonded multilayered composite steels and varied tensile deformation

behaviour. *Mater. Sci. Technol.* 28, 783–787. doi:10.1179/1743284711y.0000000116

Yu, W. X., Liu, B. X., Cui, X. P., Dong, Y. C., Zhang, X., He, J. N., et al. (2018). Revealing extraordinary strength and toughness of multilayer TWIP/Maraging steels. *Mater. Sci. Eng. A.* 727, 70–77. doi:10.1016/j.msea.2018.04.097

Zhang, S., Xiao, H., Xie, H., and Gu, L. (2014). The preparation and property research of the stainless steel/iron scrap clad plate. *J. Mater. Process. Technol.* 214, 1205–1210. doi:10.1016/j.jmatprotec.2014.01.006

Zhu, F., Yin, Y. F., and Faulkner, R. G. (2014). Microstructural control of maraging steel C300. *Mater. Sci. Technol.* 27, 395–405. doi:10.1179/026708309x12506933873503

Zhu, Z., He, Y., Zhang, X., Liu, H., and Li, X. (2016). Effect of interface oxides on shear properties of hot-rolled stainless steel clad plate. *Mat. Sci. Eng. a-Struct.* 669, 344–349. doi:10.1016/j.msea.2016.05.066

Conflict of Interest: The authors declare that the research was conducted in the absence of any commercial or financial relationships that could be construed as a potential conflict of interest.

This study received funding from the Joint Fund for Steel Research of the National Natural Science Foundation of China and Baowu Steel Group Corporation Limited.

frontiers in Materials

ORIGINAL RESEARCH
published: 28 May 2021
doi: 10.3389/fmats.2021.691551

Correlation Between Microstructure and Fracture Behavior in Thick HARDOX 450 Wear-Resistant Steel With TiN Inclusions

Zhongyang Wang†, *Xiang Wu*†, *Denghui Liu and Xiurong Zuo**

Key Laboratory of Material Physics, Ministry of Education, School of Physics and Microelectronics, Zhengzhou University, Zhengzhou, China

This work investigates the correlation between TiN inclusions and microstructural properties of HARDOX 450 steel using optical microscopy (OM), scanning electron microscopy (SEM), transmission electron microscopy (TEM), and electron backscattered diffractometer (EBSD) methods. Some amount of microsized TiN inclusions were formed in the temperature range of the solid–liquid zone; however, they exhibited fracture features of deep dimples rather than a cleavage plane, which is closely related to the ability of the microstructure to arrest cracks. Upon tensile loading, a single microcrack first appeared inside the microsized TiN inclusions, and then, multiple microcracks formed, parts of which widened in the direction of tensile stress. A schematic mechanism map was plotted to reveal the propagation behavior and fracture mechanism of the microcracks in the TiN inclusions.

Keywords: HARDOX450 wear-resistant steel, mechanical properties, microstructure, TiN inclusions, microcracks

OPEN ACCESS

Edited by:
Minghui Cai,
Northeastern University, China

Reviewed by:
Xin Zhao,
Zhengzhou University of Aeronautics, China
Lijia Zhao,
ArcelorMittal USA LLC, United States
Zhiqiang Zhang,
Northeastern University, China

***Correspondence:**
Xiurong Zuo
zuoxiurong@zzu.edu.cn

†*These authors have contributed equally to this work and share first authorship*

Specialty section:
This article was submitted to Structural Materials, a section of the journal Frontiers in Materials

Received: *06 April 2021*
Accepted: *04 May 2021*
Published: *28 May 2021*

Citation:
Wang Z, Wu X, Liu D and Zuo X (2021) Correlation Between Microstructure and Fracture Behavior in Thick HARDOX 450 Wear-Resistant Steel With TiN Inclusions. Front. Mater. 8:691551. doi: 10.3389/fmats.2021.691551

INTRODUCTION

Low-alloy high-strength wear-resistant steels have numerous advantages such as low alloying content, simple manufacturing process, high toughness, and wear resistance (Jiang et al., 2011; Ojala et al., 2014; Ryabov et al., 2017). Currently, microalloying, and heat treatment have been widely adopted to improve the strength, toughness, and wear resistance of low-alloy high-strength steels, mainly through adding elements Ti, B, Nb, and V (Nikitin et al., 2016; Shi et al., 2016). Among these microalloying elements, Ti is typically used to form nanosized precipitates with excellent high-temperature stability, eventually inhibiting the growth of austenitic grains. However, inappropriately adding Ti can cause the formation of microsized TiN inclusions, easily triggering cleavage fractures (Yan et al., 2006), which reduces the low-temperature impact toughness and the fatigue life of microalloy steel (Liu et al., 2018; Sun et al., 2020).

Efforts have been made to control the formation and growth of TiN inclusions, because these microsized particles deteriorate the toughness of steels (Fairchild et al., 2000; Fu et al., 2017; Jin and Du, 2018; Han et al., 2020). In the case of replacing Ti with Nb, Hulka et al. (Hulka et al., 2005) used Nb to replace Ti in the B-microalloyed steel to improve the toughness via more efficient grain refinement, which ensured a high resistance to brittle fracture and an excellent wear resistance. Although the use of Nb instead of Ti can effectively reduce the number of microsized TiN inclusions, the role of nanosized TiN precipitates in improving the toughness and wear resistance is irreplaceable.

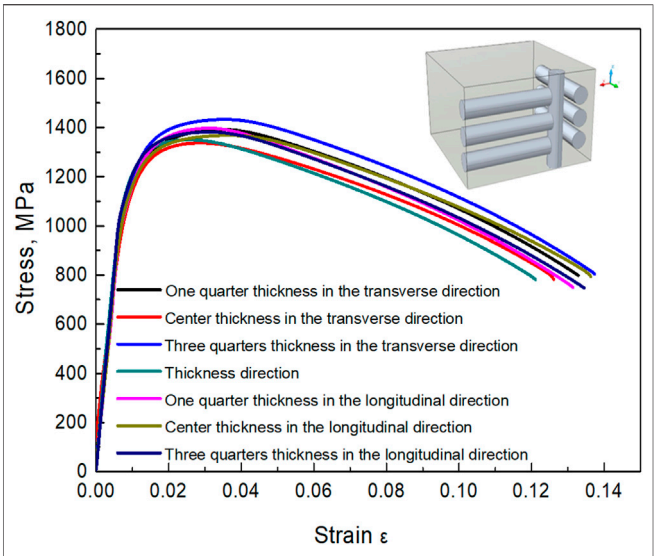

FIGURE 1 | Engineering stress–strain curves of HRADOX 450 steel in different directions.

As one of the popular wear-resistant steels, HARDOX 450 is widely used because of its unique mechanical properties and excellent wear resistance. A certain amount of Ti is typically added, inevitably leading to microsized TiN inclusions in the manufacturing process. Considering the catastrophic failure of structural components due to large-sized TiN inclusions, a detailed understanding of the formation and fracture mechanism of TiN inclusions in steels is essential. Therefore, in this study, a series of tensile tests were performed on HARDOX 450 steel with microsized TiN inclusions. The fracture mechanism of microsized TiN inclusions under a tensile stress state and its effect on the properties were analyzed in detail.

EXPERIMENTAL PROCEDURES

The HARDOX 450 steel plate is composed of 0.19C-0.96Mn-0.23Si-1.92(Ni + Cr + Al)-0.037(Nb + Mo + V)-0.015Ti, wt%. The as-received steel plate was subjected to quenching and tempering, and it exhibited a fully martensitic microstructure. The size and quantity of TiN at quarter thickness and at the center were measured using an optical microscope. The samples for the microstructural observation were polished using standard rough and finish polishing procedures and then etched in picric acid to measure the average size of the initial austenitic grain boundaries.

For the mechanical tests, cylindrical specimens were prepared at one quarter, three quarters, and at the center of the steel plate, along the longitudinal, transverse, and vertical directions, as illustrated in **Figure 1**. A gauge with a length of 25 mm and a diameter of 5 mm was used in accordance with the GB/T 228–2010 standard. Tensile testing was carried out at a speed of 2 mm per minute on a universal tensile testing machine (SANS CMT5105) at 25°C. Microstructures and fracture surfaces were examined using a scanning electron microscope (SEM, FEI Quanta 250 FEG) and energy dispersive spectrometer (EDS, INCA-ENERGY). The microstructure was characterized by transmission electron microscopy (TEM, JEM-2100). Film foils for the TEM specimens were prepared using a double-jet electro-polishing apparatus (Struers Tenupol-5) with a solution of 10% perchloric acid and 90% ethanol at −20°C under a voltage of 20 V. An electron backscattered diffractometer (EBSD) analysis was performed in a field emission gun (FEG) SEM, Zeiss Ultra 55VP equipped with an EBSD, Oxford-HKL, operated at 20 kV. A step size of 0.5 μm was chosen in this study. Data acquisition and post-processing were performed using the HKL Channel five software.

RESULTS

Tensile Properties

Figure 1 shows the tensile properties of the as-received HARDOX 450 steel plate. All the specimens exhibited similar flow behaviors and stress–strain levels under each condition. The tensile data demonstrated that these samples exhibit a high yield strength of 1100 MPa and an ultimate tensile strength of 1300 MPa, with the total elongation to fracture no less than 12%. **Table 1** lists the standard deviation of the tensile properties, indicating relatively uniform tensile properties in all directions, which means that the HRADOX 450 steel exhibited evenly uniform microstructural features.

Microstructure

Distribution of TiN Inclusions

Microsized TiN inclusions could be found in the matrix, as shown in **Figure 2**. The number of TiN inclusions at the center was relatively higher than that at one quarter thickness, and the closer to the center, the larger the TiN inclusions. Considering the difference in temperature at the center and surface of thick slabs during the cooling of continuous casting, when the temperature at the surface reaches the solidification point, the center of thick slabs remains in the liquid zone. Thus, the nucleation and growth of TiN particles at the center continue to proceed, promoting the formation of more TiN particles with a relatively larger size at the center after hot rolling. Unfortunately, these microsized TiN inclusions are largely negligible for pinning the grain boundaries. This result is inconsistent with that reported by Yan et al. (2007), Lambert-Perlade et al. (2004), who showed that the high density and large-size brittle TiN inclusions or MA can easily initiate cleavage fractures, thus reducing the fracture strength and impact energy.

Microstructural Features

Figure 3A shows the SEM microstructure of the as-received HARDOX 450 steel plate, indicating a fully martensitic microstructure. Some carbides can be observed in the martensitic lath after tempering, with a relatively high density of dislocations, as shown in **Figure 3B**. Moreover, the length-to-width ratio of the martensite lath in HARDOX 450 steel is low, which is beneficial for inhibiting crack propagation.

TABLE 1 | Standard deviations in the tensile properties of all specimens of HARDOX 450 steel in different directions.

	Tensile strength/MPa	Yield strength/MPa	Reduction of area/%	Elongation/%
Standard deviations	40.8	31.6	4.32	1.18

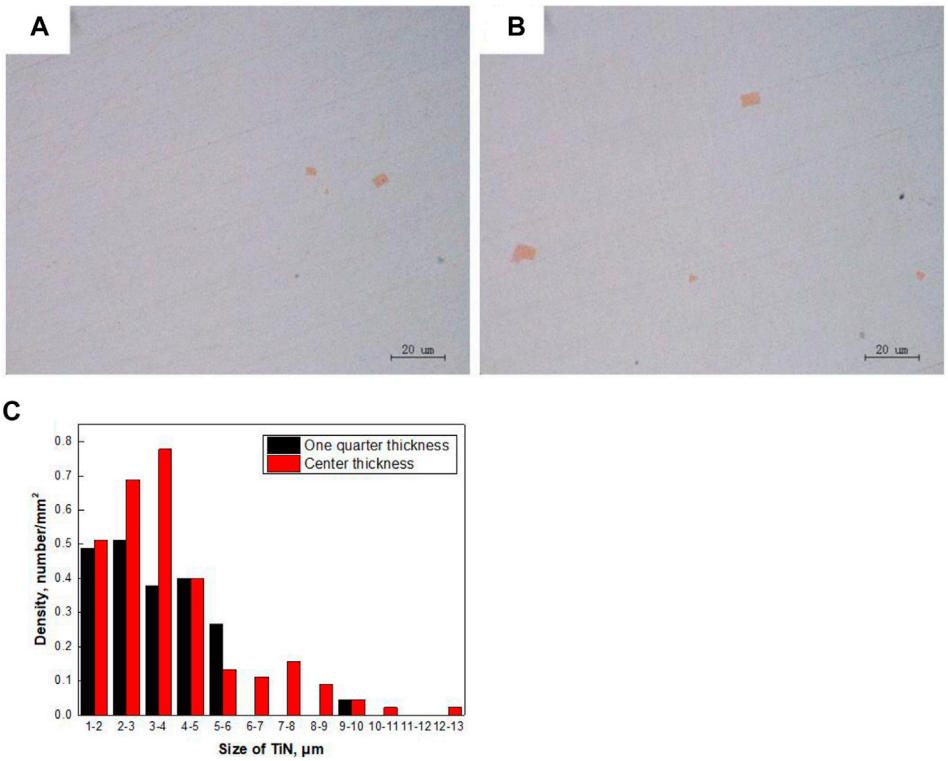

FIGURE 2 | OM images and size distribution of TiN inclusions in the investigated steel at **(A)** quarter thickness **(B)** center **(C)** size distribution of TiN.

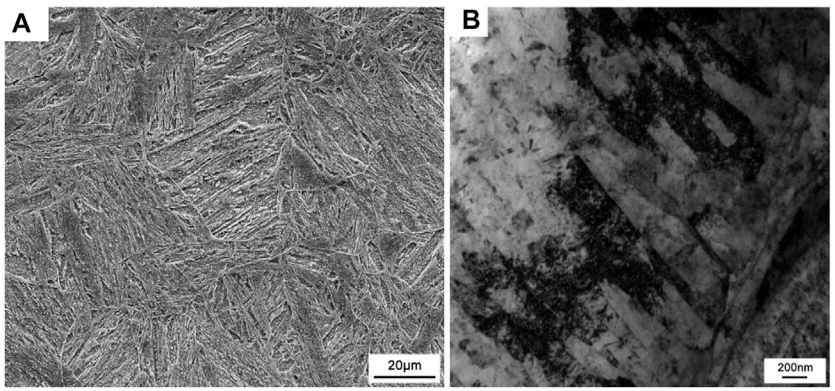

FIGURE 3 | SEM and TEM images of the investigated steel **(A)** SEM and **(B)** TEM.

The average sizes of the prior austenitic grains at both one quarter thickness and at the center are relatively small, compared with those shown in **Figures 4A,B**. Finer prior austenitic grains can give rise to finer and shorter martensitic laths, which efficiently hinder crack propagation, thereby improving the fracture toughness of the steel at both one quarter thickness and at the center.

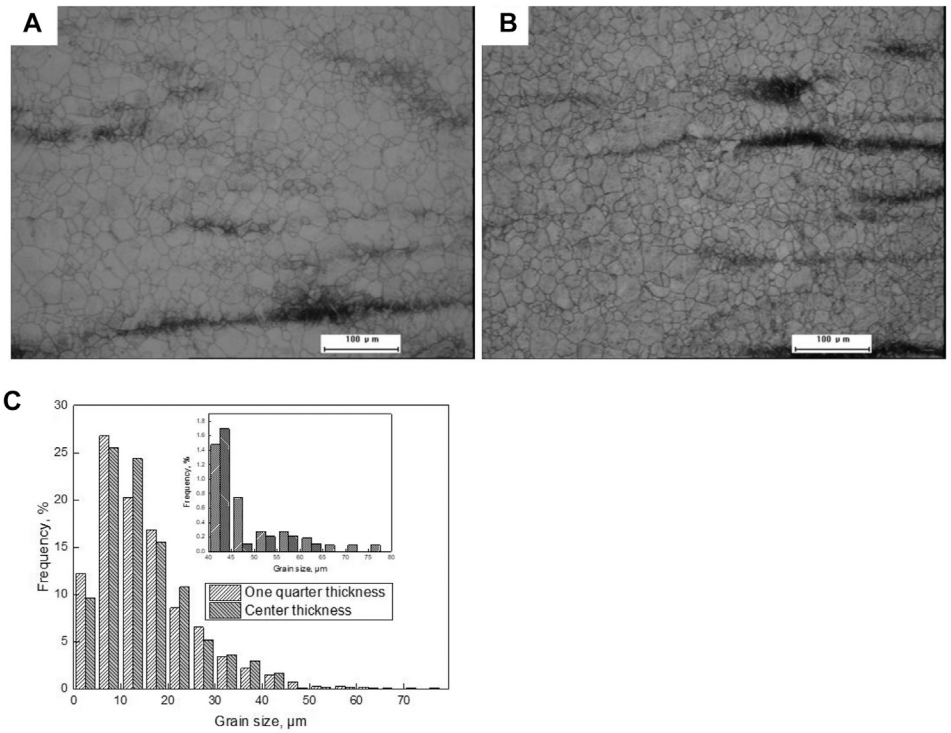

FIGURE 4 | OM graphs of austenitic grains and grain size distribution at **(A)** quarter thickness **(B)** center **(C)** grain size distribution.

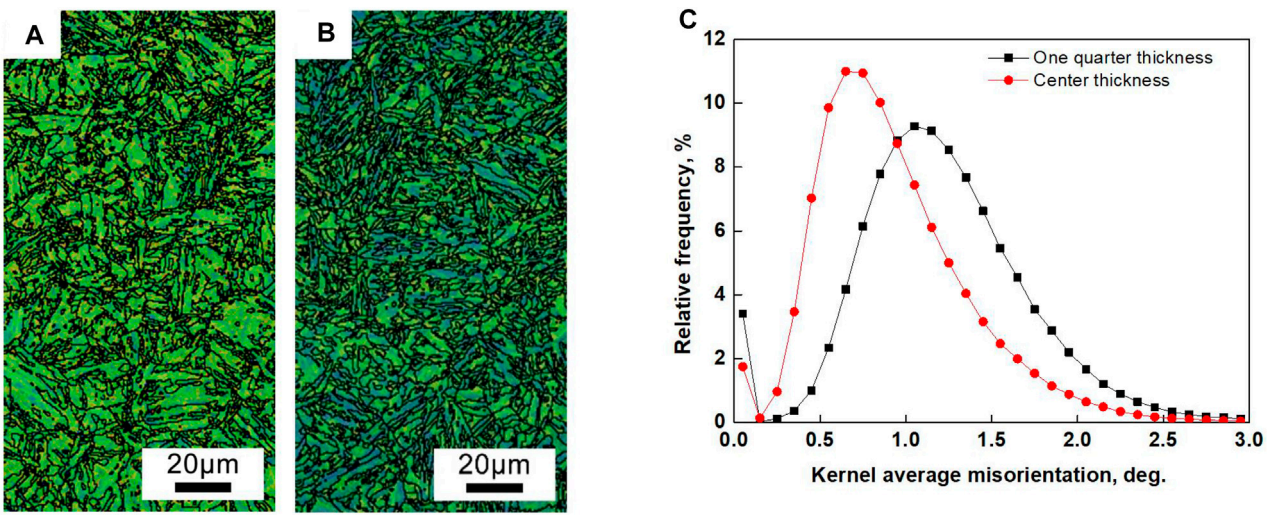

FIGURE 5 | Representative kernel average misorientation (KAM) map at **(A)** quarter thickness **(B)** center, and **(C)** corresponding KAM value distribution.

EBSD Analysis

Local disorientation was performed at one quarter thickness and at the center through the EBSD method to characterize the local stress concentration. The threshold value of the kernel average misorientation (KAM) distribution map (**Figure 5**) shows that the percentage of small local misorientations is much lower at the center than that at one quarter thickness. Thus, the local stress at one quarter thickness is higher than that at the center of the thickness.

Notably, there exists a significant difference in the cooling rates during quenching because of the thick steel plate (thickness: ~60 mm), resulting in a slight difference in the final microstructures. For example, a fully martensitic structure was obtained at one quarter thickness, whereas a mixture of

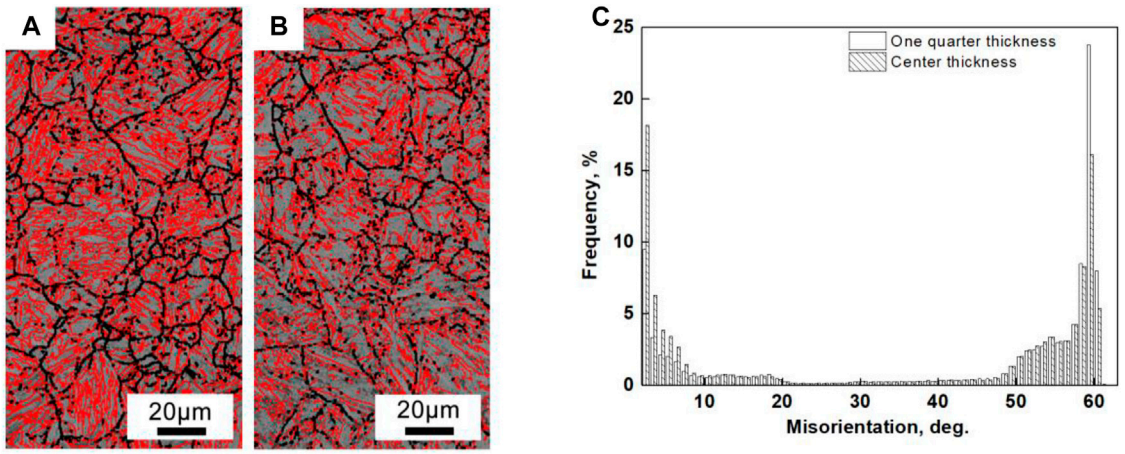

FIGURE 6 | Misorientation maps showing the crystallographic characteristics of the sample (black line $15^{\circ} \leq \theta \leq 50^{\circ}$; red line $\theta > 50^{\circ}$) at **(A)** quarter thickness **(B)** center **(C)** Misorientation distribution figure at quarter thickness and at the center.

martensite and bainite was obtained at the center. In comparison, martensite exhibited more severe lattice distortion than bainite; hence, the local stress concentration was easily induced at one quarter thickness.

Figures 6A,B show the misorientation maps of the crystallographic characteristics of the specimens and a quantitative analysis diagram of the maps. Boundaries greater than 50° account for 63.5% at quarter thickness and 53.8% at the center, as shown in **Figure 6C**.

Fractography

Fracture Surface

Figure 7A shows the overall view of the fracture surface of the HARDOX 450 steel after conducting the static tensile tests, with visible boundaries of the fiber zone and shear lip, along with secondary and delamination cracks in the fiber zone. Moreover, the fracture surface in the fiber zone can be characterized by ductile dimples (**Figure 7C**), resulting from microvoid coalescence, tear ridges, secondary cracks along various directions, and few cleavage facets.

Secondary and delamination cracks are commonly observed in controlled-rolled steel sheets. A delamination crack generally extends in a straight manner for a long distance on the tensile fracture surface, as shown in **Figure 7B**. The delamination crack observed in our study can be attributed to the three dimensional stress constraint inside the material (Sun et al., 2016). Since the delamination crack was generated before the propagation of the main crack, it was expected to consume additional energy, resulting in improved mechanical properties.

From the bottom of the deep dimples, the regular shape inclusions were found to be broken (**Figure 7D**). These deep dimple walls were passivated without protrusions. The EDS spectra shown in **Figure 7E** demonstrates that these inclusions are TiN inclusions.

Studies have found that microsized TiN inclusions are detrimental to the mechanical properties of steels, because they may initiate cleavage fractures (Yan et al., 2007; Ghosh et al., 2013). The local stress concentration in the vicinity of TiN inclusions reached a critical intensity with increasing applied load, and the cracks rapidly propagated, causing an immediate fracture without bearing larger deformation (Kang et al., 2016). However, the present microsized TiN inclusions were found to be broken when the matrix was subjected to the applied external load. Moreover, most of the microsized TiN inclusions were observed inside the ductile dimples, which implies that the present microstructure plays a role in reducing the negative effect of TiN inclusions on the overall mechanical properties, as mentioned in *Tensile Properties*.

Transverse Section of Tensile Fracture Surface

The fracture was cut along the central axis of the tensile specimen to observe the morphology of the TiN inclusions, perpendicular to the fracture surface. The size of the TiN inclusions was determined to be approximately 3 μm, as shown in **Figure 8**. A detailed analysis showed that the TiN inclusions exhibit a type of broken morphology and form multiple narrow microcracks. **Figure 8B** shows the morphology of the TiN inclusions slightly away from the tensile fracture surface. These TiN inclusions can be characterized by small pores or narrow microcracks due to the applied low tensile stress. Accordingly, narrower microcracks can be observed inside the TiN inclusions far away from the tensile fracture (**Figure 8C**), compared with that shown in **Figures 8A,B**.

In contrast, the formation of multiple microcracks dispersed the concentrated stress around the TiN inclusions, thus inhibiting the microcracks from propagating into the matrix and ensuring that the overall shape of the TiN inclusions remains intact. The large-sized TiN inclusions with an average area of 3 μm × 9 μm were subjected to a lower stress per unit length. However, the small-size TiN inclusions exhibited a sharp angle along the direction of the applied force and thus were easily broken when subjected to tensile stress given the higher stress per unit length (**Figure 8D**).

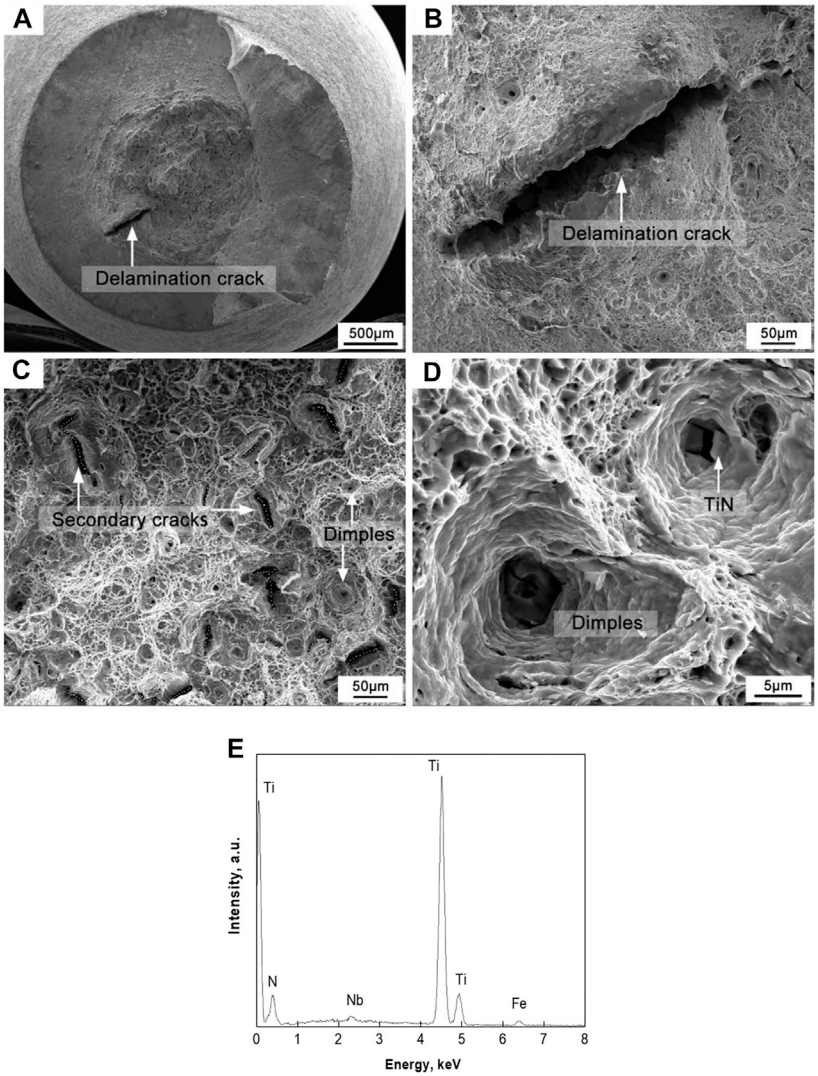

FIGURE 7 | Fracture surfaces of specimens after tensile test **(A)** tensile fracture **(B)** longer delamination crack **(C)** fiber zone **(D)** TiN; and **(E)** EDS spectra of TiN.

EBSD of Fracture and Delamination Crack

Figure 9 shows the reverse pole diagram of the vicinity of the fracture surface and the delamination crack. The martensite structure is entirely around the fracture and the delamination cracks. The influence of grain orientation on the mechanical properties is essential. The <111>||ND direction can better hinder crack propagation than the <001>||ND direction, because the <111>||ND texture exhibits relatively good plasticity in steels. There were mostly red <001>||ND and green <101>||ND near the delamination cracks. This also shows that the delamination cracks easily prorogate along the two grain orientation directions of <001>||ND and <101>||ND. The delamination cracks are wider and extend deeper.

As shown in **Figure 10**, the KAM values are used to evaluate the strain field around the tensile fracture; there are evident deformed grains and local high strain areas near the tensile fracture surface and around the delamination crack. The surrounding strain fields of the delamination crack are more evident. The high strain areas around the delamination crack indicate that the crack propagation is due to local slips. While the delamination cracks propagated inside, a significant amount of energy was consumed in the process of crack propagation.

DISCUSSION

Formation of TiN Inclusions

Adding an appropriate amount of Ti elements to steel helps ensure a certain amount of nanosized TiN particles. These fine TiN particles exhibit good high-temperature stability and

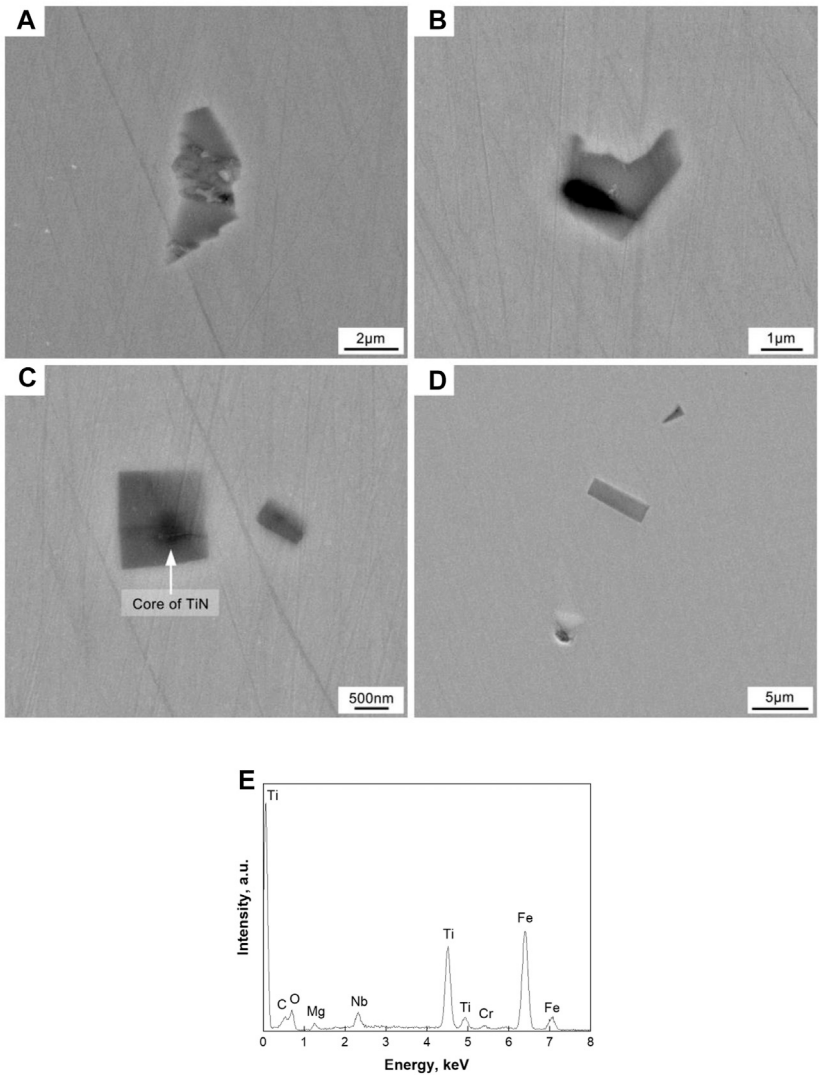

FIGURE 8 | SEM images of TiN inclusions at the longitudinal section of a tensile crack surface (**A**) near the fracture surface (**B**) slightly away from the fracture (**C**) far away from the fracture (**D**) farther from the fracture, and (**E**) EDS spectrum of TiN.

relatively low volume expansion, which is expected to effectively suppress the growth of austenitic grains at high temperatures. Thus, it plays a significant role in precipitation strengthening and grain refinement strengthening of HARDOX 450 steel. However, in the smelting process, microsized TiN inclusions are often formed because of the inappropriate addition of Ti elements, giving rise to a local stress concentration due to the difference in the thermal expansion between TiN inclusions and the matrix (Fairchild et al., 2000). Based on the thermodynamic calculation proposed by Tian et al. (2018), the formulas for TiN reaction and theoretical solubility product K_{TiN} under the liquid phase can be expressed as follows:

$$\mathrm{Ti} + \mathrm{N} = \mathrm{TiN}_{\mathrm{inclusion}}, \tag{1}$$

$$\log K_{\mathrm{TiN}} = \log([\mathrm{Ti}] \cdot [\mathrm{N}]) = -\frac{15218}{\mathrm{T}} + 5.64. \tag{2}$$

As the molten steel solidifies, Ti and N elements accumulate at the solidification front, and the concentrations of both Ti and N change with the solid fraction f_s. The actual concentration product Q_{TiN} of Ti and N in the molten steel is as follows:

$$Q_{\mathrm{TiN}} = \frac{[\mathrm{Ti}]_0 \cdot [\mathrm{N}]_0 \cdot (1 - f_s)^{k_{\mathrm{Ti}} - 1}}{1 - (1 - K_{\mathrm{N}}) \cdot f_s}, \tag{3}$$

where $[\mathrm{Ti}]_0$ and $[\mathrm{N}]_0$ represent the initial concentrations of Ti and N in the solidification front, respectively. k_{Ti} (~0.33) and k_{N} (~0.48) represent the equilibrium distribution coefficients of Ti and N, respectively.

The temperature of the solidification front can be expressed as:

$$T = T_{Fe} - \frac{T_{Fe} - T_l}{1 - f_s(T_l - T_s)/(T_{Fe} - T_s)}, \tag{4}$$

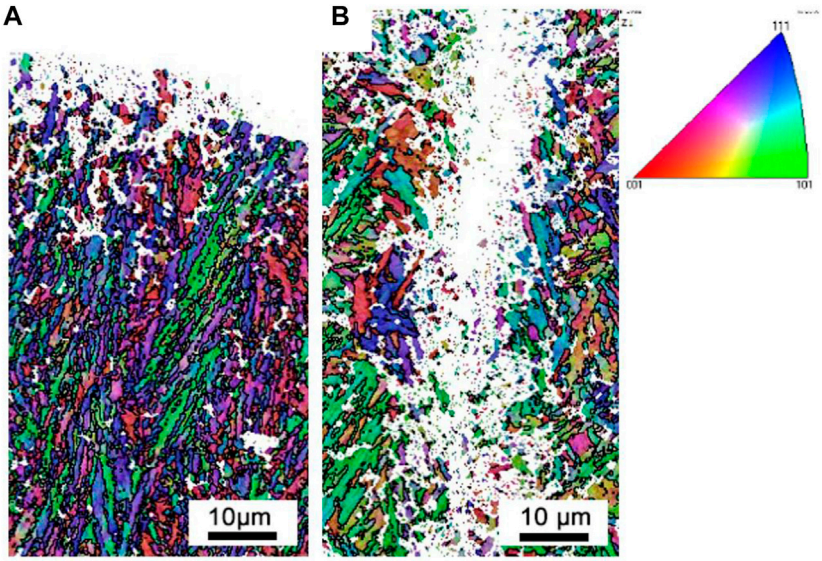

FIGURE 9 | IPF(//ND) maps of (**A**) near fracture surface, and (**B**) around delamination cracks.

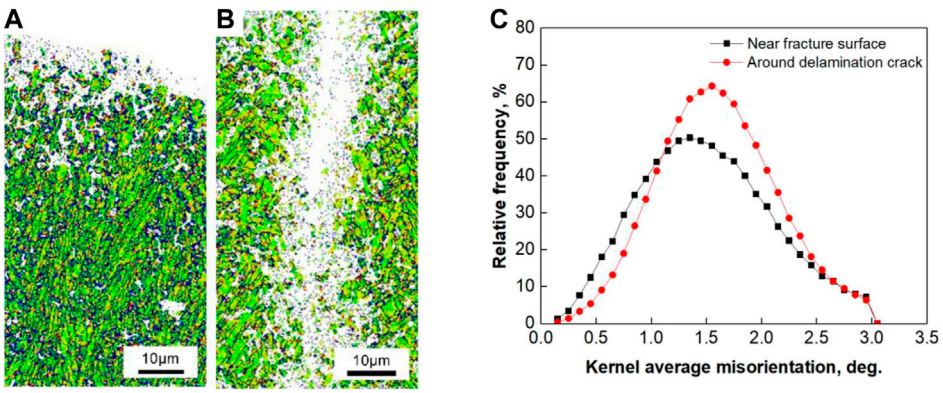

FIGURE 10 | KAM maps of (**A**) near fracture surface (**B**) around delamination cracks, and (**C**) corresponding KAM value distribution.

where T is the temperature of the solidification front of the molten steel, and T_{Fe} (~1809 K) is the melting point temperature of the molten steel.

Using the casting simulation software to analyze the solidification process of the molten steel, we determined the liquidus temperature (T_l = 1781 K) and solidus temperature (T_s = 1740 K). According to **Eqs 2**, **3**, the thermodynamic curve is plotted in **Figure 11.** Thus, the solid-phase fraction f_s was determined to be approximately 0.86 when TiN particles started to precipitate. The precipitation temperature of the TiN was approximately 1750 K. TiN was formed in the solid–liquid zone; hence, the TiN inclusions were large, as mentioned in *Microstructure*.

Propagation Behavior of Microcracks

Based on the TiN morphology observed at the transverse section of the tensile fracture surface (**Figure 8**), it is found that, the closer the TiN inclusions to the fracture surface, the more severe the breaking of TiN. **Figure 12** shows a schematic of the propagation behavior of the microcracks in the TiN inclusions when subjected to tensile stress. In this case, the following two types of fracture mechanisms may occur: 1) For TiN inclusions without a heterogeneous core, microcracks are induced at the TiN inclusions via brittle fracture. With increasing stress, a single microcrack first appeared inside the microsized TiN inclusions, and then, multiple microcracks formed, some of which widened in the direction of tensile stress. 2) For TiN inclusions with a core of oxide inclusion, the microcracks nucleate from the inclusion core and then widen along the direction of tensile stress, further giving rise to multiple microcracks.

A detailed analysis of the TiN fracture mechanism reveals why the microcracks in the TiN inclusions did not propagate into the surrounding matrix but widened and gave rise to multiple microcracks so as to disperse the local stress. This implies that the matrix had a strong ability to arrest the cracks. In martensitic

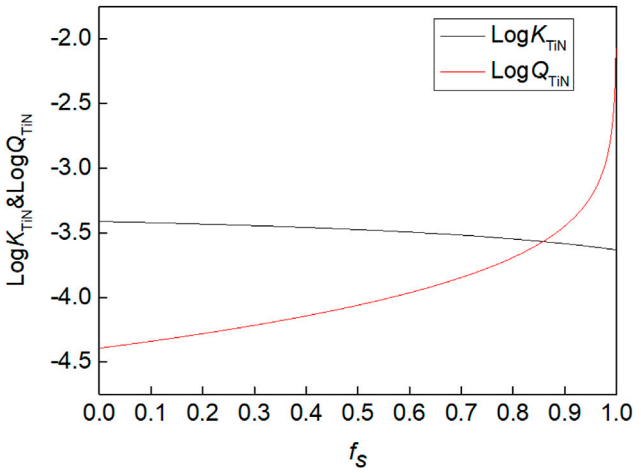

FIGURE 11 | Relationship between the theoretical (k_{TiN}) and actual concentration products (Q_{TiN}) of TiN and the solid fraction (fs).

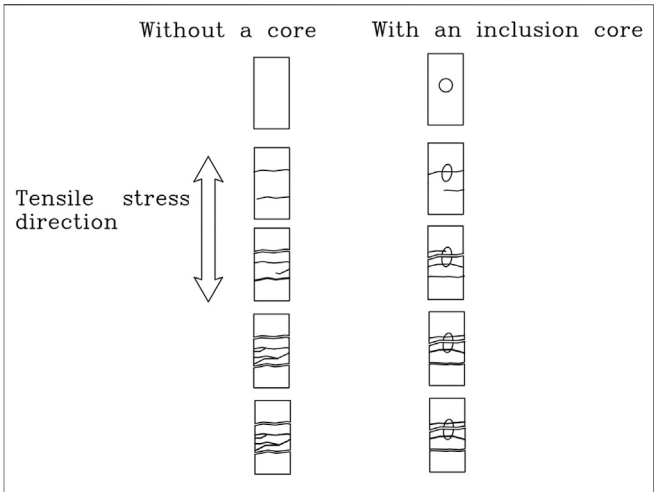

FIGURE 12 | Schematic of the microcrack growth behavior of TiN when subjected to tensile stress.

steels, the boundaries of martensite lath bundles, lath blocks, and prior austenitic grains play an important role in preventing crack propagation. The microstructures of high-angle-grain boundaries (HAGBs) of more than 50° effectively retarded crack propagation because the cracks consumed more energy when encountering these boundaries (Wang et al., 2008; Yan et al., 2014). In **Figure 4**, we can know that the average grain size of the matrix is very small. The fine grain structure provides a higher grain boundary density (Inoue et al., 2020) and smaller martensite packet size, which results in the high proportion of HAGBs of more than 50° (Wang et al., 2008; Cho et al., 2021). The proportion of HAGBs of more than 50° accounted for 63.5% at the quarter thickness and 53.8% at the center. In particular, microsized TiN inclusions in the present HARDOX 450 steel were easily broken when subjected to tensile stress. The microcracks in the TiN inclusions cannot extend into the matrix; hence, the energy cannot be released, resulting in the formation of multiple microcracks. Therefore, the excellent properties of HARDOX 450 steel can be mainly attributed to the fact that the matrix effectively arrested the microcracks and that the secondary and delamination cracks induced by the applied tensile stress released energy.

CONCLUSION

1) HARDOX 450 steel exhibited superior mechanical properties: The yield and tensile strengths were no less than 1100 MPa and 1300 MPa, respectively, with the total elongation exceeding 12%. The tensile properties in all the directions were relatively uniform.

2) The tensile fracture surface of HARDOX 450 steel could be mainly characterized by ductile dimples, tear ridges, secondary cracks, delamination cracks, and few cleavage facets. The microsized TiN inclusions gave rise to deep dimples rather than a cleavage fracture plane, which is related to the ability of the microstructure to arrest cracks.

3) TiN particles in the HARDOX 450 steel precipitated into the solid–liquid zone. Upon tensile loading, a single microcrack first appeared inside the microsized TiN inclusions, and then, multiple microcracks formed, some of which widened in the direction of tensile stress. Microsized TiN inclusions were easily broken when subjected to tensile stress, because a large proportion of HAGBs with more than 50° effectively prevented crack propagation into the matrix.

DATA AVAILABILITY STATEMENT

The original contributions presented in the study are included in the article/Supplementary Material, further inquiries can be directed to the corresponding author.

AUTHOR CONTRIBUTIONS

ZW: Writing-Original Draft, Conceptualization, Investigation. XW: Investigation. DL: Resources, Methodology. XZ: Writing-Review and Editing, Supervision, Conceptualization, Funding acquisition.

FUNDING

This work was supported by Henan Provincial Science and Technology Cooperation Project China (No.182106000016).

REFERENCES

Cho, L., Bradley, P. E., Lauria, D. S., Martin, M. L., Connolly, M. J., Benzing, J. T., et al. (2021). Characteristics and Mechanisms of Hydrogen-Induced Quasi-Cleavage Fracture of Lath Martensitic Steel. *Acta Materialia*. 206, 116635. doi:10.1016/J.ACTAMAT.2021.116635

Fairchild, D. P., Howden, D. G., and Clark, W. A. T. (2000). The Mechanism of Brittle Fracture in a Microalloyed Steel: Part I. Inclusion-Induced Cleavage. *Metall. Mat Trans. A.* 31, 641–652. doi:10.1007/s11661-000-0007-4

Fu, J., Qiu, W., Nie, Q., and Wu, Y. (2017). Precipitation of TiN during Solidification of AISI 439 Stainless Steel. *J. Alloys Compounds*. 699, 938–946. doi:10.1016/j.jallcom.2017.01.018

Ghosh, A., Ray, A., Chakrabarti, D., and Davis, C. L. (2013). Cleavage Initiation in Steel: Competition between Large Grains and Large Particles. *Mater. Sci. Eng. A*. 561, 126–135. doi:10.1016/j.msea.2012.11.019

Han, J., Zhu, Z., Wei, G., Jiang, X., Wang, Q., Cai, Y., et al. (2020). Microstructure and Mechanical Properties of Nb- and Nb + Ti-Stabilised 18Cr-2Mo Ferritic Stainless Steels. *Acta Metall. Sin. (Engl. Lett)*. 33, 716–730. doi:10.1007/s40195-019-00988-y

Hulka, K., Kern, A., and Schriever, U. (2005). Application of Niobium in Quenched and Tempered High-Strength Steels. *Mater. Sci. Forum*. 500-501, 519–526. doi:10.4028/www.scientific.net/msf.500-501.519

Inoue, T., and Ueji, R. (2020). Improvement of Strength, Toughness and Ductility in Ultrafine-Grained Low-Carbon Steel Processed by Warm Bi-axial Rolling. *Mater. Sci. Eng. A*. 786, 139415. doi:10.1016/j.msea.2020.139415

Jiang, Z. Q., Fu, H. G., Yin, E. S., and Tian, Y. T. (2011). Investigation and Application of High Strength Low Alloy Wear Resistant Cast Steel. *Mater. Technology*. 26, 58–61. doi:10.1179/175355510X12767031422841

Jin, Y. L., and Du, S. L. (2018). Precipitation Behaviour and Control of TiN Inclusions in Rail Steels. *Ironmaking & Steelmaking*. 45, 224–229. doi:10.1080/03019233.2016.1253448

Kang, Y., Mao, W. M., Chen, Y. J., Jing, J., and Cheng, M. (2016). Effect of Ti Content on Grain Size and Mechanical Properties of UNS S44100 Ferritic Stainless Steel. *Mater. Sci. Eng. A*. 677, 211–221. doi:10.1016/j.msea.2016.08.070

Lambert-perlade, A., Sturel, T., Gourgues, A. F., Besson, J., and Pineau, A. (2004). Mechanisms and Modeling of Cleavage Fracture in Simulated Heat-Affected Zone Microstructures of a High-Strength Low Alloy Steel. *Metall. Mat Trans. A*. 35, 1039–1053. doi:10.1007/s11661-004-0030-y

Liu, T., Long, M.-j., Chen, D.-f., Duan, H.-m., Gui, L.-t., Yu, S., et al. (2018). Effect of Coarse TiN Inclusions and Microstructure on Impact Toughness Fluctuation in Ti Micro-alloyed Steel. *J. Iron Steel Res. Int.* 25, 1043–1053. doi:10.1007/s42243-018-0149-5

Nikitin, V. N., Nastich, S. Y., Smirnov, L. A., Mal'tsev, A. B., Denisov, S. V., Chevskaya, O. N., et al. (2016). Economically Alloyed High-Strength Steel for Use in Mine Equipment. *Steel Transl.* 46, 742–751. doi:10.3103/S0967091216100089

Ojala, N., Valtonen, K., Heino, V., Kallio, M., Aaltonen, J., Siitonen, P., et al. (2014). Effects of Composition and Microstructure on the Abrasive Wear Performance of Quenched Wear Resistant Steels. *Wear*. 317, 225–232. doi:10.1016/j.wear.2014.06.003

Ryabov, V. V., Kniaziuk, T. V., Mikhailov, M. S., Motovilina, G. D., and Khlusova, E. I. (2017). Structure and Properties of New Wear-Resistant Steels for Agricultural Machine Building. *Inorg. Mater. Appl. Res.* 8, 827–836. doi:10.1134/S2075113317060120

Shi, C.-b., Liu, W.-j., Li, J., and Yu, L. (2016). Effect of Boron on the Hot Ductility of Low-Carbon Nb-Ti-Microalloyed Steel. *Mater. Trans.* 57, 647–653. doi:10.2320/matertrans.M2015388

Sun, F. L., Geng, K., Yu, F., and Luo, H. W. (2020). Relationship of Inclusions and Rolling Contact Fatigue Life for Ultra-clean Bearing Steel. *Acta Metall. Sin.* 56, 693–703. doi:10.11900/0412.1961.2019.00337

Sun, J., Jiang, T., Liu, H., Guo, S., and Liu, Y. (2016). Enhancement of Impact Toughness by Delamination Fracture in a Low-Alloy High-Strength Steel with Al Alloying. *Metall. Mat Trans. A*. 47, 5985–5993. doi:10.1007/s11661-016-3707-0

Tian, Q., Wang, G., Zhao, Y., Li, J., and Wang, Q. (2018). Precipitation Behaviors of TiN Inclusion in GCr15 Bearing Steel Billet. *Metall. Materi Trans. B*. 49, 1149–1164. doi:10.1007/s11663-018-1230-y

Wang, C., Wang, M., Shi, J., Hui, W., and Dong, H. (2008). Effect of Microstructural Refinement on the Toughness of Low Carbon Martensitic Steel. *Scripta Materialia*. 58, 492–495. doi:10.1016/j.scriptamat.2007.10.053

Yan, P., Liu, Z., Bao, H., Weng, Y., and Liu, W. (2014). Effect of Tempering Temperature on the Toughness of 9Cr-3W-3Co Martensitic Heat Resistant Steel. *Mater. Des.* 54, 874–879. doi:10.1016/j.matdes.2013.09.017

Yan, W., Shan, Y. Y., and Yang, K. (2006). Effect of TiN Inclusions on the Impact Toughness of Low-Carbon Microalloyed Steels. *Metall. Mat Trans. A*. 37, 2147–2158. doi:10.1007/BF02586135

Yan, W., Shan, Y. Y., and Yang, K. (2007). Influence of TiN Inclusions on the Cleavage Fracture Behavior of Low-Carbon Microalloyed Steels. *Metall. Mat Trans. A*. 38, 1211–1222. doi:10.1007/s11661-007-9161-2

Conflict of Interest: The authors declare that the research was conducted in the absence of any commercial or financial relationships that could be construed as a potential conflict of interest.

frontiers in Materials

ORIGINAL RESEARCH
published: 09 June 2021
doi: 10.3389/fmats.2021.667771

Fatigue Behavior of an Al-12.7Si-0.7Mg Alloy Processed by Extrusion and Heat Treatment

Fang Liu, Fuxiao Yu, Dazhi Zhao and Li Gao*

Key Laboratory of Lightweight Structural Materials, School of Materials Science and Engineering, Northeastern University, Shenyang, China

The fatigue life of a hot extruded Al-12.7Si-0.7Mg alloy under T1, T4, and T6 conditions was studied. The microstructure and tensile properties of the alloy were investigated in order to analyze the fatigue behavior. The results of the fatigue test showed that an extruded Al-12.7Si-0.7Mg alloy provided greater fatigue life compared to a cast Al-Si alloy, which was explained by the refined microstructure characterized by fine Si particles uniformly distributed in the Al matrix of fine equiaxed grains promoted by hot extrusion. The fatigue property of the alloy in T6 treatment was higher than that in the T4 and T1 conditions due to strengthening precipitation.

Keywords: Al-Si alloy, extrusion, heat treatment, microstructure, fatigue, fractography

OPEN ACCESS

Edited by:
Qi Chao,
Deakin University, Australia

Reviewed by:
Lu Jiang,
Deakin University, Australia
Xin Xin,
Institute of Metals Research (CAS), China

****Correspondence:***
Fuxiao Yu
fxyu@mail.neu.edu.cn

Specialty section:
This article was submitted to Structural Materials, a section of the journal Frontiers in Materials

Received: *14 February 2021*
Accepted: *03 May 2021*
Published: *09 June 2021*

Citation:
Liu F, Yu F, Zhao D and Gao L (2021) Fatigue Behavior of an Al-12.7Si-0.7Mg Alloy Processed by Extrusion and Heat Treatment. Front. Mater. 8:667771. doi: 10.3389/fmats.2021.667771

INTRODUCTION

Wrought Al-Si alloys for structural application have been generated by the combination of direct chill casting and plastic deformation (Yu et al., 2005). The microstructure of the deformed Al-12.7Si-0.7Mg alloy consists of fine and uniformly distributed Si particles on equiaxed Al grain boundaries. The alloy after artificial aging treatment exhibits good ductility and much higher proof strength as well as tensile strength compared to the 6,063 alloy, as the result of the microstructure feature (Yu et al., 2005; Liu et al., 2011).

In terms of casting Al-Si alloys, many researchers have indicated that casting defects like porosity is one factor which effects the fatigue performance (Casellas et al., 2005; Yi et al., 2006; Atxaga et al., 2013). Microstructure features including eutectic silicon characteristics (i.e., size and morphology) (Casellas et al., 2005; Ammar et al., 2008; Mbuya et al., 2011), secondary dendrite arm spacing (SDAS) (Yi et al., 2004; Shaha et al., 2015), and intermetallic compounds also influence the fatigue properties. Mbuya et al. (2011) found that larger-sized Si particles and elongated particles are more likely to cause crack initiation than average-sized Si particles. In addition, a fine microstructure with smaller SDAS and cell size could increase the fatigue life (Yi et al., 2004; Shaha et al., 2015).

The fatigue properties of wrought Al-Mg-Si alloys have also been studied. Coarse intermetallic secondary phases, Mg_2Si metastable phase, and surface qualities influence the fatigue properties (Borrego et al., 2004; Azzam et al., 2010). The wrought Al-12.7Si-0.7Mg alloy has the same elements as wrought Al-Mg-Si alloys. However, it should be pointed out that the microstructure of the wrought Al-Si alloy distinguishes itself from that of most wrought Al-Mg-Si alloys, by its fine equiaxed grains in the Al matrix and the uniform distribution of fine Si particles on the grain boundaries (Liu et al., 2011). Compared to a casting Al-Si alloy, the Si morphology distribution of the wrought Al-12.7Si-0.7Mg alloy is dispersed due to

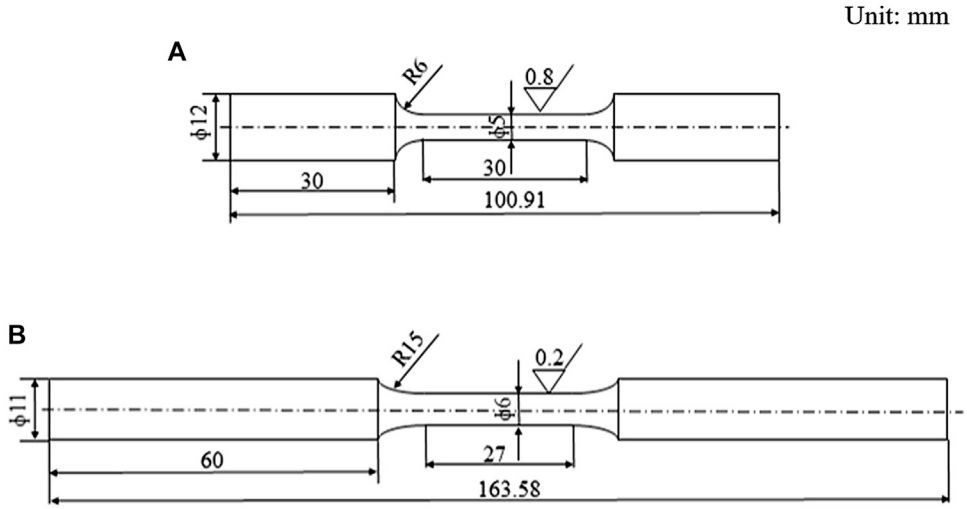

FIGURE 1 | Dimension diagram of the specimen, **(A)** mechanical test, **(B)** fatigue test.

hot-deformation (Liu et al., 2011). There are few studies reporting the fatigue behavior of extruded Al-Si alloys (Ham et al., 2017; Wang et al., 2018).

In this paper, the fatigue properties of the wrought Al-12.7Si-0.7Mg alloy were investigated to fully supplement the previously unaddressed properties of the newly developed structural applications for the Al-Si alloy when it is under repeated cyclic loading.

MATERIALS AND METHODS

An extruded Al-12.7Si-0.7Mg alloy rod was studied, which was produced by direct chill casting and then hot extruded. The diameter of the extruded rod was 12 mm. The extruded bar (T1) was subjected to T4 (solution treatment + nature aging) and T6 (solution treatment + artificial aging) heat treatment carried out in a Muffle furnace. The solution treatment of the sample was performed at 540°C for 90 min and quenched into water at room temperature. After quenching, artificial aging of the specimens was carried out at 180°C for 3 h.

Mechanical tests were performed on a SHIMADZU AG-X plus testing machine at a cross-head speed of 0.2 mm/min. The mechanical properties of the alloy in different conditions were the average for three specimens. Fatigue tests were performed on a fatigue testing machine (NYEEHF-EV200K2-040-1A) at a stress ratio of -1 using a sinusoidal cycle at a frequency of 20 Hz at room temperature. **Figure 1** shows the dimension of the specimen for the mechanical test and fatigue test. Based on tensile test results, the cyclic maximum stress levels of the extruded alloy (T1) were set to 130, 140, 150, 160, and 180 MPa, respectively. The cyclic maximum stress levels of the T4 condition were set to 150, 160, 170, 180, and 190 MPa, respectively. The cyclic maximum stress levels of the T6 condition were set to 170, 180, 190, 200, 210, and 220 MPa, respectively. Four fatigue specimens were tested at each stress level to obtain the average fatigue life. The fatigue test was stopped at 2×10^6 cycles without failure.

The microstructure of the alloys in the T1, T4, and T6 conditions were analyzed by an optical microscope (Olympus DSX500). In order to analyze the grain size, the EBSD band contrast image was carried out by FIB-SEM (crossbeam550). Image-Pro Plus image analysis software was used to investigate the Si particle size and matrix grain size. Conventional transmission electron microscope (TEM) observations were performed using a FEI Tecnai F20 electron microscope operated at 200 KV. TEM thin foils were prepared by double jet electropolishing with a solution of 30% nitric acid in methanol at −20°C and a voltage of 20 V. The fracture surfaces were studied by ZEISS Ultra Plus scanning electron microscopy (SEM) to determine the fracture mode.

RESULTS AND DISCUSSION

Microstructure

The microstructures of the longitudinal (along the extrusion direction) section of the alloy are shown in **Figure 2**. Compared with the T1 condition, the solid solution treatment changed the size of the Si particles. Si particles were gradually round and their aspect ratio was decreased in the T4 condition. The grain size of the Al matrix on the cross-section (transverse to the extrusion direction) of the extruded alloy was analyzed by electron back-scattered diffraction (EBSD). The EBSD band contrast images of the alloy under T1, T4, and T6 conditions are shown in **Figure 3**. Hot extrusion resulted in a

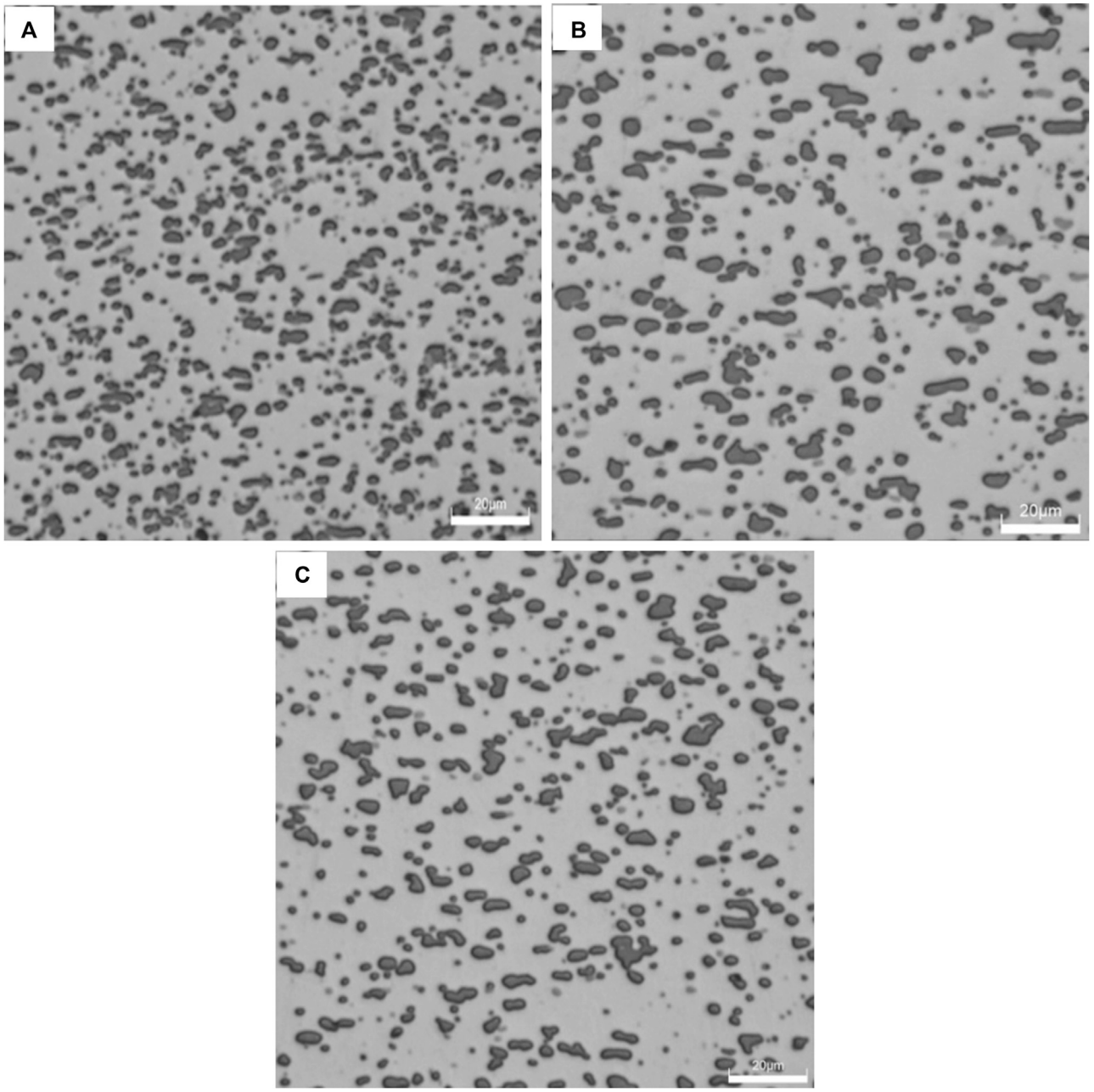

FIGURE 2 | The optimal microstructure of the alloy in different conditions, **(A)** T1, **(B)** T4, **(C)** T6.

uniform distribution of fine Si particles as well as other second phase particles in the Al matrix of fine equiaxed grains via dynamic recrystallization (Liu et al., 2011). After solution treatment, the Al grain size increased from 6.5 to 6.9 μm. It is worth noticing that the change of the size of the Si particles and the Al matrix grains was not considerable during solid solution treatment due to mutual restraint between the grain growth of the Al matrix and the coarsening of the Si particles.

Figure 4 shows the TEM images (B = $[110]_{Al}$) of the alloy in different conditions. It can be seen that in the T1 and T4 conditions a high density of dislocations in the Al matrix occurred. While needle-like precipitates were visible in the Al matrix in the T6 condition as shown in **Figure 4C**.

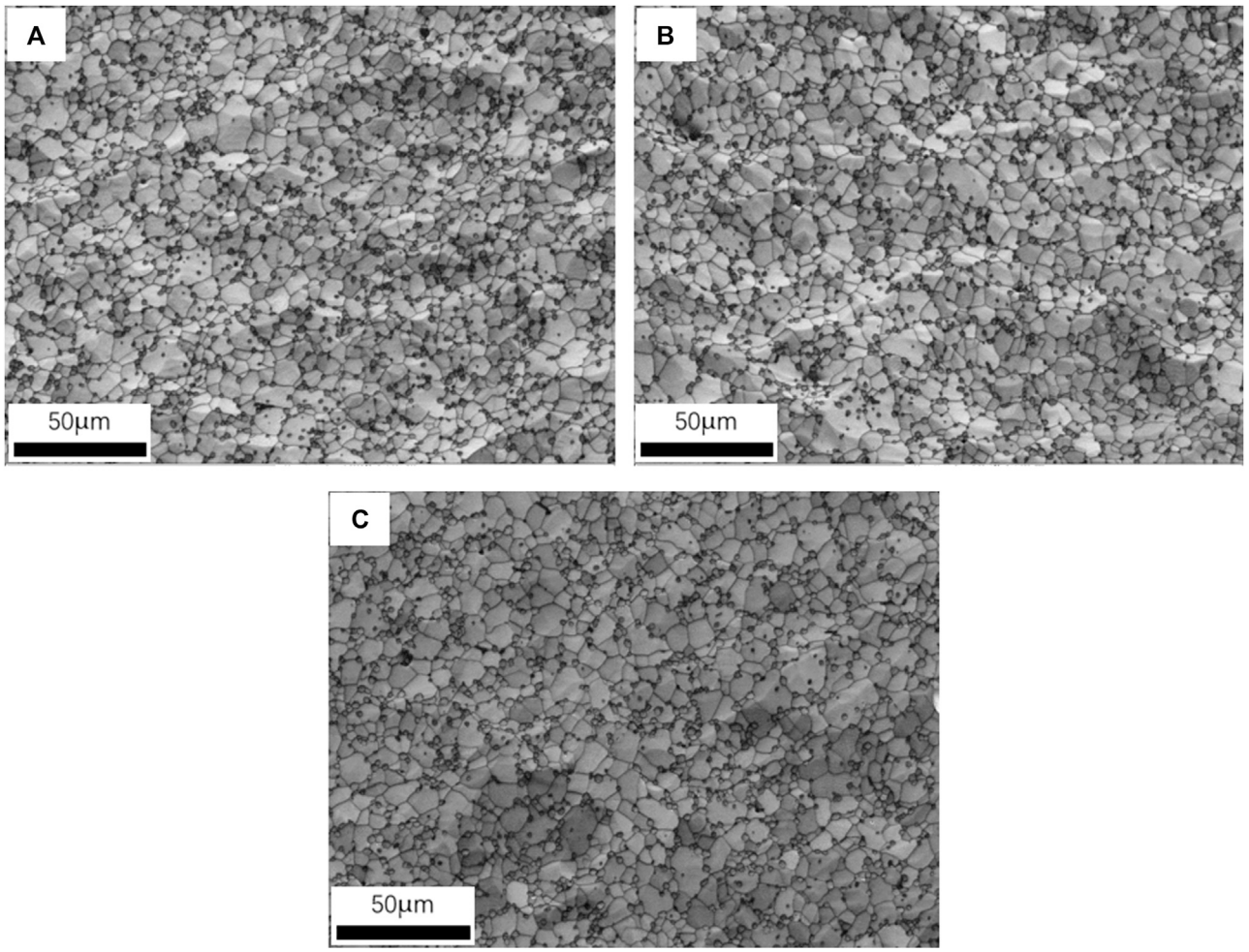

FIGURE 3 | The EBSD band contrast images of the alloy in different conditions, **(A)** T1, **(B)** T4, **(C)** T6.

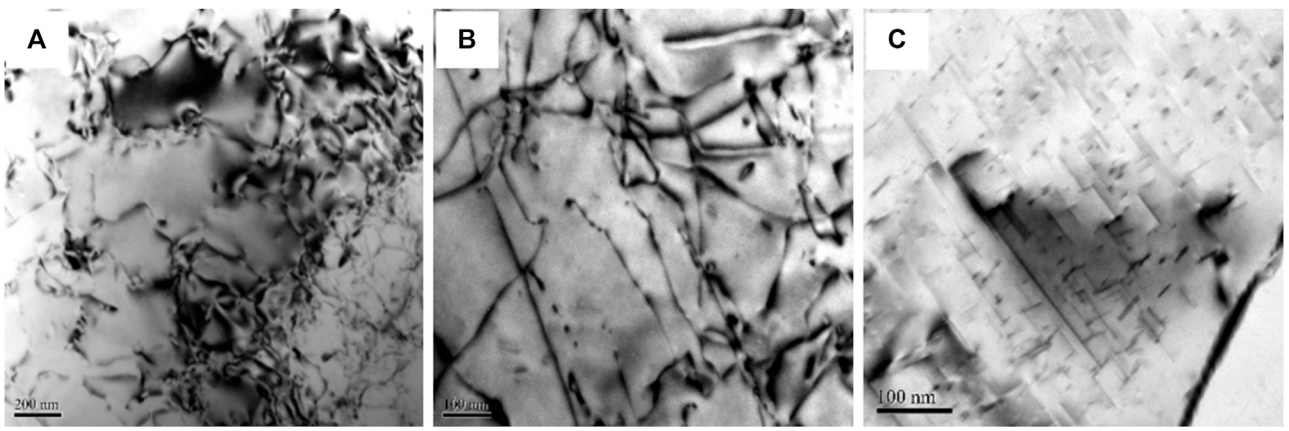

FIGURE 4 | The TEM image of the alloy in different conditions, **(A)** T1, **(B)** T4, **(C)** T6.

TABLE 1 | Mechanical properties of the alloy in different conditions.

Alloy conditions	YS (MPa)	UTS (MPa)	Elongation (%)
T1	175	265	15.5
T4	188	316	15.2
T6	300	348	6.2

TABLE 2 | Material constants of the alloy in different conditions.

Alloy conditions	*n*	C_s
T1	12.565	5.79×10^{32}
T4	9.156	1.25×10^{26}
T6	9.496	2.37×10^{27}

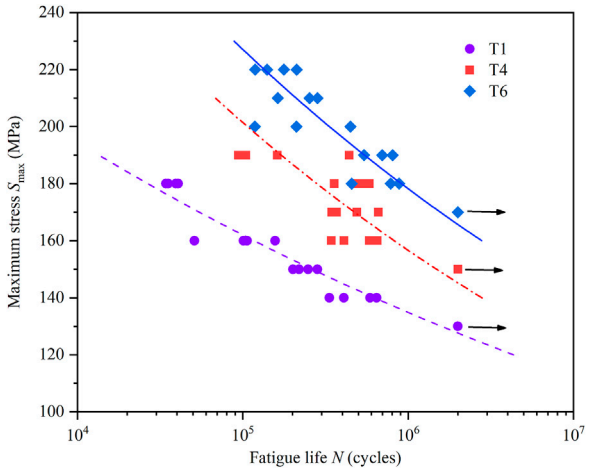

FIGURE 5 | S-N curves of the Al-12.7Si-0.7Mg alloy in different conditions.

Mechanical Properties

Table 1 lists the room temperature mechanical properties of the alloy in the three conditions. Yield strength (YS), ultimate tensile strength (UTS), and elongation of the alloy in T4 and T6 were much higher than that in the T1 condition. The Mg_2Si phase was in the form of solute atoms in the matrix in the T4 condition which led to solid-solution strengthening (Liu et al., 2011). It is clear that precipitation hardening contributed to increased YS and UTS in T6 treatment. Precipitates and Si particles had a strong pinning effect on the movement of dislocations.

Fatigue Properties

The fatigue test data were fitted by the square method based on a linear correlation between fatigue life and fatigue strength as shown in **Eq. 1**. **Table 2** lists the material constants of the samples under different conditions. And the fitted curve of the logarithmic scale was plotted, as shown in **Figure 3**.

$$\lg N = \lg C_s - n\lg S_{\max}, \quad (1)$$

N is the fatigue life, C_s and n are the material constants; and $S_{\max}$ is the maximum stress.

Figure 5 shows the S-N curves of the alloy in the T1, T4, and T6 conditions. Fatigue lives of the alloy in each condition gradually increased with a decrease in stress amplitude. It is clearly shown that fatigue lives for the specimens in T4 and T6 treatment increased compared to the T1 condition at the same stress amplitude. The fatigue strength increased significantly in T4 and T6 after heat treatment. The optical microstructures and the EBSD band contrast image shown in **Figures 2**, **3** present information about the changes of the Si particles and the grain. In contrast, the Si particles were coarsened by solid solution treatment. There was no obvious change in grain size and Si particles after aging. However, there were obvious differences between that in the T6 condition and that in the T4 and T1 conditions according to the TEM images shown in **Figure 4**. Uniform and fine distribution of precipitates were observed in the matrix. It is obvious that considerable improvement in fatigue life and fatigue strength occurred, which was attributed to solution treatment and artificial aging.

There have been no similar fatigue results of a wrought Al-Si alloy with similar compositions that could be compared with the results in this study. However, according to the study of Ammar et al. (2008), the fatigue life of A356 is between 10^6 and 4×10^6 cycles when the stress amplitude is 68 MPa, and the value also depends on the size of the pore area. The stress amplitude in this study was much higher. Yi et al. (2004) investigated the fatigue life of an A356 alloy in the T6 condition which is comparable to the extruded Al-12.7Si-0.7Mg alloy at the same stress amplitudes. It would indirectly indicate that the extruded Al-12.7Si-0.7Mg alloy especially in the T4 and T6 conditions has excellent fatigue properties.

Fractography

Macroscopic views of the fatigue fracture surface of the alloy in different conditions are illustrated in **Figure 6**. It can be clearly seen that there is a fatigue crack initiation zone, crack propagation zone, and final fracture zone under each condition. The area of crack propagation zone in T6 condition is larger and more obvious than others.

In order to investigate the fatigue crack initiation zone in detail, **Figure 7** shows the fatigue crack initiation zone of the alloy in different conditions and stress amplitudes. The observation of fatigue crack initiation of the as-extruded alloy at 140 MPa is given in **Figure 7A**. As shown in the figure, the fatigue crack initiated a crystal slip as marked by the white line frame. **Figures 7B,C** indicate that the crack of the as-extruded alloy at 160 MPa and the as-solutioned alloy at 180 MPa alloy were from the specimen surface. The crack initiation site of the alloy in the T6 condition is shown in **Figure 7D** loaded with a stress amplitude of 180 MPa. There were silicon particles deboned from the matrix near the specimen surface. Based on the above observation, the crack initiation area was commonly from the surface. Even though

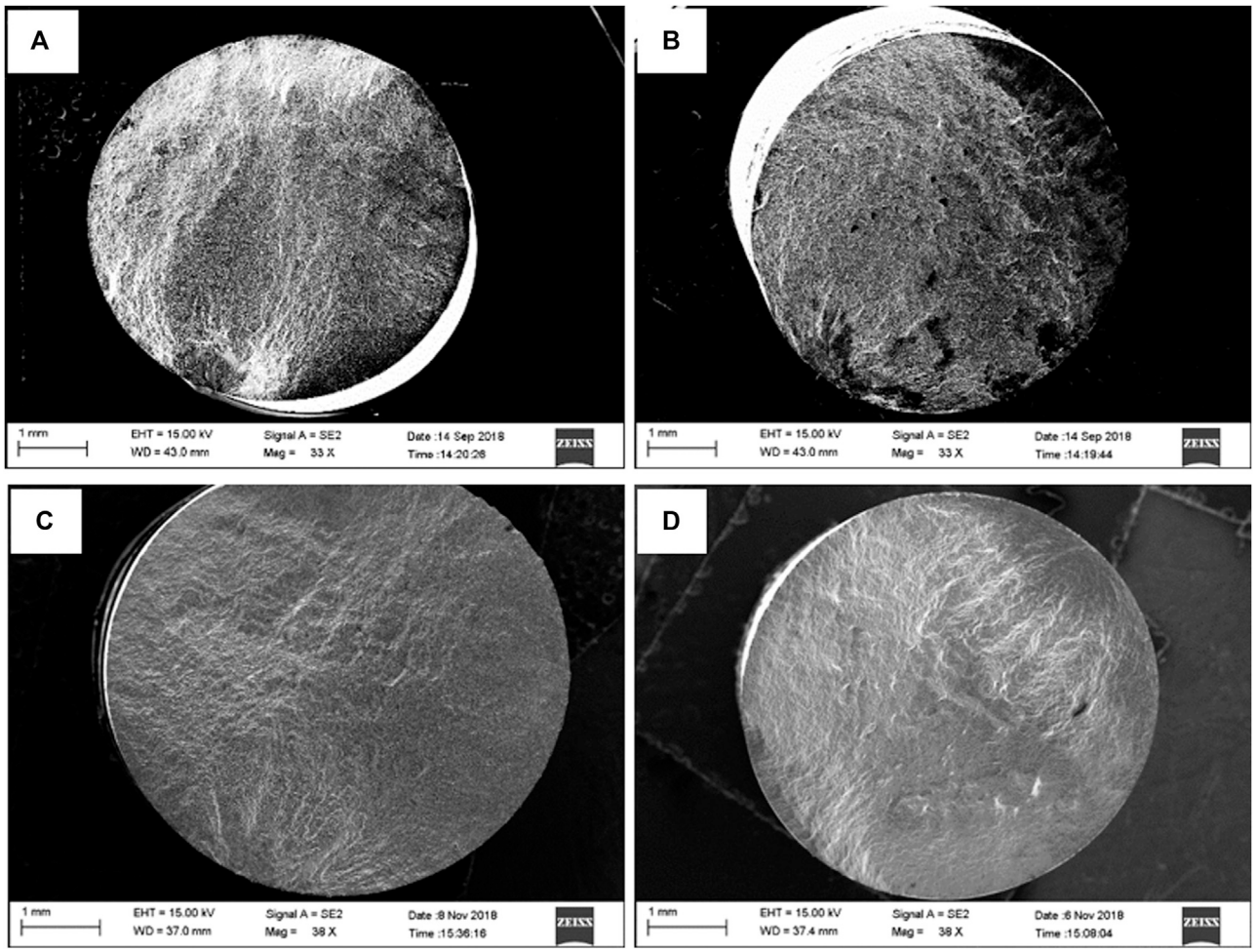

FIGURE 6 | Macroscopic view of the fatigue fracture surface of the alloy in different conditions and stress amplitudes, **(A)** T1-160 MPa, **(B)** T4-160 MPa, **(C)** T4-190 MPa, **(D)** T6-190 MPa.

crystal slip and interface debonding between the silicon and the matrix could be observed in **Figures 7A,D**, that is rare. In the cast Al-Si alloy, the defects at or near the sample surface, the larger size of eutectic Si, or intermetallic compounds acted as origin sites for crack nucleation. The wrought Al-Si alloy in this study had no casting defects due to hot extrusion. Strong interfacial bonding between the Si particle and the aluminum matrix existed because of the morphology of Si. Mbuya et al. (2011) concluded that larger-sized Si particles and elongated particles are more likely to cause crack initiation.

Figure 8 shows the crack propagation area of the alloy in different conditions. The areas are characterized by fatigue striations caused by several successive cycles. In **Figures 8A,B**, fatigue striations are accompanied by secondary cracks. The Si particles and precipitates in the T6 condition played a role in the strengthening phase by changing the crack propagation direction. The final fracture zone of the alloy is presented in **Figure 9**. It is noticeable that all tested conditions exhibited the characteristics of classic ductile fractures.

Total fatigue life is dependent on crack initiation life and crack propagation life (Yi et al., 2004). The function of the Si particles of the studied alloy was to block the movement of dislocation. A high strain concentration would occur between the Si particle and Al matrix because of dislocation accumulation. Fatigue cracks may be formed either by cracking Si particles or along the interface between Si particles and the Al matrix at the point of reaching critical stress. The debonding of Si particles was observed, as shown in **Figure 7D**. After solid solution treatment, Si particles were gradually rounded and their aspect ratio decreased which is beneficial to extending crack initiation life and crack propagation life. In addition, the matrix was strengthened by Mg_2Si in the form of solute atoms where crack growth rate and crack propagation are slow. The precipitates in the T6 condition further increased yield stress which decreased the number and size of the plastic deformation areas (Yi et al.,

2004). Moreover, precipitates increased the resistance of the crack growth to produce a longer fatigue life.

CONCLUSION

An extruded Al-12.7Si-0.7Mg alloy has excellent fatigue properties due to the refined microstructure characterized by fine Si particles uniformly distributed in the Al matrix of fine equiaxed grains promoted by hot extrusion. The mechanical properties and fatigue properties of the alloy in T6 treatment was higher than that in the T4 and T1 conditions due to precipitation strengthening. Fatigue cracks were more likely to initiate from the specimen surface. Crystal slip bands and interface debonding between the silicon and matrix may act as crack initiation sites as was found to be the case in a certain sample tested.

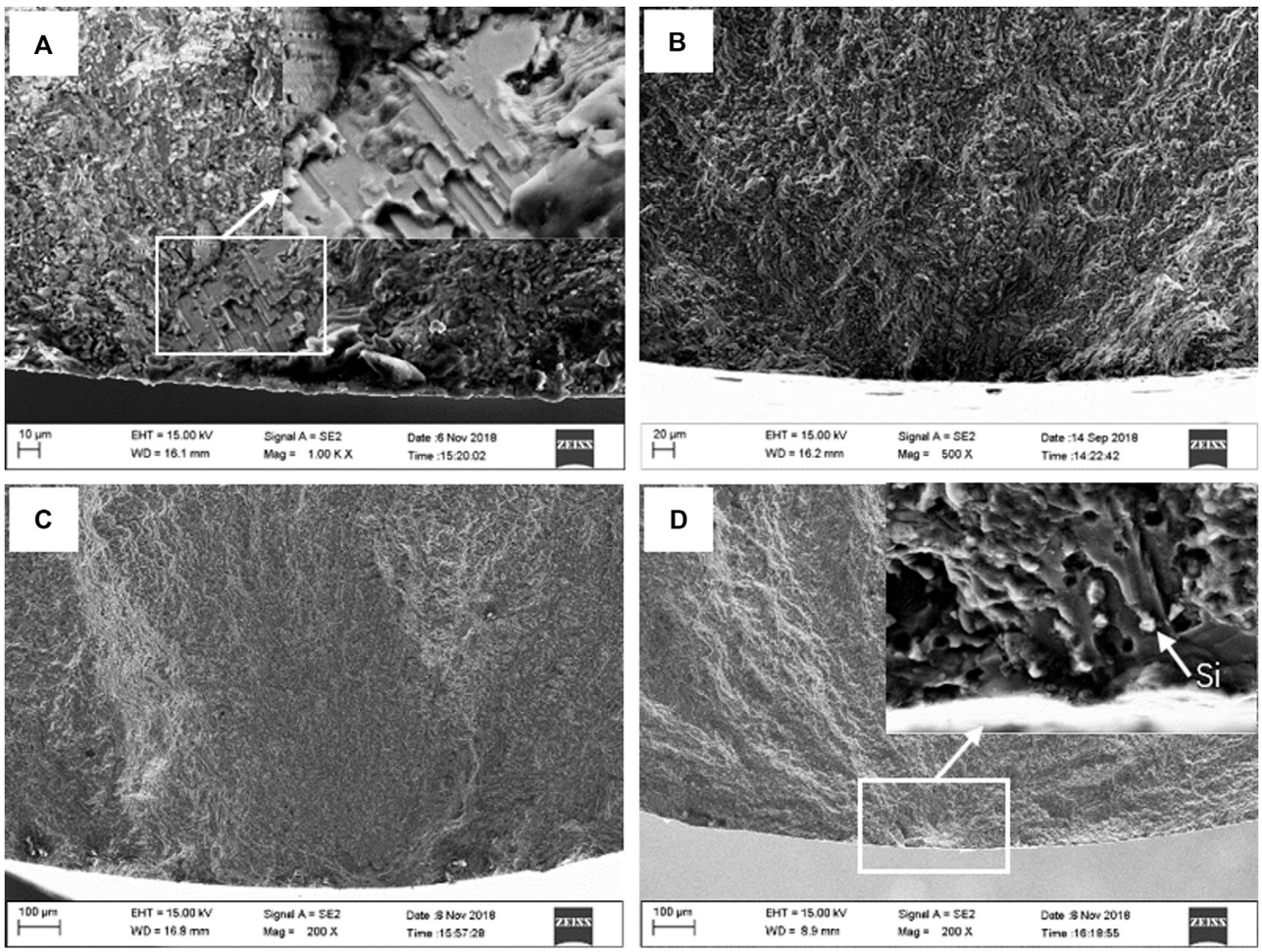

FIGURE 7 | Fatigue crack initiation zone of the alloy in different conditions and stress amplitudes, **(A)** T1-140 MPa, **(B)** T1-160 MPa, **(C)** T4-180 MPa, **(D)** T6-180 MPa.

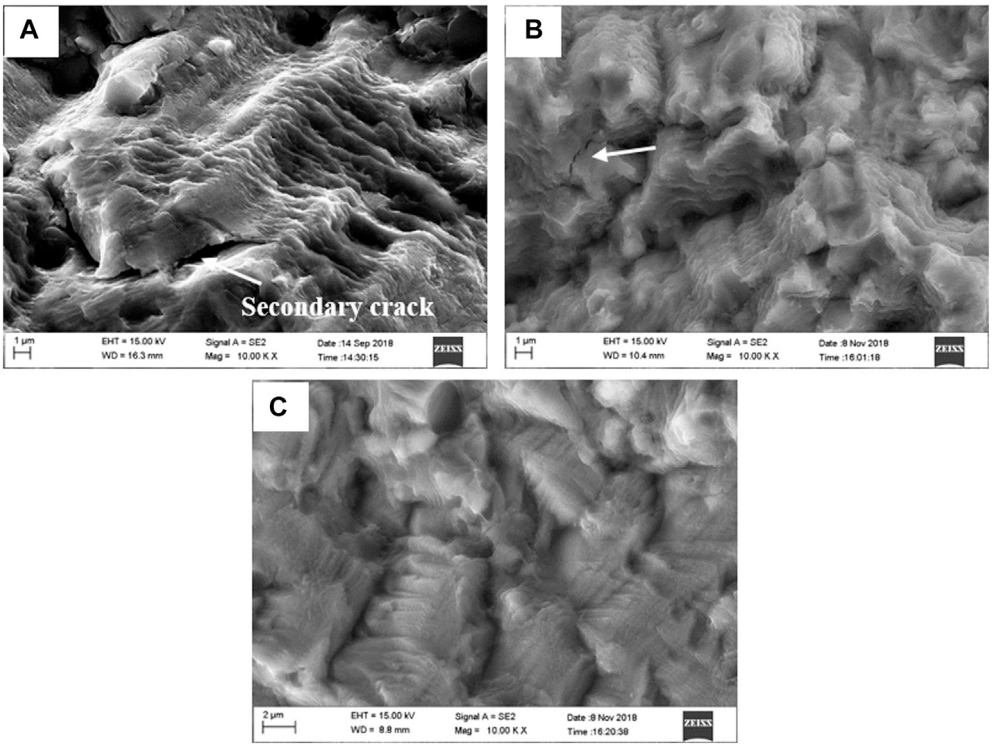

FIGURE 8 | Fatigue crack propagation zone of the alloy in different conditions and stress amplitudes, **(A)** T1-160 MPa, **(B)** T4-180 MPa, **(C)** T6-180 MPa.

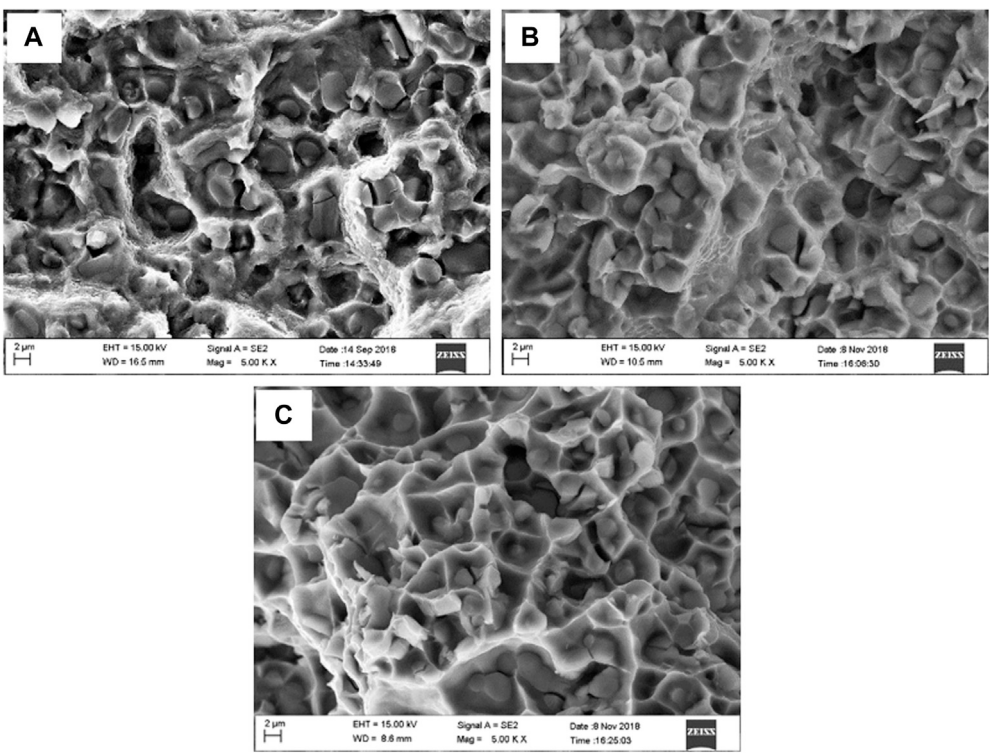

FIGURE 9 | Final fracture zone of the alloy in different conditions and stress amplitudes, **(A)** T1-160 MPa, **(B)** T4-180 MPa, **(C)** T6-180 MPa.

DATA AVAILABILITY STATEMENT

The original contributions presented in the study are included in the article/Supplementary Material, further inquiries can be directed to the corresponding author.

AUTHOR CONTRIBUTIONS

FL designed the experiments, analyzed data and wrote the manuscript. FY designed the experiments and revised the manuscript. DZ performed the experimental work of preparing the studied alloy including casting and hot deformation. LG performed the experimental work of fatigue properties tests.

FUNDING

This work was funded by the National Key R&D Program of China (2017YFB0306402) and the National Natural Science Foundation of China under the grant nos. 50771030 and 51401047.

REFERENCES

Ammar, H. R., Samuel, A. M., and Samuel, F. H. (2008). Effect of Casting Imperfections on the Fatigue Life of 319-F and A356-T6 Al-Si Casting Alloys. *Mater. Sci. Eng. A* 473, 65–75. doi:10.1016/j.msea.2007.03.112

Atxaga, G., Pelayo, A., and Irisarri, A. M. (2013). Effect of Microstructure on Fatigue Behaviour of Cast Al-7Si-Mg Alloy. *Mater. Sci. Technology* 17 (4), 446–450. doi:10.1179/026708301101510023

Azzam, D., Menzemer, C. C., and Srivatsan, T. S. (2010). The Fracture Behavior of an Al-Mg-Si alloy during Cyclic Fatigue. *Mater. Sci. Eng. A* 527, 5341–5345. doi:10.1016/j.msea.2010.04.023

Borrego, L. P., Abreu, L. M., Costa, J. M., and Ferreira, J. M. (2004). Analysis of Low Cycle Fatigue in AlMgSi Aluminium Alloys. *Eng. Fail. Anal.* 11 (5), 715–725. doi:10.1016/j.engfailanal.2003.09.003

Casellas, D., Pérez, R., and Prado, J. M. (2005). Fatigue Variability in Al-Si Cast Alloys. *Mater. Sci. Eng. A* 398, 171–179. doi:10.1016/j.msea.2005.03.034

Ham, G. S., Baek, M. S., Kim, J. H., Lee, S. W., and Lee, K. A. (2017). Effect of Heat Treatment on Tensile and Fatigue Deformation Behavior of Extruded Al-12wt %Si Alloy. *Met. Mater. Int.* 23 (1), 35–42. doi:10.1007/s12540-017-6351-3

Liu, F., Yu, F., Zhao, D., and Zuo, L. (2011). Microstructure and Mechanical Properties of an Al-12.7Si-0.7Mg alloy Processed by Extrusion and Heat Treatment. *Mater. Sci. Eng. A* 528, 3786–3790. doi:10.1016/j.msea.2011.01.041

Mbuya, T. O., Sinclair, I., Moffat, A. J., and Reed, P. A. S. (2011). Analysis of Fatigue Crack Initiation and S-N Response of Model Cast Aluminium Piston Alloys. *Mater. Sci. Eng. A* 528, 7331–7340. doi:10.1016/j.msea.2011.06.007

Shaha, S. K., Czerwinski, F., Kasprzak, W., Friedman, J., and Chen, D. L. (2015). Effect of Solidification Rate and Loading Mode on Deformation Behavior of Cast Al-Si-Cu-Mg alloy with Additions of Transition Metals. *Mater. Sci. Eng. A* 636, 361–372. doi:10.1016/j.msea.2015.03.077

Wang, G. D., Tian, N., Li, C., Zhao, G., and Zuo, L. (2018). Effect of Si Content on the Fatigue Fracture Behavior of Wrought Al-xSi-0.7Mg Alloy. *Msf* 941, 1143–1148. doi:10.4028/www.scientific.net/msf.941.1143

Yi, J., Gao, Y., Lee, P., and Lindley, T. (2004). Effect of Fe-Content on Fatigue Crack Initiation and Propagation in a Cast Aluminum-Silicon alloy (A356-T6). *Mater. Sci. Eng. A* 386, 396–407. doi:10.1016/s0921-5093(04)00964-5

Yi, J. Z., Gao, Y. X., Lee, P. D., and Lindley, T. C. (2006). Microstructure-Based Fatigue Life Prediction for Cast A356-T6 Aluminum-Silicon Alloys. *Metall. Materi Trans. B* 37 (2), 301–311. doi:10.1007/bf02693159

Yu, F. X., Li, Y. F., and Cui, J. Z. (2005). Banded Structure in the DC Cast Al-15Si alloy. *Trans. Indian Inst. Met.* 58, 591–596.

Conflict of Interest: The authors declare that the research was conducted in the absence of any commercial or financial relationships that could be construed as a potential conflict of interest.

frontiers in Materials

ORIGINAL RESEARCH
published: 16 June 2021
doi: 10.3389/fmats.2021.680776

Enhanced Mechanical Properties of Fe-Mn-Al-C Low Density Steel *via* Aging Treatment

*Li Kang[1], Hao Yuan[2], Hua-ying Li[1], Ya-feng Ji[2], Hai-tao liu[3] and Guang-ming Liu[1]**

[1]School of Materials Science and Engineering, Taiyuan University of Science and Technology, Taiyuan, China, [2]School of Mechanical Engineering, Taiyuan University of Science and Technology, Taiyuan, China, [3]State Key Laboratory of Rolling and Automation, Northeastern University, Shenyang, China

This study investigated the tensile properties and deformation behavior of an aged Fe-26Mn-6Al-1C (mass%) alloy with a stacking fault energy of approximately 60 mJ·m^{-2}. The results show that an ordered phase with a "short-range ordering" (SRO) structure formed after aging at 550°C for 10 h, further increasing the aging time to 48 h. Lamellar second-phase precipitates appeared at the austenitic grain boundaries. The aged sample at 550°C for 10 h exhibited an enhanced tensile strength (~898 MPa) without notably sacrificing uniform elongation (~46.3%), which was mainly attributed to the relatively high strain hardening in the entire plastic deformation due to the synergistic effects of planar slip, twinning-induced plasticity (TWIP), microband-induced plasticity (MBIP), and especially the formation of short-range ordering.

Keywords: Fe-Mn-Al-C alloy, age-precipitated particles, short range ordering, deformation twinning, strain hardening rate

OPEN ACCESS

Edited by:
Peter Hodgson,
Deakin University, Australia

Reviewed by:
Zhiqiang Wu,
Hunan University of Science and Technology, China
Pavlo Maruschak,
Ternopil Ivan Pului National Technical University, Ukraine

****Correspondence:***
Guang-ming Liu
brightliu2008@126.com

Specialty section:
This article was submitted to Structural Materials, a section of the journal Frontiers in Materials

Received: *15 March 2021*
Accepted: *24 May 2021*
Published: *16 June 2021*

Citation:
Kang L, Yuan H, Li H, Ji Y, liu H and Liu G (2021) Enhanced Mechanical Properties of Fe-Mn-Al-C Low Density Steel via Aging Treatment. Front. Mater. 8:680776. doi: 10.3389/fmats.2021.680776

INTRODUCTION

Fe-Mn-Al-C steels have been extensively researched over the past several decades due to the high specific strength and stiffness of this material, which is a good trade-off between high ultimate tensile strength and good tensile ductility (Frommeyer and Brüx, 2006; Li et al., 2015; Klimova et al., 2017; Sarkar et al., 2019; Choi et al., 2020; Li et al., 2020) when compared with conventional high strength steels. The composition of the light high-Mn steel is mainly based on the traditional high-Mn steel composition, by increasing the content of carbon and manganese and adding a certain amount of aluminum. As a main alloying element, Mn has the function of enlarging the austenite region and stabilizing the austenite structure. The addition of Al to high Mn austenitic steels not only reduces the weight of the automotive body due to its lower density but also varies the deformation mechanisms of steels from either transformation-induced plasticity (TRIP) or twinning-induced plasticity (TWIP) (Grässel et al., 2000; Sohn et al., 2014; Yuan et al., 2015; Huang et al., 2017; Luo and Huang, 2018) to dislocation slip due to the increased stacking fault energy (SFE) (Frommeyer and Brüx, 2006; Li et al., 2015; Choi et al., 2020; Li et al., 2020). Microband-induced plasticity (MBIP) was also discovered by Frommeyer and Brux (Frommeyer and Brüx, 2006) in high Mn-Al austenitic alloys with the relatively high SFE value of 110 mJ·m^{-2} suppressing the formation of martensitic or severe mechanical twinning.

There has been dramatically growing interest in high Mn-Al austenite alloys containing carbon due to the presence of κ-carbide ($(Fe,Mn)_3AlC$) particles (James, 1969; Kayak, 1969; Choo and Han, 1985; Han et al., 1986; Ishida et al., 1990; Choo et al., 1997; Frommeyer and Brüx, 2006; Choi et al., 2020; Li et al., 2020). In the late 1970s, the $(Fe,Mn)_3A1C$ κ-carbide precipitates with an ordered L'l2

crystal structure were first observed in high Al and C Fe-Mn-Al-C alloys by James (1969); Kayak (1969); Ishida et al, (1990) established the relationship between different α, γ and κ phases based on the phase constitutions of Fe-(20-30)Mn-Al-C alloys. Choo et al. (Choo and Han, 1985; Han et al., 1986) described the κ-carbides with a face-center cubic (fcc) based phase with an ordered L'l2 structure, which was similar to that of Ll2. Frommeyer and Brux Choi (Frommeyer and Brüx, 2006) reported that the nanosized κ-carbides with a perovskite structure in a Fe-28Mn-10Al-0.5C alloy were accompanied by shear bands, which was also verified by Choi et al., (2010). Accordingly, the tensile ductility was enhanced by the nanosized (Fe,Mn)3AlC κ-carbide precipitates in the austenitic Fe-Mn-Al-C alloys (Frommeyer and Brüx, 2006; Choi et al., 2020; Li et al., 2020) due to the so-called MBIP effect, which was comparable to the loss of ductility resulting from the unfavorable morphology of κ-carbides in ferrite or ferrite-austenite duplex lightweight Fe-Mn-Al-C steels.

The better strengthening effect of high-Mn steel could be obtained by examining the composite treatment of aging and deformation, which not only improves the ductility but also the strength of the steel. The stress flow behavior of alloys with various hot forming conditions greatly affects the evolution of their microstructure (Fang et al., 2016). At present, the discussion on the microstructure evolution of hign-Mn Fe-Mn-Al-C steels via aging treatment is still ongoing, and the influence of microstructure on the deformation mechanism also needs to be further studied, for optimizing the properties of the experimental steel.

In the present study, a lightweight Fe-26Mn-6Al-1.0C (mass, %) austenitic alloy with a stacking fault energy (SFE) value of approximately 60 $mJ{\cdot}m^{-2}$ was used to investigate the formation of a new strengthening phase with a "short-range ordering" (SRO) structure. The present study also clarifies the influence of aging temperature and time on microstructural evolution, tensile properties, and deformation behavior of Fe-26Mn-6Al-1.0C.

EXPERIMENTAL PROCEDURES

A Fe-26Mn-5.84Al-1.0C (mass, %) alloy was designed. Its SFE value was estimated to be approximately 60 $mJ{\cdot}m^{-2}$ based on the thermodynamic models reported by several researchers (Grassel et al., 1997; Dumay et al., 2008; Song et al., 2017). The alloy was prepared in an induction furnace by induction melting and then cast into small rectangular ingots. The ingots were homogenized at 1,200°C for 2 h and hot-rolled at around 1,050°C to 3 mm in thickness with a total reduction of 85%.

Tensile specimens, whose gauge width and length are 10 and 40 mm, respectively, were taken from the hot-rolled strip with the tensile axis parallel to the rolling direction. The tensile specimens were solution-treated at 1,100°C for 1 h, followed by water quenching to room temperature. Meanwhile, the solution-treated tensile specimens were further aged at temperatures ranging from 450 to 550°C for 10 h to study the precipitation behavior of experimental steel. Uniaxial tensile tests were carried out on an Instron 5,967 30 kN machine at an initial strain rate of $1 \times 10^{-3}\ s^{-1}$.

The microstructural characterization was performed using an optimal microscope (OM, Olympus DSX500) and transmission electron microscope (TEM, Tecnai $G^2$20) operated at 200 kV. TEM specimens were prepared as thin foils by mechanical grinding and twin-jet electropolishing in a mixture of 8% perchloric acid and 90% alcohol at −35°C with an applied potential of 50 V. The phase constituents were determined by an X-ray diffractometer (XRD, D/Max-Ra) with CuK_α radiation in the range of 40 to 120°.

RESULTS AND DISCUSSIONS

The hot-rolled Fe-26Mn-5.84Al-1.0C alloy shows a single fcc-structured γ phase with an average grain size of about 20 μm, together with dislocation tangle, stacking fault, and annealing twins. After solution treatment at 1,100°C for 1 h, the grain size of γ was measured at around 130 μm with some amount of annealing twins (**Figure 1A**), and only γ phase peaks were detected by XRD patterns (**Figure 2**). In addition, there existed a relatively large number of dislocations in the solution-treated alloy (**Figure 3A**). These dislocations were periodically arranged in a plane, as schematically illustrated in **Figure 3B**.

After aging treatment at temperatures ranging from 450 to 550°C for 10 h, the optical micrographs (**Figures 1B–D**) appeared no significant change, when compared with that of the solution-treated sample (**Figure 1A**). The intensities of both (200)γ and (220)γ peaks increased with increasing aging temperature, while that of (111)γ decreased, as shown in **Figure 2**. It should be noted that no second-phase particles could be observed by TEM under all experimental conditions. It has been reported that the coarse second-phase particles could be observed along the austenitic grain boundaries by optical microscopy for the Fe-(28–31.5)Mn-(8.0–9.0)Al-(0.8–1.05)C alloys aged for 120–129 h (Hwang et al., 1993), which was different from the present short-time aged Fe-26Mn-5.84Al-1.0C alloy.

Table 1 shows the tensile properties of the solution-treated Fe-26Mn-5.84Al-1.0C alloy, in conjunction with the aged samples at 450–550°C for 10 h. As a whole, the austenitic Fe-26Mn-5.84Al-1.0C alloy exhibited yield strength (YS) of 378–480 MPa, UTS of 727–898 MPa, and total elongation (δ) of 47–53.2%. The values of UTS × δ ranged from 36.0 to 45.0 GPa·% for the present alloys, which were smaller than those (67.7–84.6 GPa·%) of the Fe-28Mn-9Al-0.8C alloy fabricated by cold rolling and heating treatment studied by Yoo et al. (Choi et al., 2020). This difference was likely associated with the larger size of austenitic grains, ~130 μm for the present alloys, while that was only 5–38 μm for the Fe-28Mn-9Al-0.8C alloy (Choi et al., 2020). It was worth noting that the aged Fe-26Mn-5.84Al-1.0C alloy at 550°C for 10 h exhibited an extremely high UTS value with no loss of ductility, compared with the other solution-treated or aged samples in this study (Kayak et al., 1969; Kalashnikov et al., 2000). To investigate the reason for the enhanced ultimate tensile strength and ductility, the precipitation

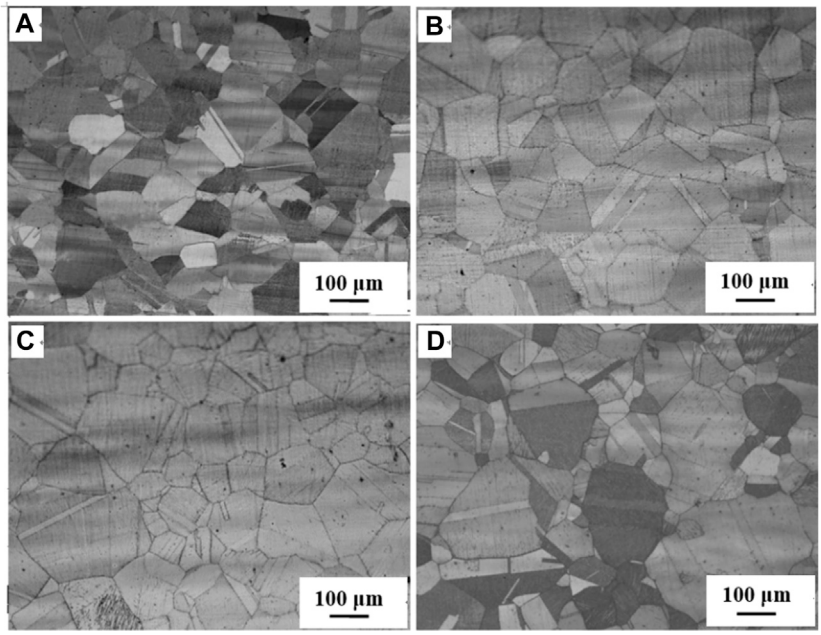

FIGURE 1 | Optical micrographs of the Fe-26Mn-5.84Al-1.0C alloy subjected to **(A)** solution treatment at 1,100°C for 1 h and ageing treatment for 10 h at three different temperatures: 450 °C **(B)**, 500°C **(C)** and 550°C **(D)**.

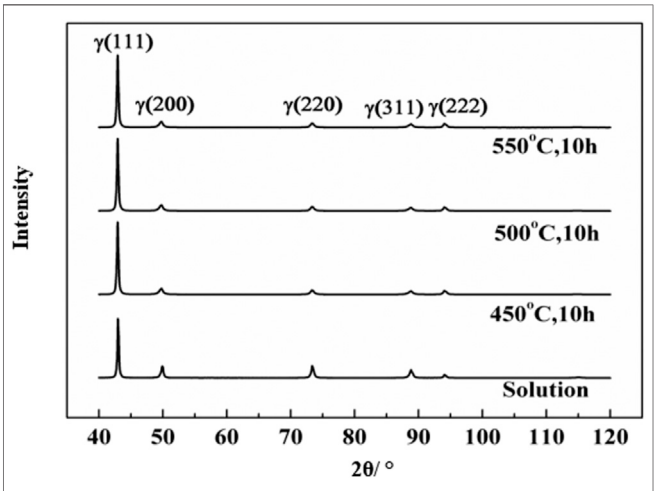

FIGURE 2 | XRD patterns of the Fe-26Mn-5.84Al-1.0C alloy subjected to solution treatment at 1,100°C for 1 h and aging treatment at 450, 500, and 550°C for 10 h.

behavior during aging treatment was clarified, together with further analysis of deformation mechanisms during tensile tests.

Figure 4 reveals the true stress (σ) and strain hardening rate (dσ/dε) with respect to true strain (ε) in the solution-treated Fe-26Mn-5.84Al-1.0C alloy, in conjunction with the aged samples at 450, 500 and 550°C for 10 h. All tensile samples exhibited continuous yielding and extensive strain hardening behaviors, which was similar to the conventional high Mn austenitic steels (Yuan et al., 2015; Huang et al., 2017). In the entire plastic deformation region, the aged Fe-26Mn-5.84Al-1.0C samples exhibited the three-stage strain-hardening behavior, regardless of aging temperature. The dσ/dε value rapidly decreased at stage I, remained a constant at stage II, and then decreased again at stage III as the true strain increased. The significant difference between the solution-treated and aged samples was that the dσ/dε value of the former gradually decreased with ε at stage II; whereas the aged sample at 550°C for 10 h showed the relatively higher strain hardening capability during the whole plastic deformation. According to the true strain value (ε) when the peak value of dσ/dε appeared, the plastic instability had been delayed after aging. This could be responsible for high UTS with no loss of ductility in the aged Fe-26Mn-5.84Al-1.0C alloy at 550°C for 10 h.

To support the dominant deformation mechanisms of an aged Fe-26Mn-6Al-1C alloy at 550 °C for 10 h, the representative TEM morphologies were supplemented. As displayed in **Figure 1D**, the initial microstructure prior to tensile testing was the coarse austenite grains and annealing twins. As the tensile strain was about 5%, microbands were observed, implying the dominant deformation mode was MB at the early stage of plastic deformation. Upon further straining, the dislocations made equal spacing arrays along the two principal directions and the dislocation densities increased without altering the slip directions (Ding et al., 2013). After a tensile fracture, the well-developed microbands and deformation twins (**Figure 5B**) became dominant, indicating that both TWIP and MBIP effects occurred in the aged Fe-26Mn-5.84Al-1.0C alloy with a relatively high SFE value of 60 $mJ \cdot m^{-2}$. The formation of microbands and deformation twins would give rise to a remarkable difference in strain hardening phenomena as both of them acted as effective obstacles to dislocation glide (Urrutia and Raabe, 2011; Ding et al., 2013). In contrast, only a large number of microbands were observed in the solution-treated

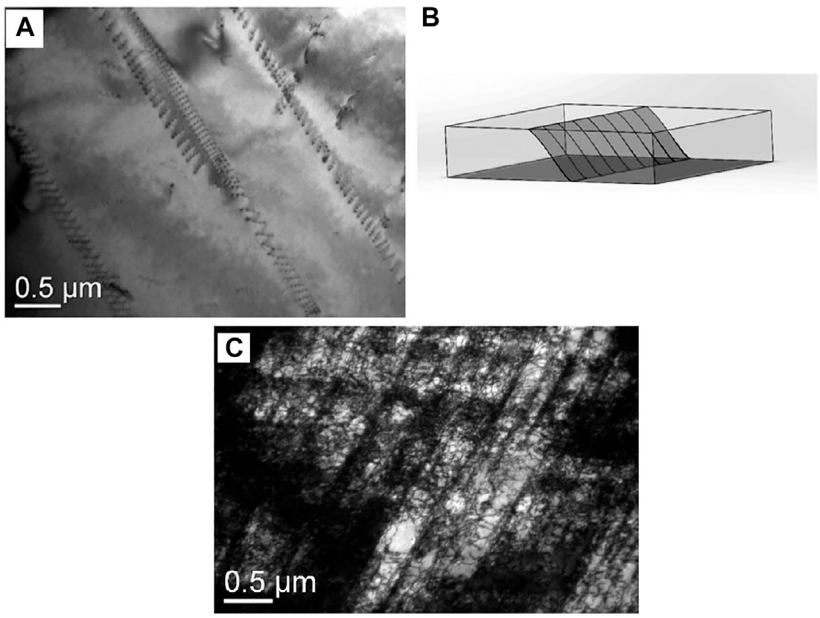

FIGURE 3 | Dislocation alignment in planar **(A)** and the corresponding schematic diagram of Fe-26Mn-5.84Al-1.0C alloy at 1,100°C for 1 h **(B)**. **(C)** shows the micro-bands after interrupted tensile deformation up to 30%.

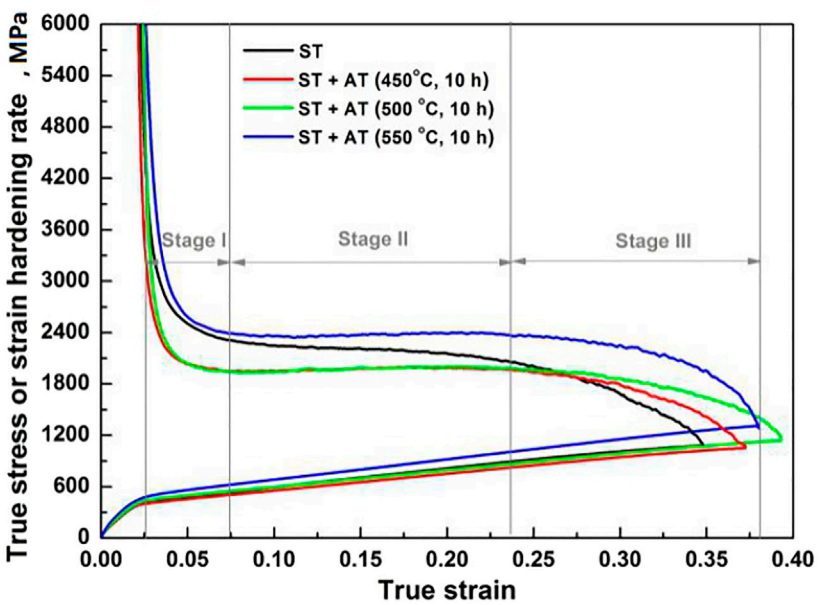

FIGURE 4 | Changes in true stress (σ) and strain hardening rate (dσ/d *& epsi*) with true strain (*& epsi*) in the solution-treated Fe-26Mn-5.84Al-1.0C alloy, along with the aged samples at 450, 500, and 550°C for 10 h.

sample (**Figure 3C**), implying that MBIP was a dominant deformation mechanism.

An island-like phase within the γ matrix was found (**Figure 5C**), which was also called an ordered phase with a "short-range ordering" (SRO) structure, as verified by the SAD pattern (see an inset at the upper right of **Figure 5C**). It was also revealed that the SRO phase exhibited a coherent orientation relationship with γ matrix [100] SRO/[100]γ, which was similar to that of SRO in $AuCu_3$ superalloys (Hiraga et al., 1982). In the preliminary work, Choo et al. reported such an ordered structure in an aged Fe-30Mn-7.8Al-1.3C alloy, which contains a carbon atom at the body center site, three Fe/Mn atoms randomly at the face center sites, and an Al atom at the corner

TABLE 1 | Room temperature tensile properties of the hot rolled Fe-26Mn-5.84Al-1.0C alloy subjected to various aging treatments.

Methods	AGS (μm)	YS (MPa)	UTS (MPa)	δ_u (%)	δ_f (%)	UTS × δ_f (GPa%)
ST (1,100°C, 1 h)	130	378	764	42.2	47.1	36.0
ST + AT (450°C, 10 h)		375	727	45.1	51.0	37.1
ST + AT (500°C, 10 h)		430	770	49.7	53.2	41.0
ST + AT (550°C, 10 h)		482	898	46.3	50.1	45.0

ST, solution treatment; AT, aging treatment; AGS, average grain size of austenite; YS, yield strength; UTS, ultimate tensile strength; δ_u, uniform elongation; δ_f, elongation to failure.

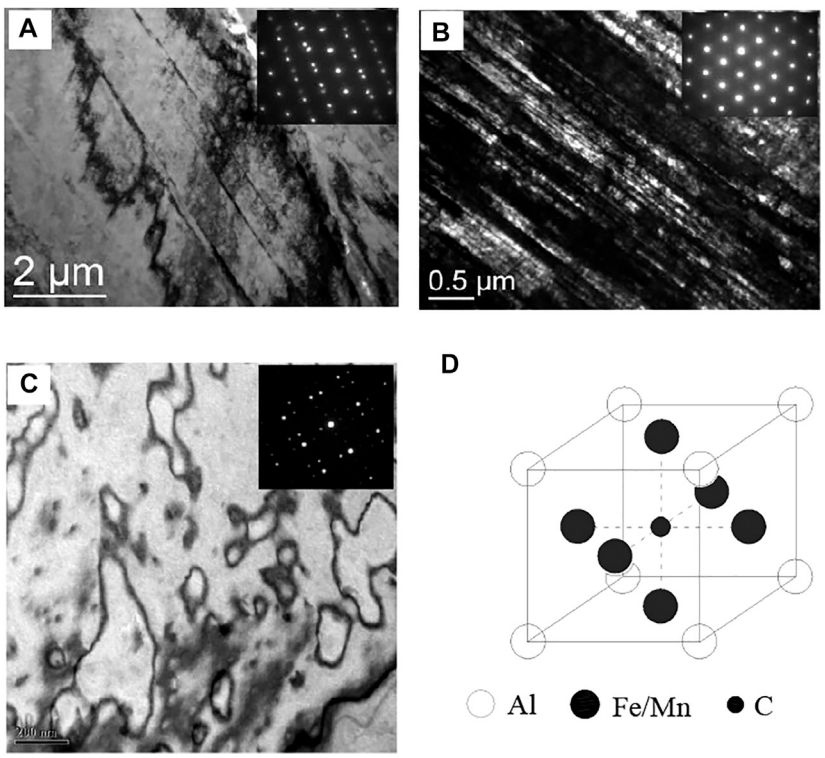

FIGURE 5 | TEM micrographs of Fe-26Mn-5.84Al-1.0C alloy at 550°C for 10 h: **(A)** shows microband and deformation twins as well as the corresponding selected-area diffraction (SAD) patterns; **(B)** shows an ordered island-like phase with a "short-range ordering" (SRO) structure and the corresponding SAD patterns. **(C)** and **(D)** show schematic diagrams of the ordered SRO structure in the Fe-Mn-Al-C quaternary alloy.

positions in its fcc-structured unit cell, as schematically illustrated in **Figure 5D**. The formation of a unit cell of SRO structure involved as follows: Al atom occupies two opposite face centers; Fe and Mn atoms are located on other face centers and each corner; C atom is placed at the center of the unit cell. Because of the ordered arrangement of Al atoms, the SRO patterns of the aged Fe-26Mn-5.84Al-1.0C alloy at 550°C for 10 h were characterized by satellite spots around the fundamental reflections in juxtaposition with superlattice reflections. Furthermore, there existed a certain small tilt angle between the [010] directions of the satellites and fundamental reflections from the [100] superlattice spot. The arrangement of the unit cell in the SRO zone indicates that the short range ordering (SRO) happened after aging treatment at 550°C for 10 h.

The transformation from the γ matrix to SRO caused the formation of short range ordering with an average size of 30–200 nm separated by anti-phase boundaries (APBs). This might be one of the most important factors to obtain the dramatically improved UTS and δ (**Table 1**), owing to the continuously increased strain hardening behavior (**Figure 3**) caused by the precipitation and grain boundary strengthening (**Figure 5**). However, as the Fe-26Mn-5.84Al-1.0C alloy was aged at 550°C for 48 h, the short range ordering disappeared, and the lamellar second-phase precipitates along the grain boundaries were observed in **Figure 6A**. These precipitates were identified as carbide precipitates (Fe, $Mn)_3C_x$ by energy dispersive X-ray spectroscopy (**Figure 6B**), which were also observed previously in Fe-Mn-Al-C alloys (Choo and Han, 1985). Their grain boundary phases were characterized by the ordered κ carbide and a disordered body centered cubic (*bcc*) α ferrite, significantly deteriorating the tensile ductility of Fe-26Mn-5.84Al-1.0C alloy.

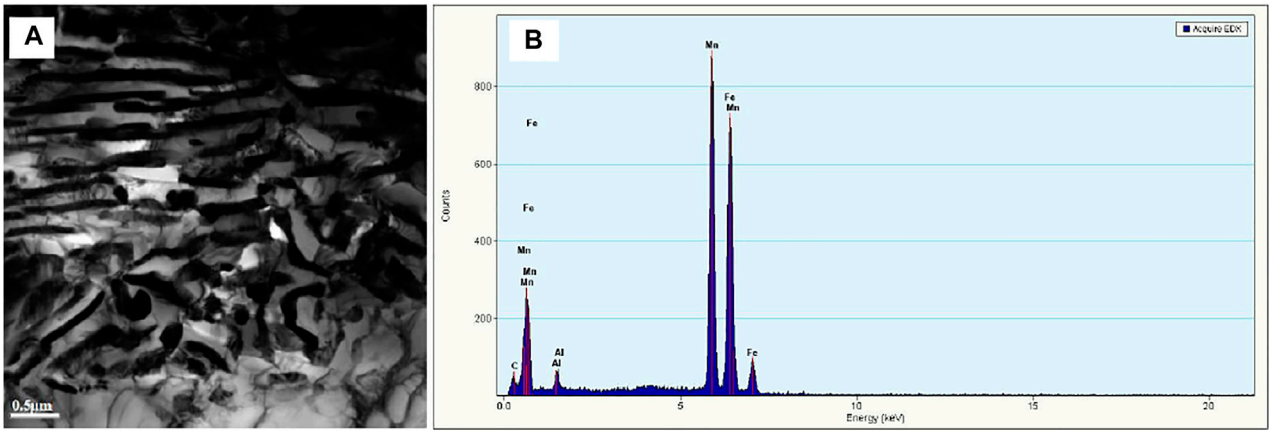

FIGURE 6 | TEM image **(A)** and energy dispersive X-ray spectroscopy (EDS) pattern **(B)** of the aged Fe-26Mn-5.84Al-1.0C alloy at 550°C for 48 h.

CONCLUSION

In summary, a lightweight Fe-26Mn-6Al-1C (mass%) austenitic alloy with a stacking fault energy (SFE) value of approximately 60 mJ·m^{-2} was subjected to solution treatment at 1,100°C for 1 h and various aging treatments at 450–550°C for 10 h. The main conclusions involved as follows:

1) The solution-treated alloy exhibited a relatively large number of dislocations, which were periodically arranged in a plane; whereas an ordered phase with a "short-range ordering" (SRO) structure was observed in the aged sample at 550°C for 10 h. With further increasing aging time to 48 h, the lamellar second-phase precipitates were distributed along grain boundaries.
2) The enhanced ultimate tensile strength (UTS = 898 MPa) and ductility (δ_u = 46.3%) of Fe-26Mn-6Al-1C alloy at 550°C for 10 h was closely associated with relatively high strain hardening in the entire plastic deformation, which was mainly attributed to the formation of an ordered short range ordering.
3) The aged Fe-26Mn-6Al-1C samples at 450–550°C for 10 h exhibited a three-stage strain-hardening behavior and constant strain hardening rate (dσ/dε) at stage II, which was significantly different from the decreased dσ/dε value at stage II for the solution-treated sample.

DATA AVAILABILITY STATEMENT

The original contributions presented in the study are included in the article/Supplementary Material, further inquiries can be directed to the corresponding author.

AUTHOR CONTRIBUTIONS

G-mL: Conceptualization, Methodology, Investigation. HY: Data curation, Writing-Original draft preparation. H-yL: Visualization, Investigation. Y-fJ: Investigation, Supervision. H-tL: Resources, Validation. LK: Formal analysis, Writing-Reviewing and Editing.

FUNDING

This work was financially supported by the National Key R&D Program of China (No. 2018YFB1307902), Open Research Fund from Key Laboratory of Ecological Metallurgy of Multi-metal Intergrown Ores of Ministry of Education (No. NEMM2020003), the Natural Science Foundation of Liaoning Province (No. 2019-KF-25-05), and the Natural Science Foundation of Shanxi Province (No. 201901D111241).

REFERENCES

Choi, K., Seo, C.-H., Lee, H., Kim, S. K., Kwak, J. H., Chin, K. G., Park, K.-T., et al. (2010). Effect of Aging on the Microstructure and Deformation Behavior of Austenite Base Lightweight Fe-28Mn-9Al-0.8C Steel. *Scripta Materialia*. 63, 1028–1031. doi:10.1016/j.scriptamat.2010.07.036

Choi, Y. W., H Dong, Z., Li, W., Schönecker, S., Kim, H., Kwon, S. K., et al. (2020). Predicting the Stacking Fault Energy of Austenitic Fe-Mn-Al (Si) Alloys. *Mater. Des.* 187, 1–8. doi:10.1016/j.matdes.2019.108392

Choo, W. K., and Han, K. H. (1985). Phase Constitution and Lattice Parameter Relationships in Rapidly Solidified (Fe0.65Mn0.35)0.83 Al0.17-xC and Fe3Al-xC Pseudo-binary Alloys. *Metallurgical Transactions A.* 16, 5–10. doi:10.1007/bf02656705

Choo, W. K., Kim, J. H., and Yoon, J. C. (1997). Microstructural Change in Austenitic Fe-30.0wt%Mn-7.8wt%Al-1.3wt%C Initiated by Spinodal Decomposition and its Influence on Mechanical Properties. *Acta Materialia.* 45, 4877–4885. doi:10.1016/s1359-6454(97)00201-2

Ding, H., Li, H. Y., Wu, Z. Q., Huang, M. L., Li, H. Z., and Xin, Q. B. (2013). Microstructural Evolution and Deformation Behaviors of Fe-Mn-Al-C Steels with Different Stacking Fault Energies. *Steel Res. Int.* 84, 1288–1293. doi:10.1002/srin.201300052

Dumay, A., Chateau, J.-P., Allain, S., Migot, S., and Bouaziz, O. (2008). Influence of Addition Elements on the Stacking-Fault Energy and Mechanical Properties of an Austenitic Fe-Mn-C Steel. *Mater. Sci. Eng. A.* 483-484, 184–187. doi:10.1016/j.msea.2006.12.170

Fang, Y., Chen, X., Madigan, B., Cao, H., and Konovalov, S. (2016). Effects of Strain Rate on the Hot Deformation Behavior and Dynamic Recrystallization in China

Low Activation Martensitic Steel. *Fusion Eng. Des.* 103, 21–30. doi:10.1016/j.fusengdes.2015.11.036

Frommeyer, G., and Brüx, U. (2006). Microstructures and Mechanical Properties of High-Strength Fe-Mn-Al-C Light-Weight TRIPLEX Steels. *steel Res. Int.* 77, 627–633. doi:10.1002/srin.200606440

Grassel, O., Frommeyer, G., Derder, C., and Hofmann, H. (1997). Phase Transformations and Mechanical Properties of Fe-Mn-Si-Al TRIP-Steels. *J. Phys. IV* 7, 383–388. doi:10.1051/jp4:1997560

Grässel, O., Krüger, L., Frommeyer, G., and Meyer, L. W. (2000). High Strength Fe-Mn-(Al, Si) TRIP/TWIP Steels Development - Properties - Application. *Int. J. Plasticity*. 16, 1391–1409. doi:10.1016/s0749-6419(00)00015-2

Han, K. H., Yoon, J. C., and Choo, W. K. (1986). TEM Evidence of Modulated Structure in FeMnAlC Austenitic Alloys. *Scripta Metallurgica*. 20, 33–36. doi:10.1016/0036-9748(86)90208-5

Hiraga, K., Hirabayashi, M., Terasaki, O., and Watanabe, D. (1982). One-dimensional Antiphase Structure of Au22Mn6studied by High-Voltage, High-Resolution Electron Microscopy. *Acta Cryst. Sect A.* 38, 269–274. doi:10.1107/s0567739482000576

Huang, Z., Jiang, Y., Hou, A., Wang, P., Shi, Q., Hou, Q., et al. (2017). Rietveld Refinement, Microstructure and High-Temperature Oxidation Characteristics of Low-Density High Manganese Steels. *J. Mater. Sci. Technology*. 33, 1531–1539. doi:10.1016/j.jmst.2017.09.012

Hwang, C. N., Chao, C. Y., and Liu, T. F. (1993). Grain Boundary Precipitation in an Fe-8.0Al-31.5Mn-1.05C alloy. *Scripta Metallurgica et Materialia*. 28, 263–268. doi:10.1016/0956-716x(93)90574-c

Ishida, K., Ohtani, H., Satoh, N., Kainuma, R., and Nishizawa, T. (1990). Phase Equilibria in Fe-Mn-Al-C Alloys. *ISIJ Int.* 30, 680–686. doi:10.2355/isijinternational.30.680

James, P. J. (1969). Precipitation of the Carbide $(Fe,Mn)_3AlC$ in an Fe-Al Alloy. *J. Iron Steel Inst.* 207, 54–57.

Kalashnikov, I., Acselrad, O., Shalkevich, A., and Pereira, L. C. (2000). Chemical Composition Optimization for Austenitic Steels of the Fe-Mn-Al-C System. *J. Mater. Eng. Perform.* 9, 597–602. doi:10.1361/105994900770345430

Kayak, G. L. (1969). Fe-Mn-Al Precipitation-Hardening Austenitic Alloys. *Met. Sci. Heat Treat.* 11, 95–97. doi:10.1007/bf00652271

Klimova, M., Zherebtsov, S., Stepanov, N., Salishchev, G., Haase, C., and Molodov, D. A. (2017). Microstructure and Texture Evolution of a High Manganese TWIP Steel during Cryo-Rolling. *Mater. Characterization*. 132, 20–30. doi:10.1016/j.matchar.2017.07.043

Li, K.-w., Zhuang, C.-l., Liu, J.-h., Shen, S.-b., Ji, Y.-l., and Han, Z.-b. (2015). Smelting and Casting Technologies of Fe-25Mn-3Al-3Si Twinning Induced Plasticity Steel for Automobiles. *J. Iron Steel Res. Int.* 22, 75–79. doi:10.1016/s1006-706x(15)30142-4

Li, Z., Wang, Y. C., Cheng, X. W., Liang, J. X., and Li, S. K. (2020). Compressive Behavior of a Fe-Mn-Al-C Lightweight Steel at Different Strain Rates. *Mater. Sci. Eng. A.* 772, 1–9. doi:10.1016/j.msea.2019.138700

Luo, Z. C., and Huang, M. X. (2018). Revisit the Role of Deformation Twins on the Work-Hardening Behaviour of Twinning-Induced Plasticity Steels. *Scripta Materialia*. 142, 28–31. doi:10.1016/j.scriptamat.2017.08.017

Sarkar, A., Sanyal, S., Bandyopadhyay, T. K., and Mandal, S. (2019). Implications of Microstructure, Taylor Factor Distribution and Texture on Tensile Properties in a Ti-Added Fe-Mn-Al-Si-C Steel. *Mater. Sci. Eng. A.* 767, 1–12. doi:10.1016/j.msea.2019.138402

Sohn, S. S., Lee, S., Lee, B.-J., and Kwak, J.-H. (2014). Microstructural Developments and Tensile Properties of Lean Fe-Mn-Al-C Lightweight Steels. *JOM*. 66, 1857–1867. doi:10.1007/s11837-014-1128-3

Song, R., Cai, C., Liu, S., Feng, Y., and Pei, Z. (2017). Stacking Fault Energy and Compression Deformation Behavior of Ultra-high Manganese Steel. *Proced. Eng.* 207, 1809–1814. doi:10.1016/j.proeng.2017.10.943

Urrutia, I. G., and Raabe, D. (2011). Dislocation and Twin Substructure Evolution During Strain Hardening of an Fe-22 wt.% Mn-0.6 wt.% C TWIP Steel Observed by Electron Channeling Contrast Imaging. *Acta Mater.* 59, 6449–6462. doi:10.1016/j.actamat.2011.07.009

Yuan, X., Chen, L., Zhao, Y., Di, H., and Zhu, F. (2015). Influence of Annealing Temperature on Mechanical Properties and Microstructures of a High Manganese Austenitic Steel. *J. Mater. Process. Technology* 217, 278–285. doi:10.1016/j.jmatprotec.2014.11.027

Conflict of Interest: The authors declare that the research was conducted in the absence of any commercial or financial relationships that could be construed as a potential conflict of interest.

frontiers in Materials

REVIEW
published: 21 December 2021
doi: 10.3389/fmats.2021.641928

Role of Grain Size and Shape in Superplasticity of Metals

Zhaoyang Lu[1]*, *Xuqiang Huang*[1] and *Jingzhe Huang*[2]

[1]School of Mechanical Engineering and Automation, Northeastern University, Shenyang, China, [2]College of Resources and Civil Engineering, Northeastern University, Shenyang, China

Superplasticity is characterized by an elongation to failure of >300% and a measured strain rate sensitivity (SRS), close to 0.5. The superplastic flow is controlled by diffusion processes; it requires the testing temperature of $0.5T_m$ or greater where T_m is the absolute melting temperature of metals. It is well established that a reduction in grain size improves the optimum superplastic response by lowering the deformation temperature and/or raising the strain rate. The low-temperature superplasticity (LTSP) is attractive for commercial superplastic forming, in view of lowering energy requirement, increasing life for conventional or cheaper forming dies, improving the surface quality of structural components, inhibiting quick grain growth and solute-loss from the surface layers, thus resulting in better post-forming mechanical properties. This paper will summarize the dependence of superplasticity on grain size and shape in various metallic materials, including ferrous and non-ferrous alloys, which has been considered as an effective strategy to enable the LTSP.

Keywords: superplasticity, grain refinement, grain size, low-temperature superplasticity, high-strain rate superplasticity, severe plastic deformation

OPEN ACCESS

Edited by:
Qi Chao,
Deakin University, Australia

Reviewed by:
Qichi Le,
Northeastern University, China
Xin Zhang,
Hebei University of Technology, China
Tingting Guo,
Xi'an Technological University, China

***Correspondence:**
Zhaoyang Lu
luchaoy@163.com

Specialty section:
This article was submitted to Structural Materials, a section of the journal Frontiers in Materials

Received: *15 December 2020*
Accepted: *30 June 2021*
Published: *21 December 2021*

Citation:
Lu Z, Huang X and Huang J (2021) Role of Grain Size and Shape in Superplasticity of Metals. Front. Mater. 8:641928. doi: 10.3389/fmats.2021.641928

INTRODUCTION

Superplasticity is the ability of metals to exhibit extremely large elongations of at least 300% prior to tensile failure, when deformation is imposed at relatively low strain rates (e.g., $\dot{\varepsilon} = 10^{-3}$ to $10^{-5}\ s^{-1}$) and elevated temperatures ($T > 0.5T_m$), where T_m is the melting temperature of metals (Edington, 1982; Langdon, 1982). To date, superplasticity has been demonstrated in various metals, such as aluminium, copper, magnesium, zinc, titanium and iron base alloys etc., (Maehara and Langdon, 1990; Chokshi et al., 1993; Langdon, 2009; Reddy et al., 2017). Basically, superplastic flow may occur in two different ways (Maehara and Langdon, 1990; Langdon, 1991; Kaibbyshev, 2002): 1) In transformation superplasticity, the superplastic effect is induced by temperature cycling through phase transformation; 2) In structural superplasticity, the superplastic flow happens at constant temperature without phase transformation. As for structural superplasticity, several essential characteristics are involved. First, the initial microstructure is very fine (usually a few microns or less) and stable equiaxed grains upon tensile loading. Second, a strain-rate sensitivity exponent ($m = \partial ln\sigma/\partial ln\dot{\varepsilon}$) ranges from 0.3 to 0.7 where σ is the true stress and $\dot{\varepsilon}$ is the strain rate. Third, a dominant grain boundary sliding (GBS) mechanism occurs to facilitate isotropic deformation.

It is well established that a reduction in grain size improves the optimum superplastic response by lowering the deformation temperature to lower than $0.5T_m$ (low temperature superplasticity) and/or raising the strain rate higher than $10^{-3}\ s^{-}$ (high strain rate superplasticity), which is beneficial for rapid superplastic forming of structural parts with nearly arbitrarily complex shapes at relatively low costs (Zhang et al., 2015). For achieving the superplasticity of metals, two groups of plastic

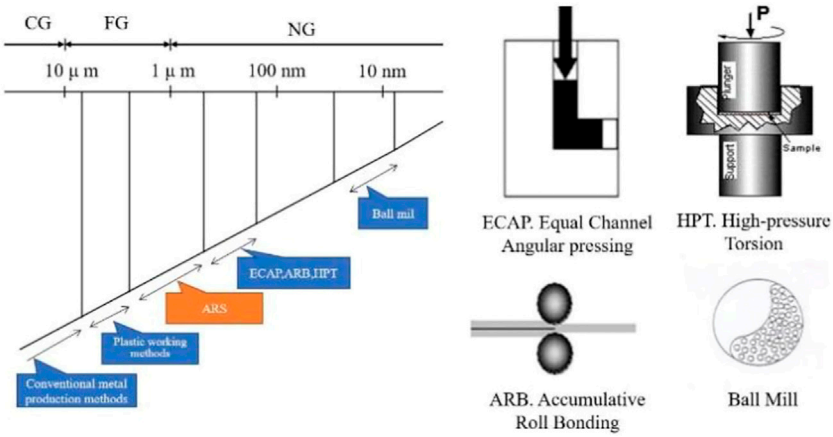

FIGURE 1 | Various techniques for production of UFG materials and the corresponding grain size levels. Note: CG-Coarse grains; FG-Fine grains; NG-Nano-sized grains.

deformation have been proposed to refine its microstructure down to ultrafine or nanoscale levels: One group is conventional plastic working processing (Tanaka et al., 2002; Tanaka et al., 2003; Xia et al., 2008), such as rolling, extrusion, forging and the other is severe plastic deformation (SPD) processing (Kumar et al., 2006; Chou et al., 2007; Yang et al., 2008; Kawasaki and Langdon, 2011) like equal-channel angular pressing (ECAP), high-pressure torsion (HPT) and friction stir welding (FSW), etc. By definition, nanoscaled materials have grain sizes of less than 100 nm and ultrafine-grained (UFG) materials have average grain sizes ranging from 100 nm to 1 μm. Various processing techniques to achieve ultra/nano-grain refinement of metals are represented in **Figure 1**.

SUPERPLASTICITY IN AL ALLOYS

An early report documented the occurrence of superplasticity in Al-based alloys over strain rates covering several orders of magnitude (Higashi, 1994; Kawasaki and Langdon, 2007). It was found that samples processed by cold rolling (CR) were not superplastic because the imposed strains were insufficient to refine the size to the ultrafine or even smaller levels. Instead, it was necessary to use powder metallurgy (PM), physical vapor deposition or other techniques for the superplasticity of Al alloys achieved at low temperatures or high strain rates.

In contrast, the Al-alloys processed by ECAP were superplastic over at least a limited range of strain rates (Komura et al., 2001). It was found that several of the Al alloys exhibited exceptionally high elongations of >2000%, and the general trend of a bell-shaped curve of total elongation against strain rate indicates three distinct flow regions where region II was superplastic at intermediate strain rates. It is also evident that superior elongations were achieved at high strain rates of no less than 10^{-2} s^{-1}, thus implying the occurrence of high-strain-rate superplasticity.

Liu and Ma (2011) investigated the influence of grain size on superplastic behavior in the Al-Mg-Sc alloy processed by friction stir processing (FSP), as plotted in **Figure 2**. It was found that the medium-grained samples exhibited the largest elongation at the highest strain rate due to the optimum combination of grain size and its thermal stability. The superplasticity of Al-Mg-Sc alloy was mainly governed by the effective grain size (the grain size just before deformation) and its distribution just before tension rather than the initial grain size.

It was worth noting that the Al-6Mg-0.25Sc-0.1Zr alloy produced by asymmetric rolling (AsR) exhibited an average grain size of ~1.5 μm, corresponding to an elongation of ~3,200% at 773 K and 5×10^{-2} s^{-1} (Xu et al., 2016). The superior superplasticity was ascribed to the ultrafine grains with a high fraction of high-angle grain boundaries (HAGBs) and disperse, coherent and nano-scaled Al_3(Sc, Zr) particles.

SUPERPLASTICITY IN TI ALLOYS

It has been demonstrated that the Ti alloy processed by conventional SPD methods exhibited an average grain size of 75–400 nm and the LTSP was achieved at temperatures as low as 823–973 K (Kim et al., 1998; Salishchev et al., 2001; Ko et al., 2005; Ko et al., 2006; Matsumoto et al., 2013; Zhang et al., 2014a; Fu et al., 2015; Wu et al., 2016; Zhang et al., 2018a), as summarized in **Table 1**.

FSP is a novel solid-state processing technique for grain refinement and microstructural modification in view of the principle of friction stir welding (FSW) (Liu et al., 2009). Wu et al. (2016) reported that the friction stir welded Ti-6Al-4V alloy with a fully lamellar morphology had an excellent superplastic ductility of ~728% at 1198 K and 3.0×10^{-3} s^{-1}, which reached 442% at 873 K and 3.0×10^{-5} s^{-1}.

In addition to the above-mentioned SPD methods, the initial microstructure also played an important role on ultra-grain

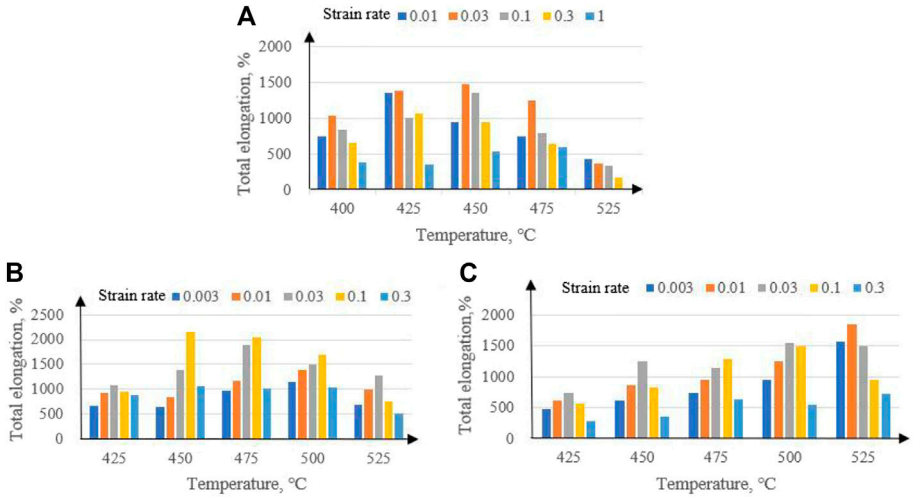

FIGURE 2 | Changes in total elongation with strain rate at different deformation temperatures in the Al-Mg-Sc alloy with grain sizes of 1.6 μm **(A)**, 2.6 μm **(B)** and 2.9 μm **(C)** (Liu and Ma, 2011).

TABLE 1 | Maximum elongations for the LTSP (below 973 K) in the SPDed Ti-6Al-4V alloy (Kim et al., 1998; Salishchev et al., 2001; Ko et al., 2005; Ko et al., 2006; Matsumoto et al., 2013; Zhang et al., 2014a; Fu et al., 2015; Wu et al., 2016; Zhang et al., 2018a).

Processing methods	d, nm	*T*, K	Strain rate, /s	Elongation, %
ECAP	300	873–973	1.0×10^{-4}–5.0×10^{-4}	296–700
HPT	75–300	873–923	5.0×10^{-4}–1.0×10^{-2}	575–780
MAF	135–400	823–973	5.0×10^{-4}–7.0×10^{-4}	640–910
Hot rolling	100–300	923–973	1.0×10^{-4}–1.0×10^{-2}	220–516
FSW	Fully lamellar	923	3.0×10^{-5}	442
FSP	510	873	3.0×10^{-4}	1130

Note: MAF, multiaxial forging.

TABLE 2 | Summary of experimental parameters and elongations in the Ti-6Al-4V alloy processed by HPT (Sergueeva et al., 2000; Sergueeva et al., 2002; Shahmir et al., 2018).

Initial microstructure	*T*, K	Strain rate, 1/s	Elongation, %
α+lamellar (α+β)	923–998	1.0×10^{-3}–1.0×10^{-2}	504–676
α+75% lamellar (α+β)	873	1.0×10^{-4}–1.0×10^{-2}	540–790
Lamellar (α+β)	973	1.0×10^{-3}–1.0×10^{-2}	640–910
Martensitic	923–973	1.0×10^{-4}–1.0×10^{-2}	410–690

refinement of Ti-6Al-4V alloy and the resultant superplastic behavior. Wang and Langdon et al. (Wang and Langdon, 2013) demonstrated that the grain size of the HPT-processed Ti-6Al-4V alloy dropped with increasing the volume fraction of lamellar structure. Preliminary work (Fu et al., 2015; Zhang et al., 2018b) has also showed that as the fraction of lamellar structure reached 70%, the grain size of the HPT-processed Ti-6Al-4V alloy was refined to 75 ± 15 nm, and an excellent LTSP of ~780% was achieved at 873 K and 5.0×10^{-4} s^{-1}.

Yoon et al. (2015) investigated the effect of initial microstructure (as-received material, furnace-cooled, material and water-quenched material) on microstructural evolution in Ti-6Al-4V alloy during FSW, and the equixaed microstructure with the smallest grain size in stir zone (SZ) center was formed for the initial martensitic microstructure. As demonstrated in Zhang et al. (2018a), an ultrafine microstructure consisting of α grains (~510 nm) and a small amount of β phase was successfully achieved in the FSPed Ti-6Al-4V alloy. The fraction of HAGBs with random crystallographic orientation was close to 90%, revealing dynamic recrystallization was responsible for ultra-grain refinement during FSP. The LTSP of such an ultrafine microstructure was found in the temperature range of 773–923 K and strain rates from 1.0×10^{-4} s^{-1} to 3.0×10^{-3} s^{-1}. Specifically, an exceptional LTSP of 1130% was achieved at 873 K and 3.0×10^{-4} s^{-1}.

Shahmir et al. (2018) examined the effect of initial microstructures, e.g. martensitic and lamellar on the superplasticity in the Ti-6Al-4V alloy processed by HPT. It was demonstrated that significant grain refinement was achieved under both conditions with grain sizes of ~30 and ~40 nm, respectively. The nanostructured samples exhibited excellent ductility at 923–1073 K, including superplastic elongations at 973 K with maximum values of 815 and 690%, respectively.

To provide a direct comparison with other published data on superplasticity in the Ti-6Al-4V alloy processed by HPT, **Table 2**

TABLE 3 | Statistic results of chemical composition, thermomechanical processing and total elongation and deformation conditions for various ferrous superplastic alloys (Zhang et al., 2014b; Li et al., 2014; Cao et al., 2017; Han et al., 2017; Cao et al., 2018).

Alloy	Composition (wt%)	TMP	El, %	T_d, °C	$\dot{\varepsilon}$(1/s)
Duplex stainless steel	25Cr-7Ni-3Mo	HR + CR	1700	1000	1.7×10^{-2}
	22Cr-5Ni-3Mo		1510	980	3×10^{-4}
	22Cr-5.4Ni-3.2Mo	HR + CR	1260	950	1.5×10^{-3}
Ultra-high Carbon steel	1.3C-0.7Mn-0.1Si	HR + WR	700	630	1.3×10^{-4}
	1.6C-0.7Mn-0.3Si		760	630	1.3×10^{-4}
	1.9C-0.8Mn-0.3Si		380	650	1.7×10^{-4}
	1.7C-1.5Cr-2.4Al-0.5Mn	multi-pass	490	700	5×10^{-4}
	1.3C-3.0Si-1.5Cr-0.5Mn	HF + WR	1300	850	1.7×10^{-4}
	1.3C-2.3Mn-1.8Si-1.1Cr-1Al	HR + WR	720	780	2×10^{-3}
	1.3C-2Mn-1.8Si-1.0Cr	HR + WQ	900	750	1×10^{-4}
Medium Mn steel	0.05C-6.6Mn-2.3Al	HR + CR	1314	850	1×10^{-3}
	0.1C-5Mn-2Al	HR + CR	1190	850	1×10^{-3}
	0.1C-5Mn-2Al	HR	340	800	1×10^{-3}

Note: TMP, thermo-mechanical process; HR, hot rolling; WR, warm rolling; WQ, water quenching; CR, cold rolling.

summarizes the results reported under various parameters including initial microstructure and tensile elongation (Sergueeva et al., 2000; Sergueeva et al., 2002; Shahmir et al., 2018). All results showed high superplastic elongations but the maximum value of 815% was obtained. From this work, it was apparent that the initial grain size of the martensitic microstructure was smaller than the lamellar one and this would contribute to higher elongations, thus exhibiting exceptional superplasticity when compared with the lamellar microstructure.

SUPERPLASTICITY IN FE ALLOYS

The development of ferrous superplastic alloys allowed the mass production of complex parts at relatively low costs. For example, a promising superplasticity was found in some duplex stainless steels (DSS) and ultrahigh carbon steels (UCS) (Li et al., 2014; Zhang et al., 2014b). However, the requirements of high alloying contents (Cr, Ni, and Mo), high temperature or low strain rate hindered broad industrial applications for intricate parts. More recently, lean-alloyed Fe–Mn–Al–C steels (e.g., medium Mn steel, MMS) revealed an extraordinary superplasticity and they have significant potentials to be used as the next-generation automotive steels due to their high strength, excellent ductility, comparatively low density and material cost (Cao et al., 2017; Cao et al., 2018; Han et al., 2017). **Table 3** summarized the chemical composition, thermomechanical processing and total elongation and deformation conditions for various ferrous superplastic alloys (Zhang et al., 2014b; Li et al., 2014; Cao et al., 2017; Han et al., 2017; Cao et al., 2018).

The superplastic MMSs were produced via either hot rolling or cold rolling followed by rapid cooling or inter-critical annealing, which evolved into a fully lath-typed or equiaxed ferrite and austenite (α+γ) duplex structure, respectively.

Han et al. (2017) investigated the superplasticity of Fe-6.6Mn-2.3Al cold rolled alloy. The tensile specimens were heated to 1123 K, where the equilibrium volume fractions of both α and γ phases were almost identical, held for 5 min and then tested at various initial strain rates. The process of lamella shearing happened during cold rolling, so that the equiaxed (α+γ) structure was quickly developed at elevated temperatures. Accordingly, a maximum elongation of ~1314% was obtained at 1.0×10^{-3} s^{-1}. In contrast, the hot-rolled (HRed) lamellar structure induced high flow stresses at initial and steady states, making intergranular deformation occur more readily than GBS. This corresponds to a relatively low ductility of ~340% at 800°C and 10^{-3} s^{-1} (Cao et al., 2018). The low temperature or high strain rate superplasticity of medium Mn steels is believed as a result of ultra-grain refinement and the slow diffusion of Mn and Al elements.

GRAIN SIZE EFFECT ON SUPERPLASTICITY OF METALS

Taking into account the grain size effect on high-temperature deformation, a model on superplastic deformation was proposed by Lou and Woo (2002), based on the theory of GBS and the theory of cavity growth, as follows:

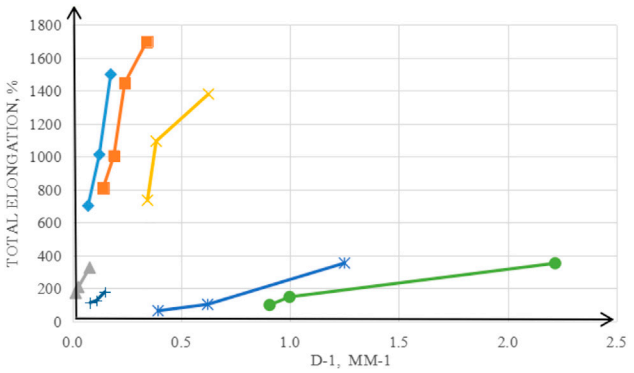

FIGURE 3 | Total elongation against inverse grain size for several superplastic materials. + Ti-6Al-4V deformed at 1200 K and 2.0 × 10^{-4} s^{-1}; Ternary brass deformed at 874 K and 1.67 × 10^{-4} s^{-1}; 7475 Al alloy deformed at 789 K and 3.0 × 10^{-4} s^{-1}; × Al-Mg-Sc alloy deformed at 698 K and 3.0 × 10^{-2} s^{-1}; × Al-14Ni-14Mn alloy deformed at 873 K and 1.0 s^{-1}; ● ZrO-dispersed Al deformed at 1727 K and 1.7 × 10^{-4} s^{-1} (Liu and Ma, 2011).

$$r_f + \frac{B}{d} = C_f exp(\varepsilon_f) \tag{1}$$

where B is defined as:

$$B = \left(\frac{45\Omega\delta}{Ab^2} - \frac{3\gamma}{2G}\right)\sqrt{\frac{AD_{gb}Gb}{\dot{\varepsilon}kT}} \tag{2}$$

where ε_f is the total elongation to fracture, C_f is an integrating constant, r_f is the valid radius of cavity in fracture, Ω is the atomic volume, δ is the grain boundary width, γ is the mean radius of cavity, b is the Burgers vector, D_{gb} is the grain boundary diffusivity, $\dot{\varepsilon}$ is the strain rate, k is the Boltzman constant, T is the absolute temperature, A is the dimensionless constant and G is the shear modulus.

The predictions of the model were compared with several published experimental data, as shown in **Figure 3** (Liu and Ma, 2011). It was apparent that the total elongation increased with decreasing the grain size at various strain rates, i.e., the linear relationship between total elongation and $1/d$ was kept in a strain rate range.

It is also well known that the contribution of GBS to the total macroscopic strain was estimated as being less than 70%, so the remainder should be accommodated by other existing mechanisms. In some cases, high dislocation activity was still visible, not only in the vicinity of interphase boundaries, but also within grains even after failure, verifying that GBS was accommodated by dislocation slip or climb mechanisms. Regarding the dislocation accommodating mechanism, a common resemblance was found with the Rachinger GBS effect. The process was generally controlled by the equilibrium subgrain size parameter λ, which can be expressed as (Alabort et al., 2015):

$$\lambda/b = \zeta\left(\sigma/\mu\right)^{-1} \tag{3}$$

where b is the magnitude of the Burgers' vector, σ is the flow stress, μ is the shear modulus and ζ is a constant. Given that average grain size (d) was constant, but λ was related to the imposed stress and hence, as a function of deformation conditions.

In the case of phases whose size $d>\lambda$, intragranular dislocations would form subgrains and even evolve into new grains upon straining; whereas for phases whose size $d<\lambda$, intragranular dislocations traveled through the softer phase, in favor of intragranular slip.

It is well known that the flow stress of materials is a function of deformation temperature T, grain size d and strain rate $\dot{\varepsilon}$during superplastic deformation, as below (Zhu and Langdon, 2004):

$$\dot{\varepsilon} = A\sigma^n d^{-p} D_0 \exp[-Q/(RT)]$$

where A is a constant, n is an exponent related to the flow stress, p is an exponent related to the grain size, Q is an activation energy, R is a gas constant. Thus, the strain rate can be found increase significantly when the grain size of materials is refined to a nano-scaled level. Langdon et al. reported that as the grain size is refined from 2 μm to 200 nm, the superplastic period is reduced from 20–30 min to 20–30 s.

CONCLUSION

This work summarized the dependence of superplasticity of various metals on grain size and shape, including Al alloy, Ti alloy and ferrous alloy, etc. The smaller grains can contribute to lowering the deformation temperature and/or raising the strain rate, which is beneficial for rapid superplastic forming of parts with nearly arbitrarily complex shapes at relatively low costs. In comparison with severe plastic deformation, most of metals processed by conventional plastic deformation were not superplastic because the imposed strains were insufficient to refine the size to the ultrafine or even smaller levels. Meanwhile, the superplasticity of metals can be significantly improved as well by tailoring the initial microstructural parameters (grain shape, phase fraction, grain size distribution etc.), which is crucial for developing novel superplastic metals with commercial application potential.

AUTHOR CONTRIBUTIONS

ZL and XH have the idea to start new research works in superplasticity. JH was responsible for collecting information, drawing figures and editing tables. The article was written by ZL and revised by XH.

REFERENCES

Alabort, E., Putman, D., and Reed, R. C. (2015). Superplasticity in Ti–6Al–4V: Characterisation, Modelling and Applications. *Acta Materialia* 95, 428–442. doi:10.1016/j.actamat.2015.04.056

Cao, W. Q., Huang, C. X., Wang, C. Y., and Weng, Y. Q. (2017). Dynamic Reverse Phase Transformation Induced High-Strain-Rate Superplasticity in Low Carbon Low alloy Steels with Commercial Potential. *Sci. Rep.* 7, 9199. doi:10.1038/s41598-017-09493-7

Cao, Z. X., Wu, G. L., Sun, X. J., Wang, C., Ponge, D., and Cao, W. Q. (2018). Revealing the Superplastic Deformation Behaviors of Hot Rolled 0.10C5Mn2Al Steel with an Initial Martensitic Microstructure. *Scripta Materialia* 152, 27–30. doi:10.1016/j.scriptamat.2018.03.046

Chokshi, A., Mukherjee, A., and Langdon, T. (1993). Superplasticity in Advanced Materials. *Mater. Sci. Eng. R: Rep.* 10, 237–274. doi:10.1016/0927-796x(93)90009-r

Chou, C. Y., Lee, S. L., Lin, J. C., and Hsu, C. M. (2007). Effects of Cross-Channel Extrusion on the Microstructures and Superplasticity of a Zn–22 wt.% Al Eutectoid alloy. *Scripta Materialia* 57, 972–975.

Edington, J. W. (1982). Microstructural Aspects of Superplasticity. *Mta* 13, 703–715. doi:10.1007/BF02642384

Fu, J., Ding, H., Huang, Y., Zhang, W. J., and Langdon, T. G. (2015). Influence of Phase Volume Fraction on the Grain Refining of a Ti-6Al-4V alloy by High-Pressure Torsion. *J. Mater. Res. Technol.* 4, 2–7. doi:10.1016/j.jmrt.2014.10.006

Han, J., Kang, S. H., Lee, S. J., Kawasaki, M., Lee, H. J., Ponge, D., et al. (2017). Superplasticity in a Lean Fe-Mn-Al Steel. *Nat. Commun.* 8, 751–757. doi:10.1038/s41467-017-00814-y

Higashi, K. (1994). Deformation Mechanisms of Positive Exponent Superplasticity in Advanced Aluminum Alloys with Nanoscale or Near-Nanoscale Grained Structures. *Mater. Sci. Forum* 170-172, 131–140. doi:10.4028/www.scientific.net/msf.170-172.131

Kaibbyshev, O. A. (2002). Fundamental Aspects of Superplastic Deformation. *Mater. Sci. Eng. A* 324, 96–102. doi:10.1016/s0921-5093(01)01407-1

Kawasaki, M., and Langdon, T. G. (2007). Principles of Superplasticity in Ultrafine-Grained Materials. *J. Mater. Sci.* 42, 1782–1796. doi:10.1007/s10853-006-0954-2

Kawasaki, M., and Langdon, T. G. (2011), Developing Superplasticity and a Deformation Mechanism Map for the Zn–Al Eutectoid alloy Processed by High-Pressure Torsion. *Mater. Sci. Eng. A*. 528, 6140–6145. doi:10.1016/j.msea.2011.04.053

Kim, J. S., Chang, Y. W., and Lee, C. S. (1998). Quantitative Analysis on Boundary Sliding and its Accommodation Mode during Superplastic Deformation of Two-phase Ti-6Al-4V alloy. *Metallurgical Mater. Trans. A* 29, 217–226. doi:10.1007/s11661-998-0174-2

Ko, Y. G., Kim, W. G., Lee, C. S., and Shin, D. H. (2005). Microstructural Influence on Low-Temperature Superplasticity of Ultrafine-Grained Ti–6Al–4V alloy. *Mater. Sci. Eng. A* 410-411, 156–159. doi:10.1016/j.msea.2005.08.080

Ko, Y. G., Lee, C. S., Shin, D. H., and Semiatin, S. L. (2006). Low-temperature Superplasticity of ultra-fine-grained Ti-6Al-4V Processed by Equal-Channel Angular Pressing. *Metallurgical Mater. Trans. A* 37, 381–391. doi:10.1007/s11661-006-0008-z

Komura, S., Horita, Z., Furukawa, M., Nemoto, M., and Langdon, T. G. (2001). An Evaluation of the Flow Behaviour during High Strain Rate Superplasticity in an Al-Mg-Sc alloy. *Metallurgical Mater. Trans. A* 32, 707–714. doi:10.1007/s11661-001-0087-9

Kumar, P., Xu, C., and Langdon, T. G. (2006). Mechanical Characteristics of a Zn–22% Al alloy Processed to Very High Strains by ECAP. *Mater. Sci. Eng. A* 429, 324–328. doi:10.1016/j.msea.2006.05.044

Langdon, T. G. (2009). Seventy-five Years of Superplasticity: Historic Developments and New Opportunities. *J. Mater. Sci.* 44, 5998–6010. doi:10.1007/s10853-009-3780-5

Langdon, T. G. (1982). The Mechanical Properties of Superplastic Materials. *Mta* 13, 689–701. doi:10.1007/BF02642383

Langdon, T. G. (1991). The Physics of Superplastic Deformation. *Mater. Sci. Eng. A* 137, 1–11. doi:10.1016/0921-5093(91)90312-b

Li, S. X., Ren, X. P., Ji, X., and Gui, Y. Y. (2014). Effects of Microstructure Changes on the Superplasticity of 2205 Duplex Stainless Steel. *Mater. Des.* 55, 146–151. doi:10.1016/j.matdes.2013.09.042

Liu, F. C., Ma, Z. Y., and Chen, L. Q. (2009). Low-temperature Superplasticity of Al–Mg–Sc alloy Produced by Friction Stir Processing. *Scripta Materialia* 60, 968–971. doi:10.1016/j.scriptamat.2009.02.021

Liu, F. C., and Ma, Z. Y. (2011). Superplasticity Governed by Effective Grain Size and its Distribution in fine-grained Aluminum Alloys. *Mater. Sci. Eng. A* 510, 548–558. doi:10.1016/j.msea.2011.10.018

Lou, T. P., and Woo, K. D. (2002). Influence of Grain Size on Fracture of Superplasticity. *Mater. Lett.* 52, 374–377. doi:10.1016/s0167-577x(01)00426-8

Maehara, Y., and Langdon, T. G. (1990). Superplasticity of Steels and Ferrous Alloys. *Mater. Sci. Eng. A* 128, 1–13. doi:10.1016/0921-5093(90)90090-P

Matsumoto, H., Yoshida, K., Lee, S. H., Ono, Y., and Chib, A. (2013). Ti–6Al–4V alloy with an Ultrafine-Grained Microstructure Exhibiting Low-Temperature–High-Strain-Rate Superplasticity. *Mater. Lett.* 98, 209–212. doi:10.1016/j.matlet.2013.02.033

Reddy, S. R., Bapari, S., Bhattacharjee, P. P., and Chokshi, A. H. (2017). Superplastic-like Flow in a fine-grained Equiatomic CoCrFeMnNi High-Entropy alloy. *Mater. Res. Lett.* 5 (6), 408–414. doi:10.1080/21663831.2017.1305460

Salishchev, G. A., MGaleyev, R., Valiakhmetov, O. R., Safiullin, O. N., Lutfullin, R. Y., Senkov, O. N., et al. (2001). Development of Ti–6Al–4V Sheet with Low Temperature Superplastic Properties. *J. Mater. Process. Technol.* 116, 265–268. doi:10.1016/S0924-0136(01)01037-8

Sergueeva, A. V., Stolyarov, V. V., Valiev, R. Z., and Mukherjee, A. K. (2000). Enhanced Superplasticiy in a Ti-6Al-4V alloy Processed by Severe Plastic Deformation. *Scripta Materialia* 43, 819–824. doi:10.1016/S1359-6462(00)00496-6

Sergueeva, A. V., Stolyarov, V. V., Valiev, R. Z., and Mukherjee, A. K. (2002). Superplastic Behaviour of Ultrafine-Grained Ti-6A1–4V Alloys. *Mater. Sci. Eng. A* 323, 318–325. doi:10.1016/S0921-5093(01)01384-3

Shahmir, H., Naghdi, F., Pereira, P. H., Huang, Y., and Langdon, T. G. (2018). Factors Influencing Superplasticity in the Ti-6Al-4V alloy Processed by High Pressure Torsion. *Mater. Sci. Eng. A* 718, 198–206. doi:10.1016/j.msea.2018.01.091

Tanaka, T., Makii, K., Kushibe, A., and Higashi, K. (2002). Room Temperature Deformation Behavior of Zn-22 mass%Al alloy with Nanocrystalline Structure. *Mater. Trans.* 43, 2449–2454. doi:10.2320/matertrans.43.2449

Tanaka, T., Makii, K., Kushibe, A., Kohzu, M., and Higashi, K. (2003). Capability of Superplastic Forming in the Seismic Device Using Zn-22Al Eutectoid alloy. *Scripta Materialia* 49, 361–366. doi:10.1016/S1359-6462(03)00328-2

Wang, Y. C., and Langdon, T. G. (2013). Influence of Phase Volume Fractions on the Processing of a Ti–6Al–4V alloy by High-Pressure Torsion. *Mater. Sci. Eng. A* 559, 861–867. doi:10.1016/j.msea.2012.09.034

Wu, L. H., Xiao, B. L., and Ma, Z. Y. (2016). Achieving superior Low-Temperature Superplasticity for Lamellar Microstructure in Nugget of a Friction Stir Welded Ti-6Al-4V Joint. *Scripta Materialia* 122, 26–30. doi:10.1016/j.scriptamat.2016.05.020

Xia, S. H., Wang, J., Wang, J. T., and Liu, J. Q. (2008). Improvement of Room-Temperature Superplasticity in Zn–22 wt.%Al alloy. *Mater. Sci. Eng. A* 493, 111–115. doi:10.1016/j.msea.2007.07.100

Xu, G. F., Cao, X. W., Duan, Y. L., Peng, X. Y., Deng, Y., and Yin, Z. M. (2016). Achieving High Strain Rate Superplasticity of an Al-Mg-Sc-Zr alloy by a New Asymmetrical Rolling Technology. *Mater. Sci. Eng. A* 672, 98–107. doi:10.1016/j.msea.2011.10.01810.1016/j.msea.2016.06.070

Yang, C.-F., Pan, J.-H., and Chuang, M.-C. (2008). Achieving High Strain Rate Superplasticity via Severe Plastic Deformation Processing. *J. Mater. Sci.* 43, 6260–6266. doi:10.1007/s10853-008-2909-2

Yoon, S., Ueji, R., and Fujii, H. (2015). Effect of Initial Microstructure on Ti–6Al–4V Joint by Friction Stir Welding. *Mater. Des.* 88, 1269–1276. doi:10.1016/j.matdes.2015.09.128

Zhang, H., Pradeep, K. G., Mandal, S., Ponge, D., Choi, P., Tasan, C. C., et al. (2014). Enhanced Superplasticity in an Al-Alloyed Multicomponent Mn–Si–Cr–C Steel. *Acta Materialia* 63, 232–244. doi:10.1016/j.actamat.2013.10.034

Zhang, N. X., Kawasaki, M., Huang, Y., and Langdon, T. G. (2015). Influence of Grain Size on Superplastic Properties of a Two-phase Pb-Sn alloy Processed by Severe Plastic Deformation. *J. Mater. Metall.* 14, 255–304.

Zhang, T. Y., Liu, Y., Sanders, D. G., Liu, B., Zhang, W. D., and Zhou, C. X. (2014). Development of fine-grain Size Titanium 6Al–4V alloy Sheet Material for Low Temperature Superplastic Forming. *Mater. Sci. Eng. A* 608, 265–272. doi:10.1016/j.msea.2014.04.098

Zhang, W. J., Ding, H., Cai, M. H., Yang, W. J., and Li, J. Z. (2018). Ultra-grain Refinement and Enhanced Low-Temperature Superplasticity in a Friction

Stir-Processed Ti-6Al-4V alloy. *Mater. Sci. Eng. A* 727, 90–96. doi:10.1016/j.msea.2018.03.009

Zhang, W. J., Ding, H., Pereira, P. H., Huang, Y., and Langdon, T. G. (2018). Grain Refinement and Superplastic Flow in a Fully Lamellar Ti-6Al-4V alloy Processed by High-Pressure Torsion. *Mater. Sci. Eng. A* 732, 398–405. doi:10.1016/j.msea.2018.07.010

Zhu, Y. T., and Langdon, T. G. (2004). The Fundamentals of Nanostructured Materials Processed by Severe Plastic Deformatioin. *JOM* 56, 58–63. doi:10.1007/s11837-004-0294-0

Conflict of Interest: The authors declare that the research was conducted in the absence of any commercial or financial relationships that could be construed as a potential conflict of interest.

Publisher's Note: All claims expressed in this article are solely those of the authors and do not necessarily represent those of their affiliated organizations, or those of the publisher, the editors and the reviewers. Any product that may be evaluated in this article, or claim that may be made by its manufacturer, is not guaranteed or endorsed by the publisher.

Advantages of publishing in Frontiers

OPEN ACCESS
Articles are free to read for greatest visibility and readership

FAST PUBLICATION
Around 90 days from submission to decision

HIGH QUALITY PEER-REVIEW
Rigorous, collaborative, and constructive peer-review

TRANSPARENT PEER-REVIEW
Editors and reviewers acknowledged by name on published articles

Frontiers
Avenue du Tribunal-Fédéral 34
1005 Lausanne | Switzerland

Visit us: www.frontiersin.org
Contact us: frontiersin.org/about/contact

REPRODUCIBILITY OF RESEARCH
Support open data and methods to enhance research reproducibility

DIGITAL PUBLISHING
Articles designed for optimal readership across devices

FOLLOW US
@frontiersin

IMPACT METRICS
Advanced article metrics track visibility across digital media

EXTENSIVE PROMOTION
Marketing and promotion of impactful research

LOOP RESEARCH NETWORK
Our network increases your article's readership